Dissertation

submitted to the

Combined Faculty of Natural Sciences and Mathematics

of Heidelberg University, Germany

for the degree of

Doctor of Natural Sciences

Put forward by

Martin Pauly

born in Frankfurt a.M.

Oral examination: October 13th, 2021

The Imprint of Spacetime:

from Networks to Particle Physics and Cosmology

Referees:

Prof. Dr. Astrid Eichhorn

Prof. Dr. Björn Malte Schäfer

Acknowledgements

First and foremost, I would like to thank my supervisor Astrid Eichhorn for creating a very respectful and fun environment, that not only prioritized science, but also personal development. Your positive energy always has been a source of great motivation. Thank you!

I would like to thank Prof. Björn Malte Schäfer for agreeing to referee this thesis.

I also would like to thank all the current and former members of Astrid's group for interesting discussions about physics, but also for being great company in the last years. A special "thank you" goes to Aaron, Alessia, Andreas, Antônio, Arslan, Fleur, Gustavo, Jan, João, Johannes and Rafael. I also would like to thank the (former) members of the Heidelberg Quantum Gravity group, especially Manuel, Stefan, Tobias and Masatoshi.

Another thank you goes to all my collaborators; to Santiago Casas, Georgios Karananas, Marvin Lüben, Mark Hindmarsh, Johannes Lumma, Passant Ali, Michael Scherer, Shouryya Ray and to Javier Rubio, whom I also would like to thank again for sharing a lot of valuable advice.

I would like to thank Aaron, Alessia, Andreas, Fleur, Gustavo, João, Johannes, Passant, Rafael and Robert for reading parts of this thesis and providing valuable feedback.

I am particularly grateful to the Studienstiftung for their support and to CP3 Origins at SDU for hosting me for an extended period of time.

I would like to thank Marc for many interesting and detailed discussions, but even more so for being a great office mate through all the ups and downs of the last three years. Without you this PhD would have been a lot less fun!

Finally, I would like to thank Mirka for her unwavering support. You cheered me up whenever I needed it and made sure I took a step back from work when that was necessary. Thank you for always being at my side!

All of the results presented in this thesis are based on work in collaboration with other scientists. In particular, the thesis draws on results from the following publications (in chronological order):

- Ref. [1]: **Safety in darkness: Higgs portal to simple Yukawa systems** - Astrid Eichhorn, Martin Pauly - *Phys.Lett.B 819 (2021) 136455* in Chap. 6

- Ref. [2]: **Constraining power of asymptotic safety for scalar fields** - Astrid Eichhorn, Martin Pauly - *Phys.Rev.D 103 (2021) 2, 026006* in Sec. 4.4, Chap. 5 and Chap. 6

- Ref. [3]: **Constraints on discrete global symmetries in quantum gravity** - Passant Ali, Astrid Eichhorn, Martin Pauly, Michael Scherer - *JHEP 05 (2021) 036* in Sec. 4.1 and Chap. 7

- Ref. [4]: **A sprinkling of hybrid-signature discrete spacetimes in real-world networks** - Astrid Eichhorn, Martin Pauly - preprint arXiv:2107.07325 in Chap. 2

- Ref. [5]: **Towards a Higgs mass determination in asymptotically safe gravity with a dark portal** - Astrid Eichhorn, Martin Pauly, Shouryya Ray - preprint arXiv:2107.07949 in Sec. 4.3.1 and 6.3.4

Material and figures from these articles will be used without further reference in the following. In addition some results in Sec. 5.4.3 were obtained in an ongoing project with Alessia Platania.
The following publications also appeared during the last three years, but their results are not discussed in detail in this thesis:

- **Scale-invariant alternatives to general relativity. III. The inflation-dark energy connection** - Santiago Casas, Georgios Karananas, Martin Pauly, Javier Rubio - *Phys.Rev.D 99 (2019) 6, 063512*

- **Phase transitions in the early universe** - Mark Hindmarsh, Marvin Lüben, Johannes Lumma, Martin Pauly - *SciPost Phys.Lect.Notes 24 (2021) 1*

Abstract

We study the link between spacetime and properties of physical systems in two settings.

First, we demonstrate how the embedding geometry constrains real-world networks, such as e.g. road networks or biological neural networks, by studying diffusion processes on such networks. Surprisingly, we find a resemblance between a class of nodes in some real-world networks and networks inspired by models of the fundamental structure of spacetime.

Second, we introduce asymptotically safe quantum gravity, a theory of quantum spacetime. Asymptotically safe quantum gravity could constrain models that aim at explaining three cosmological observations: the accelerating expansion of the universe today, a period of accelerated expansion in the early universe, and dark matter.

We strengthen indications that asymptotic safety quantum gravity flattens scalar potentials and explore consequences for said cosmological models. We find that for asymptotically safe models of the early universe it is challenging to reproduce the amplitude of spacetime fluctuations observed from this epoch.

Asymptotically safe quantum gravity could enhance predictivity in dark matter models: we find indications that an asymptotically safe extension of the Standard model by a dark scalar and a dark fermion could feature a single free parameter in the dark sector and might yield the observed amount of dark matter. The same model could also alter the Higgs boson mass predicted in asymptotic safety such that it matches present observations.

In addition, asymptotically safe quantum gravity could constrain whole classes of Standard Model extensions. We find indications that asymptotic safety might not permit a large class of models featuring a global discrete symmetry.

Zusammenfassung

Diese Arbeit untersucht, wie Raumzeit die Eigenschaften physikalischer Systeme beeinflusst.

Erstens prüfen wir, wie Netzwerke von ihrer einbettenden Geometrie beeinflusst werden. Dabei untersuchen wir beispielsweise Straßennetze und biologische neuronale Netze, indem wir Diffusionsprozesse auf diesen Netzwerken betrachten. Überraschenderweise finden wir Ähnlichkeiten zwischen einer Klasse von Knoten in einigen dieser Netzwerke und Netzwerken, die von Modellen der fundamentalen Struktur der Raumzeit inspiriert sind.

Zweitens führen wir asymptotische Sicherheit als eine Theorie der Quanten-Raumzeit ein. Asymptotische Sicherheit könnte Modelle beschränken, die darauf abzielen drei kosmologische Beobachtungen zu erklären: die beschleunigte Expansion unseres Universums heute, die beschleunigte Expansion des frühen Universums und dunkle Materie. Wir bestätigen, dass asymptotisch sichere Gravitation skalare Potentiale abflachen könnte, und untersuchen Konsequenzen für kosmologische Modelle. Wir entdecken, dass eine zentrale Herausforderung für asymptotisch sichere Modelle des frühen Universums darin besteht, die beobachtete Amplitude von Raumzeit-Fluktuationen zu reproduzieren.

Außerdem könnte asymptotische Sicherheit Dunkle-Materie-Modelle einschränken. Wir finden Anzeichen, dass eine asymptotisch sichere Erweiterung des Standardmodells um ein dunkles Skalar und ein dunkles Fermion mit Hilfe eines einzigen freien Parameters im dunklen Sektor die beobachtete Menge dunkler Materie erklären könnte. Das gleiche Modell könnte außerdem die Vorhersage der Higgs-Masse in asymptotisch sicheren Modellen so verändern, dass sie mit aktuellen Messungen übereinstimmt.

Schließlich könnte asymptotische Sicherheit ganze Klassen von Standardmodell-Erweiterungen einschränken. Wir finden Anzeichen, dass in asymptotisch sicheren Modellen eine Klasse von globalen diskreten Symmetrien nicht realisiert werden kann.

Contents

The Imprint of Spacetime

Observations of gravitational physics and experiments in particle physics have both progressed rapidly in the last decade. The observation of gravitational waves from a black hole binary merger [6] and the first picture of a black hole [7] allow probing gravitational physics in curvature regimes previously inaccessible. At the same time, the discovery of the Higgs particle [8, 9] adds the last remaining piece to the Standard Model (SM) and is a milestone for our understanding of particle physics.

While both, gravitational physics and particle physics have made impressive progress, gravitational observations in the context of cosmology tell us that there is much more to discover.

The Friedman equation

$$1 = \Omega_{\mathrm{DE},0} + \Omega_{M,0} + \Omega_{R,0} + \Omega_{k,0} \tag{1.1}$$

evaluated today describes the various components of our universe [10].
The first component $\Omega_{\mathrm{DE},0} = 0.69$ is an approximately constant energy density. We have measured that this dark energy causes our universe to expand in an accelerated way, but cannot explain its composition within the SM.
The second component $\Omega_{\mathrm{M},0} = 0.31$ is matter. However, it is not just SM matter. The SM only explains about 16% of all the matter we observe. According to present observations, the remaining 84% only interact gravitationally. They contribute to forming structures but do not produce an optical signal. We do not know what this dark matter is made of.
The third component $\Omega_{\mathrm{R},0} = 8.2 \cdot 10^{-5}$ is radiation, with a substantial fraction contributed by the cosmic microwave background. The spectrum of its fluctuations might carry the imprints of a phase of accelerating expansion in the early universe. Such a phase of inflation also naturally explains the vanishing of the final component, curvature $\Omega_{k,0} \approx 0$. However, there is no accepted model of what drove such a phase of accelerated expansion in the early universe.

We hence remain in the dark about approximately 95% of the energy content of our universe, providing a clear observational reason to extend our description of gravity and the SM. A theoretical reason arises because neither our description of gravitational physics, nor the SM remain theoretically consistent when describing short length scales.

Gravitational physics breaks down close to the center of a black hole. For a non-rotating, uncharged black hole of mass M the Kretschmann scalar $R_{\mu\nu\rho\sigma}R^{\mu\nu\rho\sigma} = 48\bar{G}^2 M^2/r^6$ that measures curvature, diverges if the radial coordinate r approaches 0. Here, $\bar{G}$ is Newton's constant. Such a divergence cannot be physical and signals the breakdown of general relativity.
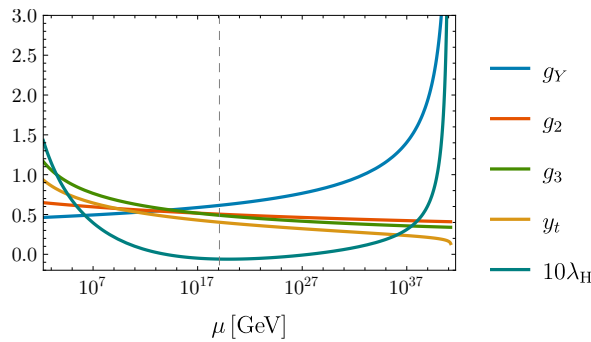
Fig. 1.1.: Running of the SM couplings at one loop. The g_i are the various gauge couplings, y_t is the top quark Yukawa coupling and λ_H is the Higgs quartic coupling. The dashed gray line marks the Planck scale. Here we neglect gravity.

SM physics breaks down at short distances. The SM couplings change depending on the observation scale. For short distances the U(1) gauge coupling and the Higgs quartic coupling grow and seem to diverge (at least in perturbative and non-perturbative approximations [11–13]), signaling the breakdown of the SM at such short length scales, see Fig. 1.1. Fascinatingly, the coupling values of the SM, and in particular the measured value of the Higgs mass $M_\mathrm{H} = 125.3 \pm 0.2\,\mathrm{GeV}$ [14] put all divergences to scales much shorter than the Planck length, indicating that gravity could play a central role in curing such divergences.

Given observational and theoretical reasons to extend our description of gravity and the SM the question becomes *how*. Gravity describes how a particle curves spacetime. The SM is a theory of quantum fields and quantum particles. The quantum nature implies that a particle's location cannot be determined with absolute certainty. But how does this uncertainty affect the curvature of spacetime? To answer this question one requires a theory of quantum gravity.

The scale at which such a theory of quantum gravity is expected to play a role is the Planck scale $M_\mathrm{Pl} = 1.22 \cdot 10^{19}\,\mathrm{GeV}$. This scale is far beyond the reach of present colliders that probe scales up to $\sim 10^4\,\mathrm{GeV}$. In order to relate to observations we hence need to find remnants of trans-Planckian spacetime physics at observational scales. Such an imprint of quantum spacetime on observational physics will be the main topic of this thesis.

Before we explore the link between the trans-Planckian physics of spacetime and the properties of matter, we study a similar link on more accessible scales. We explore how the geometry of spacetime leaves an imprint on the physical properties of objects and their relations. As an example in a simple spatial geometry consider the network of roads in a two-dimensional landscape. As we will show in more detail in Chap. 2, road networks provide a paradigmatic example of networks, that are shaped by their spatial embedding. We then explore more complex real-world networks, such as the internet or biological neural networks. These are still embedded in a space, but also feature connections between nodes at large spatial distance. These "shortcuts" effectively transmit information between parts of the network that are far apart. They also provide a link to the physics of spacetime. Networks that could describe spacetime, i.e. causal sets, feature similar "shortcuts". We compare real-world networks embedded in space to networks describing spacetime. Networks representing spacetime might

provide a relevant template to describe the physical properties of real-world networks. They provide one example of how spacetime might leave its imprint on matter on classical scales.

We then explore how quantum fluctuations of spacetime at trans-Planckian scales might leave an imprint on matter. To describe these scales we introduce a candidate for a quantum theory of spacetime in Chap. 3: asymptotically safe quantum gravity. Asymptotically safe quantum gravity realizes an additional symmetry, quantum scale symmetry, at trans-Planckian scales. Quantum scale symmetry can be achieved when balancing quantum fluctuations of spacetime and matter. This balance imposes constraints on how the gravity and the matter sector interact on short length scales. These interactions on short length scales determine physics when zooming further out. Zooming out to length scales within our observational reach, the quantum fluctuations of spacetime and matter might leave an imprint on observations.

We explore this link between the quantum fluctuations of spacetime and observable physics. We first go into detail on how quantum scale symmetry might constrain the matter sector and in particular the Standard Model in Chap. 4. We then extend the Standard Model by additional degrees of freedom and turn to the three observational challenges mentioned above: the accelerated expansion of our universe today due to dark energy, a period of inflation in the early universe and dark matter. Each of these challenges has led to a plethora of new models that go beyond the SM. Most of these models feature many free parameters. The resulting parameter space allows for a wide range of phenomenological consequences. However, typically only few points in the parameter space are consistent with quantum scale symmetry. As a result quantum scale symmetry could improve predictivity in these models.

We explore the implications for the accelerating universe both at early and late times in Chap. 5. We focus on a single scalar field as a simple model to examine how quantum scale symmetry could constrain dark energy and inflation. In Chap. 6 we discuss how quantum scale symmetry might constrain a simple dark-matter model, the Higgs portal model. We then introduce a toy model that features an additional Dirac fermion and explore how an extension of this model to the full SM compares to observation. We discover that it could provide the correct amount of dark matter. Additionally, such an extension can modify particle properties. We investigate under which conditions it could modify the Higgs mass predicted within a quantum scale symmetric model.

Beyond constraints on individual models, quantum scale symmetry might also allow ruling out whole classes of SM extensions. In Chap. 7 we explore how quantum scale symmetry might constrain the symmetries of the matter sector. In particular, we study a toy model and investigate if global discrete symmetries can be realized in the presence of quantum scale symmetry.

In Chap. 8 we summarize our conclusions and provide an outlook.

Spacetime and Networks

<div style="text-align: right">2</div>

Before we consider quantum spacetime we explore the imprint of spacetime on classical structures. In particular, we focus on networks.

Networks describe many phenomena, ranging from the fundamental structure of spacetime [15] to biological neural networks [16–18]. Networks that describe spacetime are networks *of a geometry*. Networks describing neural networks are networks embedded *in a geometry*. The embedding geometry determines some of the network's properties [19]. As a prime example road networks cover the two-dimensional surface of the earth. This spatial embedding leaves an imprint on some properties of road networks. One of these properties is the spectral dimension of a network which we will introduce below. It depends on the network's embedding space(time).

A road network provides a prototypical example for a network that encodes properties of the underlying space. In a road network, roads typically connect points at small spatial distance. In many other networks points at large spatial distance are connected via "shortcuts". Such "shortcuts" can connect two nodes at large Euclidean distance. The two nodes are far away from each other, but close in the network. To describe these "shortcuts" in a geometric way, one needs to alter the prescription to measure distances. The prescription to measure distances is encoded in the metric. Instead of using the standard flat Euclidean metric, a possibility that has been proposed in the literature [20, 21] and applied to real-world examples [22–24], is to measure distances according to a hyperbolic metric. In a hyperbolic metric, points that lie at large flat Euclidean distances can be close. The same is true in the Minkowski metric. In the Minkowski metric, defined by the line element

$$\mathrm{d}s^2 = -\mathrm{d}t^2 + \sum_{i=1}^{d-1} \mathrm{d}x_i{}^2 \tag{2.1}$$

time differences $\mathrm{d}t$ and spatial differences $\mathrm{d}x_i$ can compensate. Points that would lie far apart in a Euclidean metric can be arbitrarily close in the Minkowski metric.

Networks constructed according to the Minkowski metric might hence resemble real-world networks. To explore this possibility, we investigate (i) which imprints the embedding geometry leaves on real-world networks and (ii) if networks constructed according to the Minkowski metric play a role in real-world networks. We relate embedding geometry and network, as well as different networks, by computing the spectral dimension, that we introduce in more detail in Sec. 2.1. First, we measure the spectral dimension for synthetic networks generated according to a Euclidean, a Lorentzian and a hybrid metric in Sec. 2.2. The hybrid metric measures distances with a Lorentzian signature at short Euclidean distances and with a Euclidean signature at large Euclidean distances. We also measure the spectral dimension for synthetic networks that feature the small-world property. The synthetic networks depend on

their embedding space(time) in different ways. They provide us with templates that allow to compare with real-world networks to explore how those depend on their embedding spaces. Second, we explore real-world networks, i.e. road networks, a network representation of the internet and neural networks, in Sec. 2.3. We apply our templates to explore how these networks depend on their embedding.

We focus on the spectral dimension as it can easily be computed for undirected, connected networks, and it is particularly well suited to capture information about the embedding space(time) that is not described by other tools such as the degree distribution.

2.1 Diffusion and Scale-Dependent Spectral Dimension

A random walk on a smooth d-dimensional manifold is described in terms of the probability distribution $p(t, x, x_0)$ that solves the diffusion equation

$$\frac{\partial p(t, x, x_0)}{\partial t} = \triangle p(t, x, x_0). \tag{2.2}$$

In flat space the solution for initial conditions $p(0, x, x_0) = \delta(x - x_0)$ has the form

$$p(t, x, x_0) = \frac{1}{(4\pi t)^{d/2}} \exp\left(-\frac{(x - x_0)^2}{4t}\right), \tag{2.3}$$

In particular, the probability to return to the origin x_0 of the random walk is given by $p(t, x = x_0, x_0) = (4\pi t)^{-d/2}$. One can then define the spectral dimension

$$d_s = \lim_{t \to 0} \left(-2 \frac{\mathrm{d} \log\left(p(t, x = x_0, x_0)\right)}{\mathrm{d} \log(t)}\right). \tag{2.4}$$

In the limit $t \to 0$ the spectral dimension agrees with the topological dimension, $d_s = d$.

To adapt this expression to a network let us briefly introduce the relevant terminology [25]. Networks[1] consist of two sets (G, E), with G the set of nodes and E the set of edges connecting the nodes. In undirected networks an edge connects two nodes, while in a directed network it features a direction from node i to j. For each node, the node degree $\deg_i$ counts the number of edges attached to a node i. Traversing the edges allows to explore the graph. Starting from any node i, the path to a node j that requires traversing the smallest number of edges is the shortest path. The longest shortest path is the diameter of a network.

---

[1]Depending on the area of application networks are also called graphs. We will use both terms interchangeably in the following.

Consider a random walk on a network starting at a node x_0. At each step the walker chooses among the outgoing edges of its current node and moves along one of the edges to a new node. In analogy to Eq. (2.4) one defines the *spectral dimension* as

$$d_{\text{spec}}(\sigma) = -2 \frac{\mathrm{d} \log(p(\sigma, x = x_0, x_0))}{\mathrm{d} \log(\sigma)} \tag{2.5}$$

for a random walk. Here, σ measures the diffusion time, i.e. the number of discrete diffusion steps that the walker took. We define d_{spec} to depend on σ instead of taking the limit $\sigma \to 0$.

For small diffusion times the return probability strongly oscillates. As one example, for a regular grid the walker only returns to the origin after an even number of steps. To avoid these oscillations we introduce a parameter $\delta \in [0, 1]$. The walker remains at its current position with probability $1 - \delta$ and moves to one of the neighboring nodes with probability δ. In the following, informed by our numerical experiments, we set $\delta = 1/2$.

With increasing diffusion time σ the random walker covers more and more of the graph. For a finite connected graph the walker will cover the full graph after a finite time and approach an equilibrium distribution. As one example, in equilibrium in an unweighted graph every node i is visited with probability $p_i = \frac{1}{2|E|} \deg_i$, where $|E|$ is the total number of edges. The probability $p_i(\sigma) \approx$ const becomes approximately constant for large σ. As a consequence $\partial_\sigma p_i \approx 0$ and the spectral dimension tends to zero due to the finite size of the graph.

We explore the spectral dimension for various graphs by performing the above procedure computationally, see App. B.1 for details. We evaluate the propagation of the full probability distribution on the graph, measure the return probability as a function of σ and then evaluate Eq. (2.5) numerically by computing

$$d_{\text{spec}}(\sigma) = -2 \frac{\sigma}{p(\sigma, x = x_0, x_0)} \frac{\Delta p}{\Delta \sigma}(\sigma, x_0) \tag{2.6}$$

with

$$\frac{\Delta p}{\Delta \sigma}(\sigma, x_0) = \frac{p(\sigma + 1, x = x_0, x_0) - p(\sigma - 1, x = x_0, x_0)}{2}. \tag{2.7}$$

As an aside, we notice that the spectral dimension has been applied to study spacetime at short scales in various quantum gravity approaches. In a continuum setting, assuming an asymptotically safe description of spacetime (see also Sec. 3) the spectral dimension reduces to $d_s = 2$ in the ultraviolet (UV) [26, 27]. The scale dependence of the spectral dimension closely matches the one found in approaches, where one triangulates spacetime in terms of small building blocks [28]. In these approaches the spectral dimension has been studied in Refs. [29, 30] in the context of causal dynamical triangulations, and in Ref. [31] in the context of Euclidean dynamical triangulations. Similarly, quantum geometries inspired by loop quantum gravity feature a spectral dimension $d_s = 2$ on short scales [32]. For a brief discussion of the spectral dimension at short scales in causal sets we refer to Sec. 2.2.2 as well as Refs. [33, 34]. Even theories based on different symmetry assumptions such as Horava-Lifschitz gravity [35] or non-commutative theories [36] feature a decreasing

spectral dimension on short scales. An agreement in the spectral dimension does not imply that the corresponding spacetimes agree, and indeed there are subtleties on how to set up a random walk in spacetimes featuring a non-integer dimension [37]. However, in many approaches one observes a dimensional reduction for short length scales.

2.2 Synthetic Networks

The simple building blocks of a network permit to construct many types of networks. To establish a baseline in exploring the structure of real-world networks, we introduce two types of synthetic networks. We first study networks that can be embedded into space(time) and are constructed according to (a) a Euclidean metric, (b) a Lorentzian metric and (c) a hybrid metric. We then study synthetic networks that exhibit a property, which is also found in many real-world networks: small-world networks.

On each of these synthetic networks one can perform random walks that will lead to a scale-dependent spectral dimension for that network.

2.2.1 Networks in Euclidean Space

As a first example we consider a graph that spans a $d = 2$ torus. The corresponding spectral dimension is shown in Fig. 2.1. The spectral dimension exhibits four regimes:

1. For $\sigma \approx 50$, the walker explores the local neighborhood and encounters an approximately $d = 2$ surface. Curvature effects and the finite extent are negligible.

2. For $\sigma \approx 750$, the finite extent in one direction becomes relevant, the walker has fully covered the torus in this direction and explores the other direction. The random walk hence is effectively one-dimensional.

3. For $\sigma \approx 1500$, the walker has covered the full graph, the spectral dimension decays exponentially.

4. For $\sigma \to \infty$, the probability distribution is equilibrating, the spectral dimension approaches zero.

The different regimes illustrate, how the spectral dimension allows recovering spatial information from a given graph at different scales. The scale is set in terms of the diffusion time σ, or correspondingly the distance that the diffusor was able to cover. Note, that the spectral dimension measures more than just the number of nearest neighbors: the tessellation of a $d = 2$ plane with triangles features six neighbors for every node, as does a regular $d = 3$ lattice. Nevertheless, the spectral dimension is able to distinguish between these two structures.
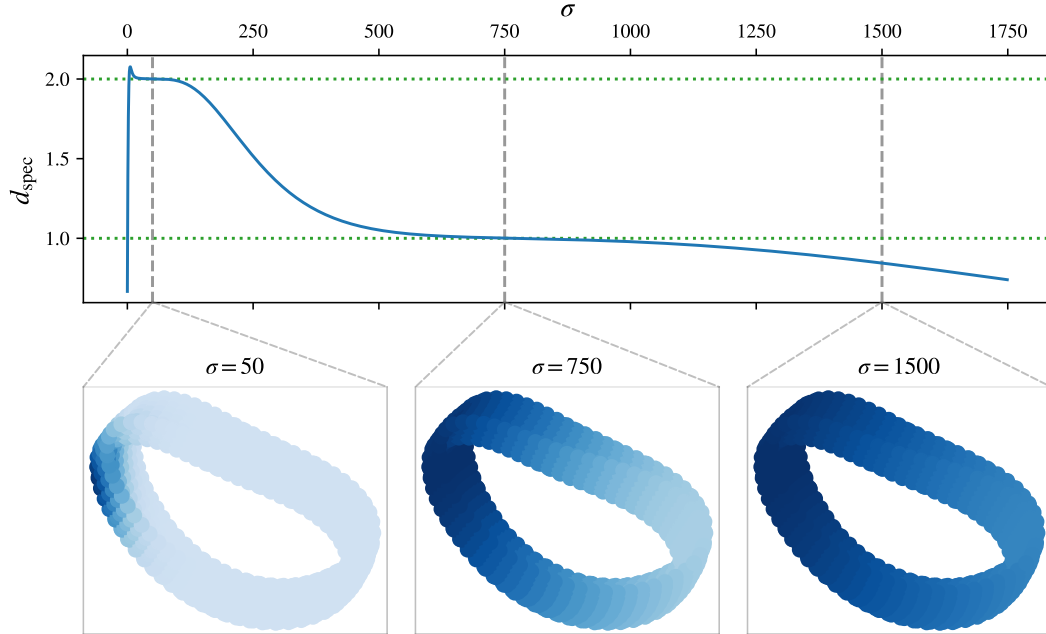
Fig. 2.1.: Random walk on a graph that represents a torus of 20×60 nodes. The three lower panels display the probability distribution at different steps in time. The darkest shade of blue is normalized to the maximum probability for each of the graphs. The green horizontal dotted lines mark $d_{\mathrm{spec}} = 1$ and $d_{\mathrm{spec}} = 2$, respectively.

Next, we explore the effect of adding non-localities. For this we consider a network embedded into the circle S^1 with 1000 nodes. The spectral dimension approaches $d_{\mathrm{spec}} = 1$ and decays for large diffusion times, see the left panel of Fig. 2.2. We then add random additional connections to the ring [38, 39]. To regulate the amount of non-locality, we first constrain the length of the additional connections to be $l \leq l_{\mathrm{max}} = 10$. The presence of additional connections modifies the spectral dimension in two ways: For short diffusion times the additional local connections lead to an increase in the spectral dimension, as the walker has more edges to explore. For large diffusion times the spectral dimension decays earlier in the presence of additional connections, as these connections reduce the diameter of the graph.

Next, we add connections between randomly selected nodes and do not restrict their length, see the right panel of Fig. 2.2. These additional connections provide "shortcuts", connecting nodes that otherwise would lie very distant. As a result, the spectral dimension develops a minimum at short diffusion times. The spectral dimension then quickly decays due to the smaller diameter of the resulting graph. The unrestricted non-local connections modify the spectral dimension on all scales, the spectral dimension does not exhibit an intermediate plateau anymore.

2.2.2 Networks in Lorentzian Spacetime

Next, we study synthetic networks constructed according to a Lorentzian metric. As a blueprint for these networks we consider causal sets.
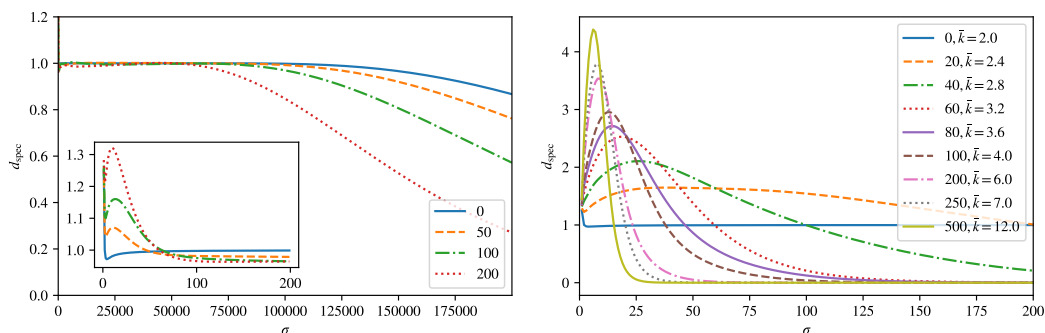
Fig. 2.2.: (left) Spectral dimension for a ring with 1000 nodes. We add $0, 50, 100$ and 200 new connections between random nodes (different colors). The maximum length of new connections is $l_{\max} = 10$. (right) Spectral dimension for a ring with 100 nodes. We add new connections between random nodes without restricting their length. We also indicate the average degree $\bar{k}$.

Causal sets model spacetime as a fundamentally discrete set of spacetime events x that are either causally related or unrelated [15]. More formally, a set C with an order relation $\prec$ is called a causal set if it is [40]:

1. Acyclic: $x \prec y$ and $y \prec x \Rightarrow x = y \quad \forall x, y \in C$

2. Transitive: $x \prec y$ and $y \prec z \Rightarrow x \prec z \quad \forall x, y, z \in C$

3. Locally finite: $\forall x, y \in C : |\mathrm{Fut}(x) \cap \mathrm{Past}(y)| < \infty$

where $|\cdot|$ is the cardinality and $\mathrm{Fut}(x) = \{y \in C | x \prec y, x \neq y\}$, $\mathrm{Past}(x) = \{y \in C | y \prec x, x \neq y\}$. Intuitively, axiom (1) excludes closed time-like curves. Axiom (3) enforces discreteness as it only allows finitely many points in any given interval.

The resulting set of events and relations define a partially ordered set. The partially ordered set can be represented as a directed acyclic graph, with events representing nodes and a causal relation $x \prec y$ represented by a directed edge between nodes x and y. The partially ordered set is able to capture the causal structure of a metric for scales larger than the discreteness scale [40]. Discreteness here is not just a regularization, that can be removed by sending the corresponding scale to zero. Instead, spacetime is fundamentally discrete at a scale that is typically assumed to be the Planck scale.

To construct a causal set that approximates a given manifold one places events onto the manifold. Placing these events regularly, e.g. in a grid, breaks Lorentz invariance at microscopic scales. One expects that such microscopic Lorentz invariance breaking could also lead to a macroscopic breaking of Lorentz invariance, and hence might conflict with experimental constraints [41]. Lorentz invariance can be maintained if one sprinkles points randomly according to a Poisson process with probability density [42]

$$P(n, V) = \frac{1}{n!} (\rho V)^n e^{-\rho V} \tag{2.8}$$

describing the probability to find n points within a volume V. Here ρ is the sprinkling density. The sprinkling density sets the fundamental scale of discreteness. When
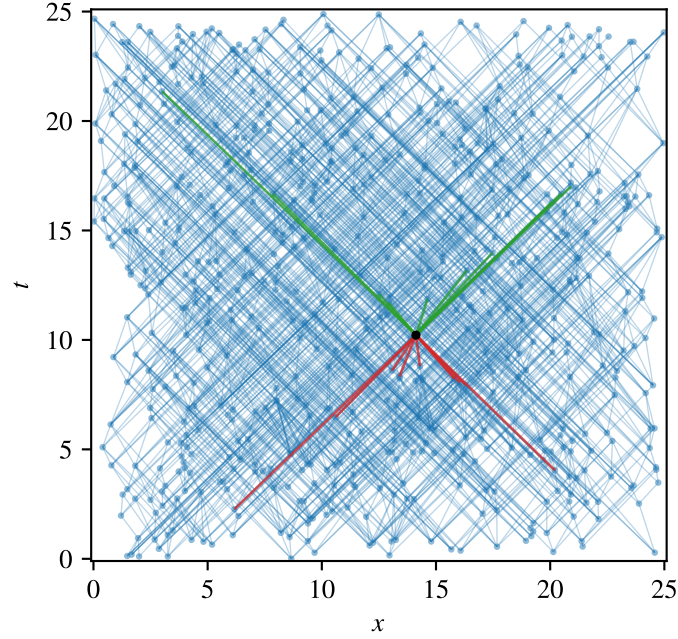
Fig. 2.3.: We show an example for a causal set obtained by sprinkling into $1 + 1$ Minkowski space. One element is singled out in black. The red links are those that connect the black element to elements in its past without intermediate nodes, green links are the corresponding future links. We display only direct links and not those that can be inferred from transitivity.

constructing a causal set that represents a d-dimensional manifold that scale is typically chosen to be $\rho \sim M_{\mathrm{Pl}}^d$. To obtain a causal set from a given manifold, in practice, one sprinkles points onto the manifold according to (2.8). By studying whether events are space-like or time-/light-like one then determines which events are connected. Here, we compute the transitive reduction of the resulting graph, i.e. we only consider those links that are not implied by transitivity.

In the following we focus on causal sets of Minkowski space. A sprinkling into $d = 1+1$ Minkowski space is illustrated in Fig. 2.3. The resulting causal sets exhibit long (in a Euclidean metric) connections, almost parallel to Minkowski null geodesics, i.e. the light cone. For a $d = 1 + 1$ dimensional infinitely extended Minkowski spacetime the number of such connections will diverge: the number of points as a function of the rapidity $\eta = \arctan\left(\frac{x+t}{x-v}\right)$ scales as $\sim \frac{1}{\sin(\eta)\cos(\eta)}$ and diverges for $\eta = 0$ and $\eta = \pi/2$. Put differently, one point in the causal set representing $d = 1 + 1$ Minkowski space will be connected to infinitely many points that are arbitrarily far away (measured with a Euclidean metric).

This intrinsic non-locality is reflected in the properties of the resulting graph. The ability to bridge large Euclidean distances with connections close to the light cone allows relating far-away points with very few hops, see also Ref. [43]. To illustrate this behavior we measure the shortest path length in a causal set that approximates d-dimensional Minkowski space. We consider the undirected version of the corresponding graph and vary the number of nodes N. For 10% of the nodes we compute the distance to all other nodes. We then average over the result. In Fig. 2.4 we show the mean shortest path length for varying d. For $d = 2, 3$ one observes that the shortest
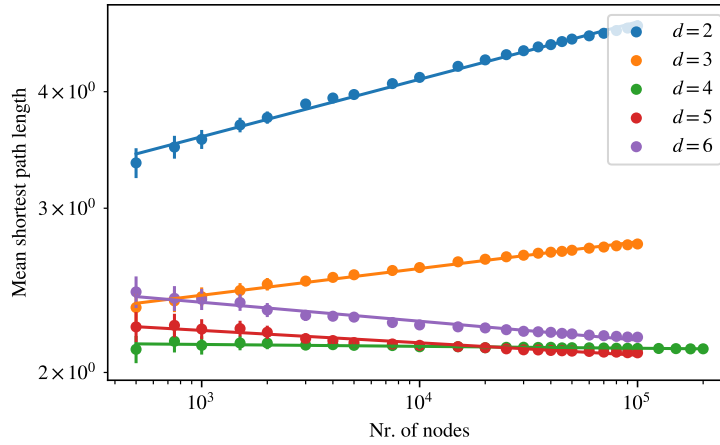
Fig. 2.4.: Mean shortest path length between two randomly selected points for a causal set that approximates d-dimensional Minkowski space. Here, d is the number of spacetime dimensions. For each N we consider 10% of all points (chosen randomly) when computing the mean shortest path length. The errorbars indicate the estimated standard error of the mean.

path length increases logarithmically as a function of the total number of nodes N. For $d = 4$ the shortest path length stays approximately constant. For $d > 4$ the shortest path length decreases, signaling that the addition of nodes decreases the average distance between nodes.

This result can be qualitatively understood by an analytical argument, see App. B.2. In this appendix, we estimate the probability of two points at distance T to be connected via exactly one intermediate node in d-dimensional Minkowski space. In the limit of a large separation T, this probability vanishes for $d = 2, 3$, it approaches a finite value smaller than one for $d = 4$ and approaches one for $d > 4$. This qualitatively agrees with the scaling of the mean shortest path length and confirms that for high-dimensional causal sets distances in the network decrease as a function of network size.

We proceed to study the spectral dimension on a causal set. We ignore the direction of the edges and instead perform a random walk on the corresponding undirected graph. Note, that the diffusion time σ is unrelated to the time-coordinate in the embedding manifold of the causal set.

In Fig. 2.5 we show the spectral dimension for a causal set corresponding to $d = 1 + 1$ Minkowski space. The causal set's large degree and high connectivity allow for rapid equilibration of the random walk. As a consequence the spectral dimension peaks at small σ and then decays quickly towards zero.

At first sight the peak in the spectral dimension at small σ appears to contradict the dimensional reduction observed in various approaches to quantum gravity. The peak in the spectral dimension is more easily understood, if one considers a different but related definition of the spectral dimension, the causal spectral dimension [44]. The causal spectral dimension depends on the meeting probability of two random walks respecting the direction in a causal set and starting at the same point. An increasing spectral dimension implies that it becomes increasingly unlikely that two random
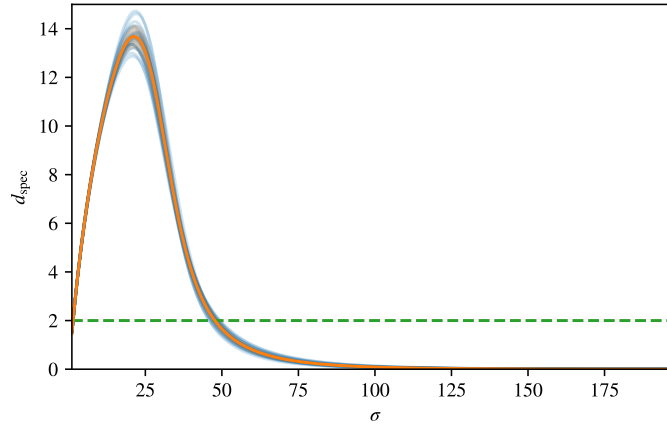
Fig. 2.5.: We show the spectral dimension for a causal set embedded into a $d = 1 + 1$ dimensional Minkowski spacetime with $N = 10^6$ elements. The green dashed line corresponds to $d_{\text{spec}} = 2$.

walkers meet. Conversely, one can think of two space-like points to be increasingly causally disconnected, light cones shrink to lines and geodesics experience a locally $d = 1 + 1$ dimensional space, leading to "asymptotic silence" [45, 46]. Results supporting this interpretation have been obtained in Ref. [33] and Ref. [34], the latter for the first time studying the spectral dimension on spatial hypersurfaces only. This interpretation could reconcile the large observed spectral dimension with the observation of dimensional reduction in other quantum gravity approaches.

In passing, let us notice that many other dimensional estimators have been applied in the context of causal sets: the Myrheim-Meyer dimension [47, 48] compares the number of causal relations of a given length to the number of nodes that occur in both, the future of one node x and the past of another one y. The mid-point scaling dimension relates the number of elements in the causal past and future to the total number of elements [49]. For other estimators see, e.g., Ref. [50] that estimates the dimension from measuring the probability $P(m)$ of a link of length m to occur, and Ref. [51] for variations of this approach. It would be interesting to study those in the context of real-world networks, see Ref. [52] for an example.

2.2.3 Networks in a Hybrid Metric

In a Euclidean metric points at a fixed distance l_{fix} to a point x lie on a sphere. All points at distances $l \leq l_{\text{fix}}$ lie inside a sphere of finite volume. Graphs constructed according to this metric have finite degree. In a Lorentzian metric points at a fixed distance l_{fix} to x lie on a hyperbola. All causally related points at distances $l \leq l_{\text{fix}}$ lie between this hyperbola and the light cone emanating from x. The corresponding volume is infinite, see Fig. 2.6. Graphs constructed according to this metric have infinite degree.

The non-locality associated with a Lorentzian metric permits the existence of "shortcuts" connecting points distant in a Euclidean metric. At the same time it leads to a diverging degree. To allow for the existence of "shortcuts", but also enforce a finite degree we introduce a cutoff L. We construct a network according to a Lorentzian
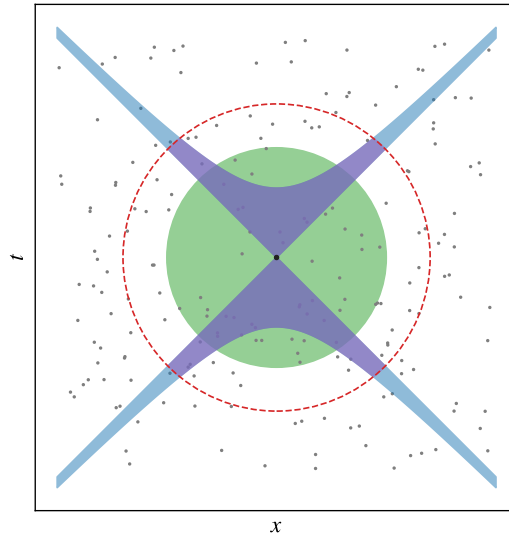
Fig. 2.6.: We illustrate regions of small Euclidean distance (green) and small Lorentzian distance (blue). These regions host the majority of the nearest neighbors for the node in the center (black). When constructing a network according to a Lorentzian metric, but with a cutoff L (red, dashed), points are effectively distributed according to a hybrid metric singling out the volume in purple.

metric, but do not permit connections with a *Euclidean* distance longer than a cutoff L. The resulting network effectively implements a hybrid metric, see the purple region in Fig. 2.6.

The effect of a cutoff L was first explored in Ref. [44]. It slows down the rapid diffusion in a causal set. The spectral dimension for a causal set constructed with a Euclidean cutoff L in $d = 1 + 1$ dimensional Minkowski space still exhibits a peak at small σ, see Fig. 2.7. For intermediate σ it approaches $d_{\mathrm{spec}} = 2$, before it decays for large σ as the random walk equilibrates.

2.2.4 Small-World Networks

Many real-world networks exhibit many "shortcuts" and are highly connected. The resulting networks are known as small-world networks. The prototypical model for such networks is the Watts-Strogatz model [53]. In the Watts-Strogatz model one again considers N nodes embedded into the circle S^1. Each node is connected to its $\bar{k}/2$ right neighbors with an undirected edge. Each of the connections is then rewired with probability β such that no connection appears twice and that no node is wired to itself. The resulting network exhibits small-world properties: while there still is a notion of a local neighborhood, it exhibits edges that connect remote points in the network. The distance between two randomly chosen nodes scales as $\sim \log(N)$ with the number of nodes N in such a network.

For an appropriate choice of β the spectral dimension for a Watts-Strogatz graph peaks at two values of σ, see Fig. 2.8. The first maximum at small σ is determined by the local neighborhood: the random walk explores the $\bar{k}$ nearest neighbors and the corresponding peak in the spectral dimension increases when increasing $\bar{k}$. The second
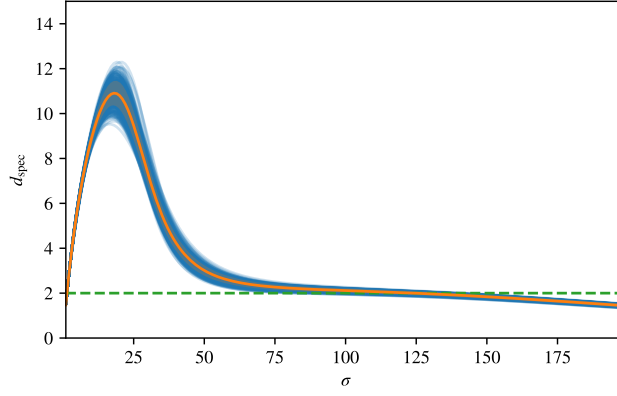
Fig. 2.7.: We show the spectral dimension for a causal set embedded into a $d = 1 + 1$ dimensional hybrid spacetime with $L = 30$ and $N = 10^6$ nodes. The green dashed line corresponds to $d_{\text{spec}} = 2$.
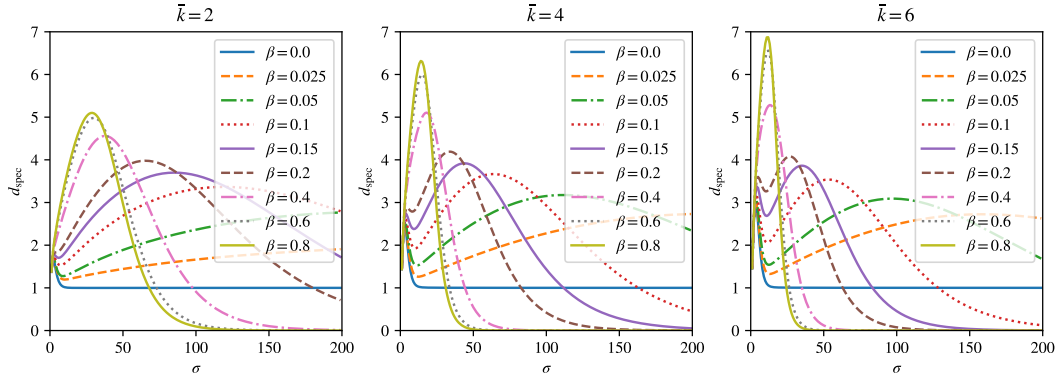

Fig. 2.8.: We show the spectral dimension for the Watts-Strogatz graph for varying degree $\bar{k}$ and rewiring probability β. The underlying networks have $N = 1000$ nodes, for each parameter combination we average over five randomly generated graphs and 25 start nodes per graph.

maximum at intermediate σ arises due to the non-local connections that result from rewiring edges. If more connections are rewired, i.e. for larger β, the walker reaches more nodes and the second maximum increases in magnitude. At the same time an average walk takes fewer steps to encounter a non-local connection and the second maximum is shifted to smaller σ. For large β the resulting graph exhibits so many non-local connections that it only exhibits one maximum and the local neighborhood disappears.

The original Watts-Strogatz model is constructed from an embedding into S^1. We generalize this construction by starting from embedding into $\mathbb{R}^d$ with periodic boundary conditions, see also Ref. [54]. We connect each node to all nodes that lie at a Euclidean distance smaller than a cutoff d_{max} and rewire each of the edges with probability β. The spectral dimension for the resulting graph behaves qualitatively similar as in the S^1 case, see Fig. 2.9. For $d > 1$ the local minimum has larger values than in the S^1 case. We assume that this is a remnant of the larger value of d but have not studied if there are degeneracies with the choice of $\bar{k}$ and β.
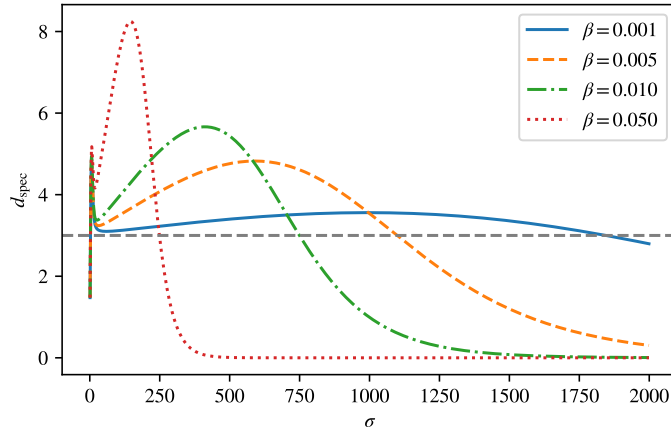
Fig. 2.9.: We show the spectral dimension for a generalization of the Watts-Strogatz graph to $d = 3$ dimensions. Each node is connected to all neighbors at a Euclidean distance $l \leq l_{\mathrm{max}} = 2$. The gray dashed line marks $d_{\mathrm{spec}} = 3$.

The synthetic networks constructed according to a Euclidean and a hybrid metric carry an imprint of their embedding space. Similarly, the Watts-Strogatz network could still allow to recover an imprint of the embedding space. All synthetic networks provide us with templates to study the spectral dimension of real-world networks.

2.3 Scale-Dependent Spectral Dimension for Real-World Networks

Given these templates we turn to the spectral dimension of real-world networks. We choose real-world networks for which we expect the spatial background structure to play a structural role [19]. Details on our data sources and data preparation procedure can be found in App. B.1.

We first explore road networks as a paradigmatic example of networks that carry imprints of their embedding into a two-dimensional space. We then explore a network representing the physical structure of the internet and neural networks as two examples of networks that are embedded into two- and three-dimensional space.

The spectral dimension of (directed) real-world networks has been analyzed previously for citation networks and metabolic networks [55], as well as for a set of proteins [56]. Interestingly, the latter reference finds a relation between the spectral dimension and the composition of a given protein, indicating a link between the stability of proteins and their spatial structure. Ref. [57] discussed a variety of networks, including proteins, the brain and the internet. This reference extracted the spectral dimension via the spectrum of the corresponding Laplacian. The resulting spectral dimension is a single number, as opposed to the scale-dependent spectral dimension that we extract here.
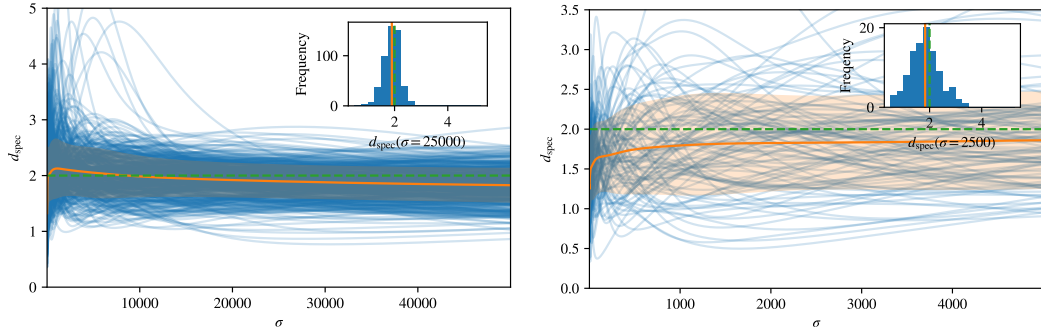
Fig. 2.10.: (left) We show the spectral dimension for a network representing roads in Pennsylvania. The blue lines correspond to individual walks, the orange line marks the average, the orange bands indicate the estimated standard deviation. Additionally, we mark the topological dimension $d = 2$ (green dashed) of the embedding space. The inset shows a histogram of the distribution of all walks at a fiducial value of σ.
(right) We show the spectral dimension for a network representing major roads in Europe.

2.3.1 Euclidean Space: Road Networks

We consider two different road networks: one representing the roads of Pennsylvania, the other one representing a network of major roads in Europe. To extract the spectral dimension we average over 500 and 100 starting positions and perform $5 \cdot 10^4$ and $5 \cdot 10^3$ steps, respectively. In Fig. 2.10 we show the resulting spectral dimension for both networks.

Both networks are inhomogeneous: every starting node has a different local neighborhood and features a different spectral dimension. The resulting (scale-dependent) distribution of spectral dimensions has a mean close to $d_{\text{spec}} = 2$. This value agrees with expectations: road networks are embedded into (mostly) two-dimensional landscapes, the spectral dimension hence agrees with the topological dimension of the embedding space.

The individual trajectories mostly agree with the templates constructed in Euclidean networks. Only few trajectories substantially deviate from $d_{\text{spec}} = 2$. We interpret this as an indication that road networks indeed serve as a prototypical example of networks constructed according to a Euclidean metric.

2.3.2 Beyond Euclidean Space: the Internet and Neural Networks

Next we consider networks that represents the physical structure of the internet and neural networks. We expect that these networks exhibit strong inhomogeneities and nodes differ in their neighborhood. Each start node triggers a particular diffusion process and leads to a particular scale-dependent spectral dimension. Starting a diffusion process at an ensemble of start nodes, one obtains an ensemble of scale-dependent spectral dimensions.

For the synthetic networks and road networks it was sufficient to average over the resulting distribution, as inhomogeneities within the networks were reasonably small. For the real-world networks in this subsection we instead classify different types of start nodes. This classification is not meant to be unique. Instead, it should be understood as a qualitative description illustrating which dynamics are possible. We leave a more quantitative description of the resulting distribution of the spectral dimension to future work.

We distinguish the following four classes of walks

1. The *non-local class* exhibits an immediate rise in the spectral dimension, followed by an immediate decay to $d_{\mathrm{spec}} \approx 0$. As a template for this class see the Euclidean network with many non-local connections, cf. the right panel of Fig. 2.2, the Lorentzian network without regularization, cf. Fig. 2.5, and the Watts-Strogatz model for large values of β, cf. Fig. 2.8. This behavior of the spectral dimension signals a highly connected network with many "shortcuts".

2. The *hybrid class* exhibits an immediate rise in the spectral dimension, followed by a plateau at $d_{\mathrm{spec}} > 0$. As a template for this class see the Lorentzian network with a cutoff, cf. Fig. 2.7. This behavior signals a locally highly connected node embedded into a larger spatial structure.

3. The *local class* exhibits no significant early maximum. Instead, it rises towards a finite value d_{spec}. As a template for this class see the Euclidean network without "shortcuts", cf. Figs. 2.1 and 2.2. This behavior of the spectral dimension signals a relatively small local connectedness.

4. The *Watts-Strogatz class* exhibits two maxima in the spectral dimension. As a template for this class see the Watts-Strogatz networks for moderate values of β, cf. Fig. 2.8. This behavior of the spectral dimension signals the existence of a well-connected local neighborhood and the existence of long-distance links.

The first three classes are geometric in nature. They represent different ways for how the embedding spacetime leaves its imprints on the network. In the following we explore which of these classes are realized in real-world networks.

We first study a network capturing some aspect of the structure of the Internet. In this context graphs have been applied to model various aspects: one can encode the hyperlinks between webpages in a graph. PageRank, the algorithm powering large search engines, approximates the equilibrium distribution of a random walk on this web graph [58]. Here, we focus on the physical structure of the internet, as this case provides a clear expectation for the embedding dimension. The nodes in the network that we consider are so-called autonomous systems. Each autonomous system can be thought of as a set of computers under the control of one network administrator. An edge between nodes, i.e. two autonomous systems, exists, if they are linked by a direct network connection.

On the one hand, the physical structure of the internet is embedded into two-dimensional space. One might expect to find imprints of this two-dimensional em-
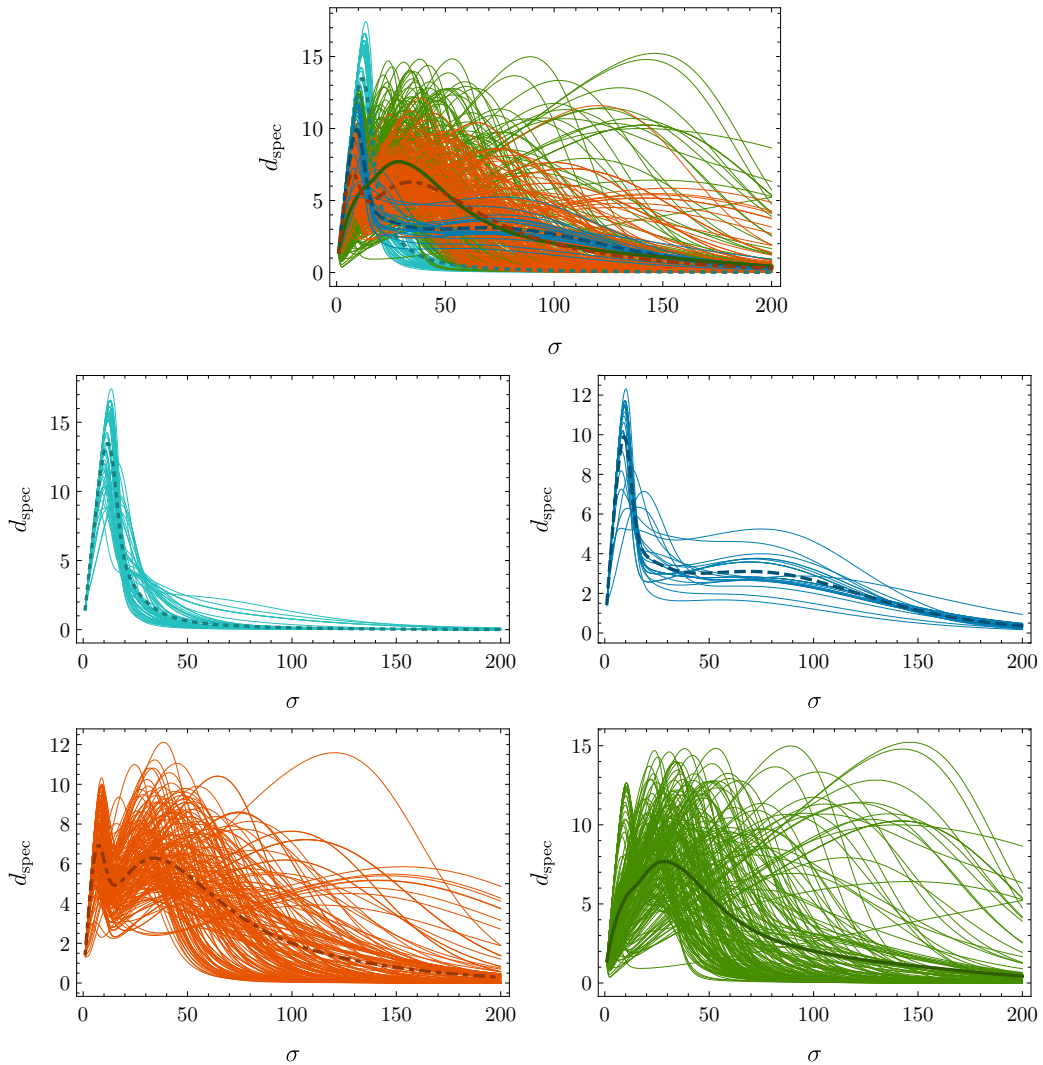
Fig. 2.11.: We show the spectral dimension for a network representing the physical structure of the internet. The top panel shows the spectral dimension for all starting nodes, while the four panels below show the individual classes with their corresponding average: non-local (cyan), hybrid (blue), Watts-Strogatz (orange) and the remainder class peaking at large values of σ (green).

bedding. On the other hand, a network architecture that is more strongly connected allows routing signals more quickly between nodes. This might favor non-local connections. To explore these two aspects we consider a snapshot from the CAIDA database [59]. The CAIDA database provides snapshots of the nodes and links corresponding to a part of the internet.

We explore one of these snapshots and distinguish the four classes of start nodes introduced above, see Fig. 2.11.

Many walks fall into the non-local class because the internet is highly connected: the non-local walks quickly explore large parts of the network.
A fraction of the walks fall into the hybrid class. For intermediate σ we observe that they plateau at $d_{\text{spec}} \approx 3$. On the contrary, no walks fall into the local class. We interpret the existence of trajectories with an intermediate plateau as an indication
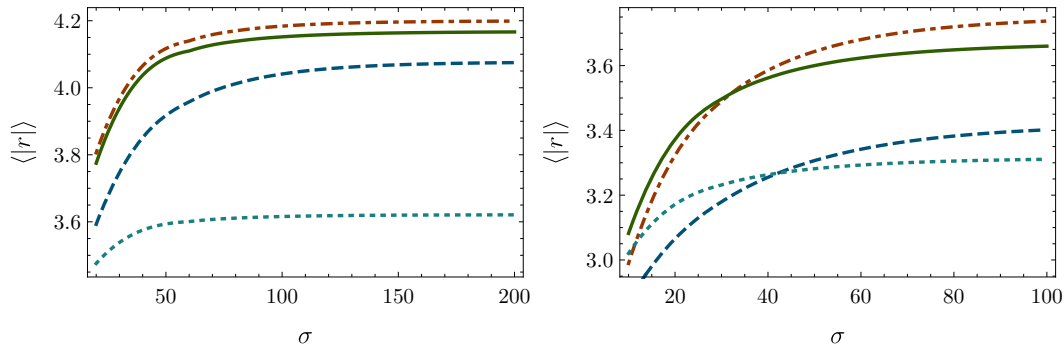
Fig. 2.12.: We show the mean value of the shortest distance $|r|$ of all nodes from the start node for a network representing the internet (left) and a neural network (right). We average over nodes and walks within a class. The class are non-local (cyan), hybrid (blue), Watts-Strogatz (orange) and the remainder class (green).

that the network retains an imprint of its spatial embedding. Surprisingly, it is not the Euclidean metric that is relevant to model this spatial embedding. Instead, networks constructed according to the hybrid metric provide a relevant template.

Many of the walks fall into the Watts-Strogatz class. For these walks the intermediate minimum appears at a spectral dimension of mostly three or larger. Comparing to our generalization of the Watts-Strogatz graph, cf. Fig. 2.9, again indicates similarities to templates for embedding spaces with $d_{\text{spec}} \geq 3$.

Finally, we find a remainder class of walks. These walks resemble Watts-Strogatz walks with a relatively low β. It might be possible to subdivide the corresponding class further and identify more walks belonging to the Watts-Strogatz class. We do not pursue this possibility here further.

To confirm the interpretation that we gave for each of the classes we explore how the average distance from the starting node $\langle |r| \rangle$ behaves as a function of σ. For each node and various time-steps σ we compute the shortest distance to the starting node r. We then weight the distance by the probability density residing on the corresponding node at time σ and average within each class, see left panel of Fig. 2.12.

The resulting average distances for each of the classes is of the order that one would expect based on a $\sim \log N$ scaling for $N = 33304$ nodes. For the non-local class the average distance is shorter than for the other classes, as the corresponding nodes are particularly well-connected and able to reach all nodes with a few steps. The Watts-Strogatz class and the remainder class exhibit very similar behavior. This again indicates that the remainder class might contain a substantial fraction of Watts-Strogatz walks with a different value of β.

Next, we consider two networks modeling the brain. Networks are applied on a variety of scales to model the structure and dynamics of brains [60, 61]. Here, we will focus on networks describing structural properties of the brain.

The first network we consider describes large parts of the brain of a drosophila fly on the level of individual cells [62]: each node corresponds to a neuron. Edges represent physical connections between neurons. The network describes the physical structure of the brain that is embedded into three-dimensional space.
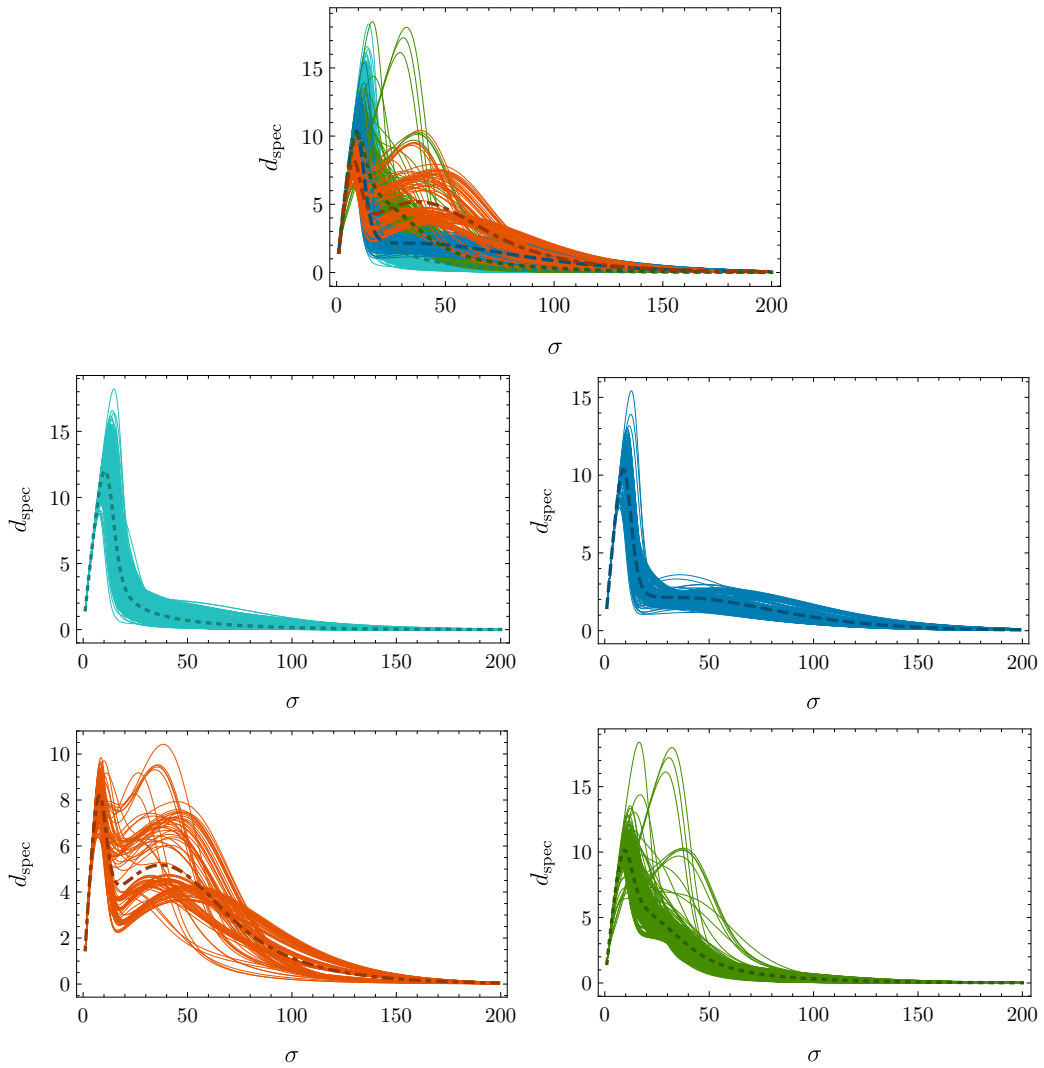
Fig. 2.13.: We show the spectral dimension for a network representing the neural network of a drosophila fly. Again, the top panel shows the spectral dimension for all starting nodes, while the four panels below show the individual classes with their corresponding average: non-local (cyan), hybrid (blue), Watts-Strogatz (orange) and the remainder class (green).

In the drosophila network we identify the same classes as in the network representing the physical structure of the internet, see Fig. 2.13. In particular, again walkers of the local class do not occur. The largest fraction of walkers is in the non-local class, see also Tab. 2.1. Their spectral dimension quickly rises and then decays. A substantial part of the walks falls into the hybrid class with a plateau at $d_{\text{spec}} \approx 2$. Compared to the internet network, the fraction of walks in the Watts-Strogatz class has substantially reduced. The remainder class features a number of walks that exhibit a near-plateau at $\sigma \approx 25$ that might also be associated with a hybrid-metric network.

The average distance again approaches values consistent with a $\log N$ scaling, as expected for a small-world network with $N = 21739$ nodes. The walks in the non-local class spread very fast. On average, they are closest to all other nodes in the network. The walks in the Watts-Strogatz class and the remainder class again behave similar.

Graph	Class 1	Class 2	Class 4	Remainder
CAIDA	73	24	194	209
Brain of Drosophila	1274	343	108	275
Brain of Mouse	70	30	—	—

Tab. 2.1.: Number of walks in classes 1,2,4 and the remainder class for the graphs that we consider.
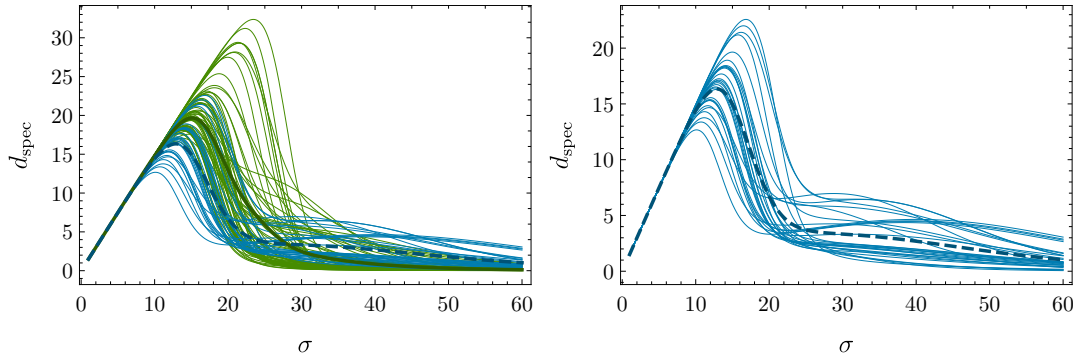
Fig. 2.14.: We show the spectral dimension for a network representing the neural network of a mouse. The graph exhibits walks in the non-local (green) and the hybrid (blue) class. The local walks are shown separately in the right panel.

For both, the internet network and the drosophila network, we find that the spectral dimension of a network constructed according to a Lorentzian metric provides a relevant template. To check the robustness of this result, we finally consider a network that represents parts of the brain of a mouse. As opposed to the drosophila case, where each node represented a neuron, here each node represents a voxel, i.e. a three-dimensional pixel. Voxels are correlated according to the amount of co-activation that they exhibit. We introduce a cutoff for the correlation, and connect all nodes for which the correlation is larger than the cutoff. We weight each edge with the correlation and perform a weighted random walk.

The resulting graph could provide a coarse grained version of a neuron-level graph. Measuring the spectral dimension on the resulting graph, two classes appear to be robust under coarse graining: the resulting network exhibits walks of the non-local class and walks of the hybrid class, plateauing at $d_{\mathrm{spec}} \approx 3$, see Fig. 2.14. In contrast, it does neither feature walks of the local class nor of the Watts-Strogatz class.

We conclude that the real-world networks that we consider might feature imprints of their embedding space. Surprisingly, the local template does not play a role in any of the three real-world networks that we consider. Instead, the non-local and in particular the hybrid metric networks provide relevant templates.

All networks exhibit many walks in the non-local class. Various templates explain such a component: networks constructed according to a Lorentzian metric and more generally any network that is sufficiently non-local could explain the quick rise and subsequent decay of the spectral dimension. The existence of walks in this class is not necessarily related to the embedding space.

All real-world networks that we consider also exhibit walks in the hybrid class. The corresponding template features an early maximum associated to a highly connected local environment. It then plateaus at a value of the spectral dimension determined by the embedding spacetime. For all real-world networks that we study, the resulting plateau in the spectral dimension is between two and three, and hence close to the value expected based on the underlying embedding space.

2.4 Conclusions: an Imprint of Lorentzian Geometry in Real-World Networks

We explored how the embedding geometry shapes the properties of real-world networks using the spectral dimension. To study these networks embedded in a geometry, we compared them to networks of a geometry, i.e. to networks describing space(time). We constructed various synthetic networks of space(time) and computed the scale-dependent spectral dimension for these networks. The spectral dimension provided a template to explore real-world networks.

We explored road networks, networks representing the internet and neural networks. For the road networks that we studied the spectral dimension is $d_{\mathrm{spec}} \approx 2$. The most relevant template is the one of a network constructed according to a Euclidean metric. This hints at a strong influence of the embedding geometry on road networks.

More complex real-world networks such as the internet or neural networks exhibit an inhomogeneous variety of nodes. To explore this variety we distinguished different classes of starting nodes. None of the more complex networks shows walks similar to a template constructed according to a Euclidean metric. Instead, one class of nodes resembles a template constructed according to a hybrid metric, that measures distances according to a Lorentzian metric on short Euclidean distances and according to a Euclidean metric on large Euclidean distances. Such hybrid networks have been studied as a regularization of causal sets [44]. Their appearance in the context of real-world networks highlights that importing further concepts from quantum gravity research might provide new perspectives on real world networks.

In the context of real-world networks a hybrid metric is able to describe networks that feature a highly connected local neighborhood but are constrained by their embedding on larger distances. Within the hybrid class of walks the spectral dimension at large distances is close to the one of the embedding space. The existence of such walks might be an imprint of the embedding space on the network.

After considering this imprint of classical spacetime on physical structures we now turn to study the imprint of trans-Planckian quantum spacetime on the matter sector.

Quantum Spacetime and the Quantization of Gravity

<div align="right">

3

</div>

So far we have focused on the question of how classical properties of spacetime impact structures on that spacetime. In this chapter, we introduce a quantum description of spacetime. While quantum fluctuations of spacetime will presumably remain observationally inaccessible in the near future[1], the impact of quantum spacetime on matter might leave imprints that are observationally relevant. In the next chapters, we will explore how quantum fluctuations of spacetime impact the matter sector, and which imprints of quantum spacetime might be relevant in the infrared (IR). This requires a quantum description of spacetime.

We focus on a quantum description in terms of the path integral and aim to evaluate the expression

$$Z = \int_{\text{geometries}} e^{iS}. \tag{3.1}$$

This expression is not well-defined. We neither specified a regularization procedure nor an integration domain. The integration domain might contain varying dimensionality and/or varying topology[2]. In the following, we fix the number of dimensions to $d = 4$ and do not explicitly consider fluctuations of the topology. We describe different geometries in terms of the metric and aim to construct a path integral over fluctuations of the metric $g_{\mu\nu}(x)$.

Quantum fluctuations in quantum electrodynamics screen the electric force and make it weaker at large distances. Quantum fluctuations in quantum chromodynamics anti-screen color charges and make this force stronger at large distances. Similarly, quantum fluctuations of the metric $g_{\mu\nu}(x)$ could screen or anti-screen. As a result the gravitational force will become scale-dependent. To describe this scale-dependence, one requires a way to measure scales. To measure scales we split the metric into a background and a fluctuation according to [3]

$$g_{\mu\nu} = \bar{g}_{\mu\nu} + h_{\mu\nu}. \tag{3.2}$$

Scales can be measured according to the background metric $\bar{g}_{\mu\nu}$. As one example, the eigenvalues of the Laplacian $-\bar{D}^2$ in $\bar{g}_{\mu\nu}$ allow to identify a generalized momentum, that reduces to the four-momentum p^2 for $\bar{g}_{\mu\nu} = \eta_{\mu\nu}$.

---

[1] Primordial gravitational fluctuations, observable in the cosmic microwave background, are a notable exception assuming the theory of inflation, see Sec. 5.1. Detecting tensor perturbations would constitute the detection of a signal that is both, highly gravity-specific (due to its tensorial nature) and of quantum origin (at least within the theory of inflation).

[2] For arguments against topology changes on spatial hypersurfaces relying on quantum field theory on curved backgrounds, see e.g. Refs. [63, 64].

[3] Here we split background and fluctuation linearly. We will exclusively work in this split in this thesis. For results in an exponential split, see e.g. [65–69].

To identify UV and IR modes in a covariant way, we order the eigenvalues of the Laplacian by size. In a Lorentzian signature this procedure is not able to distinguish UV and IR modes. Large energies can cancel with large three-momenta due to the negative sign in the time component of the metric. As an example, modes with four-momentum $p^2 = -E^2 + \vec{p}^2 = 0$ can carry arbitrary amounts of energy in Minkowski space. To overcome this problem, standard quantum field theory instead works in a Euclidean metric. In this metric $p^2 = E^2 + \vec{p}^2$ increases with increasing energy. Ordering modes according to p^2 allows sorting modes from the UV to the IR. Once ordered, one can integrate out modes momentum shell by momentum shell from the UV to the IR to compute the effect of quantum fluctuations. Results are translated back to Minkowski space by means of a Wick rotation. However, the Wick rotation cannot be unambiguously defined on all curved backgrounds. On general backgrounds $\bar{g}_{\mu\nu}$ there are several ways how to define such a procedure, all afflicted by problems that arise due to the existence of horizons [70].

In the following, we will exclusively work in a background metric $\bar{g}_{\mu\nu}$ with Euclidean metric signature. Doing so, we effectively explore fluctuations of four-dimensional space, instead of fluctuations of $3+1$ dimensional spacetime.

3.1 Scale Dependence and the Renormalization Group

Working in a Euclidean metric on a fixed background $\bar{g}_{\mu\nu}$ allows us to set up a scale-dependent description. In the following we will work in a quantum field theoretic language. We will first explore the consequences of pursuing a standard perturbative approach before we introduce a non-perturbative approach: the functional renormalization group.

3.1.1 Perturbative Quantum Gravity and the Loss of Predictivity

In a standard perturbative field theory, the effects of quantum fluctuations are computed loop order by loop order. One computes all loop diagrams at a given loop order i. The loop diagrams can induce a dependence on the renormalization group (RG) scale μ in the theory, encoded in the beta functions $\beta_g = \mu\partial_\mu g$ with g a coupling. In addition, some loop diagrams can cause divergences. One includes corresponding counterterms to cancel the divergences. The infinite part of the counterterms cancel the divergences. The finite part of the coefficients of these counterterms are free parameters. They are new couplings that need to be fixed by measurement. Proceeding to the $(i+1)$th loop order, one repeats this procedure: new counterterms might be induced, and new couplings might appear. If this iteration converges to a finite set of operators and corresponding couplings, then the underlying theory is called perturbatively renormalizable. In such a theory one can compute the running of all couplings up to a given loop order. Each of the couplings needs to be fixed at one

scale by measurement. Once all couplings are fixed the theory becomes predictive to an (in principle) arbitrary level of precision within its realm of applicability[4].

If, on the contrary, the iteration from ith to $(i+1)$th loop order enlarges the set of operators and the set of operators grows without bounds, then the resulting theory is not predictive on all scales. The operators induced at higher loop levels typically modify physics beyond a cutoff scale Λ_{cut}. For predictions at momenta $p^2 > \Lambda_{\text{cut}}^2$ one hence needs to know the finite coefficients of all infinitely many higher order operators. This requires infinitely many measurements. The theory loses predictivity and is called perturbatively non-renormalizable. For $p^2 < \Lambda_{\text{cut}}^2$ the theory can nevertheless be useful: in this regime, one can bound the error resulting from higher loop orders if one assumes all couplings to be $\leq \mathcal{O}(1)$. Given a required level of precision, one can determine the required loop order. One introduces all counterterms required at that loop order. After measuring the couplings of all counterterms, the resulting theory can be used to obtain predictions that are accurate up to the required precision.

In the case of gravity, the latter case is realized. Starting from the Einstein-Hilbert action

$$S^{\text{EH}} = \int \mathrm{d}^4x \, \sqrt{g} \frac{1}{16\pi \bar{G}_N} \left(2\bar{\Lambda} - R \right) \tag{3.3}$$

the one-loop coefficients in the case $\bar{\Lambda} = 0$ were computed in [71]. The resulting terms of order curvature squared vanish: a term $\sim R_{\mu\nu\rho\sigma}R^{\mu\nu\rho\sigma}$ can be re-expressed in terms of the invariants $R_{\mu\nu}R^{\mu\nu}$ and R^2 via the Gauss-Bonnet theorem [71]

$$R_{\mu\nu\rho\sigma}R^{\mu\nu\rho\sigma} - 4R_{\mu\nu}R^{\mu\nu} + R^2 = \text{total derivative}. \tag{3.4}$$

The invariants $R_{\mu\nu}R^{\mu\nu}$ and R^2 vanish as a result of the equations motion in vacuum $R^{\mu\nu} = 0$ and do not contribute to physical processes.

At two-loop level, one generates a term [72–74]

$$\Gamma_{\text{GS}} \sim \frac{1}{\epsilon} \int \mathrm{d}^4x \, \sqrt{g} \frac{1}{M_{\text{Pl}}^2} R_{\mu\nu}{}^{\rho\sigma} R_{\rho\sigma}{}^{\alpha\beta} R_{\alpha\beta}{}^{\mu\nu}, \tag{3.5}$$

where ϵ is the parameter introduced during dimensional regularization, with $d = 4 - \epsilon$. The finite coefficient of this term introduces a new coupling. Computing higher loop orders, the expectation is to generate higher powers of curvature operators. The theory is hence perturbatively non-renormalizable[5].

The resulting theory can still be used in the IR as an effective field theory. As one example a low-energy expansion of the two-body potential is given by [76, 77]

$$V(r) = -\frac{Gm_1 m_2}{r} \left(1 - \frac{G(m_1 + m_2)}{rc^2} - \frac{127}{30\pi^2} \frac{G\hbar}{r^2 c^3} \right). \tag{3.6}$$

Here we momentarily reintroduced factors of c and $\hbar$ to illustrate that the second coefficient in this potential is a general relativistic correction, unrelated to quantum physics. The third coefficient is of quantum origin. It scales as l_{Pl}^2/r^2, with l_{Pl} the

---

[4]The existence of Landau poles might still constrain the applicability of a renormalizable theory to a finite range of scales.

[5]In the presence of matter, new couplings already appear at one loop level [71, 75], highlighting the need to incorporate matter into any theory of quantum gravity.

Planck length. For $r \gg l_{\mathrm{Pl}}$ it is strongly suppressed. For $r \sim l_{\mathrm{Pl}}$ additional corrections with higher powers of l_{Pl}/r would become important. Some of these corrections are generated by higher loop orders and are expected to depend on the couplings of terms such as (3.5). To make a physical prediction the coupling of the finite part of (3.5) needs to be fixed by an experiment. We expect there are infinitely many of such couplings. As a result predictivity at trans-Planckian energies is lost.

3.1.2 Scale Symmetry and Fixed Points: Predictivity Restored

An additional symmetry principle could restore predictivity. Here we focus on UV quantum scale symmetry. A scale symmetric system does not change when changing the observational scale. This requires that integrating out additional quantum fluctuations does not change the description of the system. In quantum field theoretic terms the dimensionless couplings $g_i = \bar{g}_i k^{-d_{g_i}}$ do not change when changing the scale k. Here d_{g_i} is the mass dimension of the dimensionful coupling $\bar{g}_i$. At a fixed point g_{i*} all beta functions vanish

$$\beta_{g_i}\Big|_{\vec{g}=\vec{g}_*} \equiv k\partial_k g_i\Big|_{\vec{g}=\vec{g}_*} = 0 \tag{3.7}$$

and the system becomes invariant under a change of scales.

The linearized beta functions around a fixed point g_{i*} are

$$\beta_{g_i} = \sum_j M_{ij}(g_j - g_{j*}). \tag{3.8}$$

In this expression

$$M_{ij} = \frac{\partial \beta_{g_i}}{\partial g_j}\Big|_{\vec{g}=\vec{g}_*} \tag{3.9}$$

is the stability matrix. In the vicinity of the fixed point a perturbation $\tilde{g}_i$ of the fixed point value along an eigenvector of the stability matrix behaves as

$$\tilde{g}_i(k) = \tilde{g}_i(k_0)\left(\frac{k}{k_0}\right)^{-\theta_i}, \tag{3.10}$$

with k_0 some reference scale. Here,

$$\theta_i = -\mathrm{Eig}_i\left(M_{jk}\right) \tag{3.11}$$

is the critical exponent, given by the negative eigenvalue associated with the corresponding eigenvector of the stability matrix.

Deviations from a fixed point g_{i*} can either grow or shrink when integrating out quantum fluctuations or equivalently lowering k. An eigendirection is relevant if deviations from its fixed point value grow towards smaller k and hence if $\theta_i > 0$. An eigendirection is irrelevant if deviations shrink towards smaller k and hence if $\theta_i < 0$. In a theory emanating from a fixed point in the UV, a relevant coupling can assume a large range of different values in the IR. An irrelevant coupling can only take a single value. No other value is compatible with emanating from the corresponding fixed point in the UV.
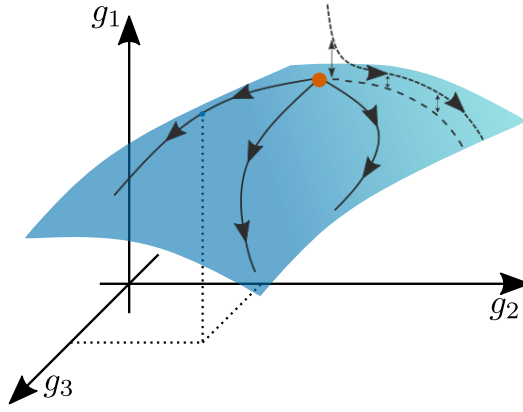
Fig. 3.1.: Critical hypersurface for three couplings g_i, two of which are relevant. The relevant directions approximately correspond to g_2 and g_3. The coupling g_1 is fixed as a function of the relevant couplings. Arrows mark the RG flow towards the infrared, the fixed point is marked in red. The critical hypersurface can be curved, as the critical value for the irrelevant coupling $g_1(g_2, g_3)$ can depend on the relevant couplings g_2 and g_3. The dashed trajectory does not emanate from a fixed point and hence does not correspond to a UV complete theory.

The prototypical example of a fixed point is the Gaussian fixed point $g_{i*} = 0$. At this fixed point all interactions vanish and as a consequence the stability matrix M_{ij} is diagonal. The eigendirections $\tilde{g}_i$ align with the couplings g_i. For a dimensionless coupling g_i, the critical exponent at the Gaussian fixed point is given by the canonical mass dimension of the corresponding dimensionful coupling, $\theta_i = d_{g_i}$. All couplings with a positive mass dimension are hence relevant, those with a negative mass dimension are irrelevant. Those that have vanishing mass dimension are marginal couplings. For these one needs to consider interactions in order to determine if they are (ir-)relevant. In a polynomial expansion in the fields, only finitely many operators will have a mass dimension smaller or equal to $d = 4$. Correspondingly, only finitely many couplings will be relevant at the Gaussian fixed point. They can take a range of values in the IR. The value realized in nature needs to be determined by a measurement. Conversely, infinitely many couplings will be irrelevant. They can take a single value in the IR that is fixed by requiring the theory to originate in the Gaussian fixed point. After measuring the relevant couplings the theory becomes predictive.

At an interacting fixed point, $g_{i*} \neq 0$, the eigendirections $\tilde{g}_i$ of (3.9) are not necessarily aligned with single couplings. Instead, they are a linear combination of various couplings. Fixing the values of the irrelevant couplings defines a surface, the critical hypersurface. The critical value of the irrelevant couplings depends on the relevant couplings. As a result, the critical hypersurface can be curved, cf. Fig. 3.1. A trajectory on the critical hypersurface will emanate from the fixed point. The different trajectories are parameterized by the relevant directions. Measuring the relevant directions at a scale k_0 determines, which trajectory on the critical hypersurface is realized. The condition of predictivity translates into a finite-dimensional critical hypersurface.

To determine whether quantum scale symmetry can be realized within a given quantum field theory, one first determines the beta functions of the theory. These allow to

identify fixed points. One can then characterize each of the fixed points and identify relevant directions.

Various mechanisms lead to the emergence of interacting fixed points. As a first mechanism a balancing of different loop orders can lead to a fixed point at non-vanishing coupling values [78]. As a second mechanism the canonical mass dimension and interactions can balance to obtain an interacting fixed point. A paradigmatic example is $\lambda_4 \phi^4$ theory in $d = 4 - \epsilon$ dimensions. The canonical dimension for the quartic coupling λ_4 is $d_{\lambda_4} = \epsilon$. The beta function for the quartic coupling hence reads

$$\beta_{\lambda_4} = -\epsilon + \frac{3}{16\pi^2} \lambda_4^2.$$
(3.12)

The first term is the dimensional one, the second arises due to interactions. The two contributions balance to feature the Wilson-Fisher fixed point [79] at $\lambda_{4*} = \sqrt{16\pi^2 \epsilon / 3}$.

To search for fixed points we need the beta functions for a theory. In the next section, we introduce the functional renormalization group as a tool to obtain the beta functions.

3.1.3 The Functional Renormalization Group

The functional renormalization group provides a description of a system at a momentum scale k. A change of momentum scale k requires to adapt this description. This change in description is described by the flow equation. Below and in App. A we provide a summary of the derivation of the flow equation, for details we refer to Ref. [80]. We focus on a single field ϕ, work in flat space and neglect any internal indices.

The central idea is to implement a momentum-shell-wise integration by making modes with momenta $p < k$ heavy and integrating out all light modes. We start by considering the scale-dependent generating functional

$$Z_k[J] = \int_\Lambda \mathcal{D}\phi \, e^{-S[\phi] - \Delta S_k[\phi] + \int J\phi}.$$
(3.13)

Here, $S[\phi]$ is the action for the field ϕ, J is a corresponding source, $\int J\phi = \int \mathrm{d}^4 x \, J(x)\phi(x)$ and the path integral is defined in the presence of a cutoff Λ_{UV}. The term

$$\Delta S_k[\phi] = \frac{1}{2} \int \frac{\mathrm{d}^4 q}{(2\pi)^4} \phi(-q) R_k(q) \phi(q)$$
(3.14)

introduces a regulator $R_k(q)$ that effectively acts as a momentum-dependent mass for the field ϕ. To make sure it acts in such a way, the regulator should fulfill a set of properties.

For modes with small momenta, $q^2 \ll k^2$, it should act as a mass term, such that these modes are not integrated out. We hence require

$$\lim_{q^2/k^2 \to 0} R_k(q) > 0.$$
(3.15)

In the limit $k^2 \to 0$ we want to integrate out all modes and remove the effect of the regulator. In this case (3.13) reduces to the definition of the standard generating functional. To ensure this behavior we demand

$$\lim_{k^2/q^2 \to 0} R_k(q) = 0. \tag{3.16}$$

As a third property we demand that

$$\lim_{k^2 \to \Lambda \to \infty} R_k(q) \to \infty. \tag{3.17}$$

This property ensures that for large k the path integral is dominated by the stationary point of the action $\frac{\delta S[\phi]}{\delta \phi(x)} = J(x)$.

All n-point functions can be obtained from the generating functional $Z_k[J]$ by functional differentiation. To only consider their connected part, we introduce

$$W_k[J] = \log Z_k[J]. \tag{3.18}$$

By performing a modified Legendre transform

$$\Gamma_k[\varphi] = \sup_J \left(\int J\varphi - W_k[J] \right) - \Delta S_k[\varphi] \tag{3.19}$$

one obtains the scale dependent effective action Γ_k that depends on $\langle \phi(x) \rangle = \varphi(x)$. The quantum equation of motion for this effective action is

$$J(x) = \frac{\delta \Gamma_k[\varphi]}{\delta \varphi(x)} + \int \mathrm{d}^4 y \, R_k(x, y) \varphi(y), \tag{3.20}$$

again supporting the interpretation of the regulator as a mass term.

By following a series of rather technical steps (see App. A) we obtain the flow equation [81–83]

$$\partial_t \Gamma_k[\varphi] = \frac{1}{2} \operatorname{STr} \left(\frac{\partial_t R_k}{\Gamma_k^{(2)}[\varphi] + R_k} \right). \tag{3.21}$$

Here, $\Gamma^{(2)}[\varphi] = \frac{\delta^2 \Gamma_k[\varphi]}{\delta \varphi(q) \delta \varphi(-q)}$ is the second functional derivative of Γ_k with respect to φ. The (super-)trace is over all internal indices, spacetime indices and over momenta (or more generally eigenvalues of the corresponding Laplacian). For Grassmanian degrees of freedom it includes an additional minus sign.

The scale-dependent effective action Γ_k interpolates between $S[\phi]$ for $k \to \Lambda_{\mathrm{UV}}$ and the effective action Γ for $k \to 0$. The choice of regulator determines how these limits are approached, Γ_k hence is regulator-dependent at finite k. In our computations we will exclusively employ a Litim-type regulator [84] of the form

$$R_k(p^2) = p^2 \, r \left(\frac{k^2}{p^2} \right), \tag{3.22}$$

with $r(x) = (x - 1)\Theta(x - 1)$ with $\Theta(x)$ the Heaviside distribution, see Eq. (C.15) for the corresponding regulator in the fermionic sector. This regulator allows to evaluate

the trace in momentum space analytically, and hence yields particularly convenient results.

Eq. (3.21) for the effective action Γ_k is exact. The effective action Γ_k contains all operators compatible with the symmetries under consideration. Accounting for all these operators is usually unfeasible (see however Refs. [85, 86]). Instead, one truncates Γ_k to a subset of operators[6]. The choice of truncation constitutes a major source of error. While the error arising from choosing a particular truncation is hard to quantify, producing consistent results with a variety of truncations usually is seen as a sign of apparent convergence, that signals that all relevant physics is captured. In addition, one can study the dependence of physical quantities on unphysical parameters such as gauge parameters or varying regulators. In a truncation that captures most of the relevant physics these dependencies should be mild.

Given a truncation

$$\Gamma_k = \int \mathrm{d}^d x \, \sqrt{g} \sum_{i=1}^{N} \bar{g}_i O^{(i)}, \tag{3.23}$$

from Eq. (3.21) one can extract the beta functions $\beta_{g_i} = \partial_t g_i$ for the dimensionless couplings g_i that correspond to each of the operators $O^{(i)}$. To compute these beta functions, in practice a diagrammatic expansion is useful. One can expand Eq. (3.21) as (see e.g. [89])

$$\partial_t \Gamma_k = \frac{1}{2} \operatorname{Tr} \tilde{\partial}_t \mathcal{P} + \frac{1}{2} \sum_{n=1}^{\infty} \frac{(-1)^{n-1}}{n} \operatorname{Tr} \tilde{\partial}_t \left(\mathcal{P}^{-1} \mathcal{F} \right)^n. \tag{3.24}$$

Here $\mathcal{P} = \Gamma_k^{(2)}[\varphi = 0] + R_k$, $\mathcal{F} = \Gamma_k^{(2)}[\varphi] - \Gamma_k^{(2)}[\varphi = 0]$. The modified derivative $\tilde{\partial}_t = \int \partial_t R_k \frac{\delta}{\delta R_k}$ acts only on the k-dependence in the regulator term [89]. $\mathcal{P}^{-1}$ represents the propagator and $\mathcal{F}$ represents vertices. The resulting diagrams have a one-loop structure, but carry an additional regulator on one of their internal propagators. The value of n counts the number of vertices in a diagram. Expansion (3.24) allows to quickly identify all terms relevant in computing the beta function for a coupling g_i.

The resulting beta functions encode how the coupling g_i changes under a change of the artificial momentum scale k. We caution that in principle one would need to take the limit $k \to 0$ and evaluate the resulting effective action at the momentum scale p that one is interested in. Instead, one often chooses to identify k with a physical momentum scale. A motivation for this identification is that it reproduces perturbative one-loop results in a massless regime (provided one appropriately accounts for the anomalous dimensions). More generally, such an RG improvement procedure produces the correct one-loop potential in QED if one replaces the classical coupling by a running one in the potential between two point charges in QED [90].

The resulting beta functions do not make use of a perturbative approximation and allow to explore a non-perturbative regime. They have been applied to a wide range of non-perturbative settings, for an overview see e.g. Ref. [91]. For reviews of the method we refer to Refs. [80, 91–94].

---

[6]One typically restricts these operators to be quasi-local. This choice is self-consistent as the flow does not generate operators with inverse powers of a derivative [87]. Non-localities in the effective action could arise when resumming infinitely many quasi-local terms, see Ref. [88] for a two-dimensional example.

3.2 Asymptotically Safe Quantum Gravity: Implementing Scale Symmetry

A quantum theory of the metric using perturbative effective field theory methods is not predictive for scales beyond the Planck scale. As the cornerstone of asymptotically safe quantum gravity, an interacting fixed point for gravity could restore predictivity and provide a UV completion [95]. We explore this scenario by applying the functional renormalization group to a gravitational theory. We will briefly outline the computation in the following, and refer to App. C for more details.

3.2.1 Asymptotic Safety in Gravity Systems

We apply the functional renormalization to the metric tensor $g_{\mu\nu}$ [96, 97]. As a simple example we focus on the Einstein-Hilbert action

$$\Gamma_k^{\mathrm{EH}} = \int \mathrm{d}^4x \, \sqrt{g} \frac{1}{16\pi \bar{G}_N} \left(2\bar{\Lambda} - R \right). \tag{3.25}$$

To apply the functional RG for the metric one uses the background field method [98]. One splits the metric into a background $\bar{g}_{\mu\nu}$ and a fluctuation $h_{\mu\nu}$, e.g. according to Eq. (3.2), and focuses on integrating out fluctuations $h_{\mu\nu}$. The scale dependent effective action depends on the background metric $\bar{g}_{\mu\nu}$ and the fluctuation $h_{\mu\nu}$. The background $\bar{g}_{\mu\nu}$ allows to (i) identify scales that can be compared to k and (ii) fix the gauge symmetry in the gravitational sector.

To evaluate the flow equation one computes the second variation of Γ_k^{EH} with respect to the fluctuation $h_{\mu\nu}$. As a consequence of diffeomorphism symmetry, this object contains zero modes and is not invertible. To fix the gauge one introduces the action

$$S_{\mathrm{gf}} = \frac{1}{2\alpha} \int \mathrm{d}^4x \, \sqrt{g} \bar{g}^{\mu\nu} \mathcal{F}_\mu \mathcal{F}_\nu, \tag{3.26}$$

with

$$\mathcal{F}_\mu = \sqrt{\frac{1}{16\pi \bar{G}_N}} \left(\bar{D}^\rho h_{\rho\mu} - \frac{1+\beta}{4} \bar{D}_\mu h_\rho^\rho \right). \tag{3.27}$$

Here, the parameters α and β are gauge parameters. The choice $\alpha \to 0$ is preferred and is a fixed point of the RG flow [99]. The parameter β does not have a preferred value. In the following we will work in the gauge $\beta = \alpha = 0$. For a discussion on the gauge dependence in pure gravity systems see Ref. [66].

The addition of the gauge fixing action (3.26) also requires to exponentiate the corresponding Jacobian by means of Faddeev-Popov ghosts with a ghost action S_{gh}

$$S_{\mathrm{ghost}} = - \int \mathrm{d}^4x \, \sqrt{\bar{g}} \bar{c}_\mu \left(\bar{D}^\rho \bar{g}^{\mu\kappa} g_{\kappa\nu} D_\rho + \bar{D}^\rho \bar{g}^{\mu\kappa} g_{\rho\nu} D_\kappa - \frac{1+\beta}{2} \bar{D}^\mu \bar{g}^{\rho\sigma} g_{\rho\nu} D_\sigma \right) c^\nu, \tag{3.28}$$

where c^μ is the corresponding ghost field.

Given the effective action $\Gamma_k = \Gamma_k^{\mathrm{EH}} + S_{\mathrm{gf}} + S_{\mathrm{ghost}}$, it is useful to decompose the metric fluctuation $h_{\mu\nu}$ as

$$h_{\mu\nu} = h_{\mu\nu}^{\mathrm{TT}} + \bar{D}_\mu v_\nu^{\mathrm{T}} + \bar{D}_\nu v_\mu^{\mathrm{T}} + \frac{1}{2}(\bar{D}_\mu \bar{D}_\nu + \bar{D}_\nu \bar{D}_\mu)\sigma - \bar{g}_{\mu\nu}\bar{D}^2\sigma - \frac{1}{4}g_{\mu\nu}h \qquad (3.29)$$

where $h_{\mu\nu}^{\mathrm{TT}}$ is a transverse-traceless tensor, v_μ^{T} is a transverse vector, and σ and h are the two scalar modes of the metric fluctuation. One can compute and invert $\Gamma_k^{(2)} + R_k$ for tensors, vectors and scalars, separately. The trace in the flow equation is most easily performed after specifying the background $\bar{g}_{\mu\nu}$ (although off-diagonal heat kernel techniques also allow for an evaluation on general backgrounds, see e.g. Ref. [100]). A computationally convenient choice are maximally symmetric backgrounds. The trace becomes a sum or integral over the corresponding eigenvalues that can either be evaluated explicitly or via heat kernel techniques. A Litim-type regulator provides a cutoff for the corresponding expression and allows to explicitly perform the trace on the right-hand side of the flow equation.

By taking appropriate derivatives of the flow equation with respect to the Ricci scalar[7] one can extract beta functions for the Newton coupling $G = \bar{G}_N k^2$ and the cosmological constant $\Lambda = \bar{\Lambda}k^{-2}$. The resulting beta functions feature two fixed points: (i) the Gaussian fixed point for vanishing Newton coupling and cosmological constant and (ii) an interacting fixed point at non-vanishing values for $G > 0$ and Λ.

The interacting fixed point gives rise to the asymptotic safety scenario [95], see Refs. [101–107] for reviews and lecture notes. Gravity remains a field theory even at trans-Planckian energies. An interacting UV fixed point realizes scale symmetry and allows to extend the field-theoretic description to arbitrary energies. If it features a finite number of relevant directions, the resulting theory is predictive. The Newton coupling and the cosmological constant remain relevant at the fixed point and allow to connect the fixed point values to their observed IR values [108, 109].

The Einstein-Hilbert truncation Γ_k^{EH} has been extended in various ways. Studies of higher curvature operators support the existence of a non-perturbative fixed point in the purely gravitational system. One line of research is the extension along particular "rays" in theory space. These truncations feature at most one curvature invariant at each mass dimension [110–114]. If these curvature invariants are evaluated on a four-sphere then each of them corresponds to a power of the Ricci scalar R^n. Comparing coefficients of the Ricci scalar then allows to extract the beta functions for each coupling. Such truncations have been extended up to order 144 in curvature invariants [114] and confirm the existence of an interacting fixed point with a finite number of relevant directions. As one example Ref. [113] considered an expansion in powers of the Ricci scalar $\sum_{n=0}^{70} b_n R^n$. The critical exponents for the couplings b_n approximately scale as [113]

$$\theta_n = 2.9 - 2.0n. \qquad (3.30)$$

---

[7]To extract the couplings one takes derivatives with respect to the Ricci scalar $\bar{R}$ build from the background metric $\bar{g}_{\mu\nu}$. The right-hand side of the flow equation still depends on $\frac{\delta^2 \Gamma_k[\bar{g}_{\mu\nu}, h_{\mu\nu}]}{\delta h_{\mu\nu}\, \delta h_{\rho\sigma}}$ and hence on fluctuation couplings. In this thesis we exclusively employ the background approximation: we assume that the fluctuation couplings can be approximated by background couplings.

This scaling exhibits an $\mathcal{O}(1)$ shift compared to the canonical scaling $\theta_n = 4 - 2n$. It implies that curvature operators R^n with $n \gg 2$ remain irrelevant. The critical exponents scale near-canonically, indicating that canonical power-counting allows setting up truncations that capture all relevant directions. While higher order curvature couplings remain irrelevant, the (ir-)relevance of curvature-squared couplings is not settled and the precise number of relevant directions is not fully determined. Depending on the truncation under consideration it is either two or three[8].

An alternative line of investigation studies all operators up to a fixed mass dimension. Disentangling the different curvature invariants is technically challenging, such that truncations are limited to relatively low orders in curvature invariants [100, 115–117]. As notable examples, Ref. [115] provides a first study of all invariants at quadratic order in curvature, and Ref. [116] studies the truncation (3.25) together with the Goroff-Sagnotti counterterm. Ref. [100] is the first reference to study all quadratic curvature invariants on a general background. All these computations confirm the existence of a gravitationally interacting fixed point with a number of relevant directions smaller or equal to three.

In addition, various technical advances provide new insights. Form factor computations aim to resolve larger parts of the momentum dependence of the gravitational action [118–122]. As one example, capturing part of this momentum dependence could remove the $r \to 0$ divergence in the Newtonian potential [122] and might resolve other singularities in general relativity. In addition, resolving the momentum dependence of the propagator provides information on the propagating degrees of freedom and the existence of ghosts in an asymptotically safe theory, see Ref. [123] for recent progress.

Fluctuation computations deal with the split of the metric into a background and a fluctuation without applying the background approximation [107]. Computations in the background approximation identify the correlation functions for background quantities and the correlation functions for fluctuation quantities. In the fluctuation approach these are treated separately. The resulting beta functions feature a fixed point with a finite-dimensional critical surface [99, 118–120, 124–128]. Trajectories emanating from this fixed point qualitatively reproduce the scaling of gravitational couplings expected in general relativity in the IR [118, 120, 127]. In this context extended truncations in the gravity sector have been studied on flat and curved backgrounds in Refs. [99, 126, 128].

In a fluctuation computation one also naturally distinguishes multiple avatars of the Newton coupling, a feature that also appears in non-perturbative quantum chromo-dynamics [125, 129, 130]. As one example, the Newton coupling can be extracted from various vertices. The coupling $\bar{G}_{N,h}$ is extracted from a three-graviton vertex $\sqrt{\bar{G}_{N,h}}h(\partial h)(\partial h)$ with h schematic notation for a graviton. The Newton coupling $\bar{G}_{N,\phi}$ is extracted from a graviton-scalar vertex $\sqrt{\bar{G}_{N,\phi}}h(\partial \phi)(\partial \phi)$ with ϕ a scalar. The two

---

[8]Ref. [114] identifies a fixed point with four relevant directions in the gravitational sector in a truncation featuring Ricci scalars and Kretschmann scalars. The same reference also identifies two fixed points that lie close to the fixed point found in the original Einstein-Hilbert truncation. These can be interpreted as higher order extensions of the fixed point in the Einstein-Hilbert truncation. One of these features only three relevant directions.

couplings $\bar{G}_{N,h}$ and $\bar{G}_{N,\phi}$ in general will not agree in a non-perturbative setting. The two couplings are however expected to agree in a perturbative setting. Refs. [125, 129, 130] found that different avatars of the same coupling are numerically close at the interacting fixed points, providing an additional argument for the near-perturbative nature of the gravitational fixed point.

Additional indications for the existence of an asymptotically safe fixed-point arise in perturbation theory [131, 132] and from studying gravity in $2 + \epsilon$ dimensions perturbatively [133–137]. Going forward, other non-perturbative methods such as dynamical triangulations [31, 138] or tensor models [139] have the potential to test the asymptotic safety scenario beyond the functional renormalization group.

This plethora of encouraging results lends credibility to the existence of an interacting gravitational fixed point. Next, we will discuss how the gravitational fixed point behaves under the addition of matter.

3.2.2 Impact of Matter on the Gravitational Fixed Point

To be compatible with observations, the gravitational fixed point also needs to support matter. On the one hand, the existence of matter influences the properties of the fixed point on the gravitational side. On the other hand, the gravitational fixed point constrains the structure in the matter sector. This interplay has been extensively studied in both directions. In this subsection we will focus on the constraints that the existence of matter provides on the gravitational parameter space. In the next chapter we discuss constraints that the existence of a combined fixed point puts on matter.

A combined gravity-matter system might allow to accommodate all SM degrees of freedom [140]. This result has been confirmed in fluctuation computations [141, 142] and computations in a setup that singles out a preferred direction [143]. Even in extended gravitational settings [144] and under technical variations [145] a combined fixed point persists.

The presence of matter shifts the gravitational fixed point values Λ_* and G_*. A simple form of the beta functions was computed in Ref. [140, 146] and given explicitly in Ref. [147], and will be quoted here for future reference

$$\beta_G = 2G - G^2 f_G, \tag{3.31}$$

$$\begin{aligned}\beta_\Lambda =\ & -2\Lambda - G\Lambda f_G \\ & -\frac{G}{2\pi}\left(7 - \frac{3}{2(3-4\Lambda)} + N_w - \frac{N_s}{2} - N_v - \frac{5}{2(1-2\Lambda)} - 8\log(3/2)\right),\end{aligned} \tag{3.32}$$

with

$$\begin{aligned}f_G =\ & \frac{5}{6\pi(1-2\Lambda)} + \frac{5}{3\pi(1-2\Lambda)^2} - \frac{1}{2\pi(3-4\Lambda)} \\ & +\frac{11 + 32\log(3/2)}{12\pi} - \frac{1}{6\pi}\left(N_w + N_s - 4N_v\right),\end{aligned} \tag{3.33}$$

and N_w, N_s and N_v being the number of Weyl fermions, scalars and gauge-fixed vector bosons, respectively. We employ these beta functions together with the results of our

computations in the scalar sector, see App. C. The presence of SM matter shifts the interacting gravitational fixed point to

$$\Lambda_* = -9.97, \quad G_* = 7.63. \tag{3.34}$$

Notice that the fixed point lies at negative Λ. This is not in contradiction with observations as the flow towards the IR can still yield a positive cosmological constant in the IR [148].

The fixed point values for Λ and G depend on the matter content and on a variety of technical choices, see e.g. [66]. In the following we will hence often take the fixed point values Λ_* and G_* as free parameters to explore the resulting phenomenology in the matter sector. This should be understood as a parametrization of both, technical uncertainty and the effect of additional matter degrees.

The resulting space of gravitational fixed point values is bounded by $G_* = 0$ and $\Lambda_* = 1/2$. The bound $G_* = 0$ arises because all contributions in β_G are proportional to G. An RG trajectory cannot cross $G = 0$. The observation of positive G in the IR hence requires positive G at all scales. The bound $\Lambda_* = 1/2$ arises because gravitational contributions to beta functions from the transverse-traceless sector are proportional to powers of $\sim \frac{1}{1-2\Lambda}$. These contributions feature a pole at $\Lambda_* = 1/2$. This pole provides an upper bound for the fixed point value of Λ_*. For small G and small $\Lambda \ll 0$ the gravitational contributions become small. In the associated region of the $\Lambda - G$ plane gravitational fluctuations weaken. Conversely, close to the pole $\Lambda = 1/2$ and for large G gravitational effects are enhanced. Strong gravitational fluctuations potentially lead to divergences in the matter sector, see Sec. 4.1.2. Accordingly, the regime of relatively weak gravitational fluctuations appears to be preferred in the presence of matter.

3.2.3 Effective Asymptotic Safety

Before we study the effect of an asymptotically safe fixed point on the matter sector, let us briefly introduce a scenario that leverages the predictive power of asymptotic safety in a different setting [148–150]: so far, we assumed that at high energy scales metric fluctuations induce an interacting fixed point. Breaking with this assumption, let us now assume that new degrees of freedom take over for $k > k_{\mathrm{UV}}$, with k_{UV} an energy scale set by the UV theory. Below k_{UV} an effective description in terms of metric degrees of freedom is applicable.

The UV theory sets the initial conditions for the effective theory at k_{UV}. The RG flow translates these initial conditions into IR physics, see Ref. [148] for an example. For irrelevant couplings, the RG flow will damp out deviations from their fixed point values. It focuses a wide interval of initial conditions onto a small interval. This focusing implies a preference for coupling values close to their fixed point value. This preference for certain regions in coupling space can be interpreted as an enhancement of predictivity [150]. Hence, even in the absence of a metric UV completion the RG flow enhances predictivity for irrelevant couplings.

If $k_{\rm UV} < M_{\rm Pl}$, then one only needs to take matter degrees of freedom into account. As an example, the SM beta functions feature an infrared fixed point relating the top Yukawa coupling, the strong gauge coupling and the Higgs quartic coupling. The fixed point prefers masses for the Higgs and top mass close to the observed ones [151, 152]. If $k_{\rm UV} > M_{\rm Pl}$, one needs to take quantum fluctuations of the metric degrees of freedom into account. Their effect can be computed with the help of the framework that we presented in this chapter. Assuming that $k_{\rm UV} > M_{\rm Pl}$, in the following, we will also explore arbitrary initial conditions for matter couplings and study how they evolve under the impact of gravitational fluctuations. In this scenario irrelevant couplings are driven towards their asymptotically safe value. For an observer in the IR the theory approximately emanates from an asymptotically safe fixed point. This scenario is hence called effective asymptotic safety. It additionally motivates considering asymptotically safe theories.

To summarize, we introduced the scenario of asymptotic safety: an interacting fixed point might allow for a UV-complete description of gravity in terms of the metric. This scenario has been studied in a variety of truncations and approximations using the functional renormalization group. All existing computations find an interacting fixed point that typically features two or three relevant directions. As the number of relevant directions is finite (and even small) predictivity is restored. In addition, the fixed point might enhance predictivity in the matter sector, as we will explore in the following section.

Matter in Asymptotically Safe Quantum Gravity

4

We have discussed how gravitational interactions could become asymptotically safe at an interacting fixed point. The interacting fixed point might provide a scale-invariant description of quantum spacetime. To bear resemblance with the universe we observe, any description of spacetime also requires a description of matter. A fixed point in the combined gravity-matter system could allow to extend the description of quantum spacetime and matter to arbitrarily high energies and could restore predictivity.

The resulting highly predictive theory should be contrasted with a standard effective field theory. Within an effective field theory every new coupling yields an additional free parameter. The resulting parameter space is huge, leading to a loss of predictivity. However, only very few sets of parameters are consistent within an asymptotically safe theory of gravity and matter. Such a theory allows to delineate the swampland of UV inconsistent theories and the landscape of UV consistent theories[1]. Here, we explore the landscape of asymptotically safe quantum gravity: we ask how an asymptotically safe gravity-matter system constrains the matter sector.

Ultimately, one should pose that question for the full SM and its extensions. However, uncertainties in the gravitational fixed point values lead to uncertainties in the matter sector, making precise quantitative predictions challenging. As a stepping stone towards such computations we will explore qualitative and semi-quantitative features that arise in asymptotically safe matter models, see also Refs. [102, 154] for reviews. We first discuss the relation between symmetries and the RG flow in Sec. 4.1. We then introduce three building blocks that comprise the most defining interactions of the SM: quartic interactions, Yukawa interactions and gauge interactions in Sec. 4.2. In Sec. 4.3 we relate these building blocks to the SM and its extensions. The results we review in these three sections almost exclusively assume that matter is minimally coupled. In Sec. 4.4 we extend the truncation and study how a non-minimal coupling might affect results in the Yukawa sector.

4.1 Global Symmetries and the RG Flow

The global symmetry structure determines which fixed points exist in a given theory[2]. Consider a scale-dependent effective action Γ_k invariant under the global symmetry G. The symmetry G is compatible with a set of operators. These operators come with

---

[1]While the metaphor of a landscape was first used in a string theoretic setting, see Ref. [153] for a review, the underlying program is more general and also applies to asymptotically safe gravity-matter theories.

[2]In order not to deviate from conventional notation, we use G for the symmetry group in this and the next subsection. G is the Newton coupling in the rest of this thesis.

h_{i*}	(ir-)relevant	G broken in the IR
$= 0$	irrelevant	no
$= 0$	relevant	depends on trajectory
$\neq 0$	irrelevant	depends on critical hypersurface
$\neq 0$	relevant	depends on trajectory

Tab. 4.1.: We classify various ways to realize H, but not G, in the IR. The first column indicates whether h_i has a non-vanishing fixed point value, the second column indicates whether the coupling is relevant or irrelevant at the fixed point. The second row corresponds to the RG-flow-breaking scenario, the third and fourth row to the fixed-point-breaking scenario.

couplings g_i. The space spanned by the g_i is a hypersurface $\mathcal{G}$ in the more general theory space spanned by all possible couplings.

The right-hand side of the flow equation (3.21) depends on Γ_k and the regulator R_k. In the following we will assume that R_k is chosen such that it respects the same global symmetries as Γ_k. If Γ_k is invariant under G at one scale k_0, then the right-hand side of the flow equation is invariant under that symmetry. The RG flow does not generate any terms incompatible with the symmetry G. If initialized on the hypersurface $\mathcal{G}$, the RG flow will not leave it.

The variation $\Gamma_k^{(2)}$ depends on the kinetic term for the underlying field. The flow will generate all interactions compatible with the symmetries of the kinetic term G_{kin}, at least for an interacting theory. Accordingly, the choice $G = G_{\text{kin}}$ is maximal.

Now consider an interaction that does not respect the global symmetry G, but instead only respects a reduced global symmetry $H \subset G$. The symmetry group H is a subset of G. Conversely, the set of operators respecting H is a superset of the operators respecting G. The operators compatible with H, but not G, come with couplings h_i. The hypersurface $\mathcal{H}$ spanned by the couplings g_i, h_i is higher dimensional than the one spanned by the g_i alone. The hypersurface $\mathcal{H}$ reduces to the hypersurface $\mathcal{G}$ under the restriction $h_i = 0$, under this restriction one recovers the G-symmetric theory.

Whenever the theory is G-symmetric it trivially is also H-symmetric as $H \subset G$. We investigate under which conditions one can break the symmetry G, but realize the theory H.

We distinguish two different scenarios, see Fig. 4.1 and Tab. 4.1:

- In the fixed-point-breaking scenario the symmetry G is broken at a fixed point with $h_{i*} \neq 0$.

- In the RG-flow-breaking scenario the symmetry G is realized at a fixed point with $h_{i*} = 0$, but broken along the RG flow by a relevant coupling h_i.

The fixed-point-breaking scenario requires a fixed point with $h_{i*} \neq 0$. If any of the beta functions β_{h_i} features such a fixed point, then the breaking of G to H permeates into the other couplings $h_j, \ldots$ compatible with H. Geometrically, such a fixed point lies in $\mathcal{H} \setminus \mathcal{G}$. It violates G and only realizes H.
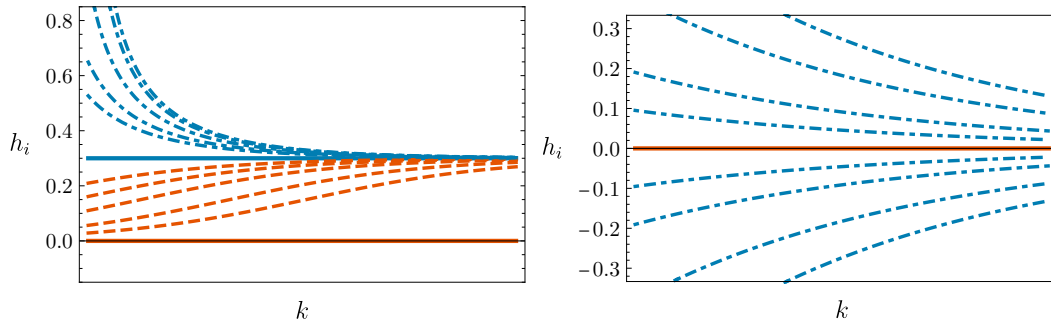
Fig. 4.1.: Possible scenarios to obtain a non-vanishing coupling $h_i \neq 0$ in the IR. Blue fixed-point trajectories realize H in the IR, red fixed-point trajectories approximately realize G (and only realize H trivially). (left) In the fixed-point-breaking scenario, an interacting fixed point for h_i realizes $h_{i*} \neq 0$. The value of h_i in the IR depends on the RG trajectory and the (ir-)relevance of the corresponding surface at $h_i = 0$. For this plot we assume that at the interacting fixed point h_i is relevant. (right) In the RG-flow-breaking scenario, a relevant coupling h_i allows deviating from $h_{i*} = 0$ towards the IR.

Such a breaking of G to H can persist into the IR. If the hypersurface $\mathcal{G}$ is IR attractive, then there are trajectories that approach $h_i = 0$. For these trajectories G is approximately realized in the IR. If the hypersurface $\mathcal{G}$ is IR repulsive, then only H, but not G, will be realized in the IR.

The RG-flow-breaking scenario requires a coupling h_i relevant at the fixed point $h_{i*} = 0$. The fixed point $h_{i*} = 0$ is G-symmetric. This symmetry can be broken by the RG flow. For a relevant coupling h_i, the RG flow enhances deviations from $h_{i*} = 0$. The flow deviates from the hypersurface $\mathcal{G}$. The resulting theory is H-symmetric in the IR.

If neither of the two scenarios is realized, i.e. if there are no fixed points that break G, and no G-breaking coupling is relevant, then G will be realized at all scales. As a consequence H can only be realized trivially in an asymptotically safe theory in this case.

4.1.1 Global Symmetries in Gravity-Matter Systems

Let us apply this argument to the matter sector of a combined gravity-matter theory. We first focus on symmetries that are a true subset of the symmetry of the kinetic term, $G \subset G_{\text{kin}}$. We consider G to be a symmetry of the matter sector only. The couplings g_i belong to matter interactions invariant under G.

Consider the beta function for a coupling g_i

$$\beta_{g_i} = \beta_{g_i}^{\text{without grav}} + \Delta\beta_{g_i}^{\text{grav}}. \tag{4.1}$$

Here $\beta_{g_i}^{\text{without grav}}$ is the beta function in the absence of gravity and $\Delta\beta_{g_i}^{\text{grav}}$ are contributions that arise due to gravitational fluctuations.

For $g_i = 0$ the theory is invariant under G_kin. The flow preserves this symmetry and does not generate any of the g_i, hence $\beta_{g_i}(g_i = 0) = 0$. This statement holds both in the absence and in the presence of gravitational interactions. In the absence of gravity $\beta_{g_i}^\text{without grav}$ must vanish for $g_i = 0$. In the presence of gravity β_{g_i} must vanish for $g_i = 0$. Hence, any gravitational contribution must be proportional to one of the g_i.

The gravitational contributions hence take the form [3]

$$\Delta\beta_{g_i}^\text{grav} = -f_{g_i}g_i + \mathcal{O}\!\left(g_j^2\right). \tag{4.2}$$

Here, f_{g_i} encodes the gravitational contributions to the beta function.

If the sector G_kin features a fixed point for non-vanishing gravitational couplings, then this fixed point can be extended to one with vanishing $g_{i*} = 0$.

One can realize G non-trivially in the IR by either (i) the fixed-point-breaking scenario, i.e. by additional non-vanishing fixed points with $g_i \neq 0$ or (ii) the RG-flow-breaking scenario, i.e. a relevant coupling g_i.

The fixed-point-breaking scenario is realized if new fixed points are present under the impact of gravitational fluctuations. This can happen if the term f_{g_i} and terms in $\beta_{g_i}^\text{without grav}$ balance at $g_i \neq 0$. The RG-flow-breaking scenario is realized if a coupling becomes relevant at the partial fixed point $g_{i*} = 0$ as a consequence of gravitational fluctuations. The critical exponent of the partial fixed point $g_{i*} = 0$ is modified by gravitational contributions f_{g_i}. If $f_{g_i} > 0$ the gravitational contributions can make a coupling g_i relevant.

Notice that within asymptotic safety there are no indications against the existence of a global symmetry G [105] (at least in the absence of topological fluctuations, see Ref. [155]). This should be contrasted with arguments suggesting the violation of global symmetries by quantum gravity in a string-inspired context [156–159]. These arguments can be strengthened further in the context of the AdS/CFT correspondence [160–162]. In the following we will work under the assumption that global symmetries exist in the presence of quantum gravity.

4.1.2 Weak Gravity Bounds

So far, we focused on symmetries that are a subset of G_kin. We assumed the existence of a fixed point that realizes G_kin at non-vanishing gravitational couplings. However, in the presence of non-vanishing gravitational couplings such a fixed point is not guaranteed to exist. Let us focus on the example of a single scalar ϕ [163, 164]. The kinetic term $\frac{1}{2}g^{\mu\nu}\partial_\mu\phi\partial_\nu\phi$ is invariant under a combined $\mathbb{Z}_2$ and shift symmetry $\phi \to \phi + C$. It couples to the metric. This coupling induces an infinite tower of interactions between matter fields and gravitational fluctuations. However, the gravitational sector is interacting. These interactions percolate into the matter sector

---

[3]A term linear in g_j ($i \neq j$) can only appear if there is a coupling with the same symmetry structure and the same number of external matter legs. We neglect this case here, as it does not qualitatively change our argument. However, such terms do appear in the presence of non-minimal couplings.
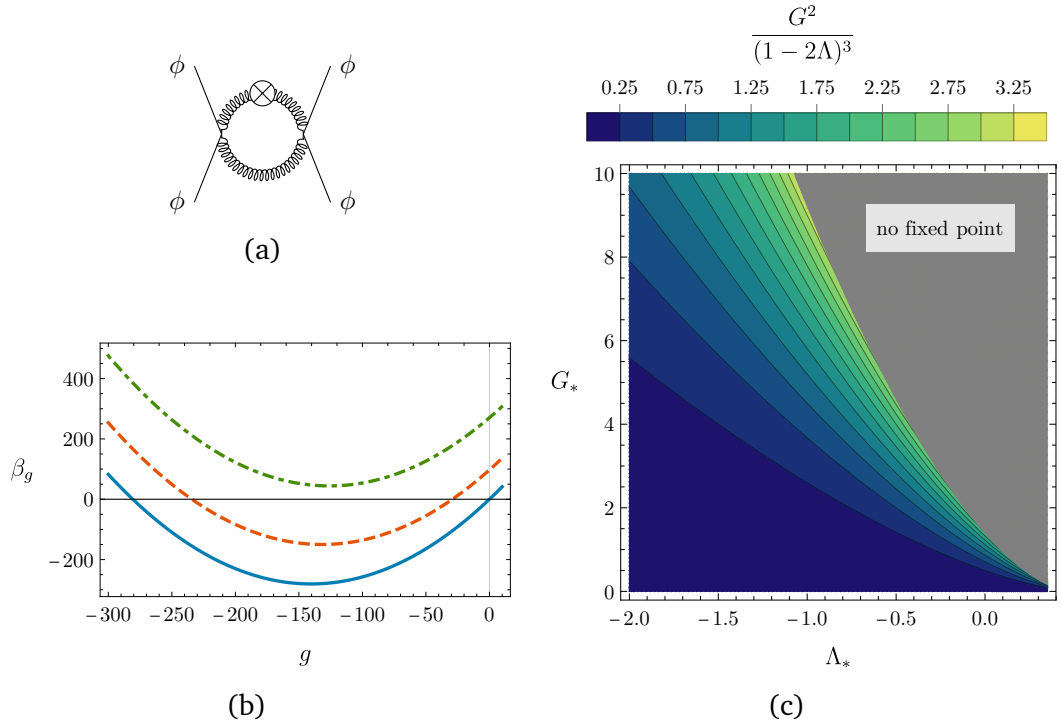
Fig. 4.2.: (a) Candy diagram inducing the coupling g. The cross marks a regulator insertion. The curly lines correspond to gravitons. (b) Beta function β_g for varying values of the Newton coupling G. For $G = 0$ the Gaussian fixed point $g = 0$ is realized (solid, blue). For values of G smaller than a critical value it is shifted to finite coupling $g \neq 0$ (dashed, orange). For values G larger than a critical value the fixed point does not exist (dot-dashed, green). (c) Gravitational parameter space. In the gray region no fixed point for g exists. The color-coding indicates the value of $\frac{G^2}{(1-2\Lambda)^3}$. The beta functions are taken from Ref. [164].

and induce all interactions compatible with G_{kin}. The operator $(g^{\mu\nu}\partial_\mu\phi\partial_\nu\phi)^2$ is induced via a graviton-mediated candy diagram, see panel (a) in Fig. 4.2. The beta function for its coupling g has the form [164]

$$\beta_g = 4g + \frac{9}{64\pi^2}g^2 - f_g(\Lambda, G)g + F_g(\Lambda)G^2, \qquad (4.3)$$

with G the Newton coupling. Crucially, it features a contribution $F_g(\Lambda)G^2$ independent of g.

For non-vanishing Λ_*, G_* the contribution $F_g(\Lambda)G^2$ shifts the Gaussian fixed point $g = 0$ to $g_* \neq 0$, see panel (b) in Fig. 4.2. If the contribution becomes too large, then the coupling g does not feature a fixed point anymore. The underlying theory is no longer asymptotically safe.

To avoid such a situation gravitational fluctuations need to be weak. The gravitational transverse-traceless mode contributes terms that are proportional to powers of $\frac{1}{(1-2\Lambda)}$ to matter beta functions, and similar for the other modes. These terms decrease when $|\Lambda|$ increases. Consequently, the gravitational contribution $F_g(\Lambda)G^2$ becomes small when (a) G is small or (b) $|\Lambda|$ is large. In this regime gravitational fluctuations become

"weak". As one example we show the expression $\frac{G^2}{(1-2\Lambda)^3}$ that is proportional to one of the three terms appearing in F_g in Fig. 4.2.

The requirement of an asymptotically safe theory hence translates into the requirement of sufficiently weak gravitational fluctuations. The corresponding weak-gravity bounds have been explored in the scalar sector [163, 164], gauge sector [165] and for fermions and Yukawa systems [166–168]. The qualitative picture is similar in all cases: if gravitational fluctuations become too strong, then some interactions compatible with the symmetries of the kinetic term do not feature fixed points anymore. As a result the theory is not asymptotically safe.

4.2 Building Blocks of Matter Systems

After focusing on the special case G_{kin}, we now turn back to interactions that break some symmetries of the kinetic term. We discuss scalar quartic interactions, Yukawa interactions and gauge interactions as toy models for the defining interactions of the SM. For each of the interactions we review existing results obtained within a toy model that highlights the impact of gravitational fluctuations on matter interactions.

4.2.1 Quartic Interactions

As a toy model one considers a real scalar ϕ with the effective action $\Gamma_k = \Gamma_k^{\text{EH}} + \Gamma_k^{\text{scal}} + S_{\text{gf}} + S_{\text{gh}}$ with

$$\Gamma_k^{\text{scal}} = \int \mathrm{d}^4 x \sqrt{g} \left(\frac{Z_\phi}{2} g^{\mu\nu} \partial_\mu \phi \partial_\nu \phi + \frac{\bar{m}^2}{2} \phi^2 + \frac{\lambda_4}{4} \phi^4 \right), \tag{4.4}$$

and the Einstein-Hilbert action Γ_k^{EH} in the gravitational sector. The kinetic term for the scalar features a $\mathbb{Z}_2$ symmetry and is invariant under shifts $\phi \to \phi + C$ with C a constant. The couplings $m^2 = \bar{m}^2/k^2$ and λ_4 break the shift symmetry and only maintain the $\mathbb{Z}_2$ symmetry.

As higher-order interactions of the type discussed in the last section are absent, a shift symmetric fixed point, i.e. a fixed point at $m^2 = \lambda_4 = 0$ is guaranteed to exist. In the following we explore in how far one can deviate from this fixed point.

For vanishing mass $m^2 = 0$, the beta function for the quartic coupling λ_4 reads

$$\beta_{\lambda_4} = \frac{3}{16\pi^2} \lambda_4^2 - f_s \lambda_4. \tag{4.5}$$

Here the term f_s encodes the influence of gravitational fluctuations. It is generally found to be negative $f_s < 0$ [68, 145, 169–178], see also the discussion in Sec. 5.3.1 below. The beta function (4.5) does not feature an interacting fixed point with a stable potential. At the Gaussian fixed point $\lambda_{4*} = 0$, the sign of f_s determines the critical exponent of the quartic coupling. As $f_s < 0$, the quartic coupling is irrelevant. The coupling vanishes not only at the fixed point but also in the IR. Shift symmetry remains unbroken, and the scalar potential remains flat.

If gravitational fluctuations are not too strong, then the mass parameter remains relevant at the Gaussian matter fixed point; the fixed point is compatible with a range of IR masses. If the mass acquires a non-vanishing value along the flow, then gravitational fluctuations couple to it. A graviton-mediated candy diagram (see panel (a) in Fig. 4.2) and other diagrams then induce the quartic coupling. The quartic coupling does not vanish because shift symmetry is broken. The breaking of shift symmetry due to a non-vanishing mass induces a non-vanishing λ_4. As long as $m^2 \ll M_{\mathrm{Pl}}^2$ the corresponding diagrams will lead to a tiny value of the quartic coupling $\lambda_4 \ll 1$, and shift symmetry remains an approximate symmetry.

We conclude that in the scalar system shift symmetry is not violated via the fixed-point-breaking scenario. The scalar mass enables a breaking of shift symmetry via the RG-flow-breaking scenario.

4.2.2 Yukawa Interactions

To violate shift symmetry not only along the flow to the IR, but already at the fixed point, one additionally introduces a Dirac fermion ψ. The two fields ψ and ϕ are coupled via a Yukawa interaction. The resulting effective action $\Gamma_k = \Gamma_k^{\mathrm{EH}} + \Gamma_k^{\mathrm{scal}} + \Gamma_k^{\mathrm{ferm}} + S_{\mathrm{gf}} + S_{\mathrm{gh}}$ contains the fermionic part

$$\Gamma_k^{\mathrm{ferm}} = \int \mathrm{d}^4 x \, \sqrt{g} \left(i Z_\psi \bar{\psi} \slashed{\nabla} \psi + i y \phi \bar{\psi} \psi \right). \tag{4.6}$$

The beta function for the quartic coupling additionally contains a term independent of λ_4 proportional to y^4.

For the effective action defined above the beta function for the Yukawa coupling reads

$$\beta_y = \frac{5}{16\pi^2} y^3 - f_y y \tag{4.7}$$

if one neglects masses, $m^2 = 0$. Here the first term is the standard perturbative result, the second term again arises due to gravitational fluctuations and depends on the gravitational fixed point values [166, 168, 172, 174, 178–181]. For Λ_* larger than a critical value Λ_{crit}, one finds that $f_y < 0$. The only fixed point is the Gaussian fixed point and the Yukawa coupling is irrelevant at that fixed point.

For $\Lambda < \Lambda_{\mathrm{crit}}$, the gravitational contributions switch sign, $f_y > 0$ [166, 168, 178, 181]. In this case, the Yukawa coupling becomes relevant at the Gaussian fixed point. Similar to the scalar mass, the breaking of shift symmetry by the relevant coupling y permeates into the scalar sector and induces other shift-symmetry breaking couplings such as λ_4. As long as $y < 1$, that breaking is small, such that $\lambda_4 \ll 1$. A range of IR values for y is compatible with the Gaussian fixed point in the UV.

Additionally, for $\Lambda < \Lambda_{\mathrm{crit}}$, a new interacting fixed point

$$y_* = \sqrt{\frac{16\pi^2 f_y}{5}}, \tag{4.8}$$
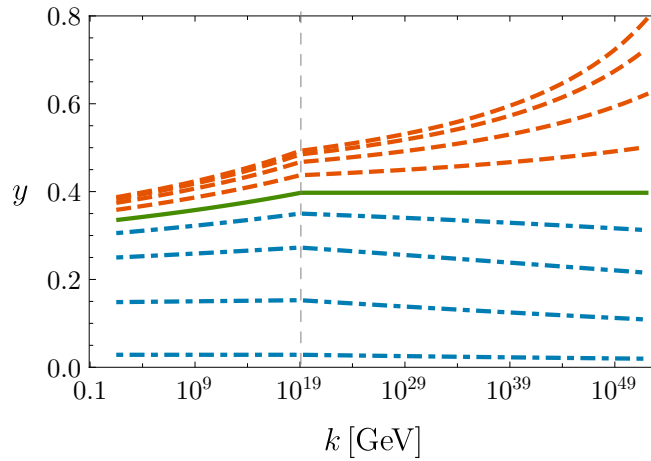
Fig. 4.3.: We show the Yukawa coupling as a function of the RG scale k for a fiducial value $f_y = 0.005$. The green solid trajectory corresponds to the interacting fixed point. The dot-dashed blue trajectories emanate from the free fixed point. The dashed red trajectories are asymptotically unsafe. The interacting fixed point acts as an upper limit for all asymptotically safe trajectories. The dashed vertical line marks the Planck scale. Below the Planck scale we switch of the gravitational contributions and set $f_y = 0$.

appears. At this fixed point the Yukawa coupling is irrelevant. The trajectory emanating from this fixed point singles out a single value for y in the IR. In addition, it acts as an upper bound for asymptotically safe IR values of the Yukawa coupling, see Fig. 4.3. At the interacting fixed point shift symmetry is broken. The beta function for the quartic coupling does not admit the solution $\lambda_{4*} = 0$ anymore, and λ_{4*} has a non-vanishing value. The coupling λ_4 remains irrelevant.

The presence of an interacting fixed point for the Yukawa coupling enables a fixed-point-breaking scenario for the scalar shift symmetry in part of the gravitational parameter space.

4.2.3 Gauge Interactions

In the absence of gravitational interactions, non-Abelian gauge theories exhibit the simplest form of asymptotic safety: they are asymptotically free. Various results indicate that they remain asymptotically free in the presence of gravitational fluctuations [182–184]. The corresponding gauge couplings hence vanish at a UV fixed point.

Abelian gauge theories exhibit a Landau pole in the absence of gravitational interactions. Their gauge coupling diverges for large but finite energies, see also Fig. 1.1. This pathology might be cured by gravitational interactions [185, 186]. As a toy model for Abelian gauge interactions one can consider a complex scalar field charged under a gauged $U(1)$ symmetry [186]. The resulting beta function for the gauge coupling ρ has the form [186]

$$\beta_\rho = \frac{1}{48\pi^2}\rho^3 - f_\rho\rho \tag{4.9}$$

where again f_ρ summarizes gravitational contribution to the corresponding beta function. The resulting fixed point structure resembles the one in the Yukawa case:

for values of the cosmological constant $\Lambda_* > \Lambda'_{\text{crit}}$ one finds $f_\rho < 0$. Only the Gaussian fixed point exists, the gauge coupling ρ is irrelevant at that fixed point and vanishes at all scales. For $\Lambda_* < \Lambda'_{\text{crit}}$, one finds that $f_\rho > 0$ and hence ρ is relevant at the Gaussian fixed point. Additionally, an interacting fixed point emerges. At this interacting fixed point ρ is irrelevant. The trajectory $\rho(k)$ emanating from the interacting fixed serves as an upper bound for the range of values that is compatible with asymptotically safe quantum gravity. Extensions of this scenario to higher order operators have been studied in Ref. [165], see also Ref. [187] for a proposal relating the existence of an upper bound on the gauge coupling and the number of spacetime dimensions.

4.3 Implications for the Standard Model

Equipped with these toy models, in this section we explore the potential implications of a gravity-matter fixed point for the SM. We caution that we extrapolate our results from simple toy models to the full SM. For the full SM the existence of an interacting gravity-matter fixed point has not yet been established. If such a fixed point exists, then its irrelevant directions correspond to predictions of the theory. They might allow fixing marginal couplings in the SM, thereby enhancing its predictivity.

Note that the Higgs vacuum expectation value v_{EW} is a canonically relevant parameter in the SM. It typically remains relevant at an interacting gravity-matter fixed point. Accordingly, a range of IR values is compatible with the UV fixed point. The observed value of $v_{\text{EW}} \approx 246\,\text{GeV}$ singles out the particular RG trajectory realized in nature. To obtain this trajectory the UV initial conditions need to be perturbed with a very high degree of precision to obtain the correct infrared value. This high degree of fine-tuning is an incarnation of what often is called the "hierarchy problem". From an asymptotically safe point of view this is not problematic — the correct trajectory is just singled out by measurement. In the following we will assume that the vacuum expectation value is fixed to the measured value.

4.3.1 Prediction of the Higgs Mass

The Higgs mass in the SM is

$$M_{\text{H}} = \sqrt{2\lambda_{\text{H}}(k_{\text{IR}})v_{\text{EW}}^2}, \tag{4.10}$$

where λ_{H} is the Higgs quartic coupling evaluated at the scale k_{IR} (typically chosen to be the top mass). The Higgs mass directly depends on the Higgs quartic coupling.

The discovery of the Higgs particle [8, 9] at a mass of $M_{\text{H}} = 125.3 \pm 0.2\,\text{GeV}$ [14] falls into a unique range in parameter space. On the one hand, for considerably larger Higgs masses the Higgs quartic coupling diverges before the Planck scale [188, 189]. This would require new degrees of freedom or a strongly coupled regime below the Planck scale. On the other hand, a small Higgs mass implies a small Higgs quartic coupling in the infrared. Reversing the RG flow, a small quartic coupling in the infrared might lead to a negative quartic coupling at high energies. Equating the RG scale μ with the field value Φ, a negative quartic coupling gives rise to a second minimum of the Higgs potential. If the probability to decay to this new vacuum is sufficiently high,

then one predicts a lifetime for the electroweak vacuum that contradicts observations. As a consequence, for much smaller Higgs masses the electroweak vacuum is unstable [190–196].

Given the experimental mean values for the Higgs mass and other SM parameters the quartic coupling turns negative before the Planck scale. This gives rise to a new minimum at large field values. But the probability of decaying to this new minimum is tiny. The predicted lifetime of the (false) electroweak vacuum is larger than observable time spans and the electroweak vacuum is meta-stable [190–196]. Note however, that these conclusions are sensitive to the presence of higher-order operators [197–203].

The Higgs mass and vacuum stability concern very different energy scales. A link between these scales is provided by the running of the quartic coupling λ_{H}. In an FRG computation that (i) neglects mass-like terms, (ii) neglects anomalous dimensions that arise from regulator derivatives and (iii) considers the SM gauge group, the top quark, the Higgs and the Einstein-Hilbert action this running will be given by

$$
\begin{aligned}
\beta_{\lambda_{\mathrm{H}}} = -f_s \lambda_{\mathrm{H}} \quad & + \quad \frac{1}{16\pi^2} \left(-6y_t^4 + \frac{3}{8} \left(2g_2^4 + (g_2^2 + \frac{5}{3}g_Y^2)^2 \right) \right) \\
& + \quad \frac{1}{16\pi^2} \lambda_{\mathrm{H}} \left(12y_t^2 - 9g_2^2 - 5g_Y^2 \right) + \frac{3}{2\pi^2} \lambda_{\mathrm{H}}^2,
\end{aligned} \tag{4.11}
$$

where g_i and y_t are the gauge couplings and the top Yukawa coupling, respectively. The term f_s encodes gravitational contributions to the beta function. We neglect all quarks apart from the top quark as their contribution to the running is numerically subdominant. For $f_s = 0$ Eq. (4.11) reduces to the standard one-loop result.

For the numerical values realized in the SM, the contributions from the gauge couplings and those from the top Yukawa coupling approximately cancel over a large range of scales. As a result the quartic coupling only runs very slowly. This delicate balance strongly depends on the value of the top Yukawa coupling. The top Yukawa coupling is extracted from the measured top mass. The top mass hence strongly influences the running of the quartic coupling.

Measuring the top mass in turn is an intricate procedure. In standard measurements one extracts the top mass from Monte Carlo event generators. The resulting mass is typically assumed to be equal to the pole mass. However, it is unclear how well existing Monte Carlo event generators account for higher order non-perturbative effects, see Ref. [204] for a review. As a result, the systematical errors on the top mass are still of the order of one to two GeV. In particular, this still allows for a significantly lower top mass. At the same time, direct measurements of the pole mass prefer such a lower value [205–207]. A lighter top would alter the flow of the quartic coupling. It might even lead to a positive quartic coupling λ_{H} all the way up to the Planck scale. It will be interesting to observe how the top mass will evolve as a result of new measurements and an improved theoretical understanding of non-perturbative uncertainties. For the remainder of this section we will assume that the top mass is given by the currently measured central value of $M_{\mathrm{top}} = 172.8 \pm 0.3\,\mathrm{GeV}$ [14]. In the following we explore the resulting flow of the quartic coupling within asymptotic safety in more detail.

The beta function (4.11) relates the IR Higgs mass and the Higgs potential at large field values. While so far we explored the stability of the resulting potential for a given Higgs mass, in the context of an asymptotically safe UV completion the reverse point of view is more appropriate. An asymptotically safe UV completion sets the initial conditions deep in the UV at a scale k_* with $M_{\mathrm{Pl}} \ll k_* \to \infty$. The beta function (4.11) with the gravitational contribution allows computing $\lambda_{\mathrm{H}}(M_{\mathrm{Pl}})$. The same beta function without the gravitational contribution allows computing $\lambda_{\mathrm{H}}(k_{\mathrm{IR}})$. Given a quartic coupling in the IR, one can then compute the resulting Higgs mass. For vanishing Yukawa and gauge interactions, asymptotic safety implies UV initial conditions $\lambda_{\mathrm{H}*} = 0$ at $k_* \gg M_{\mathrm{Pl}}$. In addition, the quartic coupling is irrelevant. As a result it vanishes not only at the fixed point, but also at the Planck scale, $\lambda_{\mathrm{H}}(M_{\mathrm{Pl}}) \approx 0$, as long as Yukawa and gauge interactions are negligible. Below the Planck scale the quartic coupling is regenerated by gauge and Yukawa interactions. Solving the RG equations with this boundary condition for $k < M_{\mathrm{Pl}}$, one obtains a prediction for the IR Higgs mass [208]. The resulting value is about $\sim 129\,\mathrm{GeV}$ using three-loop beta functions and two-loop matching [209]. It is slightly larger than the observed value.

Due to the presence of gauge and Yukawa interactions the condition $\lambda_{\mathrm{H}*}(M_{\mathrm{Pl}}) = 0$ will not hold exactly. Instead, the value of the quartic coupling will depend on the gauge and the Yukawa coupling. For these we can distinguish two different scenarios: If the gauge and the Yukawa coupling vanish at a UV fixed point, then all λ_{H}-independent contributions in (4.11) vanish. As a consequence, $\lambda_{\mathrm{H}*}$ also vanishes at the fixed point. If at least one of the gauge and Yukawa interactions is relevant and deviates from its fixed point value, it will pull the other couplings along. This generates a non-vanishing but tiny quartic coupling at the Planck scale and $\lambda_{\mathrm{H}}(M_{\mathrm{Pl}}) \approx 0$ still holds to a good approximation. The resulting Higgs mass still is of the order of $M_{\mathrm{H}} \approx 129\,\mathrm{GeV}$.

If either the Abelian gauge coupling or the top Yukawa coupling or both realize an interacting fixed point, $g_{i*} \neq 0$ or $y_{t*} \neq 0$, then the λ_{H}-independent contributions in (4.11) do not vanish. As a consequence $\lambda_{\mathrm{H}*} \neq 0$ at the UV fixed point. If only the gauge coupling is interacting, then $\beta_{\lambda_{\mathrm{H}}}$ only features a fixed point for large enough f_s. Without gravitational contributions no fixed point exists. We do not consider this case here. If either only the Yukawa coupling is interacting or both, the gauge and the Yukawa coupling are interacting at the fixed point, then Yukawa contributions dominate over gauge contributions in (4.11). One obtains a positive quartic coupling $\lambda_{\mathrm{H}*} > 0$ at the fixed point. Up to small corrections this value permeates to the Planck scale, $\lambda_{\mathrm{H}}(M_{\mathrm{Pl}}) \approx \lambda_{\mathrm{H}*} > 0$. Due to the positive quartic coupling the resulting IR Higgs mass is even larger, see also Tab. 4.2.

We explore this effect quantitatively by evolving the measured infrared values for the top Yukawa coupling and the U(1) gauge coupling to the Planck scale using the SM beta functions. We assume that the resulting coupling values agree with the coupling values predicted at an interacting fixed point. The non-Abelian gauge couplings vanish at the UV fixed point. We set them to zero. Substituting into (4.11), we can then compute the resulting quartic coupling fixed point value

$$\lambda_{\mathrm{H}}(M_{\mathrm{Pl}}) \approx \lambda_{\mathrm{H}*} = \frac{5}{48}g_Y^2 - \frac{1}{4}y_t^2 + \frac{\pi^2}{3}f_s + \frac{1}{48}\sqrt{\left(12y_t^2 - 5g_Y^2 - 16\pi^2 f_s\right)^2 + 576y_t^4 - 100g_Y^4}.$$
(4.12)

Below the Planck scale the flow is given by (4.11) with $f_s = 0$. As a result we can compute the IR value for quartic coupling λ_{H} and deduce the Higgs mass. Fig. 4.4

g_{Y*}	y_{t*}	$\lambda_{\mathrm{H}}(M_{\mathrm{Pl}})$	M_{H}
0	0	≈ 0	$\approx 133\,\mathrm{GeV}$
> 0	0	< 0	-
0	> 0	> 0	$\approx 143\,\mathrm{GeV}$
> 0	> 0	> 0	$\approx 144\,\mathrm{GeV}$

Tab. 4.2.: Fixed point value for the Higgs quartic coupling and approximate resulting Higgs mass (for $f_s = 0$) for the various non-interacting/interacting fixed points in the U(1) gauge and the Yukawa sector in a one-loop approximation. We assume that the fixed point values in the U(1) and the Yukawa sector are given by their SM values evolved to the Planck scale. At the fully interacting fixed point, non-vanishing gauge coupling leads to larger Higgs mass as the term $\sim g_Y^2$ numerically is larger than the one $\sim g_Y^4$. The case $g_{Y*} > 0, y_{t*} = 0$ does not feature a fixed point.
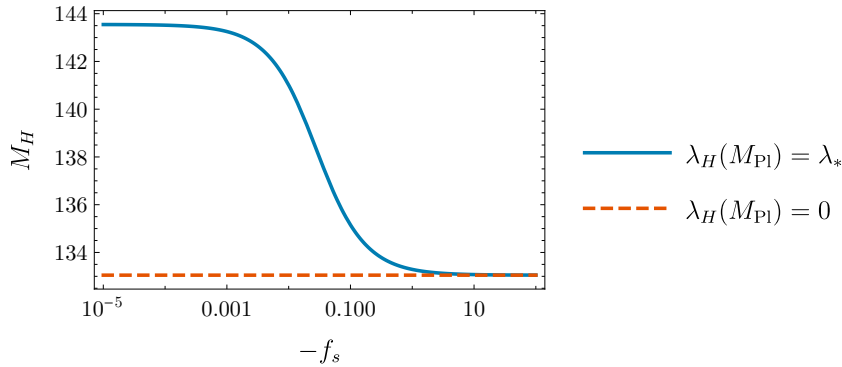
Fig. 4.4.: Resulting IR Higgs mass under the assumption that y_t and g_Y are correctly predicted by the interacting fixed point for varying strength of the gravitational contributions f_s. The offset of about $\sim 4\,\mathrm{GeV}$ for the case $\lambda_{\mathrm{H}*} \approx 0$ is a result of our one-loop approximation.

shows the resulting Higgs mass as a function of f_s. For large values of $|f_s|$ the fixed point value approaches $\lambda_{\mathrm{H}*} \approx 0$ and one recovers the result at vanishing quartic coupling. For $f_s \approx 0$ the non-vanishing values of the Yukawa coupling and the gauge coupling induce a finite value of the quartic coupling that leads to a change in the Higgs mass of about $10\,\mathrm{GeV}$. Many extensions of the SM modify the flow of the quartic coupling and hence the resulting Higgs mass. This might allow to alleviate the tension between the measured and the predicted value.

We discussed how the top mass strongly influences the predicted Higgs mass. A lighter top quark might lead to a match between predicted and measured value even in the absence of new physics. Next, we turn to the top quark, and an independent prediction of its mass.

4.3.2 Prediction of the Top Mass

At the interacting Yukawa fixed point the Yukawa coupling y is irrelevant. Along every RG trajectory emanating from this fixed point, the Yukawa coupling's IR value is predicted. In the following, we review how this might allow to compute the top mass within asymptotically safe quantum gravity.

The fixed point (4.8) can be extended to a model featuring the bottom and the top quark [147]. At the corresponding fixed point in this model (i) the gauge couplings vanish, (ii) the bottom Yukawa coupling vanishes and (iii) the top Yukawa coupling does not vanish, $y_t \neq 0$. The two Yukawa couplings feature a relevant and an irrelevant direction. The relevant direction is a mixture of the two Yukawa couplings. It can be fixed by matching the measured value of the bottom Yukawa coupling. The irrelevant direction then fixes the top Yukawa coupling. Its IR value is predicted. This allows to compute the top mass. The resulting value in Ref. [147] is $M_{\text{top}} \approx 171\,\text{GeV}$ and hence slightly lighter than the measured value. The value is determined by properties of the interacting fixed point and in particular by the magnitude of f_y. The strength of the gravitational corrections f_y is dependent on the gravitational fixed point values. As a result a shift of $\mathcal{O}(1)$ in the fixed point value of the cosmological constant can modify the resulting top mass prediction by $\mathcal{O}(50)\,\text{GeV}$ [147].

It is intriguing that the resulting value falls in close vicinity of the measured value. Note that the value computed in this way is independent of vacuum stability considerations. The fact that the top mass needed for a stable Higgs and the one cited here lie in close vicinity is a numerical coincidence.

By focusing on a fixed point featuring even more irrelevant directions one can further enhance predictivity. Ref. [210] studied the top and bottom Yukawa couplings together with the U(1) gauge coupling and focused on the fixed point at which all three couplings are non-vanishing and irrelevant. The two Yukawa couplings have different values at this fixed point as a result of their different charge assignments in the SM. They both feature the same gravitational contribution f_y in their respective beta functions, as gravitational fluctuations do not distinguish between the bottom and the top quark. The gravitational contribution to the beta function for the U(1) gauge coupling is f_ρ. One can only adjust the two parameters f_y and f_ρ to accommodate the measured values of two Yukawa couplings and the gauge coupling in the IR. As a result, a consistency relation between the three parameters arises. This consistency relation is approximately fulfilled in the SM, but would be violated if the quarks had a different charge assignment than the one in the SM [210]. This demonstrates that the SM coupling values could be consistent with an interacting UV fixed point. The result is insensitive to a large part of the uncertainty related to the gravitational contributions f_y and f_ρ. If these were known to high precision, then instead of fixing one coupling in terms of the other two, one could compute all three couplings from first principles.

A detailed discussion of all fixed points in the bottom and top quark system, as well as an extension to more generations can be found in Ref. [211]. An extension to multiple generations requires studying the flow of the full CKM matrix. The resulting beta functions in this extended system feature denominators $\sim \frac{1}{y_i^2 - y_j^2}$. These denominators cause a repulsion between different Yukawa couplings along the RG flow. The emerging IR structure does not match the SM quantitatively, but agrees qualitatively with the hierarchy of Yukawa couplings in the SM. Beyond-SM degrees of freedom will alter these results.

The interacting Yukawa fixed point might allow to predict the top Yukawa coupling. The Yukawa beta function and the U(1) gauge coupling beta function are structurally similar. Consequently, a similar result exists for the U(1) gauge coupling.

4.3.3 Bounds on the Gauge Coupling

The interacting fixed point for the U(1) gauge coupling might put bounds on the $U(1)$ hypercharge coupling in the SM [186]. The corresponding beta function features an interacting fixed point $g_{Y*} \neq 0$ and a free fixed point $g_{Y*} = 0$. The former is irrelevant, the latter is relevant. Given gravitational fixed point values one can compute the interacting fixed point value g_{Y*}. This UV value can be related to the IR via the RG flow. The resulting IR value $g_{Y\,\mathrm{crit}}$ serves as an upper bound for the U(1) gauge coupling. $g_{Y\,\mathrm{crit}}$ will be realized if the system emanated from the interacting fixed point. A value in the range $0 \leq g_Y < g_{Y\,\mathrm{crit}}$ will be realized if the system emanated from the free fixed point. The measured SM matter value falls into this range.

If the interacting fixed point is realized, it enhances predictivity and might predict the IR value of the gauge coupling g_Y.

4.3.4 Chiral Symmetry and Light Fermions

We have given two examples for how interacting fixed points might enhance predictivity in the SM. In addition, asymptotically safe quantum gravity might provide consistency relations between different observational SM properties.

As one such observational property, all fermions in the SM are light with respect to the Planck scale. The lightness of fermions arises due to chiral symmetry. If chiral symmetry was broken at the Planck scale, one would expect to observe fermion masses of the order of the Planck scale [146]. Hence, the observation of light fermions implies that chiral symmetry should be unbroken at the Planck scale.

To diagnose the onset of chiral symmetry breaking one can consider four-fermion interactions [212–214]. If these interactions do not feature a fixed point, they necessarily diverge along the RG flow. This divergence signals the onset of condensation into bound states and hence chiral symmetry breaking.

The beta function for a four-fermion interaction receives contributions from matter and gravitational fluctuations and depends on the number of matter degrees of freedom. Requiring the beta function to feature a fixed point then translates into bounds on the matter degrees of freedom. Whether chiral symmetry is broken or remains unbroken depends on the number of fermions.

The SM might pass the resulting consistency test: there are indications that chiral symmetry remains unbroken at the Planck scale for SM fermion content [212–214], at least in the absence of topological fluctuations. The latter might trigger chiral symmetry breaking [155].

On a classical level, chiral symmetry can be broken in the presence of curved backgrounds, see e.g. [215–219]. This mechanism, known as gravitational catalysis, might also allow to establish a relation between the presence of light fermions in the SM and the SM particle content [220, 221].

4.3.5 Extensions of the Standard Model

Asymptotic safety might (i) fix marginal couplings in the SM (ii) provide consistency tests of the various SM properties. Having highlighted the enhancement in predictivity within the SM, the next step is to constrain extensions of the SM. Here we will briefly review two extensions, namely neutrino masses and grand unified theories, for other beyond SM scenarios see e.g. Refs. [222, 223]. We go into more detail on cosmologically motivated extensions in the next chapters.

A first step beyond the SM is the incorporation of neutrino masses. The observation of neutrino flavor oscillations [224–226] requires the presence of neutrino masses. The corresponding masses are tiny. Assuming a standard cosmological model, one can infer that $\sum m_\nu < 0.12$eV [10, 227]. Direct measurements set constraints on the order of eV [228]. However, in the SM neutrinos are massless. To accommodate non-vanishing neutrino masses one can extend the SM in various ways. One such possibility is the introduction of Majorana masses. These are compatible with an asymptotically safe fixed point and provide neutrino masses for parts of the gravitational parameter space [229]. The phenomenological implications of extending the SM with right-handed neutrinos within an asymptotically safe model were studied in Ref. [230]. In both cases asymptotically safe quantum gravity reduces the number of free parameters and enhances the predictivity of the underlying model.

A similar enhancement in predictivity might be possible for grand unified theories. These assume that the SM originates in a theory that only features one simple gauge group. This large gauge group is spontaneously broken to the $\mathrm{SU}(3) \otimes \mathrm{SU}(2) \otimes \mathrm{U}(1)$ structure of the SM in a chain of phase transitions. The required symmetry breaking pattern is highly intricate and depends on various scalar quartic couplings. Ref. [231] has studied which resulting breaking chains are compatible with an asymptotically safe UV completion in light of the fixed points for quartic couplings discussed in Sec. 4.2.1. In addition, Ref. [232] has investigated the $U(1)$ gauge coupling in grand unified settings.

These examples illustrate how asymptotic safety could enhance predictivity in and beyond the SM. In the next chapter we apply this principle to cosmologically motivated extensions of the SM. Before we go to beyond-SM physics we focus on the Yukawa fixed point again.

4.4 Non-Minimal Couplings and an Extended Truncation

The top mass prediction is made possible by the interacting Yukawa fixed point, see Sec. 4.3.2. We explore the stability of this fixed point by extending the truncation by a marginal coupling that has been neglected so far: the non-minimal coupling between the Higgs scalar and the Ricci scalar $\xi\Phi\Phi^\dagger R$. This coupling is the only marginal non-minimal coupling compatible with the symmetries of the SM. As it is compatible with all symmetries, it will inevitably be generated by quantum fluctuations. It is crucial to understand how it impacts the scenarios presented in the last sections.
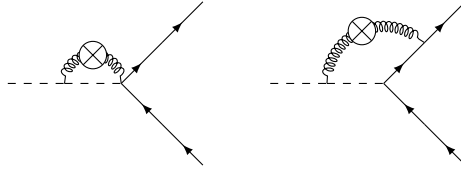
Fig. 4.5.: Additional diagrams that arise due to the presence of the non-minimal coupling and the mass that contribute to f_y. The curly line corresponds to a graviton, the dashed line is a scalar and the solid line is the fermion. We show the diagram with one possible regulator insertion (crossed vertex). The regulator could also sit on any other of the internal propagators.

Here, we focus on a toy model for this coupling. We introduce a real scalar ϕ and a single Dirac fermion ψ and consider the effective action

$$
\begin{aligned}
\Gamma_k^{\mathrm{ferm}} = \int \mathrm{d}^4 x \sqrt{g} \quad & \left(\frac{1}{2} Z_\phi g^{\mu\nu} \partial_\mu \phi \partial_\nu \phi - \xi \phi^2 R + \frac{\bar{m}^2}{2} \phi^2 + \frac{\lambda_4}{8} \phi^4 \right. \\
+ \quad & i Z_\psi \bar{\psi} \slashed{\nabla} \psi + i y \phi \bar{\psi} \psi \\
- \quad & \left. \frac{1}{16\pi \bar{G}_N} (R - 2\bar{\Lambda}) \right).
\end{aligned}
\tag{4.13}
$$

The fermion ψ represents the SM top quark. We neglect all the lighter quarks. The scalar field represents the SM Higgs field. In this system we derive the beta functions by projecting onto Eq. (3.21). For details on this computation, see App. C.

In addition, we compute the anomalous dimension $\eta_\phi = -\partial_t \log Z_\phi(k^2)$. The resulting expression is given in App. F.1. It remains small as long as $|\xi|$ is small and the fixed point value Λ_* is far away from the pole at $\Lambda = 1/2$. In the following we only consider the canonical anomalous dimension term and neglect the anomalous dimension that appears in the numerator of the flow equation.

The resulting beta functions for the Yukawa coupling y feature the one-loop term cubic in y and a gravitational term that is linear in y, such that β_y again takes the form (4.7). Due to the presence of the non-minimal coupling, f_y reads

$$
f_y = f_y^{\mathrm{min}} + f_y^{\mathrm{non\text{-}min}},
\tag{4.14}
$$

where the individual terms are spelled out in detail in App. F.1. The first term arises without a non-minimal coupling and agrees with Ref. [168]. It solely depends on the cosmological constant Λ_* and the Newton coupling G_*. The second term arises due to the additional diagrams in Fig. 4.5. It depends on Λ_* and G_*, as well as the non-minimal coupling ξ and the scalar mass m^2.

Additionally, the gravitational fixed point values are shifted. A non-minimally coupled scalar modifies the beta functions for G and Λ by

$$\beta_\Lambda\Big|_{\text{scal}} = \frac{g}{2\pi}\frac{1}{2(1+m^2)} - G\,\Lambda\,\Delta f_g, \tag{4.15}$$

$$\beta_G\Big|_{\text{scal}} = -G^2\,\Delta f_g, \tag{4.16}$$

$$\Delta f_g = -\frac{1}{6\pi(1+m^2)} - \frac{6\xi}{6\pi(1+m^2)^2}. \tag{4.17}$$

For $\xi = m^2 = 0$ these contributions reduce to a contribution by $\Delta N_s = 1$ in (3.31). As long as $|\xi| \ll 1$, the resulting shift in the gravitational fixed point values remains small.

4.4.1 Fixed Point Structure

We compute the beta functions for the effective action (4.13). The beta functions for all couplings are given in App. F.2. They feature a fixed point at gravitational fixed point values

$$\Lambda_* = -0.146 \quad G_* = 3.2. \tag{4.18}$$

All couplings in the matter sector vanish. It has critical exponents

$$\theta_1 = 2.92, \qquad \theta_2 = 0.728, \qquad \theta_{3/4} = 0.0921 \pm 1.58i,$$
$$\theta_5 = -0.524, \qquad \theta_6 = -1.94. \tag{4.19}$$

The first two relevant directions correspond to the two gravitational couplings Λ and G. The third/fourth relevant directions are associated with the mass and the non-minimal coupling ξ. The quartic coupling and the Yukawa coupling remain irrelevant.

The gravitational fixed point values depend on the matter degrees of freedom and technical choices. In the following we treat them as free parameters and solve the matter beta functions. Varying the gravitational fixed point values also changes the number of relevant directions at the Gaussian fixed point. The number of relevant directions in the matter sector is shown in Fig. 4.6. For $\Lambda > \Lambda_{\text{crit}} = -3.3$ the Yukawa coupling remains irrelevant at the fixed point $y_* = 0$. For $\Lambda < -3.3$, f_y becomes positive, triggering the mechanism discussed in Sec. 4.2.2. Firstly, the Gaussian fixed point for the Yukawa coupling becomes relevant. As a consequence, quantum scale symmetry in the UV allows for a non-vanishing Yukawa coupling in the IR. Secondly, the interacting Yukawa fixed point emerges. We briefly discuss its properties without the non-minimal coupling in more detail, and subsequently contrast with the case including a non-minimal coupling.

For $\xi = m^2 = 0$ and gravitational fixed point values (3.34), one finds two fixed points

$$\lambda_{4,*} = -1.15 \quad y_* = 0.58 \tag{4.20}$$

and

$$\lambda_{4,*} = 0.18 \quad y_* = 0.58, \tag{4.21}$$
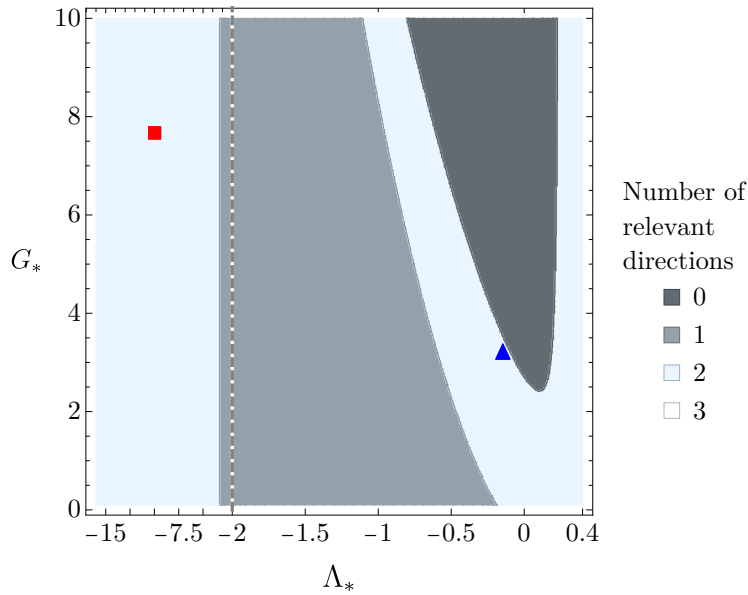
Fig. 4.6.: Number of relevant directions for the four matter couplings m^2, λ_4, ξ, y at the Gaussian matter fixed point as a function of the gravitational fixed point values. In the light blue area at large negative values for the cosmological constant the Yukawa coupling is relevant. The blue triangle/red square mark the position of the fixed points (4.18)/(3.34). At $\Lambda = -3.3$ the Yukawa coupling switches from being irrelevant (for $\Lambda > -3.3$) to being relevant (for $\Lambda < -3.3$). The change in the number of relevant directions above $\Lambda \approx -1$ happens in the scalar sector, see Sec. 5.3.1 for a detailed explanation. Notice the change of scales at the dashed line around $\Lambda = -2$.

featuring negative and positive λ_4, respectively. We want to study the fate of these two fixed points under the inclusion of a non-minimal coupling. This requires to quantify (i) the ξ-dependence of f_y and (ii) the impact of non-vanishing y_* on the fixed point value ξ_*.

Regarding (i), in the left panel of Fig. 4.7 we freely vary the fixed point value of the non-minimal coupling ξ_* and the cosmological constant Λ_*. We then compute the resulting f_y. As apparent from the figure, only small values of $|\xi_*|$ permit $f_y > 0$ and hence allow for an interacting fixed point. Regarding (ii), i.e. the backreaction of non-vanishing Yukawa on ξ, consider the beta function

$$\beta_\xi = \left(\xi + \frac{1}{12} \right) \left(\frac{y^2}{4\pi^2} + \frac{3\lambda_4}{16\pi^2} \right) + G\xi \left(\frac{2(3-\Lambda)}{3\pi(3-4\Lambda)^2} - \frac{5(3+10\Lambda)}{18\pi(1-2\Lambda)^3} \right). \quad (4.22)$$

When the first term in (4.22) dominates, i.e. for dominating matter interactions, the beta function features a fixed point that realizes conformal symmetry for $\xi_* \approx -1/12$ [233]. When the second term in (4.22) dominates, i.e. for dominating gravitational interactions, the only fixed point is at vanishing non-minimal coupling $\xi_* \approx 0$.

The right panel of Fig. 4.7 illustrates this competition of gravity- and matter-fluctuations. We show the fixed point value ξ_* as a function of the ratio G_*/y_* at fixed value Λ_* and vanishing quartic coupling. As long as the system is dominated by the Yukawa coupling, $G_*/y_* \ll 1$, it is driven towards the conformal fixed point at $\xi_* = -1/12$.
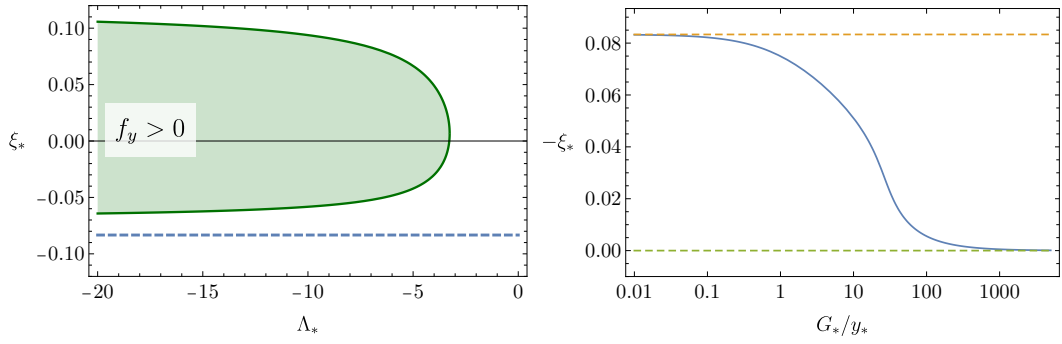
Fig. 4.7.: (left) We plot the region in which $f_y > 0$ (green) with freely varying fixed point values Λ and ξ at vanishing mass $m^2 = 0$. The region is independent of G. The dashed line corresponds to the conformal value $\xi = -1/12$.
(right) We compute the fixed point value ξ_* for freely varying G_* and y_* with $\Lambda_* = -9.97$, cf. Eq. (3.34).

If gravitational interactions dominate, $G_*/y_* \gg 1$, the same fixed point is shifted towards $\xi_* = 0$.

Here we have varied G_*/y_* freely. At the fixed points (4.20) and (4.21) this ratio is set by the coupling values. If these fixed points are to persist in the presence of a non-minimal coupling, then gravity needs to interact sufficiently strongly. Only for strong gravitational fluctuations, ξ_* will be small. Only for small ξ_*, $f_y > 0$ will be positive. And only for positive f_y the fixed point persists.

We first focus on the fixed point (4.20) with negative quartic coupling. Neglecting the impact of ξ on the other couplings, the coupling values at this fixed point allow to compute the resulting ξ_*. It does not allow for $f_y > 0$. Indeed, the full set of beta functions does not feature a corresponding fixed point. The inclusion of the non-minimal coupling hence disfavors the existence of this fixed point.

We then focus on the fixed point (4.21). At this fixed point gravitational fluctuations are sufficiently strong for the fixed point to persist. Here, we solve the matter and gravity beta functions in the presence of SM matter. The resulting fixed point lies at

$$\Lambda_* = -9.49, \qquad G_* = 7.26, \qquad \lambda_{4*} = 0.139,$$
$$y_* = 0.381, \qquad \xi_* = -0.04, \qquad m_{\phi*}^2 = 0.00086 \qquad (4.23)$$

and features critical exponents

$$\theta_1 = 3.98, \qquad \theta_2 = 1.99, \qquad \theta_3 = 1.91,$$
$$\theta_4 = -0.0364, \qquad \theta_{5/6} = -0.00855 \pm 0.0108i. \qquad (4.24)$$

The first and third critical exponents are associated with G and Λ, the second one corresponds to a direction mostly aligned with the scalar mass m_ϕ^2. The fourth critical exponent corresponds to an eigenvector approximately aligned with the Yukawa coupling, and the fifth and sixth to a mixture of ξ and λ_4.

We hence find that the interacting fixed point (4.21) persists upon the inclusion of a non-minimal coupling. At this fixed point the non-minimal coupling is irrelevant.
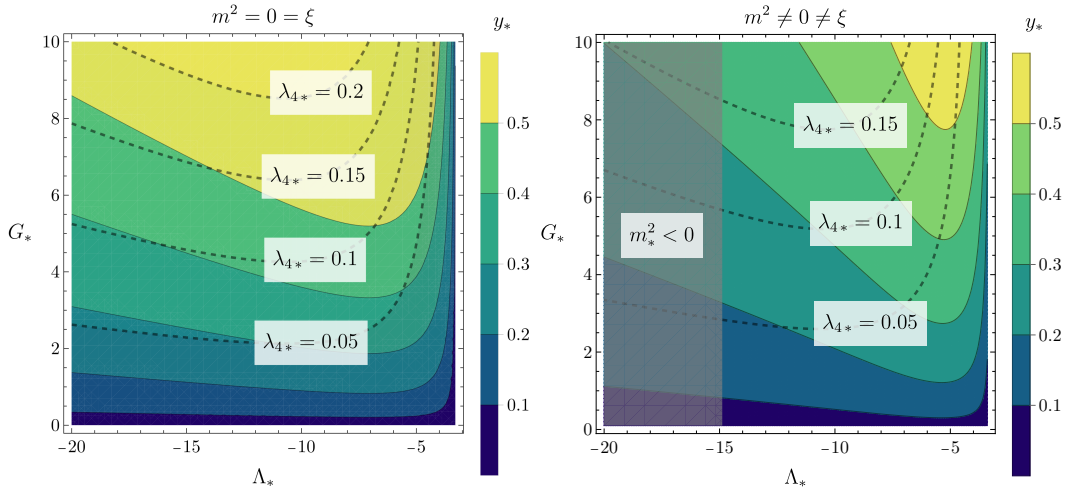
Fig. 4.8.: Fixed point values for various matter couplings. The value of the Yukawa coupling is color-coded, contours of the quartic coupling are given by the dashed lines as a function of the gravitational fixed-point values without(with) non-minimal coupling and mass on the left (right).

Varying the gravitational fixed-point values and only solving the matter beta functions, we obtain Fig. 4.8. As apparent from this figure, the inclusion of the non-minimal coupling at fixed values for the gravitational couplings lowers both the Yukawa coupling and the quartic coupling. At the same time, a non-vanishing non-minimal coupling will shift the gravitational fixed-point value. On the one hand, a lowering of the quartic coupling might aid to realize the scenario of Ref. [147] described in Sec. 4.3.2 by lowering the resulting value of the quartic coupling and hence the Higgs mass. On the other hand, a lowering of the Yukawa coupling might lead to a top quark that becomes too light. A quantitative exploration of these competing effects requires going beyond our toy model and consider the full SM. We leave this to future work.

In addition, a regime with spontaneously broken $\mathbb{Z}_2$ symmetry at the fixed point appears. We will explore this regime in the following.

4.4.2 Symmetry Breaking at the Fixed Point

The real scalar field ϕ exhibits a (global) $\mathbb{Z}_2$ symmetry $\phi \to -\phi$. This symmetry can be spontaneously broken if the scalar acquires a non-vanishing vacuum expectation value $\langle \phi \rangle \neq 0$. The onset of spontaneous symmetry breaking is signaled by a negative mass term, $m^2 < 0$. We find this is realized for values of the cosmological constant $\Lambda < -14.9$. The mass term turns negative due to a competition of various contributions in the beta function for the mass parameter. At $\mathcal{O}(m^2 y, m^2 \lambda_4, m^2 \xi)$ the fixed point for the mass is

$$
\begin{aligned}
m^2_{\phi,*} = \ & \frac{1}{8\pi} y^2 - \frac{3}{64\pi^2} \lambda_4 - \frac{9}{\pi(3-4\Lambda)} g\xi^2 \\
& - \frac{3G\xi}{\pi(3-4\Lambda)^2} - \frac{5G\xi}{3\pi(1-2\Lambda)^2} - \frac{27g\xi^2}{\pi(3-4\Lambda)^2}.
\end{aligned}
\tag{4.25}
$$

Without a non-minimal coupling the Yukawa term dominates over the term proportional to the quartic coupling λ_4 and the resulting fixed point value for the mass
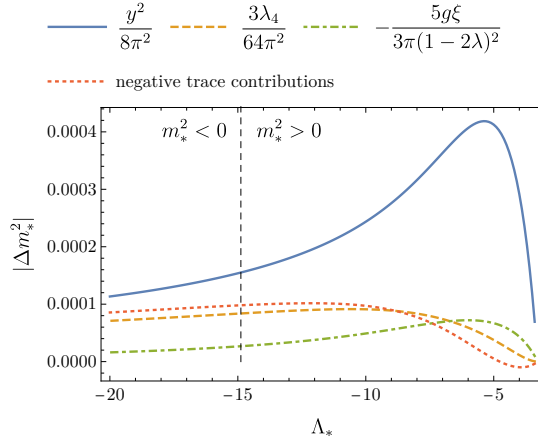
Fig. 4.9.: Various contributions to the fixed point value for m^2 at $G = 1$. For $\Lambda < -14.9$ the resulting fixed point value is negative, signaling spontaneous symmetry breaking.

parameter remains positive. With a non-minimal coupling, the gravitational modes lead to additional contributions: the transverse-traceless contribution, proportional to $\frac{1}{(1-2\Lambda)^2}$, and the contributions from the scalar trace mode proportional to $\frac{1}{(3-4\Lambda)^a}$, with a a positive number, come with a negative sign. They reduce the value of the fixed point for the mass parameter, cf. Fig. 4.9. For $\Lambda < -14.9$ this leads to a fixed point in the symmetry broken regime. Such a fixed point is not a priori excluded. The fixed-point potential could feature a non-vanishing vacuum expectation value $\langle \phi \rangle$. However, in the presence of a vacuum expectation value additional vertices arise. As one example the interaction $\lambda_4 \phi^4$ leads to a vertex $\lambda_4 \langle \phi \rangle \delta \phi^3$, where $\delta \phi = \phi - \langle \phi \rangle$ is an excitation around $\langle \phi \rangle$. These additional vertices lead to additional diagrams that arise as $\langle \phi \rangle \neq 0$. We have not computed these diagrams and leave this interesting region of parameter space to further studies.

In summary, the truncation extended by a non-minimal coupling ξ further refines the results on the interacting Yukawa fixed point. In the absence of ξ two fixed points feature non-vanishing Yukawa coupling y_*. The fixed point with negative quartic coupling (4.20) does not persist in the extended truncation. The fixed point (4.21) persists in the extended truncation. At this fixed point the non-minimal coupling is irrelevant. The quantitative properties of the fixed point are modified. For large negative values of the cosmological constant the inclusion of a non-minimal coupling might trigger symmetry breaking at the fixed point. We proceed to leverage the high predictive power of this fixed point in beyond-SM settings.

4.5 Conclusion: Enhanced Predictivity in the Matter Sector

We highlighted how asymptotically safe gravity could constrain marginal couplings in and beyond the SM: interacting fixed points arise for gauge and Yukawa couplings and might allow predicting various properties of the SM. We focus on the prediction of the Higgs mass and the top mass [147, 208]. The mechanism underlying the Higgs mass prediction has been confirmed in a variety of approximations. The resulting

value is slightly too large if one assumes the current central values for the Higgs and the top mass, but is highly sensitive to uncertainties in the top mass [204, 209] and the effect of higher-order operators [197–203]. In addition, new degrees of freedom might alter the resulting Higgs mass.

The interacting Yukawa fixed point underlying the top mass prediction remains stable under an extension of the truncation by non-minimal couplings. This finding is non-trivial as it only holds for a range of ξ. The resulting fixed point value ξ_* falls into that range. In addition, our results indicate that for large negative values of the cosmological constant Λ_* the interacting Yukawa fixed point might feature a symmetry broken scalar potential.

The high predictive power of the interacting Yukawa fixed point might allow predicting the top mass in the SM. In addition, it predicts the non-minimal coupling. This could allow drawing conclusions in the context of Higgs inflation, as we will do in Chap. 5. In addition, we will leverage its predictive power in beyond-SM settings in Chap. 6.

Scalar Matter for Accelerated Expansion in Asymptotic Safety

In the last section we investigated how asymptotic safety could enhance predictivity in particle physics. In the next two chapters we will explore how it could enhance predictivity in cosmology. We will focus on two observational puzzles: (i) the observation of an accelerated expansion in various stages of the history of the universe and (ii) the stipulated existence of dark matter. In this chapter we focus on the first of these two observations.

We observe that our universe presently is expanding in an accelerated fashion. In addition, a phase of accelerated expansion in the early universe explains many observations in the present universe. As a driver for the expansion, both phases require physics beyond the SM. Here, we introduce a simple model to explore how asymptotic safety could constrain such beyond-Standard-Model physics.

We first review observations and the relevant formalism for accelerated expansion in Sec. 5.1. To explore how scale invariance could provide accelerated expansion, we briefly introduce classically scale invariant models in Sec. 5.2. In Sec. 5.3 we introduce a model featuring a single scalar ϕ with a potential $V(\phi)$ and discuss its fixed point structure and RG flow. We then apply this simple model and discuss the implications for inflation and asymptotic safety in Sec. 5.4 and dark energy and asymptotic safety in Sec. 5.5.

5.1 The Observation of Accelerated Expansion: Dark Energy and Inflation

Measuring the red-shift and apparent magnitude of high-redshift supernovae provided the first observation of an accelerating universe [234, 235]. Since then a plethora of data confirms that $\ddot{a} > 0$, where $a(t)$ is the scale factor and t is a derivative with respect to cosmic time. According to the acceleration equation

$$\frac{\ddot{a}}{a} = -\frac{4\pi\bar{G}}{3}\rho(1 + 3w) \tag{5.1}$$

this requires our universe to be dominated by a component Ω_{DE} with density ρ and equation of state $w < -1/3$. For a scalar field $\phi(t)$ evolving in a potential $V(\phi)$ the equation of state reads

$$w = \frac{\frac{1}{2}\dot{\phi}^2 - V(\phi)}{\frac{1}{2}\dot{\phi}^2 + V(\phi)}. \tag{5.2}$$

In the limit of a non-moving scalar $\dot{\phi} \approx 0$ one recovers the equation of state $w = -1$ for a cosmological constant. Present observations limit $w(a) = w_0 + (1-a)w_a$ to $w_0 = -1.007 \pm 0.089, w_a = -0.222 \pm 0.407$, see Ref. [236]. The next generation of galaxy surveys will be able to probe the equation of state $w(a)$ to percent-level accuracy [237]. This opens up the perspective to distinguish between the cosmological constant and dynamical dark energy as the driving force for the accelerated expansion of our universe.

The observational hints for a second period of accelerated expansion in the early universe are less direct. The first hint concerns the spatial flatness of our observed universe. The density parameter Ω_k measuring spatial curvature evolves according to

$$\frac{\mathrm{d}\Omega_k}{\mathrm{d}\log a} = (1 + 3w)(1 + \Omega_k)\Omega_k \tag{5.3}$$

in a universe dominated by one component with equation of state w. This differential equation features two fixed points $\Omega_k = 0$ and $\Omega_k = -1$. We observe a universe with almost vanishing spatial curvature $\Omega_k = 0.0007 \pm 0.0019$ [10], implying that Ω_k is in the vicinity of the fixed point $\Omega_k = 0$.

Throughout the radiation- and matter-dominated phase the equation-of-state is $w > -1/3$. For $w > -1/3$ the fixed point $\Omega_k = 0$ is repulsive. Deviations away from it grow in time. However, we do not measure any deviation from $\Omega_k = 0$ today.

To explain why this is the case one has two options. Either one assumes that at early times the fixed point $\Omega_k = 0$ was realized to very high accuracy. Deviations from this fixed point grow similar to a relevant direction along the RG flow. Or one invokes a dynamical principle that prefers the fixed point $\Omega_k = 0$.

During a phase of accelerated expansion, or correspondingly $w < -1/3$, the fixed point $\Omega_k = 0$ becomes attractive. Such a period could predate the conventional radiation dominated phase in the history of the universe. If it lasts long enough, generic initial conditions will end up extremely close to the fixed point $\Omega_k = 0$. In the subsequent radiation- and matter-dominated phase deviations from $\Omega_k = 0$ grow. If the phase of accelerated expansion was long enough one nevertheless expects to observe $\Omega_k \approx 0$, and hence a spatially flat universe.

The second hint relates to the observed isotropy: cosmic microwave background measurements confirm that the universe appears statistically alike in all spatial directions. Without an inflationary period before radiation domination this finding is surprising. In a universe dominated by a component with equation of state w the maximum comoving distance τ that a photon can travel is

$$\tau \sim \frac{1}{1 + 3w} a^{\frac{1}{2}(1+3w)}. \tag{5.4}$$

For $w > -1/3$, regions that are in causal contact hence grow.

If one assumes that our universe was purely radiation dominated before the cosmic microwave background formed, then one can compute the size of causally connected regions. Under this assumption patches of the cosmic microwave background sepa-

rated by more than $\sim 2°$ have never been in causal contact. However, these patches look isotropic. On the one hand, this isotropy might be the result of very specific highly isotropic initial conditions[1]. On the other hand, the isotropy could arise dynamically during a phase of accelerated expansion, $w < -1/3$. During such a phase the comoving volume of points that could have been in causal contact shrinks. Larger volumes were in causal contact in the more distant past. For a sufficiently long period of accelerated expansion all patches of the cosmic microwave background could have been in causal contact in the distant past, explaining dynamically why they are highly isotropic.

Inflation dynamically explains the observation of a flat and isotropic cosmological background [239–243]. To drive inflation, the most simplistic models consider a scalar field ϕ in a potential $V(\phi)$.

Going beyond the background, one can study perturbations of the scalar and the metric, see e.g. Ref. [244]. To study perturbations of the metric, it is convenient to decompose these perturbations into irreducible representations under the group of three-dimensional rotations. After fixing the gauge symmetry, a scalar, a vector and a transverse-traceless tensor mode remain. Vector modes decay on cosmic timescales. We neglect them in the following.

To quantize the scalar and tensor perturbations, one promotes the corresponding fields to operators and imposes canonical commutation relations. The resulting creation and annihilation operators act on states. To define a vacuum state one takes a limit in which the cosmological horizon is much larger than the scale of a perturbation. The vacuum of (approximate) Minkowski space defines the (Bunch-Davies) vacuum [245].

Given creation and annihilation operators and a vacuum one can compute correlation functions. The resulting spectra for the two-point function in Fourier space are conventionally parameterized as

$$\Delta_s^2 = A_s \left(\frac{q}{q_0}\right)^{n_s-1} \qquad \Delta_t^2 = A_t \left(\frac{q}{q_0}\right)^{n_t} \tag{5.5}$$

where the subscripts s and t stand for scalar and tensor modes, respectively. Here q_0 is a reference scale.

Each Fourier mode q corresponds to a length scale $1/q$. If the length scale $1/q$ is larger than the cosmic horizon, the corresponding perturbations do not evolve any longer. Perturbations are conserved on super-horizon scales [246, 247].

The perturbation spectra (5.5) are generated in the inflationary regime. The corresponding perturbations leave the horizon during inflation and remain conserved. They reenter the horizon mostly during radiation domination. The spacetime fluctuations cause fluctuations in the primordial plasma. These plasma fluctuations evolve and freeze out to form the cosmic microwave background. Observing the cosmic mi-

---

[1] See Ref. [238] for a motivation of such initial conditions due to a finite action in the gravitational path integral.

crowave background allows to constrain the spectra (5.5). The current observational constraints on both spectra are [248]

$$\log\left(10^{10} A_s\right) = 3.044 \pm 0.014, \quad n_s = 0.9668 \pm 0.0037, \quad r = \frac{A_t}{A_s} < 0.063. \quad (5.6)$$

The spectrum of scalar perturbations is close to scale-invariant ($n_s = 1$), and tensor modes have not been detected so far.

To relate these observables to the scalar potential, one defines the slow-roll parameters

$$\varepsilon = \frac{M_{\text{Pl}}^2}{2}\left(\frac{1}{V}\frac{dV}{d\phi}\right)^2, \quad \eta = M_{\text{Pl}}^2 \frac{d^2V}{d\phi^2}. \quad (5.7)$$

In terms of these parameters the computation outlined above yields the three observables [244]

$$A_s = \frac{1}{24\pi^2 \varepsilon}\frac{V}{M_{\text{Pl}}^4}, \quad n_s = 1 + 2\eta - 6\varepsilon, \quad r = 16\varepsilon \quad (5.8)$$

to first order in the slow-roll parameters. These expressions allow relating observations of the cosmic microwave background to the inflationary scalar potential.

5.2 Scale Invariance as a Guiding Principle

In the last section we described the dynamics of inflation and dynamical dark energy in terms of a scalar field. However, one has a large amount of freedom in constructing the corresponding potential. This leads to a plethora of models of inflation and dark energy [249]. The near-scale invariance of the spectrum of scalar perturbations indicates that scale invariance could be a useful guiding principle. In this section, we review classically scale invariant models. In the next sections, we turn to quantum scale invariance, i.e. the asymptotically safe case.

A classically scale-invariant theory is invariant under a multiplicative rescaling of all fields and coordinates according to their energy dimension [250]. The corresponding Lagrangian does not contain any dimensionful parameter. That does not imply, that the theory cannot contain any scales: a scale can be set by the expectation value of a field. Notice that this expectation value is not necessarily a *vacuum* expectation value, i.e. not a minimum of the underlying potential. Instead, the scalar expectation value might evolve throughout the cosmological history.

5.2.1 Classically Scale-Invariant Inflation

Classically scale-invariant models of inflation are abundant [251–257]. We will focus on a model that exhibits approximate scale-invariance and features the most relevant observational characteristics. Higgs inflation assumes that the scalar responsible for

the inflationary expansion of the universe at early times is the SM Higgs field [258]. The important part of the action reads [2]

$$S^{\text{HI,Jordan}} = \int \mathrm{d}^4x \sqrt{-g} \left(\frac{M_{\text{Pl}}^2 + \xi\varphi^2}{2} R - g^{\mu\nu}\partial_\mu\varphi\partial_\nu\varphi - \frac{\lambda_{\text{H}}}{4}\varphi^4 \right) \qquad (5.9)$$

where φ is the radial mode of the SM Higgs field Φ, which couples to the Ricci scalar non-minimally. The electroweak vacuum expectation value is small at the scales we will consider and has been neglected. For large values of $\varphi \geq M_{\text{Pl}}$ the action (5.9) is approximately scale-invariant.

To obtain physical observables it is useful to transform (5.9) to a frame in which φ is minimally coupled to gravity via a conformal transformation. Assuming $\xi \gg 1$, the resulting action is [259]

$$S^{\text{HI,Einstein}} = \int \mathrm{d}^4x \sqrt{-g} \left(\frac{M_{\text{Pl}}^2}{2} R - \frac{1}{2}M_{\text{Pl}}^2 \frac{6(\partial\varphi)^2}{\varphi^2} + \frac{\lambda_{\text{H}}}{4}\frac{\varphi^4}{(1+\xi\varphi^2)^2} \right). \qquad (5.10)$$

In this action, the scalar field φ is not canonically normalized. Instead, it features a quadratic pole in the kinetic term. When redefining φ to a canonically normalized field, one solves the differential equation $\frac{\partial\varphi}{\varphi} \sim \partial\chi$, where χ is the canonically normalized field. The quadratic pole causes an exponential stretching of the underlying potential. The physical observables become insensitive to the precise shape of the potential and are predominantly governed by the quadratic pole [260], see also Ref. [250] for a reference that rewrites a large class of models in terms of the corresponding pole structure.

After introducing the field χ one computes the standard slow roll parameters and obtains [259]

$$\varepsilon = \frac{3}{4N^2}, \quad \eta = \frac{3/4 - N}{N^2}, \qquad (5.11)$$

where $N \approx 60$ counts the number of e-folds of inflation. To first order in ε and η, the amplitude of the scalar power spectrum is

$$A_s = \frac{1}{72\pi^2}\frac{\lambda_{\text{H}}}{\xi^2}N^2 \qquad (5.12)$$

and the spectral tilt and tensor to scalar ratio approximately equal

$$n_s = 1 - \frac{2}{N}, \quad r = \frac{12}{N^2}. \qquad (5.13)$$

The small observed value of A_s requires

$$\lambda_{\text{H}}/\xi^2 \approx 4 \cdot 10^{-10}. \qquad (5.14)$$

This ratio corresponds to the prefactor of the Einstein-frame potential: For large ξ and large field values φ, the potential in (5.10) is approximately flat. Its amplitude is given by $\frac{\lambda_{\text{H}}}{\xi^2}$. It is the magnitude of this potential that determines the amplitude of scalar fluctuations. The small value of A_s signals, that the corresponding potential values lie significantly below the Planck scale. To obtain the correct amplitude A_s, generically ξ

---

[2]In this subsection all expressions will be in Lorentzian signature. We consider purely classical physics and there is no need to Wick rotate.

has to be very large. Assuming that λ_H is tiny at the relevant scales allows to evade these large values of ξ to some degree but still requires $\xi \sim 10$ [261].

The observables (5.13) are not unique to Higgs inflation. The same expressions arise in Starobinsky inflation, for α-attractors [260], but also for other scale-invariant models of inflation [252, 262]. They are predominantly determined by the quadratic pole. In terms of a canonically normalized field this pole stretches or equivalently flattens the inflationary potential. This flattening of the potential leads to agreement with the inflationary observables n_s and r.

5.2.2 Classically Scale-Invariant Dark Energy

Flat scalar potentials naturally arise in scale-invariant models in the inflationary domain. They also appear naturally for models of dynamical dark energy.

Scale invariance can be spontaneously broken by the expectation value of a field. The spontaneous breaking of scale invariance leads to a massless Goldstone boson [250]. For an approximately scale invariant theory, the corresponding direction in field space is only approximately flat. In quintessence models, the field evolves along this approximately flat direction in the late universe [263–265]. The resulting potential typically decays exponentially $V(\phi) \sim \exp(-\gamma\phi/M_\text{Pl})$. It acts as a dark energy or quintessence component. In such a potential, the equations of motion feature a fixed point $\Omega_\text{DE} = 1, w = -1 + \gamma^2/3$ [266]. For small γ the universe hence expands in an accelerated fashion. The equation of state deviates from $w = -1$. Such scenarios will be tested by the next generation of observations [237].

In inflation as well as dark energy, classically scale invariant models can directly be compared to observational data. We observe that classical scale invariance induces flat potentials, as required by observations. Similar models might arise in the context of quantum scale symmetry [267]. The corresponding models do not (yet) allow to bridge the gap between a UV fixed point and observational data to the required level of quantitative accuracy. In the following, we explore the qualitative features of asymptotically safe models of inflation and dark energy.

5.3 Single Scalar in Asymptotic Safety

A single scalar could be relevant both in the context of inflation and dynamical dark energy. To study how quantum scale invariance constrains such models we consider the effective action for a single real scalar ϕ

$$\Gamma_k = \int \text{d}^4x \sqrt{g} \left[\frac{1}{2} Z_\phi g^{\mu\nu} \partial_\mu \phi \partial_\nu \phi - \left(\frac{1}{16\pi\bar{G}_N} + \xi\phi^2 \right) R + V(\phi^2) \right] + S_\text{gf} + S_\text{gh} \quad (5.15)$$

with a scalar potential $V(\phi)$. Below, we typically choose the potential

$$V(\phi^2) = \frac{2\bar{\Lambda}}{16\pi\bar{G}_N} + \frac{\bar{m}_\phi^2}{2} \phi^2 + \frac{\lambda_4}{4} \phi^4. \quad (5.16)$$

In addition, we consider dimensionless quantities

$$G = \bar{G}_N k^2, \quad \Lambda = \bar{\Lambda} k^{-2}, \quad m_\phi^2 = \bar{m}_\phi^2 k^{-2}. \tag{5.17}$$

Applying Eq. (3.21) allows computing beta functions for these quantities. We provide more details on the computation in App. C. For previous work on similar truncations in the context of the functional RG see [68, 145, 169–172, 174, 176].

To evaluate the effect of quantum fluctuations it is convenient to split the scalar ϕ into a background piece $\bar{\phi}$ and a fluctuation $\delta\phi$. In the presence of a non-minimal coupling ξ, both the regulator, and the gauge-fixing term, can (and will for common choices) depend on the background scalar $\bar{\phi}$. In addition, the gauge fixing term implies a ghost action for the gravitational ghosts, that in general will also depend on $\bar{\phi}$. We have studied this technical complication and refer to App. C.3 for details. The following results are largely independent of these technical choices.

5.3.1 Fixed Point Structure

The resulting beta functions feature the Gaussian matter fixed point with vanishing matter couplings and gravitational couplings [3]

$$\Lambda_* = 0.13, \quad G_* = 1.32. \tag{5.18}$$

The fixed point has critical exponents

$$\theta_{1/2} = 2.46, \pm 1.37i \qquad \theta_{3/4} = 0.46, \pm 1.37i \qquad \theta_5 = -2.12, \tag{5.19}$$

and hence is relevant in two directions in the matter sector. These relevant directions approximately correspond to the mass and the non-minimal coupling. Consistent with the discussion of quartic couplings in Sec. 4.2.1, the quartic coupling remains zero due to gravitational fluctuations. We do not find any fixed points beyond the partial Gaussian fixed point (5.18).

While the fixed point values G_* and Λ_* can be computed at the fixed point (5.18), in common approximations their values depend on the matter degrees of freedom under consideration. In the following we vary these values to explore possible phenomenological implications. As Fig. 5.1 illustrates, one can distinguish three different regimes with regard to the (ir-)relevance of the couplings m_ϕ^2, λ_4 and ξ:

1. In the light blue region two of the three couplings remain relevant. While the stability matrix is not fully diagonal, the relevant directions roughly correspond to m_ϕ^2 and ξ, rendering λ_4 irrelevant.

2. In the light gray region only one of the three couplings is relevant. The relevant direction is approximately aligned with the mass parameter.

3. In the dark gray region all three couplings are irrelevant.

---

[3]This fixed point is obtained without SM matter.
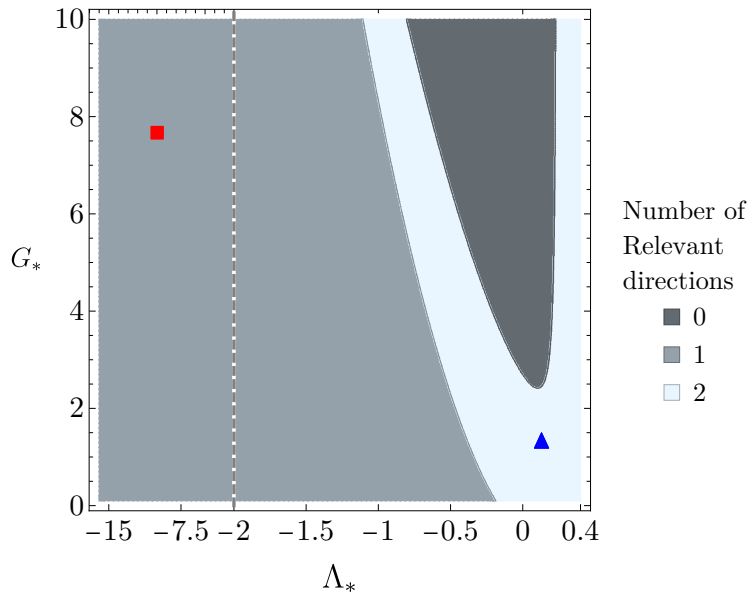
Fig. 5.1.: Number of relevant directions for the three couplings m^2, λ_4, ξ at the Gaussian matter fixed point. The blue triangle (red square) marks the position of the gravitational fixed points (5.18) / (3.34). Notice the change in scaling of the Λ_* axis at $\Lambda_* = -2$, also indicated by the vertical dashed line.

In the figure, we also highlight the shift of the gravitational fixed point values under the inclusion of matter: while two directions in the matter sector are relevant at the fixed point (5.18), only the scalar mass is relevant at the fixed point (3.34) that takes SM matter into account.

To understand the origin of the boundary between these three regions we neglect off-diagonal terms in the stability matrix. In agreement with previous results we find that gravitational fluctuations act to make the couplings of the scalar potential irrelevant [68, 145, 169–178]. This renders the quartic coupling irrelevant, independent of the values of the gravitational couplings. In addition, in the regime of strong gravitational fluctuations even the mass and the non-minimal coupling become irrelevant. At fixed value of the cosmological constant Λ this happens for a critical value of G,

$$ G > G_{\text{crit}} = \frac{12\pi(1 - 2\Lambda)^2(3 - 4\Lambda)^2}{159 - 460\Lambda + 352\Lambda^2 - 16\Lambda^3}. \tag{5.20} $$

To understand the irrelevance of ξ in the weak gravity regime consider the linear coefficient in β_ξ at vanishing matter couplings

$$ \beta_\xi = \left(\frac{3}{2\pi(3 - 4\Lambda)^2} - \frac{5(6 + 20\Lambda)}{36\pi(1 - 2\Lambda)^3} + \frac{1}{6\pi(3 - 4\Lambda)} \right) G\xi + \mathcal{O}\left(\xi^2\right). \tag{5.21} $$

This linear coeffient changes sign for $\Lambda < \Lambda_{\text{crit}} = 0.17$. At $\Lambda = \Lambda_{\text{crit}}$ the fixed point becomes degenerate, see Fig. 5.2. The additional zeros of the beta function that arise for $\Lambda \neq \Lambda_{\text{crit}}$ are no fixed points of the full system. The G-dependence of the boundary arises as a result of the mixing between the different scalar couplings.

The fixed point (5.18) is $\mathbb{Z}_2$ and shift symmetric. The corresponding theory space features all interactions compatible with these symmetries. This in particular includes
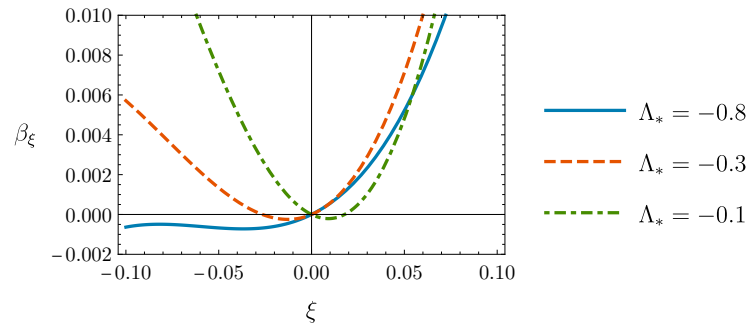
Fig. 5.2.: Beta function β_ξ for various fixed point values of the cosmological constant Λ at fixed $G = 1$ and vanishing matter couplings $m^2 = \lambda_4 = 0$.

higher-order derivative interactions. These interactions do not vanish as gravitational interactions induce them. Only if gravitational interactions are sufficiently weak, will the couplings corresponding to these interactions feature fixed points, see Sec. 4.1.2 and in particular Ref. [164]. Such interactions are not part of our truncation. Hence, a fixed point with the symmetries of the kinetic term, i.e. a fixed point at vanishing scalar potential must necessarily appear.

To obtain a non-vanishing potential, one needs to deviate from the fixed point. This is possible if a coupling is relevant, and hence quantum fluctuations enhance a perturbation in the corresponding coupling along the flow. We find that throughout the gravitational parameter space at least one combination of m^2, λ_4 and ξ is irrelevant and hence predicted. In an approximation in which the stability matrix is diagonal, the irrelevant direction corresponds to the quartic coupling λ_4. The quartic coupling hence approximately vanishes along the RG flow. For strong gravitational fluctuations all scalar couplings become irrelevant. This situation might make the resurgence mechanism viable [173]: flowing from some UV scale k_{UV} to the Planck scale with a negative critical exponent strongly suppresses the scalar mass parameter at the Planck scale. Below the Planck scale the mass parameter then grows approximately according to its canonical mass dimension. The strong trans-Planckian suppression then naturally explains a large hierarchy of scales between the Planck mass and the scalar mass parameter, potentially explaining hierarchies such as the one of the Higgs vacuum expectation value and the Planck scale in the SM.

More generally, in an effective asymptotic safety scenario, each irrelevant direction is attracted towards its fixed point value. If all three directions are irrelevant, then in the trans-Planckian regime quantum gravitational fluctuations flatten the scalar potential by driving the RG trajectory towards $m^2(M_{\mathrm{Pl}}) = \lambda_4(M_{\mathrm{Pl}}) = \xi(M_{\mathrm{Pl}}) = 0$. More relevant directions allow accommodating more deviations from flatness.

5.3.2 Slow-Roll-Inspired Parameters from Asymptotic Safety

The flattening of a scalar potential due to gravitational fluctuations can also be observed in the slow-roll parameters. Computing the flow of the standard slow-roll parameters (5.7) is involved as they depend explicitly on the Planck mass. The Planck mass depends on G. The flow of the slow-roll parameters then mixes with the flow of G.
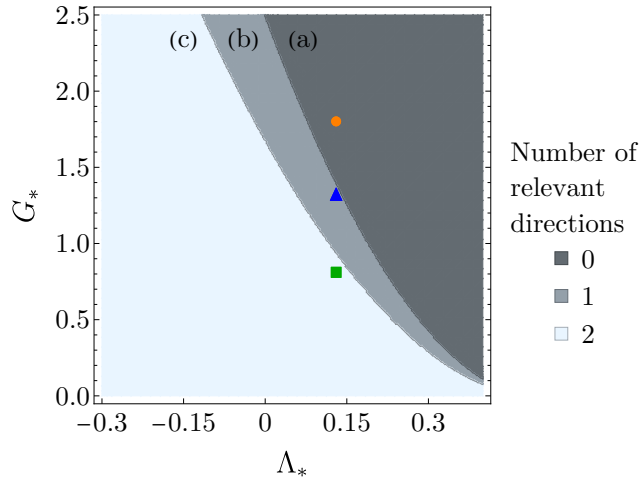
Fig. 5.3.: The number of relevant directions as a function of the gravitational fixed point values in this approximation. The three symbols indicate the gravitational fixed point values used for the plots in Fig. 5.4.
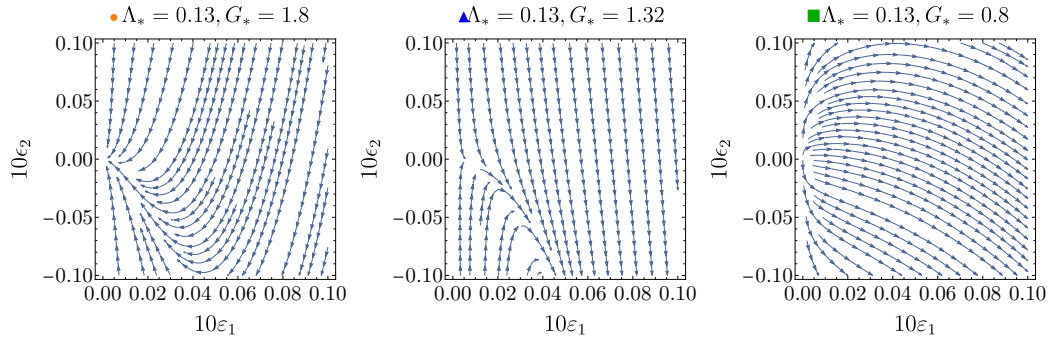
Fig. 5.4.: Flow of the slow-roll-inspired parameters (5.22) for varying values of the gravitational fixed point values.

To disentangle these flows we instead consider the slow-roll-inspired parameters

$$\epsilon_i = \frac{1}{k^{4-i}} \frac{\partial^i V(\phi^2)}{\partial \phi^i}. \tag{5.22}$$

The standard slow-roll parameters are defined for a canonically normalized and minimally coupled scalar field. Given that $\xi_* = 0$ is a fixed point, here we work in the approximation $\xi = 0$. Additionally, we neglect the anomalous dimension. Taking derivatives of Eq. (3.21) we compute the flow of the parameters (5.22). The flow for ϵ_i depends on ϵ_{i+1} and ϵ_{i+2}, as well as explicitly on ϕ. To close the resulting set of equations we set $\epsilon_i = 0$ for $i > 2$. The beta functions for the ϵ_i's are given in App. F.3. As expected, they feature a fixed point at $\epsilon_i = 0$, corresponding to vanishing potential. As an example we evaluate ϵ_1, ϵ_2 at $\phi/k = 1$. We vary the gravitational fixed point values G and Λ, see Fig. 5.3, and show the resulting flow for ϵ_1, ϵ_2 in Fig. 5.4. For increasing values of G, the gravitational fluctuations are able to overcome larger canonical dimensional scaling and more ϵ_i become irrelevant.

5.4 Inflation and Asymptotic Safety

Both, the near-scale-invariance of inflationary perturbations and the success of classically scale-invariant models, point at the importance of scale invariance for inflationary model building. Next, we focus on the implications of quantum scale invariance realized by a UV fixed point for inflationary models. We will first discuss a vanilla inflationary model, then Higgs inflation and finally Starobinsky inflation. We first focus on the vanilla model — a real scalar ϕ with a potential $V(\phi)$ — and assume that ϕ is not coupled to the SM degrees of freedom. Due to the interacting nature of the gravitational fixed point, derivative interactions are necessarily present, cf. Sec. 4.1.2. We assume that these are negligible.

5.4.1 Single Scalar: Vanilla Model

We first apply a description in terms of the slow-roll-inspired parameters ϵ_i and assume $\xi = 0$. The condition $\xi = 0$ is realized at the fixed point. We assume that it remains a good approximation along the RG flow.

We distinguish three regions (a), (b), (c), cf. Fig. 5.3. In region (a) all derivatives of the potential vanish. The potential stays flat, and there is no graceful exit from inflation.

In region (b) the second derivative ϵ_2 is predicted as a function of ϵ_1. As apparent from the second panel of Fig. 5.4, the resulting values of ϵ_2 are negative. This implies a concave potential. This qualitative behavior is in accordance with observational data [248]. A more quantitative comparison requires a more detailed mapping between the slow-roll parameters and the ϵ_i. We leave this for future work. Additionally, we caution that accommodating the correct amplitude of scalar fluctuations A_s might be challenging, see below.

In region (c), both ϵ_1 and ϵ_2 are relevant. They can be adjusted to match the measured scalar spectral tilt n_s and the tensor-to-scalar ratio r. Conversely, the amplitude of scalar fluctuations A_s is unrelated to the ϵ_i. Instead, it is determined by the overall magnitude of the scalar potential $V(\phi_{\mathrm{infl}})$ according to (5.8). $V(\phi_{\mathrm{infl}})$ is a relevant quantity in an asymptotically safe setting. In principle, it can be adjusted freely. However, the inflationary potential cannot be treated in isolation: fixing the value of the potential $V(\phi_{\mathrm{infl}})$ at field values relevant for inflation will also determine the value of the potential $V(\phi_{\mathrm{late}})$ at field values relevant for the late universe. The value of the potential $V(\phi_{\mathrm{late}})$ in the late universe determines the energy density Ω_{DE} in the cosmological constant/a dynamical dark energy component. Accommodating the values $V(\phi_{\mathrm{infl}})$ and $V(\phi_{\mathrm{late}})$ in one potential might be challenging.

Let us point out that region (a) in particular, and the general tendency of flattening scalar potentials, might also be relevant in an effective asymptotic safety scenario in conjunction with string theory: in such a scenario metric degrees of freedom only play a role below k_{string}. At scales $k_{\mathrm{string}} \gg M_{\mathrm{Pl}}$ stringy degrees of freedom provide a UV completion. String theory might put a lower bound on the flatness of potentials, see e.g. [153, 268, 269]. At k_{string} a scalar potential hence might be relatively steep. If the string scale k_{string} is higher than the Planck scale, cf. Ref. [148], then such a steep
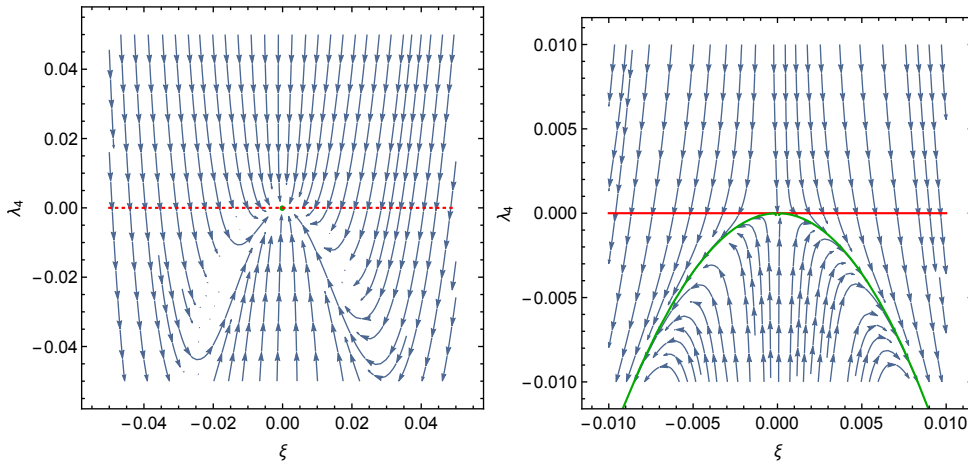
Fig. 5.5.: Flow for the couplings ξ and λ_4 in the trans-Planckian regime for $g = 1$. In the left (right) panel none (one) of the two couplings is relevant and the cosmological constant takes the value $\Lambda = 0$ ($\Lambda = -1$). The green line in the left plot indicates the fixed-point trajectory. The observational constraint $\lambda_4/\xi^2 \sim 10^{-9}$ is highlighted in red. The fixed-point trajectory and the observational constraint only intersect for $\lambda_4 = 0$.

potential could be flattened by gravitational fluctuations. Hence, flatter potentials might become viable within string theory in this scenario.

Next, we provide an alternative perspective on the flattening of scalar potentials by switching to a polynomial truncation. We consider the polynomial truncation (5.16) with the couplings m^2, ξ, λ_4. For $\xi = 0$, the resulting potential is purely polynomial. It generates an exceedingly large tensor-to-scalar ratio. For $\xi \neq 0$, one typically eliminates the non-minimal coupling by means of a conformal transformation. The conformal transformation maps the frame with a non-minimal coupling to a frame without a non-minimal coupling. Here, we instead stay in the non-minimally coupled frame and quote constraints for coupling values typically obtained in the minimally coupled frame, see also Sec. 5.2.1.

We first focus on the case with negligible mass term $m^2 = 0, \lambda_4 \neq 0$. In that case the amplitude of primordial fluctuations typically leads to the constraint $\frac{\lambda_4}{\xi^2} \sim 10^{-9}$, cf. (5.14). We do not find a fixed point with $\xi_* \neq 0$. In order to match the observational constraint, the corresponding ratio of λ_4 and ξ^2 has to emerge along the flow towards the IR. The corresponding flows can be split into two regimes: the flow first takes place in the trans-Planckian regime $k > M_{\text{Pl}}$ in which scalar and gravitational fluctuations contribute, before it enters the sub-Planckian regime $k < M_{\text{Pl}}$ in which only scalar fluctuations contribute.

In the trans-Planckian regime, $k > M_{\text{Pl}}$, the flow depends on the gravitational fixed point values. These determine the (ir-)relevance of λ_4 and ξ. At least one of the two will be irrelevant. If both couplings are irrelevant, then the flow in the left panel of Fig. 5.5 emerges. No deviation from the fixed point with vanishing potential occurs and the scalar potential cannot drive inflation. If one of the two couplings is irrelevant, then the flow in the right panel of Fig. 5.5 emerges. The critical surface is approximated by $-\lambda_4/\xi^2 \sim \mathcal{O}(10^{-2})$. In particular, it only intersects the surface given by $\lambda_4/\xi^2 \sim 10^{-9}$ at the Gaussian fixed point.
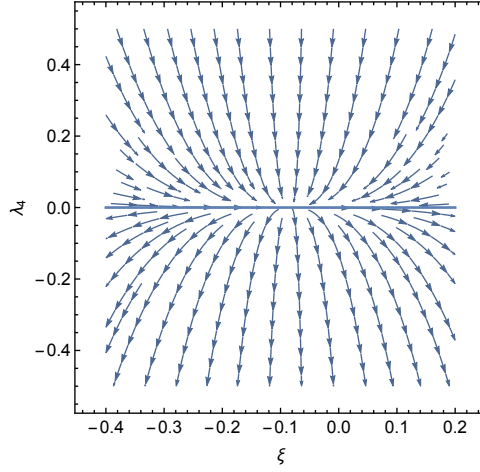
Fig. 5.6.: Flow for the couplings ξ and λ_4 at vanishing mass in the sub-Planckian regime ($G = 0$). For $\lambda_4 = 0$ the flow vanishes identically.

In the sub-Planckian regime, $k < M_{\mathrm{Pl}}$, gravitational fluctuations decouple. The resulting beta functions for ξ and λ_4 both are proportional to a power of λ_4. For $\lambda_4 = 0$, both beta functions vanish, independent of the value of ξ, cf. Fig. 5.6. The resulting line of fixed points is IR attractive for $\lambda_4 > 0$ and IR repulsive for $\lambda_4 < 0$. Obtaining $\lambda_4/\xi^2 \sim 10^{-9}$ in the IR requires finely tuned initial conditions at M_{Pl} at non-vanishing values for λ_4 and ξ. We do not find any hints for such initial conditions.

In summary, we do not find any indication that one can realize $\lambda_4/\xi^2 \sim 10^{-9}$ and hence the right amplitude of scalar fluctuations in the case $\lambda_4 > 0, m^2 = 0$. We therefore consider the case $m^2 > 0, \lambda_4 = 0$. For non-vanishing $\xi \sim \mathcal{O}(10^{-3})$ and $m^2 \sim \mathcal{O}(10^{-11})$, the corresponding Einstein-frame potential develops a peak at the field values explored during inflation. The potential allows for an inflationary scenario [270]. We find that the corresponding coupling values cannot be realized in the vicinity of the Gaussian fixed point. At this fixed point, a value of $\xi \sim \mathcal{O}(10^{-3})$ will immediately induce a quartic coupling $\lambda_4 \neq 0$, cf. Figs. 5.5 and 5.6. The resulting value of λ_4 is so large that it significantly alters the shape of the potential and invalidates our assumption $\lambda_4 = 0$.

In this subsection, we have explored a variety of scenarios for the vanilla inflationary model. We conclude that within our approximations none of the scenarios gives rise to inflation and matches the observed amplitude of scalar fluctuations A_s, indicating that the vanilla inflationary model might not be viable within an asymptotically safe context.

5.4.2 Higgs Inflation

The case of Higgs inflation (cf. Sec. 5.2) is structurally different from the $\lambda_4\phi^4$ potential discussed in the last section and the one considered in Ref. [271]: the Higgs field also couples to the top quark in the SM. As a toy model, we again couple a single Dirac fermion, representing the top quark, to the scalar ϕ, representing the Higgs field, via a Yukawa coupling and hence consider the same system as in Sec. 4.4. The Yukawa
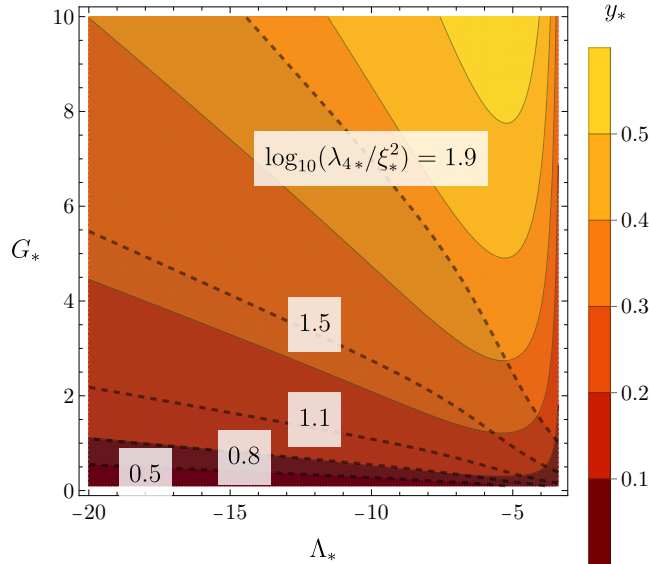
Fig. 5.7.: We show contours for λ_{4*}/ξ_*^2 at the interacting Yukawa fixed point (dashed) and corresponding contours for the Yukawa coupling y_* (color) as a function of the gravitational fixed point values Λ_*, G_*.

coupling can deviate from $y_* = 0$ only for a fixed point value of the cosmological constant $\Lambda_* < -3.3$. Only in this regime there is an interacting fixed point and the Gaussian fixed point for the Yukawa coupling is relevant. As a consequence, only in this regime a non-vanishing Yukawa coupling is possible in the IR.

To obtain a non-vanishing IR top Yukawa coupling we hence focus on $\Lambda_* < -3.3$. In this regime the non-minimal coupling is irrelevant. In addition, we focus on the interacting fixed point, for the non-interacting fixed point the results of the last subsection apply. The resulting ratio λ_4/ξ^2 at the interacting fixed point is of order one as long as the Yukawa coupling does not become tiny, cf. Fig. 5.7. The ratio in this figure is the one at the fixed point. However, there are no indications that the flow towards the IR will significantly enhance this ratio, see also Fig. 5.6. Accommodating both, the correct top Yukawa coupling and the correct ratio λ_4/ξ^2, i.e. the correct amplitude of primordial scalar fluctuations, is impossible within our toy model. Within our approximations this disfavors Higgs inflation in the context of asymptotic safety.

5.4.3 Starobinsky Inflation

An inflationary model with a single scalar ϕ and Higgs inflation are both challenging to reconcile with observational data within the context of asymptotically safe gravity. At the same time, at an asymptotically safe fixed point quantum fluctuations naturally generate higher-order curvature terms. These higher-order curvature terms can cause an inflationary period in the early universe, a scenario known as Starobinsky inflation [240]. In the following we review whether Starobinsky inflation might occur within asymptotically safe gravity [272].

Starobinsky inflation extends the Einstein-Hilbert action by a term quadratic in the scalar curvature $\sim R^2$. The resulting action is classically equivalent to a scalar

minimally coupled to Einstein-Hilbert gravity. For large R^2 coupling the resulting scalar potential permits an era of inflation compatible with all present observations of the cosmic microwave background [248].

To study the compatibility of asymptotically safe Starobinsky inflation with observational data one line of research applies an RG improvement procedure [273–276], identifying the RG scale and the Ricci scalar $k^2 \sim R$, see also Ref. [87] for a critical discussion of RG improvement and Ref. [277] for a discussion of how to choose the RG scale. Under this identification all scales in the action are proportional to R. Scale invariance implies that at the fixed point the action scales as R^2. Deviations from this fixed point scaling are encoded in the critical exponents. Close to the fixed point (but not at the fixed point) the resulting action scales with a combination of integer and non-integer powers of R [273–276]. The resulting $f(R)$-type actions can give rise to inflationary cosmology, see Refs. [273–276, 278]. Deviations from the $R + R^2$ scaling could lead to deviations in the observables n_s and r from the standard Starobinsky values.

To explain not only the shape, but also the amplitude A_s of the power spectrum, in Starobinsky inflation the R^2 coupling has to be large. Within existing truncations such a large coupling does not appear to be realized at an asymptotically safe fixed point. However, the R^2 coupling is a relevant coupling in many truncations. A large coupling value could hence be generated along the RG flow. As one example, Ref. [109] fixed observationally informed values for the cosmological constant $\Lambda(k)$, the Newton coupling $G(k)$ and the R^2 coupling at scales k that are identified with the corresponding observational scales. This reference then demonstrated that a trajectory realizing all three values could emanate from an asymptotically safe fixed point.

However, such a large R^2 coupling is not expected to remain isolated. Within a polynomial truncation, this coupling will induce a large R^3 coupling. Such a coupling might spoil the observed flatness of the inflationary potential. In other inflationary models this is known as the η problem (see e.g. Ref. [279] for a discussion). In asymptotically safe gravity this problem has not been investigated outside the fixed point regime.

To demonstrate the relevance of this constraint, in the following we estimate the magnitude of the R^3 coupling resulting from the RG flow. We take the beta functions for an action

$$\Gamma_k^{f(R)} = \int \mathrm{d}^4 x \, \sqrt{g} \, \frac{k^4}{16\pi} \left(b_0 + b_1 \frac{R}{k^2} + b_2 \frac{R^2}{k^4} + b_3 \frac{R^3}{k^6} \right), \qquad (5.23)$$

from Ref. [111]. We consider the fixed point

$$b_0 = 0.26 \quad b_1 = -0.98 \quad b_2 = 0.035 \quad b_3 = -0.49 \qquad (5.24)$$

that is an extension of the fixed point found in the Einstein-Hilbert truncation [111]. It features three relevant directions, which are approximately aligned with b_0, b_1 and b_2, i.e. with the cosmological constant, the Newton coupling and the R^2 coupling. The coupling b_3 is irrelevant.
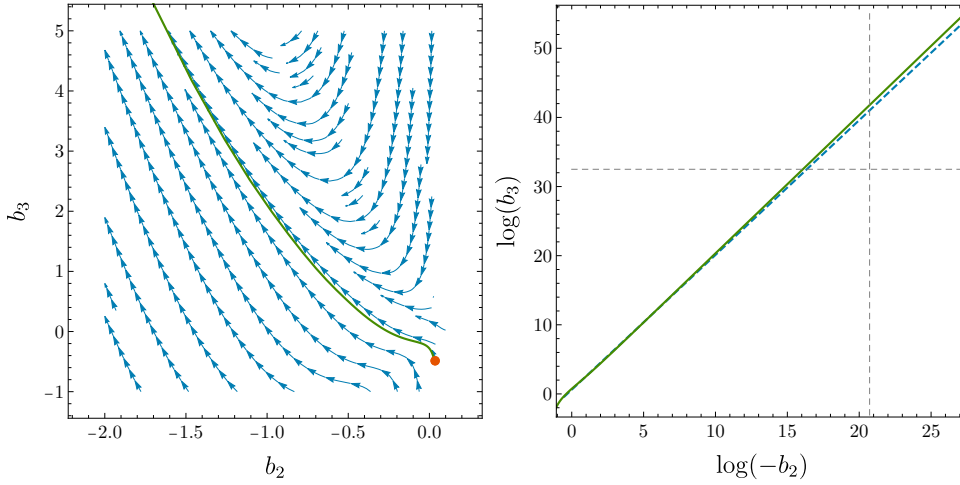
Fig. 5.8.: We plot the flow for the two couplings b_2 and b_3. (left) Flow of the couplings close to the fixed point (orange dot). The green line is the trajectory that relates b_2 and b_3. (right) Relation of the two couplings b_2 and b_3. The dashed blue line corresponds to the linear fit. The vertical dashed line corresponds to the value of b_2 required to match the amplitude of scalar fluctuations, the horizontal dashed line corresponds to the limit $\left|\tilde{b}_3/b_2^2\right| < 10^{-4}$, with $\tilde{b}_3 = b_3 M_{\text{Pl}}^2$.

We study the flow away from the fixed point. Gravitational fluctuations contribute for $k > k_{\text{trans}}$. Here k_{trans} is a transition scale at which gravitational fluctuations freeze out and the couplings Λ and G leave the fixed point regime. For $k < k_{\text{trans}}$ the couplings Λ and G, or correspondingly b_0 and b_1 run according to their canonical mass dimension. For $k > k_{\text{trans}}$ gravitational fluctuations contribute to the flow. As a simplifying assumption we set b_0 and b_1 to their fixed point values, assuming that they do not strongly deviate from their fixed point values for $k > k_{\text{trans}}$.

We can then solve the remaining system of differential equations for $b_2(k)$ and $b_3(k)$ numerically. The coupling b_3 is irrelevant. On the critical hypersurface it is given in terms of the couplings b_0, b_1 and b_2. For fixed b_0 and b_1 its value on the critical hypersurface is a function of b_2 only, cf. Fig. 5.8. The resulting relation between b_2 and b_3 is approximately given by[4]

$$\log(b_3(k)) = 0.51 + 2.05 \log(-b_2(k)). \tag{5.25}$$

It parameterizes the only trajectory compatible with an asymptotically safe fixed point.

The relation (5.25) determines the relation of the couplings b_2 and b_3 at k_{trans}. It does not capture the running below k_{trans}. Below k_{trans} we assume that gravitational fluctuations freeze out, such that (i) b_2 remains approximately constant and (ii) b_3 scales according to its mass dimension as $(k/k_{\text{trans}})^{-2}$. The first assumption is in line with Ref. [109], finding that b_2 remains approximately constant below k_{trans}. In addition, that reference finds that $k_{\text{trans}} = 10^{15}$ GeV is considerably lower than the Planck scale. The second assumption could be checked by solving the full system of b_0, b_1, b_2 and b_3 numerically. We leave this to future work.

---

[4]This relation breaks down close to the fixed point (orange dot in the left panel of Fig. 5.8) as b_2 becomes positive there.

Our simplifying assumptions about the flow clearly need to be tested. In the presence of large couplings b_2 and b_3 the flow of G and Λ might be altered considerably. In addition, the relation (5.25) will experience modifications in extended truncations, that potentially have to go beyond a polynomial truncation.

Here we proceed to illustrate how such a relation compares to observations. In an action

$$S_{\text{Starobinsky}} = \int \mathrm{d}^4x \sqrt{-g} \left(M_{\text{Pl}}^2 R + b_2 R^2 + \frac{\tilde{b}_3}{M_{\text{Pl}}^2} R^3 \right) \tag{5.26}$$

matching the amplitude of scalar fluctuations requires $b_2 \sim 10^9$ [280, 281]. The ratio $\frac{\tilde{b}_3}{b_2^2}$ is bound by the spectral tilt n_s such that $\left| \frac{\tilde{b}_3}{b_2^2} \right| < 10^{-4}$ [280, 281].

We assume that these constraints hold at $k_{\text{infl}} < k_{\text{trans}}$. By assumption, the coupling b_2 is approximately constant, and thus $b_2(k_{\text{infl}}) = b_2(k_{\text{trans}})$. In addition, we rewrite

$$\frac{\tilde{b}_3}{M_{\text{Pl}}^2} = \frac{b_3(k_{\text{infl}})}{k_{\text{infl}}^2}. \tag{5.27}$$

In terms of b_3 the observational bound on $\frac{\tilde{b}_3}{b_2^2}$ then reads

$$\frac{b_3(k_{\text{infl}})}{b_2(k_{\text{infl}})^2}(M_{\text{Pl}}/k_{\text{infl}})^2 < 10^{-4}. \tag{5.28}$$

If b_3 scales canonically between k_{infl} and k_{trans}, as we assume within this simplified model, then this bound implies

$$\frac{b_3(k_{\text{trans}})}{b_2(k_{\text{trans}})^2}(M_{\text{Pl}}/k_{\text{trans}})^2 < 10^{-4} \tag{5.29}$$

at k_{trans}.

We now combine the observational constraint (5.29) and the relation (5.25) that arises as a result of the flow away from the fixed point. For $b_2(k_{\text{trans}}) \approx b_2(k_{\text{infl}}) \sim 10^9$ the relation (5.25) implies $b_3(k_{\text{trans}}) \sim 6 \cdot 10^{17}$ at k_{trans}. Inserting the numeric values for b_2, b_3 into (5.29) then yields

$$k_{\text{trans}} \geq 70 M_{\text{Pl}}, \tag{5.30}$$

see also Fig. 5.9.

The transition scale would need to be larger than the Planck scale, and in particular much larger than $k_{\text{trans}} = 10^{15}$ GeV, as found in Ref. [109]. This result has an intuitive interpretation: if higher order operators run canonically, then operators of the type $R^n, n \geq 3$ are suppressed by the transition scale k_{trans}. By raising the transition scale we lower the impact of higher order operators and avoid potential conflict with observational bounds. For canonical values of $k_{\text{trans}} \approx M_{\text{Pl}}$ an excessively large R^3 coupling might be generated. Hence, the existence of a relevant R^2 direction does not guarantee the viability of Starobinsky inflation within asymptotically safe gravity. Irrelevant directions might spoil the flatness of the inflationary potential and hence lead to disagreement with observations.
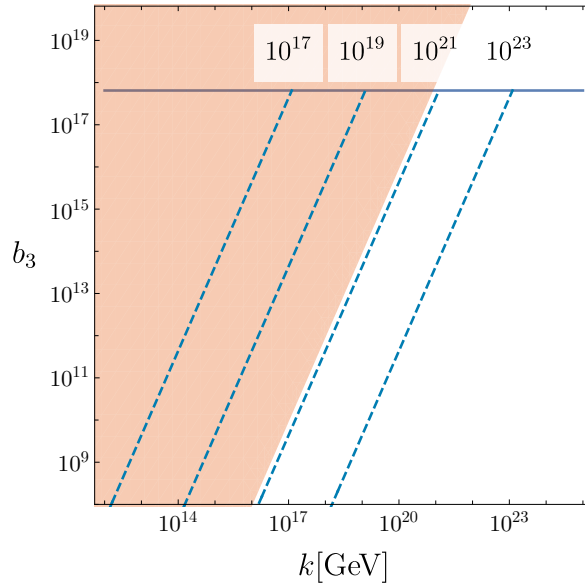
Fig. 5.9.: We show the flow for the coupling b_3 below k_{trans}. The red region marks the observational constraint (5.29). The horizontal solid line is the initial condition $b_3(k_{\text{trans}}) \sim 6 \cdot 10^{17}$ that might arise in asymptotic safety from the relation (5.28). The dashed lines indicate RG trajectories for different transition scales k_{trans}, with the transition scale indicated over each trajectory in GeV.
The bound on k_{trans} is independent of k_{infl}, as both the bound and b_3 scale canonically below k_{trans}.

We again caution that the argument presented here is strongly simplified. It depends on the relation (5.25) between b_2 and b_3, which in turn arises as a result of the simplifying assumptions of our model. Studying the resulting flow at sub-Planckian scales numerically is required to check our assumptions. In addition, going beyond a polynomial truncation is necessary to obtain firmer conclusions.

Going beyond such polynomial truncations also points to a more fundamental question with regard to Starobinsky inflation: in Starobinsky inflation one inflates using a scalar degree of freedom present in $f(R)$ type actions. It is not clear if this scalar degree of freedom exists in an extended theory space featuring all invariants allowed by diffeomorphism symmetry.

Beyond Starobinsky models the fixed point solution for $f(R)$ truncation might feature de Sitter solutions [282–285]. At present, it is not clear if these solutions in the fixed point regime can be connected to an inflationary regime at the correct energy scales to generate the observed curvature perturbations.

In summary obtaining an inflationary phase that matches the small value of A_s is challenging for a single scalar, in the context of Higgs inflation and in the context of Starobinsky inflation. Making progress on these questions is particularly interesting in light of upcoming improvements on observational constraints of the cosmic microwave background. As a key observational milestone, the LiteBIRD satellite aims to reduce the observational error on the tensor-to-scalar ratio r below $\delta r < 0.001$ [286]. This observational error allows to probe the prediction (5.13), and hence to test Higgs inflation and the Starobinsky model of inflation.

5.5 Dark Energy and Asymptotic Safety

The accelerating expansion of the universe takes place on the largest length scales accessible to observations. Quantum gravity describes physics at length scales too short to be observed with present technology. One could conclude that the relevant scales are separated from each other, and the two are unrelated questions. However, various approaches to quantum gravity have challenged this conclusion. As one example causal set theory might predict a cosmological constant of the right order of magnitude [287–289]. As a second example, the swampland conjectures express a preference for steeper potentials in string theory. Within these conjectures, the first derivative of scalar potentials has to be at least of order one in units $M_{\mathrm{Pl}} = 1$ [268, 269]. In particular, a cosmological constant cannot be realized and deviations from an equation of state $w \approx -1$ should occur [290].

Within asymptotically safe gravity we distinguish the case of a cosmological constant from the case of dark energy. The cosmological constant is relevant at the gravitational fixed point. This renders an interval of IR values compatible with the UV fixed point. In particular, the measured IR value can be accommodated. To obtain a corresponding trajectory is numerically challenging but has been performed in Ref. [109]. Within asymptotically safe quantum gravity a cosmological constant with $w = -1$ hence is viable.

Dynamical dark energy typically is modeled as a scalar in a non-flat potential. We again consider the model of a real scalar field ϕ with potential $V(\phi)$. The resulting potential is determined by the relevant couplings. If all couplings are irrelevant, the potential remains flat, and one is back to the case of a cosmological constant. If only the mass is relevant — which is the case at the fixed point values (3.34) corresponding to SM matter — then only a quadratic potential is permitted within our truncation. If the mass and ξ are relevant, the non-minimal coupling again allows to flatten the effective Einstein-frame potential. This would imply equations of state closer to $w \approx -1$.

Notice that these results rely on an expansion around the origin of field space, which might not be suitable for some quintessence potentials. To study the behavior at finite field values we again expand the flow in ϵ_i according to (5.22). Below the Planck scale the ϵ_i strongly increase in accordance with their canonical mass dimension, such that dimensionful couplings stay constant, cf. Fig. 5.10. Above the Planck scale the ϵ_i decrease due to gravitational fluctuations. Small ϵ_i correspond to a flat potential. The gravitational fluctuations in asymptotically safe quantum gravity might induce flat potentials, or an equation of state $w \approx -1$. This puts asymptotically safe quantum gravity in contrast to string-inspired models that prefer an equation of state different from $w = -1$.

At the same time, the observational constraints on the equation of state w are expected to strongly improve in the near future: At present they are at $\sim 10\%$ level at small redshifts, see e.g. Ref. [290] for a discussion in the context of the string swampland. Ongoing observational efforts such as DESI [291] will deliver data in the next few years. By the end of this decade, the EUCLID satellite will map out the observable universe up to $z \sim 2$ to a precision of approximately 2% in the equation of state [237,
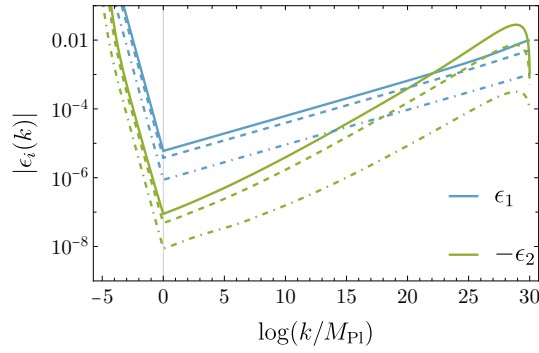
Fig. 5.10.: Flow of the two slow-roll-inspired parameters ϵ_1, ϵ_2 towards the IR at a fiducial value $\phi/k = 1$. The solid, dashed and dashed-dotted lines correspond to different initial conditions. Here, for $k > M_{\text{Pl}}$, we set $G = 1.5, \Lambda = 0.13$, corresponding to the region (a) with no relevant parameters in Fig. 5.3.

292]. In addition, observations by the Square Kilometer Array promise to tightly constrain the dark-energy equation of state up to $z \sim 3$ at percent level in the future [293, 294].

5.6 Conclusion: Obstacles to Realizing Inflation

We discussed how asymptotically safe quantum gravity might constrain the accelerating universe. As a disclaimer we remind the reader that all our results are obtained within a Euclidean setup. In addition, we study polynomial truncations, mostly expanding around the origin. An expansion around the origin might not be well suited to study potentials of the runaway type that often occur in the context of quintessence. Obtaining global numerical solutions for the fixed-point potential and the flow towards the IR are hence important extensions, see Refs. [177, 295, 296]. Given the role of the structure of the kinetic term, a particular focus on a field-dependent renormalization of the kinetic term might be important.

We find that within our approximations asymptotically safe quantum gravity drives potentials towards flatness. Throughout the gravitational parameter space the quartic coupling remains irrelevant. For SM matter the non-minimal coupling is irrelevant as well. We introduce a set of parameters inspired by the slow-roll parameters to illustrate the flattening of scalar potentials. For appropriate gravitational parameters the flow again prefers values corresponding to a flat potential.

In an inflationary context, the flattening of scalar potentials is promising in light of the approximate scale invariance of the spectrum of primordial scalar fluctuations. However, we highlighted that matching the amplitude A_s of the spectrum is challenging. In a model featuring a single scalar we do not find indications that the ratio λ_4/ξ^2 can take the required values. Similarly, we find indications against the viability of Higgs inflation. Within our approximations, realizing the correct ratio of λ_4/ξ^2 at the corresponding interacting fixed point implies a top Yukawa coupling in tension with inputs from particle physics. Finally, within Starobinsky inflation the required large value of the R^2 coupling might percolate into higher order couplings and spoil the flatness of the corresponding potential. Understanding if and how asymptotically safe

gravity can lead to a phase of early accelerated expansion with the correct amplitude of fluctuations hence remains an interesting open question.

Within an asymptotically safe model the observed accelerated expansion in the present universe could be driven either by the cosmological constant or dynamical dark energy. If a scalar field is responsible for the observed expansion, asymptotically safe gravity again could flatten the corresponding potential. This might lead to a preference for a value close to $w \approx -1$ within asymptotically safe gravity.

These conclusions highlight how asymptotically safe gravity could constrain models to explain the accelerated expansion of the early and the late universe. After focusing on the background evolution, we next turn to a central ingredient to explain the structure that we observe in our universe: dark matter.

Dark Matter in Asymptotic Safety 6

In the last chapter we focused on an approximately constant energy density, dominating the background expansion in the earliest and the most recent cosmic epoch. Beyond this expanding background, our universe is rich in structure. Visible matter forms galaxy clusters, galaxies and even smaller structures. These structures form when clouds of matter collapse gravitationally. To explain the level of structures observed in today's universe, the observed amount of visible matter is not sufficient.

An additional component that scales as $\sim a^{-3}$, i.e. as matter and interacts gravitationally but not electromagnetically could explain the observed amount of structure and other observations. Introducing such a dark matter component is a major motivation to go beyond the SM. However, taking steps beyond the SM entails a large amount of freedom. Even simple models feature many free parameters. The large number of free parameters allows to accommodate a variety of observations and leads to little predictivity.

To enhance predictivity, theoretical guiding principles are needed. As one such principle, scale invariance might improve predictivity. Indeed, classical scale invariance has been applied to construct predictive dark-matter models, for examples see e.g. [297–301]. In the following, we explore how quantum scale invariance can enhance predictivity in the context of dark matter. We first summarize the observational need for dark matter and discuss relevant candidates to account for dark matter in Sec. 6.1. In Sec. 6.2, we investigate which constraints quantum scale symmetry imposes on one of the simplest dark-matter models, a Higgs portal model. We then extend this model with an additional dark fermion and study the resulting model. We discuss phenomenological implications for dark matter and the Higgs mass in Sec. 6.3. Finally, in Sec. 6.4 we explore a scenario that goes beyond the standard dark matter production mechanisms.

6.1 The Observational Need for Dark Matter

The first important observation suggesting the existence of a dark matter component in our universe arises from the study of the rotational velocity of stars. One observes the radial velocity profile $v_{\mathrm{rot}}(r)$ of stars within a galaxy [302]. The radial velocity allows to infer the enclosed mass if one assumes the validity of Newtonian gravity and a spherical mass distribution. Observationally, the rotational velocity $v_{\mathrm{rot}} \approx \mathrm{const}$ is approximately constant for radii r larger than the radius of the optically observable disk [303]. As a consequence, the enclosed mass scales as $M(r) \sim r$, in a region where one observes practically no visible matter. This observation suggests that a dark matter component extends beyond the visible disk.

The second observation is gravitational lensing [304]. The presence of a large mass — typically a galaxy or galaxy cluster — bends the light from a background source, such as a supernova [305, 306]. Observations of the bending allow to reconstruct the mass distribution of the galaxy. The total mass reconstructed in such a way does not match the one that is explainable with visible matter only. The reconstructed mass requires the presence of dark matter.

The third observation is the growth of cosmic structure [14]. Cosmic structure is described in terms of density perturbations, which can be quantified in terms of the density contrast $\delta = \frac{\rho - \bar{\rho}}{\bar{\rho}}$, with ρ the density and $\bar{\rho}$ the average density. The typical density contrast δ can be estimated from the amplitude of cosmic microwave background fluctuations. It is of order $\delta \sim 10^{-5}$ at $z \sim 1100$. During matter domination $\delta \sim a$. This would imply $\delta \sim 10^{-2}$ today, and hence far smaller than what one observes. The larger density contrast can be explained by a component that does not couple electromagnetically, and hence does not experience radiation pressure. This component can already have a higher density contrast at CMB formation, leading to larger density contrasts observed today.

All three observations, and many others, are explained by an additional matter component in the universe that is not observable in the electromagnetic spectrum but interacts gravitationally.

6.1.1 Candidates for Dark Matter

The constituents of this additional matter component are unknown to date. Many candidates could constitute an additional matter-like component making up dark matter. Here, we will focus on two candidates that only require minimal extensions of the SM[1].

As a first candidate we consider black holes. Such black holes need to be formed before CMB formation to explain all existing observations. Hence, they are called primordial black holes [308]. Such black holes form, if a large density fluctuation in the early universe collapses gravitationally.

One possibility to produce large density fluctuations is via a feature in the inflaton potential[2]. A very flat region in the potential triggers a phase of ultra-slow-roll inflation and induces large curvature fluctuations [311], cf. Eq. (5.8). The expression in Eq. (5.8) is not applicable during ultra-slow-roll, but it motivates the emergence of large fluctuations from a flat region in the potential, for which $\epsilon \approx 0$ [312]. To avoid spoiling inflationary observables such a feature needs to be strongly localized in the inflaton potential [313, 314]. While asymptotic safety might allow for very flat regions in the potential, it is unclear how to realize a localized feature in the potential without spoiling other regions of the potential within asymptotic safety.

---

[1]One could also consider modifications of gravity to explain these observations, see e.g. Refs. [307]. Accounting for all mentioned observations is challenging within such approaches.

[2]For cases aiming at realizing a scenario where the inflaton is the Higgs field see Ref. [309] and for challenges realizing that scenario e.g. Ref. [310].

A second possibility arises if during inflation the Higgs remains a spectator field and the true minimum of the Higgs potential $\Phi_{\min}$ lies at field values $v_{\mathrm{EW}} \ll \Phi_{\min} < M_{\mathrm{Pl}}$. In this case excitations during inflation can trigger vacuum decay to the minimum $\Phi_{\min}$. Vacuum decay then leads to the formation of primordial black holes [315]. An additional minimum $\Phi_{\min}$ is unlikely to exist within asymptotically safe quantum gravity, cf. Sec. 4.3.1.

In addition, all primordial black hole scenarios are substantially constrained by observations. Depending on the credibility of micro-lensing observations, a scenario in which primordial black holes contribute all the dark matter might already be ruled out [308, 316].

The second candidate, particle dark matter, has been explored in detail, see e.g. Chap. 26 in [14] for a review and Ref. [317] for lecture notes. In this scenario, a particle beyond those in the SM constitutes dark matter. Such a particle can be introduced in many ways, and a large variety of models exist. The resulting space of dark-matter models is vast.

We focus on one of the most minimalistic extensions. In Higgs portal models the SM is extended by an additional scalar [318–320]. This additional dark scalar ϕ_d couples to the SM Higgs Φ via an operator $\lambda_{\mathrm{P}} \Phi \Phi^\dagger \phi_d^2$. The resulting parameter space has been extensively explored [321–326]. If one assumes that the scalar ϕ_d should constitute all of dark matter and is produced via thermal freeze out, then at present two regions are still observationally viable [327–329]. Either the scalar mass is of the order $\approx M_{\mathrm{Higgs}}/2$ and the portal coupling is of order $\sim \mathcal{O}(10^{-3})$ or the scalar mass is larger than approximately $10^3 \, \mathrm{GeV}$ with a portal coupling of $\lambda_{\mathrm{P}} \sim 1$.

In an EFT setting the scalar mass and the portal coupling are free parameters. Even in this minimalistic extension the resulting parameter space is at least two-dimensional, and might be higher-dimensional if one includes the quartic self-coupling $\frac{\lambda_d}{8} \phi_d^4$ or a non-minimal coupling $\xi_d \phi_d^2 R$. Both are inevitably generated by quantum corrections.

To constrain this large parameter space and improve predictivity additional theoretical input is needed. In the following, we will explore how quantum scale symmetry might enhance predictivity in the portal model.

6.2 Higgs Portal to a Dark Scalar in Asymptotic Safety

To study how asymptotically safe quantum gravity constrains Higgs-portal models, we again construct a suitable toy model, see also Ref. [175]. We study the effective action

$$
\Gamma_k = \int \mathrm{d}^4 x \sqrt{g} \Bigg(\left[\frac{Z_{\phi_v}}{2} g^{\mu\nu} \partial_\mu \phi_v \partial_\nu \phi_v + \frac{\bar{m}_v^2}{2} \phi_v^2 + \frac{\lambda_v}{8} \phi_v^4 - \xi_v \phi_v^2 R \right]
$$
$$
+ [v \to d] + \frac{\lambda_{\mathrm{HP}}}{4} \phi_v^2 \phi_d^2
$$
$$
- \frac{1}{16\pi \bar{G}_N} (R - 2\bar{\Lambda}) \Bigg), \tag{6.1}
$$

for a visible real scalar ϕ_v that represents the SM Higgs, and a dark real scalar ϕ_d. Here $[v \to d]$ represents all terms in the first square bracket under the replacement $v \to d$. The subscripts v and d indicate a visible and a dark scalar.

6.2.1 Vanishing Higgs Portal

The set of beta functions resulting from (6.1) only features the Gaussian matter fixed point. For the SM matter degrees of freedom with an additional scalar, the gravitational fixed point lies at

$$
\Lambda_* = -12.4, \quad G_* = 9.66 \tag{6.2}
$$

and all couplings in the matter sector vanish. The critical exponents are

$$
\theta_1 = 3.99 \qquad \theta_{2/3} = 1.97 \qquad \theta_4 = 1.92
$$
$$
\theta_{5/6} = -0.0173 \qquad \theta_{7/8/9} = -0.0353. \tag{6.3}
$$

The relevant directions approximately align with the gravitational couplings G, Λ and the two scalar masses. The two non-minimal couplings, the two quartic couplings and the portal coupling are irrelevant. The fixed point and critical exponents qualitatively agree with those in Ref. [175]. Compared to this reference, we extended the truncation by the non-minimal couplings.

The irrelevance of the portal coupling and the other two quartic couplings is determined by $\theta_{7/8/9}$. These three critical exponents coincide. Four other critical exponents come in pairs of two. The pairs arise due to an exchange symmetry $(v \leftrightarrow d)$ in the beta functions: the two scalars ϕ_v and ϕ_d are exchangeable in the action (6.1). This accidental exchange symmetry will be broken in an extension of our toy model to the SM Higgs and a dark scalar. In such an extension ϕ_v plays the role of the SM Higgs and couples to additional degrees of freedom.

The portal coupling vanishes at the fixed point. It is irrelevant and hence approximately vanishes at all scales, effectively decoupling the visible and the dark sector. Both sectors additionally would couple via derivative interactions of the type $(\partial \phi_v)^2 (\partial \phi_d)^2$,

see Sec. 4.1.2. However, these interactions are Planck suppressed and typically remain small [164].

The visible and dark masses are relevant and can hence deviate from their fixed point value $m_{v(d)}^2 = 0$. In deviating from this value they will generate a tiny non-vanishing value for the portal coupling along the RG flow. The dark and the visible sector couple extremely weakly. The weak coupling excludes thermal production of the observed amount of dark matter. Non-thermal production could still produce the observed amount of dark matter. In Sec. 6.4 we explore this possibility. In addition, gravitational production [330] or derivative interactions [331, 332] might allow producing sufficient amounts of dark matter but do require further study.

6.2.2 Regenerating the Portal Coupling

To avoid decoupling between the dark and the visible sector, larger values of the portal coupling are required. If the portal coupling is radiatively regenerated below the Planck scale, then it can take sizable values in the IR. To regenerate the portal coupling additional degrees of freedom are necessary.

As one example, the portal could be regenerated by an additional gauge symmetry. Ref. [333] charges the dark scalar under the (gauged) $U(1)_{B-L}$ of the SM. Additionally, that reference introduces a dark fermion. Either the dark scalar or the dark fermion could provide a dark matter candidate, depending on their mass hierarchy. The resulting dark matter scenario is constrained by bounds on the gauge and Yukawa couplings arising from asymptotic safety. As a second example, Ref. [334] also introduces an additional gauge symmetry. This reference assumes a fixed point structure with both vanishing quartic couplings and vanishing masses at trans-Planckian scales. These asymptotic safety inspired boundary conditions again lead to a more predictive dark matter scenario.

Both scenarios invoke asymptotic safety to enforce vanishing portal coupling at the Planck scale. They introduce additional matter degrees of freedom to regenerate the portal coupling below the Planck scale. Both scenarios still feature numerous parameters in the infrared.

Here, we construct a fixed point that features non-vanishing portal coupling at the Planck scale. The fixed point features numerous irrelevant directions, fixing the corresponding couplings at all scales. The resulting scenario could be highly predictive in the IR.

6.3 Extended Dark Sector: Dark Yukawa System

The dark sector approximately decouples because at the fixed point the dark scalar is invariant under the shift symmetry $\phi_d \rightarrow \phi_d + C$ with C a constant. This symmetry protects the fixed point at vanishing portal coupling. It would need to be violated at a fixed point with non-vanishing portal coupling.

The interacting fixed point at non-vanishing Yukawa coupling introduced in Sec. 4.2.2 explicitly breaks shift symmetry. To realize such a fixed point in the dark sector, we introduce an additional dark fermion ψ_d. The effective action then reads

$$\Gamma_k = \int \mathrm{d}^4 x \sqrt{g} \Bigg(\left[\frac{Z_v}{2} g^{\mu\nu} \partial_\mu \phi \partial_\nu \phi + \frac{\bar{m}_v^2}{2} \phi_v^2 + \frac{\lambda_v}{8} \phi_v^4 - \xi_v \phi_v^2 R + i Z_{\psi_v} \bar{\psi}_v \slashed{\nabla} \psi_v + i y_v \phi_v \bar{\psi}_v \psi_v \right]$$

$$+ [v \to d] + \frac{\lambda_{\mathrm{HP}}}{4} \phi_v^2 \phi_d^2$$

$$- \frac{1}{16\pi \bar{G}_N} (R - 2\bar{\Lambda}) \Bigg). \tag{6.4}$$

The visible sector of this model mimics the Higgs-top sector of the SM. The model features an accidental symmetry under the exchange $v \leftrightarrow d$. In an extension to a more realistic model this symmetry will be broken, as additional SM degrees of freedom couple to the visible scalar.

6.3.1 Fixed Point Structure

We explore the resulting fixed point structure and focus on the parameter region $\Lambda_* < -3.3$. In this region a free and an interacting fixed point exist for each of the Yukawa couplings, see also Sec. 4.2.2. The combined system features four fixed points for $\Lambda_* < -3.3$: one with vanishing Yukawa couplings in both sectors, two with vanishing Yukawa coupling in one sector and non-vanishing Yukawa coupling in the other sector, and one with non-vanishing Yukawa couplings in both sectors. At all four fixed points the gravitational couplings Λ and G and the two masses $m_{v(d)}^2$ are relevant.

At the fixed point with $y_v = y_d = 0$ all couplings in the matter sector vanish. Two of the remaining marginal matter couplings are relevant. The corresponding eigendirections have large overlap with the Yukawa couplings.

At the fixed point with $y_{v(d)} \neq 0, y_{d(v)} = 0$, one of the Yukawa couplings does not vanish and shift symmetry in the corresponding scalar sector is broken. Scalar interactions in this sector are induced. The other Yukawa coupling vanishes and shift symmetry in the corresponding scalar sector remains unbroken. The portal coupling and scalar interactions in this sector vanish. The partially interacting fixed point exists both in the dark and the visible sector. The two fixed points can directly be mapped into each other as a result of the accidental symmetry $v \leftrightarrow d$. The non-vanishing Yukawa coupling is irrelevant, and the vanishing Yukawa coupling is relevant.

At the fixed point with $y_v \neq 0 \neq y_d$, both Yukawa couplings are non-vanishing and shift symmetry in both scalar sectors is broken. Scalar interactions in both sectors are induced. As a consequence the portal interaction does not vanish. At the interacting fixed point, all marginal interactions are irrelevant.

Below, we focus on the interacting fixed point $y_v \neq 0 \neq y_d$, i.e. the one with the smallest number of relevant directions. Doing so, we either choose the UV completion realized in an asymptotically safe setting, and focus on the most predictive fixed

point. Or we study the case most relevant in effective asymptotic safety. Every irrelevant direction attracts the flow. For generic initial conditions, the flow hence has a preference towards the fixed point with the largest number of irrelevant directions.

A chain of interactions, triggered by the non-vanishing Yukawa coupling, leads to the non-vanishing portal coupling. We consider the effect of a non-vanishing Yukawa coupling. The Yukawa coupling appears in the beta function of the non-minimal coupling

$$\beta_{\xi_{v(d)}} = \frac{1}{192\pi^2}(1 + 12\xi_{v(d)})\left(4y_{v(d)}^2 + 3\lambda_{v(d)}\right) + \frac{1}{192\pi^2}(1 + 12\xi_{d(v)})\lambda_{\text{HP}} + \mathcal{O}\left(\xi_{v(d)}\right). \tag{6.5}$$

If the Yukawa coupling does not vanish at the fixed point, then $\xi_{v(d)*} = 0$ is not a solution of the fixed point equation $\beta_{\xi_{v(d)}} = 0$ anymore, a finite value for $\xi_{v(d)}$ is induced.

The non-vanishing non-minimal coupling induces a non-vanishing portal coupling. The beta function for the portal coupling reads

$$\beta_{\lambda_{\text{HP}}} = \frac{1}{4\pi^2}\lambda_{\text{HP}}^2 + \frac{3}{16\pi^2}\lambda_{\text{HP}}(\lambda_v + \lambda_d) + \frac{\lambda_{\text{HP}}}{4\pi^2}(y_v^2 + y_d^2) + f_y\lambda_{\text{HP}} + \beta_{\lambda_{\text{HP}}}^{\text{ind}} \tag{6.6}$$

with

$$\begin{aligned}
\beta_{\lambda_{\text{HP}}}^{\text{ind}} &= g^2\frac{160\xi_v\xi_d}{(1-2\Lambda)^3} + g^2\frac{864\xi_v\xi_d}{(3-4\Lambda)^3} + g^2\frac{82944\xi_v^2\xi_d^2}{(3-4\Lambda)^3} + g^2\frac{27648\xi_v^2\xi_d^2}{(3-4\Lambda)^2} \\
&+ g^2\frac{576(108-48\Lambda)}{5(3-4\Lambda)^3}(\xi_v^2\xi_d + \xi_d^2\xi_v).
\end{aligned} \tag{6.7}$$

The inducing term $\beta_{\lambda_{\text{HP}}}^{\text{ind}}$ does not vanish as soon as $\xi_{v(d)} \neq 0$. As soon as $\beta_{\lambda_{\text{HP}}}^{\text{ind}}$ does not vanish, $\lambda_{\text{HP}*} = 0$ ceases to be a fixed point solution, and the portal coupling is induced due to the presence of non-vanishing non-minimal couplings. This completes the chain of interactions leading to a non-vanishing portal: in each of the sectors the non-vanishing Yukawa coupling induces a non-vanishing non-minimal coupling, which in turn induces a non-vanishing portal coupling.

To compute the resulting value of the portal coupling, we neglect the influence of the non-minimal couplings and masses on the gravitational fixed point values. Assuming SM degrees of freedom with an additional dark scalar and dark fermion, the fixed point values are

$$\begin{aligned}
\Lambda_* &= -6.52, & G_* &= 4.55, & m_{v(d)*}^2 &= 1.6 \times 10^{-3}, \\
y_{v(d)*} &= 0.37, & \xi_{v(d)*} &= -2.7 \times 10^{-2}, \\
\lambda_{v(d)*} &= 6.5 \times 10^{-2}, & \lambda_{\text{HP}*} &= -8.5 \times 10^{-3}.
\end{aligned} \tag{6.8}$$

Only the two gravitational couplings and the scalar masses are relevant. All seven marginal couplings in the second and third line are irrelevant.

If we vary the gravitational fixed point values and only solve the matter beta functions, then the fixed point values in the matter sector change, cf. Fig. 6.1. The portal coupling changes sign for $\Lambda_* \approx -7$. We confirmed that even in the region of negative portal coupling the criterion $\lambda_v\lambda_d - \lambda_{\text{HP}}^2 > 0$ for global stability of the scalar potential
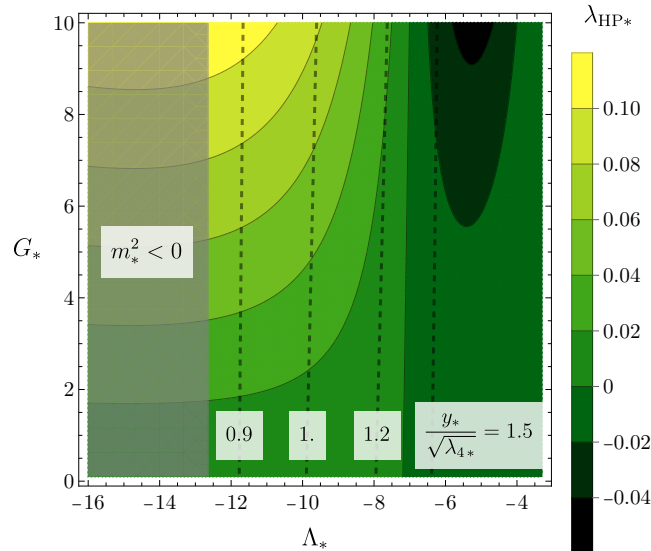
Fig. 6.1.: Value of the fixed point portal coupling $\lambda_{\mathrm{HP}*}$ as a function of the gravitational fixed point couplings. The dashed contours indicate the ratio of dark fermion and dark scalar mass.

is fulfilled. For $\Lambda_* < -12.6$, the fixed point lies at $m^2_{v(d)} < 0$ and hence in the symmetry-broken regime, see also comments on a similar region in the Yukawa system in Sec. 4.4.2. In this case an extended truncation is needed to obtain quantitatively reliable results.

The hierarchy of masses between the scalar and the fermion is determined by the fixed point. At the fixed point the ratio $y_{d*}/\sqrt{\lambda_{d*}}$ is larger(smaller) than one as long as $\Lambda_* \gtrsim -10 (\Lambda_* < -10)$. We compute this ratio at the fixed point. Both couplings are marginal and only flow logarithmically between the fixed point and the IR. Hence, the fixed point ratio can indicate the resulting IR ratio. The IR ratio equals the ratio of the dark fermion mass and the dark scalar mass. Depending on the fixed point ratio, in the IR either the dark scalar or the dark fermion might be the lightest particle.

In order to obtain the fixed point (6.8) we relied on a truncation based on canonical power counting and assumed that the fixed point is near-perturbative. To check this assumption we compare the critical exponents to their canonical values. We compute the quantity

$$\Delta_\theta = \sqrt{\frac{\sum_i (\mathrm{Re}\,\theta_i - d_{g_i})}{\sum_i}} \tag{6.9}$$

that relates the ith critical exponent θ_i to its canonical value given by the mass dimension d_{g_i}. We sum over all matter couplings. At both, the Gaussian, and the interacting matter fixed point the deviations from canonical scaling remain small, cf. Fig. 6.2. The small deviations from canonical scaling indicate that the matter sector remains near-perturbative, and indeed canonical power counting can guide setting up a truncation. Our treatment hence is self-consistent.
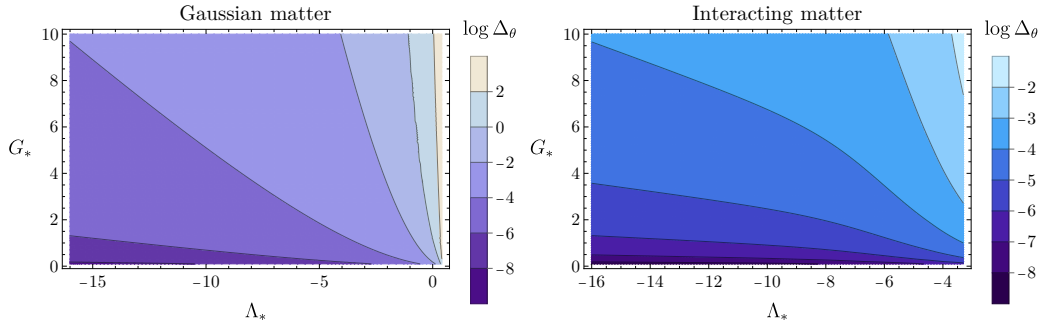
Fig. 6.2.: Deviation of the critical exponents from their canonical values Δ_θ for the Gaussian (interacting) matter fixed point on the left (right). The deviation remains small for large parts of the gravitational parameter space.
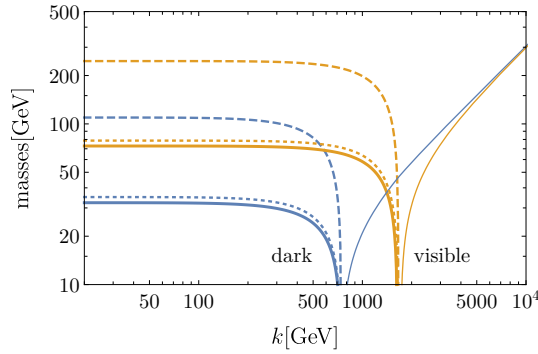
Fig. 6.3.: Masses of the visible and dark scalar (solid), visible and dark fermion (dotted) and the corresponding vacuum expectation value (dashed). We show a representative trajectory to illustrate how all quantities freeze out in the IR. For k larger than the symmetry breaking scale, i.e. in the symmetric regime, we only plot the scalar masses.

6.3.2 Flow Towards the Infrared

The interacting fixed point provides the initial condition at a scale $k_{\mathrm{UV}} \gg M_{\mathrm{Pl}}$. All marginal couplings are irrelevant and set to their fixed point value. The two scalar masses $m_{v(d)}^2$ are relevant. We perturb their values at k_{UV}. We then flow until $k = M_{\mathrm{Pl}}$. Between k_{UV} and M_{Pl} we set the gravitational couplings to their fixed point values. Below M_{Pl} we set the gravitational couplings to zero. This simple approximation amounts to setting $g = g_* \Theta(k/M_{\mathrm{Pl}} - 1)$, with $\Theta(x)$ the Heaviside distribution. It models the rapid decoupling of gravitational fluctuations around the Planck scale. Below the Planck scale the matter couplings evolve according to the pure matter beta functions. For k much smaller than all masses the RG flow freezes out and all fluctuations decouple, cf. Fig. 6.3.

Varying the perturbations in $m_{v(d)}^2$ at k_{UV} also varies the resulting RG flow and varies the resulting IR scalar potential. We directly control the perturbation at k_{UV}, and hence indirectly control the IR scalar potential. The SM potential features a symmetry-breaking minimum. In analogy, we adjust the IR scalar potential such that ϕ_v has a symmetry-breaking minimum $\langle \phi_v \rangle = v_v$. Further, we adjust the IR scalar potential such that ϕ_d has a symmetry-breaking minimum $\langle \phi_d \rangle = v_d$. If ϕ_d would not undergo spontaneous-symmetry breaking, then ϕ_d particles could decay to ψ_d particles. The

latter would remain massless and might provoke a tension with bounds on relativistic degrees of freedom during big bang nucleosynthesis [335, 336].

Both scalars acquire a vacuum expectation value. The IR scalar potential can then conveniently be expressed as

$$V(\phi_v, \phi_d) = \frac{\lambda_v}{8} \left(\phi_v^2 - v_v^2 \right)^2 + \frac{\lambda_d}{8} \left(\phi_d^2 - v_d^2 \right)^2 + \frac{\lambda_{\text{HP}}}{4} \left(\phi_v^2 - v_v^2 \right) \left(\phi_d^2 - v_d^2 \right). \quad (6.10)$$

The two propagating degrees of freedom correspond to eigendirections of the Hessian in field space. They mix the scalars ϕ_v and ϕ_d with a mixing angle [326, 337]

$$\tan(2\alpha) = \frac{-2 v_v v_d \lambda_{\text{HP}}}{\lambda_v v_v^2 - \lambda_d v_d^2} \quad (6.11)$$

and have masses

$$M_{V/D}^2 = \frac{1}{2} \left(\lambda_v v_v^2 + \lambda_d v_d^2 \pm \sqrt{(\lambda_v v_v^2 - \lambda_d v_d^2)^2 + 4\lambda_{\text{HP}}^2 v_v^2 v_d^2} \right). \quad (6.12)$$

Additionally, the two fermions acquire masses

$$M_{\psi_{v(d)}} = y_{v(d)} v_{v(d)}, \quad (6.13)$$

via their Yukawa couplings to $\phi_{v(d)}$. The spontaneous symmetry breaking for the field $\phi_{v(d)}$ occurs at energy scales k_{SSB} similar to the vacuum expectation value of the corresponding field, cf. Fig. 6.3.

By adjusting the perturbations at k_{UV} we can adjust the vacuum expectation values for both scalars. In the visible sector, we adjust the perturbation such that $v_v \approx 246\,\text{GeV}$. In the dark sector, we can adjust the dark vacuum expectation value freely. The dark vacuum expectation value then determines all marginal couplings. It also determines the dark scalar mass. We choose to express the resulting relations as a function of the dark scalar mass instead of the dark vacuum expectation value.

The relation between the dark scalar mass and various marginal couplings is illustrated in Fig. 6.4. The relation remains qualitatively stable, and varies mildly quantitatively, if one varies the gravitational fixed point values, cf. Fig. 6.4. The dark scalar mass determines all seven marginal couplings in the matter sector.

In an effective field theory all seven marginal couplings would be free. By fixing the marginal couplings, the asymptotically safe UV completion shrinks the toy model parameter space dramatically and strongly enhances predictivity. The same enhancement of predictivity might occur in a model that features all SM degrees of freedom. In such an extended model the portal coupling would be fixed as a function of the dark scalar mass. This might allow to compute the dark matter relic density as a function of the dark scalar mass. We explore this possibility in the next section.

6.3.3 Towards Phenomenological Implications: Dark Matter

Our toy model illustrates qualitatively how asymptotically safe quantum gravity enhances predictivity in a dark-matter model. The enhanced predictivity might
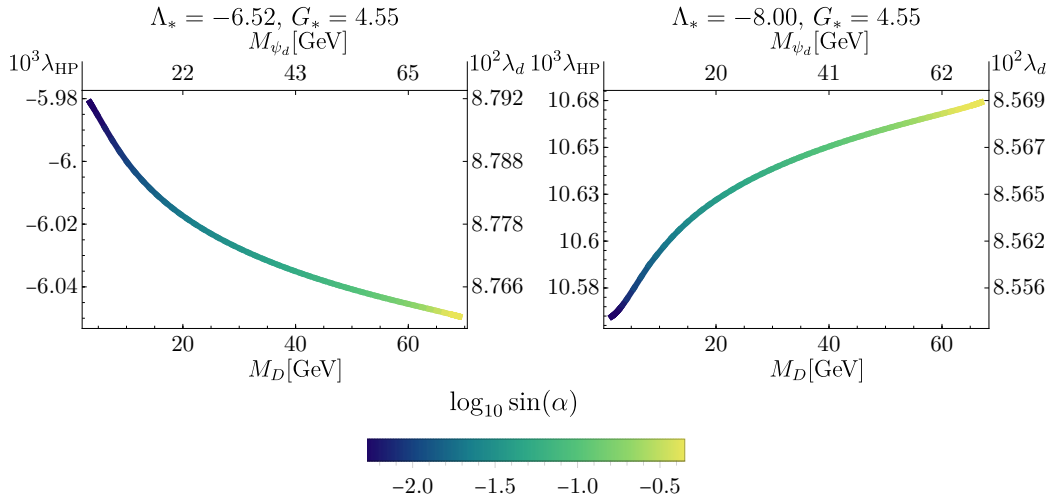
Fig. 6.4.: Resulting infrared relation between the dark scalar mass M_D and the portal coupling λ_{HP} for various values of the gravitational couplings. The right-hand and top axis provide reference values for the resulting dark quartic coupling and fermion mass, the color-coding encodes the mixing angle. The gravitational fixed point values in the left panel are obtained in an approximation in which one considers SM matter, a dark scalar and dark fermion, but neglects the backreaction of masses and non-minimal couplings on the fixed point. In the right panel the portal coupling is positive, the effect in $|\lambda_{\mathrm{HP}}|$ is qualitatively similar to the left panel.

ultimately allow computing how the dark scalar mass and the dark matter relic density are related. To illustrate the relation between dark scalar mass and relic density, we assume that an extension of our toy model to an SM setting exists. This extension consists of the SM extended by a dark scalar and a dark fermion. We assume that this extension produces the same fixed point values for the portal coupling and the dark sector couplings. Under these assumptions we compute the resulting dark matter relic density.

The discrete $\mathbb{Z}_2$ symmetry for the dark scalar is spontaneously broken. It hence decays to SM particles and dark fermions. On the contrary, the dark fermion is stable on cosmological time scales. It plays the role of the dark matter candidate.

The fermion's abundance is determined by the process $\bar{\psi}_d\psi_d \leftrightarrow \phi_d\phi_d$ freezing out. This process occurs with a temperature-dependent cross-section. One thermally averages over the cross-section. The thermally averaged cross-section then enters the right-hand side of the Boltzmann equation. The Boltzmann equation allows to compute the final abundance of dark fermions. The resulting abundance of dark fermions can be translated to a dark matter relic density. We perform these computations in App. D.

As a benchmark scenario we consider the values

$$m_{\psi_d} = 45.8\,\mathrm{GeV}, \qquad M_D = 41.3\,\mathrm{GeV}, \qquad y_D = 0.32,$$
$$v_D = 143.7\,\mathrm{GeV}, \qquad \lambda_{\mathrm{HP}} = -0.0077 \tag{6.14}$$

in the dark sector together with a realistic SM. The resulting relic density is $\Omega_{\mathrm{DM}}h^2 \approx 0.119$, see App. D. It lies in close vicinity to the measured value $\Omega_{\mathrm{DM}}h^2 = 0.1198 \pm 0.0012$ [10]. We caution that this result strongly depends on the precise coupling
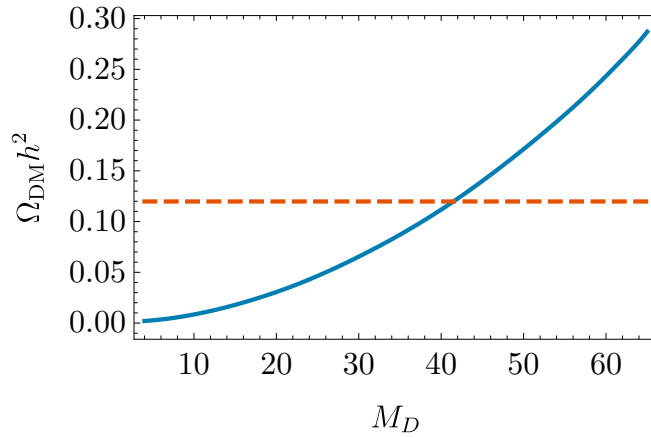
Fig. 6.5.: We show the resulting dark matter relic abundance $\Omega_{\text{DM}}h^2$ in a model that contains all SM particles, a dark scalar and a dark fermion assuming that our toy-model fixed point values set the coupling values in the dark sector. The dashed line indicates the value measured by the Planck collaboration [10].

values. These will change in an extension of our toy model to the full SM. The resulting relic density indicates that a more complete model might yield the correct dark matter abundance.

In reverse, one could use the dark matter abundance to fix the dark scalar mass and hence the only free parameter, see Fig. 6.5. To obtain this figure we computed the relic density for various sets of parameters along the curve in the left panel of Fig. 6.4. By adjusting M_D such that one obtains the observed value for $\Omega_{\text{DM}}h^2$ one can eliminate the last free parameter in the dark sector. One could then confront the realistic model with direct constraints [338–341] and indirect constraints [323], as well as constraints on invisible Higgs decays [337, 342–346].

6.3.4 Towards Phenomenological Implications: Higgs Mass

The additional dark sector also has implications on particle physics phenomenology. As discussed in Sec. 4.2.1, within a given model, asymptotic safety could determine the value of the quartic coupling at the Planck scale. This value sets the boundary condition for the sub-Planckian RG flow. The RG flow then determines the quartic coupling in the IR, and as a result predicts the Higgs mass, see Sec. 4.3.1. Assuming the current central values, within the SM this leads to a Higgs mass that is slightly larger than the measured value. We extended the SM by a Higgs portal to account for dark matter. In the following, we explore how the same extension also affects the Higgs sector and hence the resulting Higgs mass[3].

To capture the resulting effect on the Higgs mass with quantitative precision requires a computation with all SM degrees of freedom. Here, we instead explore the effect of adding the dark sector within our toy model.

---

[3]See Ref. [347] for a study of the purely scalar portal within the FRG, Ref. [348] for a study of a fermionic Higgs portal model and Refs. [230, 349] for studies of the Higgs mass in other beyond-SM scenarios within asymptotic safety.

Within our toy model the visible mass M_V differs from the Higgs mass in the SM, mostly because the top Yukawa coupling runs differently below the Planck scale in our toy model and the SM. Neglecting masses, in our toy model the beta function for the Yukawa coupling below the Planck scale is

$$\beta_{y_v} = \frac{5}{16\pi^2} y_v^3. \tag{6.15}$$

The Yukawa coupling decreases towards the IR. Within the SM, the gauge couplings contribute to the running of the top Yukawa coupling y_t

$$\beta_{y_t} = \frac{y_t}{16\pi^2} \left(\frac{9}{2} y_t^2 - \frac{85}{36} g_Y^2 - \frac{9}{4} g_2^2 - 8 g_3^2 \right). \tag{6.16}$$

Their contribution in β_{y_t} has a negative prefactor. They hence tend to increase the Yukawa coupling towards the IR. As a result the top Yukawa coupling in the SM increases from M_{Pl} to the infrared. The larger Yukawa coupling enters the beta function for the quartic Higgs coupling $\beta_{\lambda_H} \sim -y^4$. This contribution increases the quartic coupling towards the IR. The larger quartic coupling leads to a larger Higgs mass. Hence, the absence of gauge field fluctuations leads to a lower Higgs mass in our toy model.

We consider the following benchmark scenario: we again focus on the interacting fixed point. As above, we fix $v_v = 246$ GeV. We consider the case without a dark sector at $\Lambda_* = -6.52$ and G_* adjusted such that $y_* = 0.37$ remains constant. In this benchmark scenario the representative of the Higgs mass in our toy model is $M_V \approx 73$ GeV. The absolute magnitude of the "Higgs" mass hence is lower in our toy model. We expect that qualitative and semi-quantitative effects of adding the dark sector remain indicative of the corresponding effects in a (conjectured) extension of our model to the full SM. Under this assumption we explore the effect of adding the dark sector on the Higgs mass in the following. Extrapolating our results to the SM might allow drawing conclusions on the resulting Higgs mass in an extension of our toy model to the full SM.

In the following we neglect the running of couplings above the Planck scale. We assume that the initial conditions at the Planck scale are given by the fixed point values. Coupling the dark sector to the visible sector via the portal coupling has five effects on M_v that we also illustrate in Fig. 6.6:

(UV1) The presence of additional degrees of freedom will shift the gravitational fixed point values. This shift in the gravitational fixed point values also causes a shift in the matter fixed point values. The fixed point hence sets UV initial conditions depending on the matter degrees of freedom. This even holds in the case when the additional matter degrees of freedom are fully decoupled.

(UV2) The portal coupling contributes directly to β_{λ_v} with a contribution $\sim \lambda_{\mathrm{HP}}^2$. This contribution reduces the fixed point value λ_{v*}.

(UV3) The portal coupling contributes indirectly to β_{λ_v}. The portal coupling enters the beta functions for the visible mass and non-minimal coupling linearly and shifts
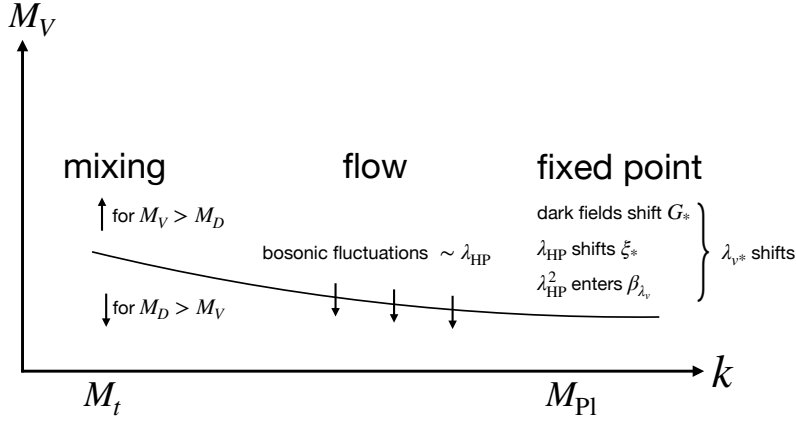
Fig. 6.6.: Sketch of the different effects that the addition of a dark sector has on the flow of the quartic coupling. A lower quartic coupling in the IR also corresponds to a lower visible scalar mass.

the corresponding fixed point values. These enter β_{λ_v} and shift the fixed point λ_{v*}. The resulting shift depends on the sign of λ_{HP}.

(F) At fixed value $\lambda_v(M_{\mathrm{Pl}})$ the presence of additional bosonic contributions in β_{λ_v} decreases the resulting quartic coupling along the flow. The quartic coupling is smaller in the IR and leads to a smaller Higgs mass (in the absence of mixing).

(IR) If $\langle\phi_d\rangle \neq 0$ the dark scalar mixes with the visible scalar ϕ_v. As a result of this tree-level effect, the visible mass M_v increases (decreases) for $M_V > M_D (M_V < M_D)$.

Effects (UV1)-(UV3) concern the Planck scale initial conditions for the RG flow. They are specific to the asymptotically safe scenario that we consider. While studying these effects we vary the gravitational fixed point values. We distinguish between two different scenarios:

- In a *gravitational scan* we vary the gravitational fixed point values freely and explore the resulting fixed point values in the matter sector. This implies that we vary the Yukawa coupling.

- In a *fixed-Yukawa scan* we vary the cosmological constant Λ_* and adjust G_* such that the Yukawa coupling $y_* = 0.37$ remains constant. The resulting scenarios feature approximately the same IR mass for the visible fermion.

Effects (F) and (IR) also occur in an EFT treatment. In the following, we explore how the various effects compare semi-quantitatively.

UV effects: Additional degrees of freedom shift the gravitational fixed point values according to (3.31). We show the dependence of λ_v on the gravitational fixed point values in Fig. 6.7. For reference, we also refer back to Fig. 6.1 that shows the contours for the portal coupling as a function of the gravitational fixed point couplings. As a result of the inclusion of the dark sector, the fixed point value of the quartic coupling
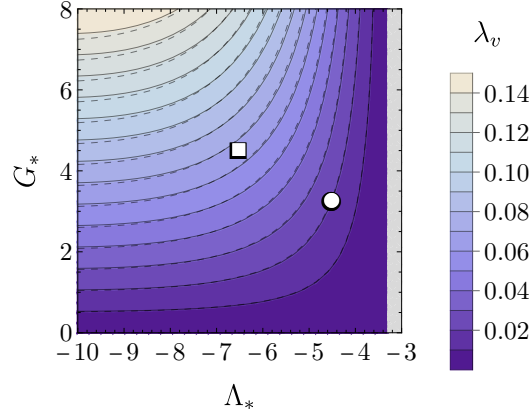
Fig. 6.7.: Contours for the fixed point value of the visible quartic coupling λ_v as a function of the gravitational fixed point values Λ_* and G_*. The circle (square) marks the position of the fixed point without (with) a dark sector, cf. Eq. (6.8).
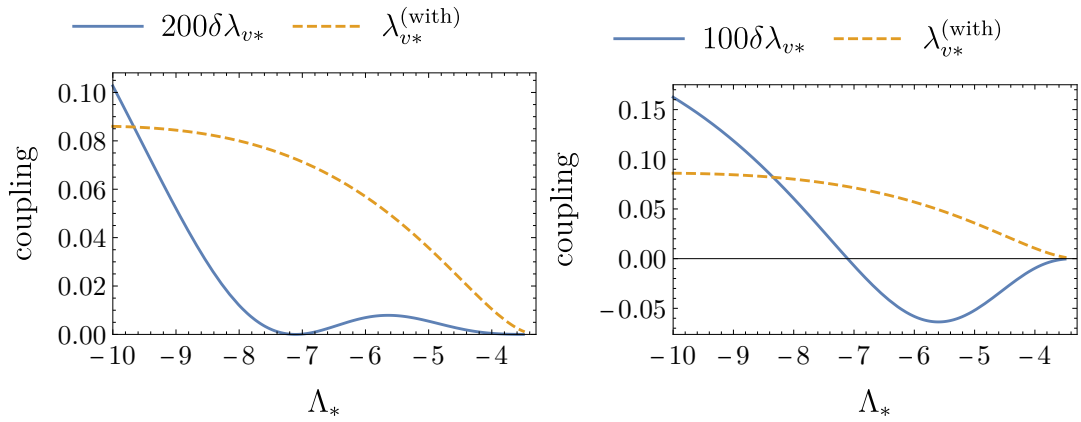
Fig. 6.8.: Difference $\delta\lambda_* = \lambda_{v*}^{\text{(without)}} - \lambda_{v*}^{\text{(with)}}$ in the fixed point value of the quartic coupling without and with a dark sector for varying cosmological constant Λ_* at fixed $G_* = 4.55$ in a gravitational scan.
(left) $\lambda_{v*}^{\text{(without)}}$ corresponds to the fixed point value obtained when setting $\lambda_{\text{HP}} = 0$ in β_{λ_v}. All other couplings remain at the same fixed value. The quartic coupling is always lowered. (right) $\lambda_{v*}^{\text{(without)}}$ corresponds to the fixed point value computed by solving all matter beta functions. As long as $\lambda_{\text{HP}} < 0$ we also find $\delta\lambda_* < 0$.

shifts by almost a factor of two in our simple approximation. This large shift highlights why we vary the gravitational fixed point values: even small shifts in these values can lead to very different phenomenology in the matter sector that we explore by varying Λ_* and G_*.

Even when Λ_* and G_* remain constant, β_{λ_v} changes when the dark sector is included. As a result λ_{v*} also changes. First, β_{λ_v} has a direct contribution $\sim \lambda_{\text{HP}}^2$ that comes with a positive sign. The contribution $\sim \lambda_{\text{HP}}^2$ and the fermionic contribution $-y_v^4$ in β_{λ_v} compensate. The fixed point value λ_{v*} is lowered. The resulting shift in λ_{v*} is small because $\lambda_{\text{HP}} \ll \lambda_v$ in most of the gravitational parameter space, see left panel of Fig. 6.8.

Second, there are indirect contributions. These depend on the sign of λ_{HP}. The Higgs portal coupling contributes linearly to the beta function of the mass m_v^2 and
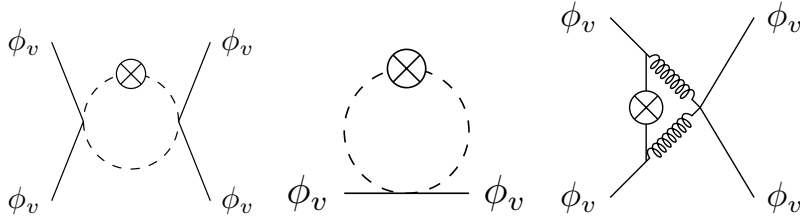
Fig. 6.9.: The left diagram displays the direct contribution of the portal coupling to β_{λ_v}. It is quadratic in the portal coupling λ_{HP}^2. Additionally, indirect contributions odd in λ_{HP} arise: the middle diagram induces a linear dependence of $m_{v(d)}^2$ and $\xi_{v(d)}$ on the portal coupling λ_{HP}. These couplings in turn enter at odd order into β_{HP}. One corresponding contribution is depicted in the right diagram. A solid (dashed) line represents the visible (dark) scalar, curly lines represent gravitons. We have displayed one possible regulator insertion, the regulator can also be inserted on any of the other internal lines in these diagrams.
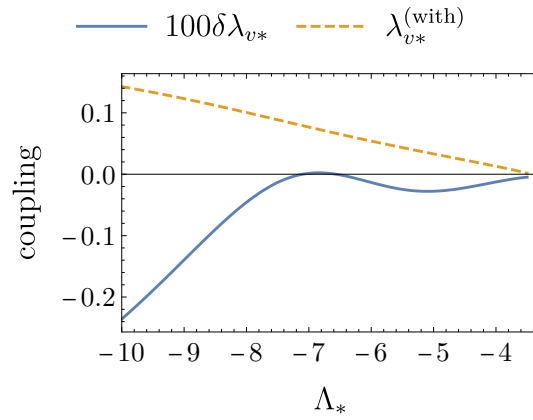
Fig. 6.10.: We perform a fixed-Yukawa scan by varying Λ_* and adjusting G_* such that $y_* = 0.37$. We plot $\delta\lambda_* = \lambda_{v*}^{(\mathrm{without})} - \lambda_{v*}^{(\mathrm{with})}$ where $\lambda_{v*}^{(\mathrm{without})}$ corresponds to the fixed point value computed by solving all matter beta functions.

the non-minimal couplings ξ_v. These quantities enter the beta function β_{λ_v} with both, even and odd powers, cf. Fig. 6.9. As a result, the quartic coupling increases when $\lambda_{\mathrm{HP}} < 0$, see right panel of Fig. 6.8. Both effects are numerically small.

In addition to the gravitational scan, we also perform a fixed-Yukawa scan in Fig. 6.10. In such a scan the IR fermion mass remains approximately constant. For fixed Yukawa coupling, the fixed point value for the quartic coupling becomes larger almost everywhere in the presence of the dark sector. For $\Lambda_* > -6.5$ this happens due to the odd contributions of λ_{HP} in β_{λ_v} (see above), for $\Lambda_* < -6.5$ the Newton constant G_* is larger for fixed y_* in the presence of the dark sector. The larger value of G_* leads to a larger λ_{v*}.

Direct and indirect effects mostly remain at the sub-percent level. As a result the overall shift is small. The only numerically relevant change in the quartic coupling in the UV happens due to a shift in the gravitational fixed point values.

Effects along the flow: The fixed point sets initial conditions in the far UV, and (by our simplifying assumption) at the Planck scale. Using these initial conditions, we
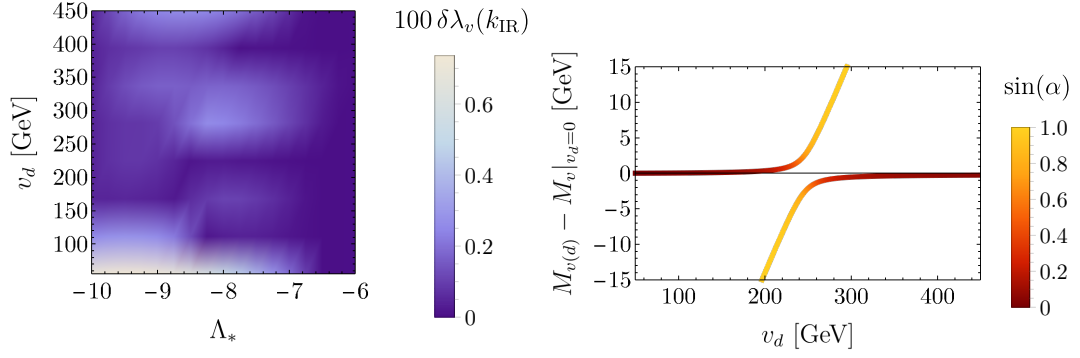
Fig. 6.11.: Left panel: We perform a fixed-Yukawa scan by varying Λ_* and adjusting G_* such that $y_* = 0.37$. We then show the IR difference $\delta\lambda_v(k_{\mathrm{IR}}) = \lambda_v^{(\mathrm{without})}(k_{\mathrm{IR}}) - \lambda_v^{(\mathrm{with})}(k_{\mathrm{IR}})$ in the quartic coupling for identical Planck-scale initial conditions with and without portal terms in β_{λ_v}.

Right panel: We show the visible and dark mass as a function of the dark vacuum expectation value $\langle\phi_d\rangle = v_d$ for fiducial values $\lambda_v = \lambda_d = 8.8 \cdot 10^{-2}, \lambda_{\mathrm{HP}} = -6.2 \cdot 10^{-3}$. The mixing angle is color coded.

integrate the beta functions towards the IR. The beta function for the quartic coupling β_{λ_v} receives a contribution $\sim \lambda_{\mathrm{HP}}^2$ from the portal coupling [321, 350, 351]. The integrated effect of such a contribution to the quartic coupling in the infrared is negative. In the left panel of Fig. 6.11 we keep the UV values for all couplings constant and compare the IR values for the quartic coupling with and without portal contributions in the flow. As $|\lambda_{\mathrm{HP}}| \ll 1$ the resulting effect is small throughout the relevant parameter region.

Effect in the IR: In the infrared we distinguish two scenarios. If $\langle\phi_d\rangle = 0$, then the dark scalar does not affect the visible mass beyond the effects already discussed. If $\langle\phi_d\rangle \neq 0$, then the two scalars mix with the mixing angle (6.11). The resulting masses are given in (6.12), see also the right panel of Fig. 6.11. The two corresponding eigenvalues repel each other. This repulsion decreases the mass of the lighter scalar and increases the one of the heavier scalar. To lower the Higgs mass one requires $M_V < M_D$ in this scenario.

Interestingly, even in the limit $M_V \ll M_D$, the dark scalar contributes [352–354]. In the limit of slowly varying fields one can solve the equation of motion for ϕ_d and substitute it back into potential. As a result one obtains the potential

$$V(\phi_v) = \frac{\lambda_v - \frac{\lambda_{\mathrm{HP}}^2}{\lambda_d}}{8}\left(\phi_v^2 - v_v^2\right)^2. \tag{6.17}$$

This amounts to a redefinition of the quartic coupling $\tilde{\lambda}_v = \lambda_v - \lambda_{\mathrm{HP}}^2/\lambda_d$.

The shift in the quartic coupling remains finite even in the limit of large M_D as (i) the propagator decays as $\sim 1/M_D^2$ and (ii) the vertices increase as v_d. For some tree-level diagrams the scaling in powers of v_d compensates and one remains with a finite contribution even in the limit $M_D \to \infty$.

Putting all UV, flow and IR effects together, we distinguish two scenarios:
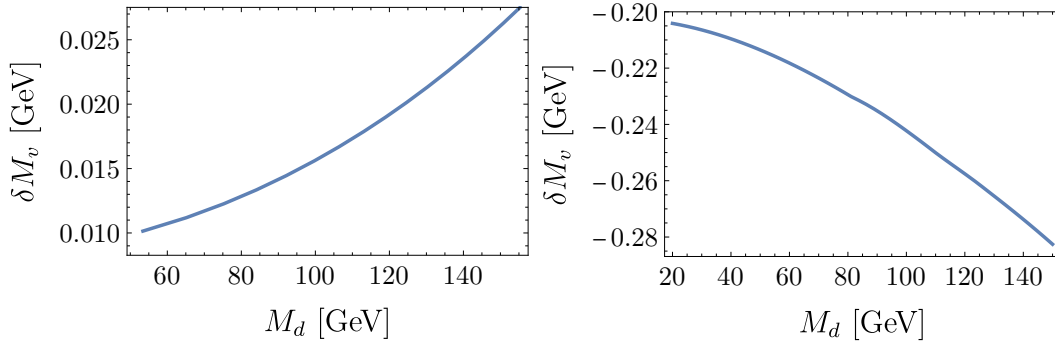
Fig. 6.12.: Change in the visible mass (6.18) with and without a dark sector in the case $\langle\phi_d\rangle = 0$. We set the cosmological constant to $\Lambda_* = -10$ ($\Lambda_* = -6.52$) in the left (right) panel. We perform a fixed-Yukawa scan, i.e. we adjust the Newton constant such that $y_* = 0.37$. Notice that for the two different values of Λ_* the sign of the portal coupling differs.

First, we consider the case in which the dark scalar does not undergo spontaneous symmetry breaking, $\langle\phi_d\rangle = 0$. The change in the visible mass

$$\delta M_v = M_v\Big|^{\text{(without)}} - M_v\Big|^{\text{(with)}} \tag{6.18}$$

with and without the dark sector is small and depends on the sign of $\lambda_{\text{HP}*}$, see Fig. 6.12. This is a consequence of the small absolute value of the portal coupling $|\lambda_{\text{HP}}| \sim 10^{-3}$. For small $|\lambda_{\text{HP}}|$ the effects (UV2), (UV3) and (F) are small, the effect (IR) does not apply. Up to shifts in the gravitational fixed point values the resulting change in the visible mass remains small.

Second, we consider the case in which the dark scalar undergoes spontaneous symmetry breaking and acquires a vacuum expectation value $\langle\phi_d\rangle \neq 0$. The effects (UV2), (UV3) and (F) again do not lead to a substantial shift in the Higgs mass, they are comparable to the previous case. However, effect (IR) is sizable: the tree-level mixing between the two scalars substantially modifies the resulting visible mass, see Fig. 6.13. For $M_D > M_V$ the visible mass is lowered substantially. A lowering of the visible mass by $\sim 7\,\text{GeV}$ ($\sim 1\,\text{GeV}$) implies a mixing angle of $\sin\alpha \approx 0.3$ at $\Lambda_* = -10.0$ ($\Lambda_* = -6.5$). We again caution that these are just toy model numbers. Extrapolating our results to the SM, they indicate that in order to substantially lower the SM Higgs mass one would require a dark scalar in the broken phase that is slightly heavier than the SM Higgs.

Adjusting the Higgs mass to the measured value fixes the dark scalar mass, i.e. the single free parameter in the model. The resulting model again does not violate bounds on the number of additional degrees of freedom during Big Bang nucleosynthesis [335, 336] as the dark fermion acquires a mass. The fermion's mass is fixed. A simple estimate similar to the one in the last section indicates that the resulting relic density might be too large by about one order of magnitude. Going beyond our toy model this raises the intriguing question whether an extension to the full SM has the potential to (i) predict the correct Higgs mass by adding a dark scalar and a dark Dirac fermion and (ii) provide a dark matter candidate with the correct relic density at the same time.
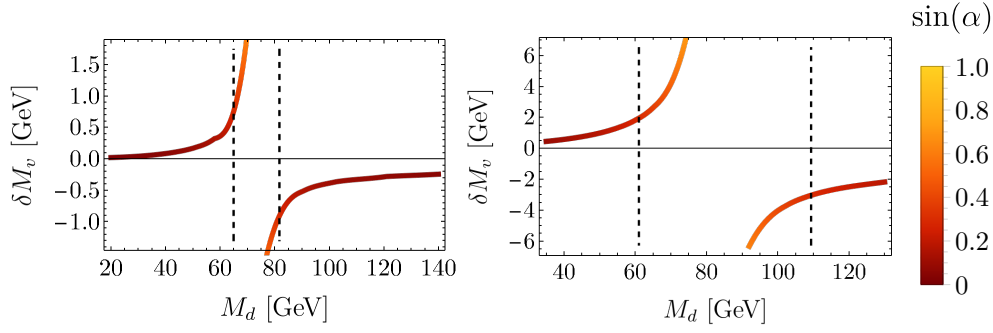
Fig. 6.13.: Shift of the visible scalar mass under the inclusion of a dark sector for varying dark mass in the case $\langle\phi_d\rangle \neq 0$. In both panels we keep $y = 0.37$ fixed by varying G_*, i.e. we perform a fixed-Yukawa scan. The left (right) panel corresponds to $\Lambda_* = -10$ ($\Lambda_* = -6.5$). The mixing angle is color-coded, the vertical lines mark the value $|\sin(\alpha)| = 0.3$.

6.4 Beyond Thermal Production

Finally, we explore non-thermally produced dark matter. In the standard dark matter scenario the dark and the visible sector are in thermal equilibrium at large temperatures and visible and dark particles constantly annihilate into each other. When the temperature decreases, the thermally averaged cross-section declines and the corresponding annihilation freezes out. The dark sector decouples. To maintain thermal equilibrium a sizable cross-section, and hence sizable couplings, are required.

We consider the toy-model of Sec. 6.2, that features a dark sector consisting of a single scalar ϕ_d (and no dark fermion). Within an asymptotically safe realization of this toy model the portal coupling is far too small to maintain thermal equilibrium between the visible and the dark sector long enough to produce the correct abundance, see Sec. 6.2. The correct dark matter abundance is not produced thermally. Instead, it might be produced non-thermally. This requires a non-thermal production mechanism. As one example, we discuss feebly interacting dark matter [355, 356].

In this scenario, the dark sector couples very weakly to the SM. The dark and the visible sector are never in thermal equilibrium. Instead, the thermal history proceeds as follows: by assumption early in the radiation dominated phase, the energy density is dominated by the visible sector. The dark sector is not populated[4]. Dark particles are then generated due to annihilations of SM particles. The dark matter fraction increases. This increase continues until the temperature falls below a critical value. Below the critical value, the density of annihilating SM particles is thermally suppressed. The annihilations cease and the comoving dark matter density remains approximately constant. It only reduces due to rare annihilations of the dark particle to SM particles.

In the following, we explore if such a scenario is viable within asymptotic safety. We consider the Higgs-top toy model extended by a single dark scalar and hence consider the effective action (6.4) without the fermion ψ_d. The resulting set of beta functions exhibits two fixed points, one that is non-interacting in the visible sector and one that

---

[4]This situation could for example arise if the inflaton only decays to visible matter.

is interacting in the visible sector. Both fixed points are non-interacting in the dark sector. We exclusively focus on the fixed point that is interacting in the visible sector and non-interacting in the dark sector. The resulting combined fixed point lies at

$$\Lambda = -11.62, \qquad G_* = 9.02, \qquad m_v^2 = 0.00022,$$
$$\lambda_v = 0.17, \qquad y = 0.38, \qquad \xi_v = -0.044, \qquad (6.19)$$

and vanishing portal coupling and dark-sector couplings. It has critical exponents

$$\theta_1 = 3.98, \qquad \theta_2 = 1.99, \qquad \theta_3 = 1.97,$$
$$\theta_4 = 1.91, \qquad \theta_{5/6} = -0.010 \pm 0.011i, \qquad \theta_7 = -0.016,$$
$$\theta_8 = -0.036, \qquad \theta_9 = -0.039. \qquad (6.20)$$

The fixed point combines the interacting Yukawa fixed point in the visible sector, discussed in Sec. 4.2.2, and the non-interacting purely scalar fixed point in the dark sector, discussed in Sec. 4.2.1.

Similar to fixed point (6.8), this fixed point only exhibits two relevant directions in the matter sector: only the two scalar masses are relevant. All marginal matter couplings are predicted.

The non-vanishing Yukawa coupling breaks shift symmetry in the visible sector. In the dark sector shift symmetry is broken by the dark mass m_d^2. The dark mass is relevant at the UV fixed point and generated along the RG flow. It will induce all shift-symmetry violating couplings along the flow, in particular the portal coupling. The resulting coupling values are far too small to lead to thermal production. They might however allow for a feebly interacting Higgs portal.

We again initialize the flow at $k_{\mathrm{UV}} \gg M_{\mathrm{Pl}}$. The initial conditions for all couplings are given by the fixed point (6.19). We perturb the initial conditions for the relevant couplings, i.e. for the two masses. We again assume that the gravitational degrees of freedom decouple instantaneously, see the discussion in Sec. 6.3.2.

Adjusting the perturbations in the relevant couplings at k_{UV} allows to adjust the IR scalar potential. We adjust the perturbation in m_v^2 such that the visible scalar undergoes spontaneous symmetry breaking. Due to the associated technical complexity we do not solve the flow in the symmetry-broken phase and do not extract the resulting vacuum expectation value. Instead, we evaluate the flow at the symmetry breaking scale k_{SSB}, defined by $m_v^2(k_{\mathrm{SSB}}) = 0$. The symmetry breaking scale approximately coincides with the vacuum expectation value, $k_{\mathrm{SSB}} \approx v_v$, cf. Fig. 6.3. Inspired by the SM, we adjust the symmetry breaking scale to $k_{\mathrm{SSB}} \approx 246$ GeV.

We adjust the perturbation in m_d^2 such that the dark scalar does *not* undergo spontaneous symmetry breaking. Instead, adjusting this perturbation allows us to vary the resulting IR value $m_d^2(k_{\mathrm{SSB}})$. The value of m_d^2 then determines all marginal couplings in the matter sector as these are irrelevant. We focus on the resulting relation between the dark mass $m_d^2(k_{\mathrm{SSB}})$ and the portal coupling $\lambda_{\mathrm{HP}}(k_{\mathrm{SSB}})$ evaluated at the scale $k = k_{\mathrm{SSB}} \approx 246$ GeV. For vanishing mass, $m_d^2 = 0$, the portal coupling vanishes exactly, $\lambda_{\mathrm{HP}} = 0$. For small mass (with respect to the Planck scale) the portal coupling can be
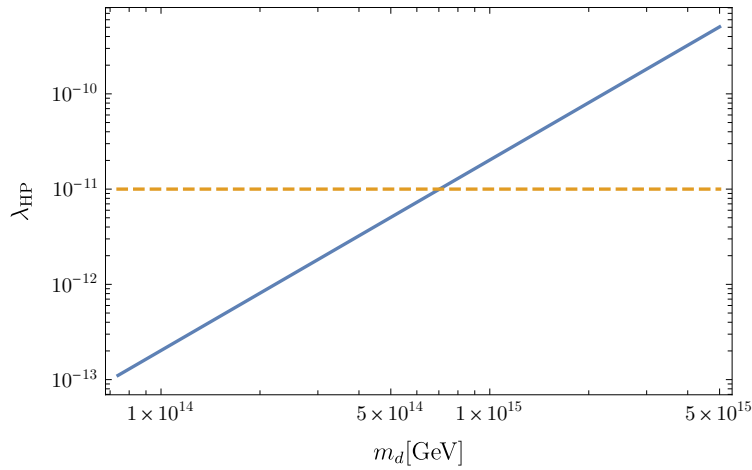
Fig. 6.14.: Relation between dark scalar mass m_d and the Higgs portal coupling λ_{HP} evaluated at $k_{\mathrm{SSB}} = 246\,\mathrm{GeV}$. The horizontal dashed line marks the phenomenologically relevant value $\lambda_{\mathrm{HP}} = 10^{-11}$.

expanded, $\lambda_{\mathrm{HP}} \approx \lambda_{\mathrm{HP,0}} \left(\frac{m_d^2}{M_{\mathrm{Pl}}^2} \right)$, where we chose the Planck scale as a reference scale. The relation between dark mass m_d^2 and portal coupling λ_{HP} hence is approximately linear for small $\frac{m_d^2}{M_{\mathrm{Pl}}^2}$, see also Fig. 6.14. We confirm this expectation and determine the prefactor $\lambda_{\mathrm{HP,\,0}}$ by numerically solving the flow for a range of starting values down to $k = k_{\mathrm{SSB}}$.

In an extension of our toy model to the full SM, the resulting relation will change. We do not expect changes by orders of magnitude. The relation's magnitude can hence be compared to observational constraints.

A feebly interacting Higgs portal coupling of order $\lambda_{\mathrm{HP}} \sim 10^{-11}$ produces the correct dark matter relic density [357, 358]. This value is independent of the mass: in the freeze-in scenario the dark-particle mass sets the temperature at which dark matter is not produced in large amounts any longer. Heavier particles freeze in earlier (the corresponding final yield scales as $Y \sim \lambda_{\mathrm{HP}}^2 M_{\mathrm{Pl}}/T \sim \lambda_{\mathrm{HP}}^2 M_{\mathrm{Pl}}/m_d$), but each particle also contributes more mass to the final dark matter density. These two effects compensate, and the dark matter abundance is independent of the dark scalar mass over a large range of scales [355].

We combine the phenomenological value $\lambda_{\mathrm{HP}} \sim 10^{-11}$ with the relation from Fig. 6.14, given by asymptotically safe quantum gravity. Within our model a portal coupling $\lambda_{\mathrm{HP}} \sim 10^{-11}$ implies a mass of $m_d \approx 7 \cdot 10^{14}\mathrm{GeV}$ for the dark scalar. Creating two dark scalars in an annihilation hence requires two particles with a combined energy of $\approx 10^{15}\mathrm{GeV}$. In a very naive estimate, the annihilating particles, and hence the SM plasma, needs to be present at $T \approx 10^{15}\mathrm{GeV}$ [355]. Within an inflationary setting, the SM plasma is generated during reheating. The reheating temperature hence needs to be larger than $T \approx 10^{15}\mathrm{GeV}$. Such high reheating temperatures are only realized in some inflationary scenarios [359, 360]. Whether this scenario can be realized hence depends on the specific assumptions about inflation.

Let us point out two simplifying assumptions. First, for large enough dark sector self interactions, the dark sector can thermalize, leading to a modified phenomenology [361]. Given the irrelevance of λ_d at the fixed point $\lambda_{d*} = 0$ it is unlikely that such self interactions will occur in an asymptotically safe model. Second, higher-order operators alter the observational value of λ_{HP} [362, 363]. In particular, gravitational tree level effects might raise the required coupling value [363]. For more quantitative conclusions extended studies are required.

Our simple estimate indicates that in an asymptotically safe portal model, for generic dark scalar masses $< 10^{14}$ GeV, the freeze-in scenario does not produce enough dark matter. This result further motivates extensions in the dark sector such as the one presented in Sec. 6.3. It also illustrates how, more generally, asymptotic safety constrains phenomenological models. Asymptotic safety might not only reduce the parameter space within one model relevant for experimental searches. It might also shrink the parameter space for some models far enough to fully rule them out.

6.5 Conclusions: A Highly Predictive Dark-Matter Model

We have illustrated that the Higgs portal coupling to a dark scalar vanishes at a fixed point within our approximation, strengthening the result of Ref. [175] by also including non-minimal couplings. As a result the dark sector nearly decouples. The small portal coupling might enable non-thermal production via the freeze-in mechanism, however this requires further assumptions about the cosmological history.

To obtain a model that allows for thermal production of dark matter we introduce a Dirac fermion in the dark sector. The Yukawa coupling to the dark scalar breaks shift symmetry and allows to generate a non-vanishing portal. The resulting model is highly predictive, it only features one free parameter in the dark sector.

The phenomenology in a conjectured extension of our (Euclidean) toy-model to the full SM is highly predictive: First, the model might yield the correct relic density of dark matter. Second, it might lower the Higgs mass by a few GeV via a tree-level mixing effect. Both these effects happen when the dark sector undergoes spontaneous symmetry breaking and at masses for the dark scalar that lie within an order of magnitude of the Higgs mass. Investigating whether both effects can be realized at the same time would be highly interesting.

Asymptotic safety strongly constrains the resulting available parameter space for the portal model with an extended dark sector. After going into depth on this model, we investigate if similarly asymptotically safe gravity might constrain a broader class of models.

7

Discrete Symmetries in Asymptotic Safety

Asymptotic safety could allow to constrain the parameter space within a given SM extension. Infinitely many of such extensions exist. In this chapter, we explore how asymptotic safety might constrain the space of possible SM extensions and in particular the set of possible symmetries of SM extensions.

This is motivated by a simple observation. While in condensed matter physics all kinds of discrete symmetries play a role, on particle physics scales only continuous symmetries are observed. This begs the question if there is any mechanism that prevents discrete symmetries on a fundamental level. Indeed, Ref. [364] argued that in a string-inspired context spontaneously broken discrete symmetries are excluded. Here, we take first steps towards determining if discrete global symmetries can be realized in asymptotic safety.

We focus on the example of a global $\mathbb{Z}_n$ symmetry. Such a theory can be realized in two possible ways in the IR, see Sec. 4.1. First, a $\mathbb{Z}_n$ symmetry could be realized at an interacting UV fixed point. In this case it will generically be realized in the IR as well. Second, a $\mathbb{Z}_n$ symmetry might emerge along the RG flow towards the IR. In this case it does not need to be realized at the UV fixed point.

We study both scenarios for a complex scalar field φ. In the absence of interactions, a complex scalar field naturally is $U(1)$-symmetric. Additional interactions can break the $U(1)$ symmetry explicitly. In addition, the $U(1)$ symmetry can be spontaneously broken at a scale k_{SSB}. In the presence of both, spontaneous and explicit breaking, a hierarchy of scales can emerge [365], as we will investigate in more detail below.

7.1 A Scalar Model

We focus on a simple scalar model featuring a $\mathbb{Z}_n$ symmetry, where we impose $n > 2$. We introduce a complex scalar φ invariant under the $\mathbb{Z}_n$ symmetry and study the scale-dependent effective action

$$\Gamma_k^{\text{scal}} = \int \mathrm{d}^4x \sqrt{g} \left(Z_\varphi g^{\mu\nu} \partial_\mu \varphi^* \partial_\nu \varphi + V(\varphi, \varphi^*) \right), \tag{7.1}$$

with a potential

$$V(\varphi, \varphi^*) = V_{\text{U}(1)}(\varphi\varphi^*) + V_{\mathbb{Z}_n}(\varphi, \varphi^*), \tag{7.2}$$

that we split into a $U(1)$-symmetric part $V_{\text{U}(1)}$ and a $\mathbb{Z}_n$-symmetric part $V_{\mathbb{Z}_n}$.

To control the scalar potential we introduce an auxiliary fermion ψ. We already anticipate that the scalar potential $V_{\mathrm{U}(1)}$ will only feature a shift-symmetric fixed point. Breaking shift symmetry is possible via a Yukawa interaction, see Sec. 4.2.2. Additionally, fermionic fluctuations lower the mass parameter in the scalar potential towards the IR and hence trigger spontaneous symmetry breaking. We introduce an auxiliary Dirac fermion ψ with the scale-dependent effective action

$$\Gamma_k^{\mathrm{ferm}} = \int \mathrm{d}^4 x \, \sqrt{g} \left(i Z_\psi \bar{\psi} \slashed{\nabla} \psi + y(\varphi^* \bar{\psi}_R \psi_L - \varphi \bar{\psi}_L \psi_R) \right). \tag{7.3}$$

The fermion provides a valuable tool to manipulate the scalar potential, but it is not central to our results. In (7.3) ψ_L and ψ_R are the left- and right-handed part, $\psi = \psi_R + \psi_L$. For our conventions in the fermionic sector, see Refs. [366, 367].

We expand the $U(1)$ invariant part of the potential in terms of the invariant $(\varphi \varphi^*)$

$$V_{\mathrm{U}(1)} = \sum_{i=0}^{i_{\max}} \frac{\bar{\lambda}_{2i}}{i!} (\varphi \varphi^*)^i, \tag{7.4}$$

and the $\mathbb{Z}_n$ invariant part of the potential as [365, 368–373]

$$V_{\mathbb{Z}_n} = \bar{z}_n \left(\varphi^n + (\varphi^*)^n \right). \tag{7.5}$$

The dimensionless counterparts of the couplings $\bar{\lambda}_n, \bar{z}_n$ are defined as

$$\lambda_n = \bar{\lambda}_n k^{n-4} \quad z_n = \bar{z}_n k^{n-4}. \tag{7.6}$$

Applying the flow equation (3.21), we can compute the beta functions for all couplings in the effective action $\Gamma_k = \Gamma_k^{\mathrm{scal}} + \Gamma_k^{\mathrm{ferm}}$. We again take into account direct contributions from the anomalous dimension $\eta_\varphi = -\partial_t \log Z_\varphi$ and neglect those that arise from regulator derivatives. The resulting beta functions are given in App. F.4.

The beta function for z_n takes the form, see also Sec. 4.1.1,

$$\beta_{z_n} = -(4-n)z_n - f_s z_n + \mathrm{int.} \tag{7.7}$$

In this expression the last term symbolizes terms arising due to interactions. The term f_s encodes the effect of gravitational fluctuations. Gravitational fluctuations are "blind" to the symmetry structure of the coupling z_n. They predominantly contribute via the diagrams in Fig. 7.1[1]. The structure of these diagrams is independent of the number of external legs. Hence, the contribution f_s does not dependent on n.

Similarly, the beta function for the Yukawa coupling reads

$$\beta_y = \frac{1}{4\pi} y^3 - f_y y \tag{7.8}$$

where the cubic term is the universal one-loop result. The term f_y again parameterizes the impact of gravitational fluctuations.

---

[1]In the presence of masses or non-minimal couplings there will be additional diagrams. We neglect these diagrams here.

Fig. 7.1.: Feynman diagrams for the predominant gravitational contributions f_s to β_{z_n}. Dashed lines correspond to scalars φ, curly lines to gravitons. The regulator insertion (marked by a cross) can also occur on any other internal line. All three diagrams are assumed to have n external legs, as indicated by the dots.

Both, f_s and f_y depend on the gravitational fixed point values. The gravitational contribution f_s is smaller than zero. Gravitational fluctuations push scalar couplings towards irrelevance [68, 145, 169–178]. The gravitational contribution f_y can take both signs, depending on the value of Λ_*, cf. Sec. 4.2.2. Instead of varying the gravitational fixed point values, in the following we vary $f_s < 0$ and f_y. Doing so we explore how gravitational fluctuations might impact the fixed point structure.

We study whether the global $U(1)$ symmetry can be explicitly broken to a global $\mathbb{Z}_n$ symmetry. The $\mathbb{Z}_n$ symmetry is realized if $z_n \neq 0$. A non-vanishing coupling $z_n \neq 0$ can arise in two ways, see Sec. 4.1. Firstly, a fixed point can feature $z_n \neq 0$. This is the fixed-point-breaking scenario of Sec. 4.1. Secondly, Eq. (7.7) admits the Gaussian matter fixed point [2] $z_n = 0$ for all n. This fixed point ought to exist as it is protected by the global $U(1)$ symmetry and we neglect higher-order momentum dependent interactions. If at the Gaussian fixed point perturbations in z_n are relevant, then these perturbations grow towards the IR, and z_n does not vanish in the IR; $z_n \neq 0$. This is the RG-flow-breaking scenario of Sec. 4.1. In both cases $z_n \neq 0$ and the IR theory is $\mathbb{Z}_n$-symmetric.

To explore if either of the two cases is realized we will focus on the lowest order coupling z_n in the $\mathbb{Z}_n$-symmetric theory. The coupling z_n features the highest mass dimension. We expect that for z_n a balancing of the canonical term and interactions is most easily achieved. If there is an interacting fixed point in a near-perturbative regime we expect it to be realized in this coupling. If this coupling is non-vanishing, then it will induce all other $\mathbb{Z}_n$-symmetric couplings.

In the near-perturbative regime, the mass dimension allows approximating which couplings are (ir-)relevant. The mass dimension depends on n. For $n > 4$ the coupling z_n is irrelevant, for $n = 4$ it is marginal and for $n = 3$ it is relevant. In the following we will discuss these cases separately. In each case we first focus on a near-perturbative regime, allowing us to argue based on the canonical mass dimension of the corresponding operators. We then explore the non-perturbative regime.

7.1.1 The Case $n > 4$

We investigate the structure of possible terms in β_{z_n} for $n > 4$. Within the functional renormalization group, all contributions to β_{z_n} arise from diagrams that are structurally one-loop. Each vertex in a one-loop diagram is connected to at most two other

---

[2]Note this fixed point is non-interacting in the matter sector only. We assume that it is interacting in the gravity sector by allowing for non-vanishing f_s, f_y.

vertices by exactly two internal propagators. If we consider a diagram with two (or more) z_n vertices, then each of these vertices has $(n-2)$ external legs. The total diagram has at least $2(n-2)$ external legs. At the same time only diagrams with n external legs contribute to β_{z_n}. But for any $n > 4$ it holds that $2(n-2) > n$. There are no diagrams contributing to β_{z_n} that feature two z_n vertices. The beta function β_{z_n} only has direct contributions that are at most proportional to z_n.

We first focus on the near-perturbative regime with weak interactions in the matter sector. The linear coefficient in β_{z_n} is given by $-(d_{\bar{z}_n} + f_s)z_n$. Both, the mass dimension and f_s are negative. The coupling z_n is canonically irrelevant. The irrelevance of z_n is only enhanced by gravitational fluctuations. If we neglect higher-order interactions, the resulting beta function β_{z_n} will be proportional to z_n with a positive constant of proportionality, $\beta_{z_n} \sim z_n$. The beta function only features the Gaussian fixed point. At this fixed point z_n is always irrelevant. The coupling z_n vanishes at the fixed point and subsequently at all scales. Hence, in this approximation, an asymptotically safe theory does not feature a $\mathbb{Z}_n, n > 4$ symmetry in the UV and cannot generate one towards the IR.

In the fully non-perturbative regime the beta function β_{z_n} will remain linear in z_n, but two new types of terms appear: First, a z_n-independent term proportional to a coupling $z_{n,2}$ appears. It arises due to interactions of the form $z_{n,2}\varphi\varphi^*(\varphi^n + (\varphi^*)^n)$. Note that the beta function $\beta_{z_{n,2}}$ for such a coupling will contain contributions proportional to z_n. Second, the term linear in z_n is modified by a single diagram that generates a contribution $\sim \lambda_4 z_n$. This contribution remains positive as long as λ_4 is positive.

To exclude that the combined system of beta functions exhibits additional fixed points, we search for fixed points up to $n = 8$, always taking into account operators up to energy dimension $2n$. For all n apart from $n = 7$ we find additional zeros of the beta function. In Fig. 7.2 we show the average deviation from canonical scaling, cf. Eq. (6.9),

$$\Delta_\theta^2 = \frac{1}{N} \sum_i^N \left(\mathrm{Re}(\theta_i) - d_i \right)^2, \tag{7.9}$$

for each of these zeros. Here θ_i is the i-th critical exponent and d_i the corresponding canonical dimension. As evident from this figure, for $n > 4$ all zeros of the beta function are highly non-perturbative. The non-perturbative nature of these zeros renders our truncation insufficient to draw strong conclusions.

We hence find no indications that for $n > 4$ a fixed point exists in the fully non-perturbative regime. In the near-perturbative regime such a fixed point cannot exist. The coupling z_n stays irrelevant at the Gaussian fixed point.

Including gravity only enhances the irrelevance of the coupling z_n and only makes it more challenging to obtain an interacting fixed point, or rendering the coupling z_n at the Gaussian fixed point relevant. Including gravity hence makes it even more challenging to obtain a $\mathbb{Z}_n$-symmetric theory in the IR.
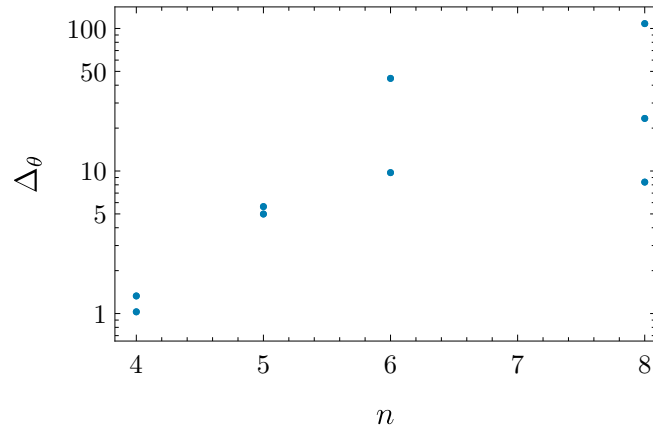
Fig. 7.2.: Deviation from canonical scaling Δ_θ for all zeros of the beta function at order n. The different dots correspond to different zeros. For $n = 7$ we do not find any real zero of the beta functions. For $n > 4$ the deviation from canonical scaling is large.

7.1.2 The Case $n = 4$

In the case $n = 4$, the highest order coupling z_4 is marginal. Within a truncation up to order $2n$ we find a zero of the beta function that features deviations from perturbativity $\Delta_\theta \sim \mathcal{O}(1)$, cf. Fig. 7.2. However, within a truncation up to order $3n = 12$, we do not find a corresponding fixed point. This indicates that the zero visible in Fig. 7.2 is spurious, and that no additional interacting fixed point exists.

At the Gaussian fixed point z_4 remains irrelevant. The beta function β_{z_4} reads

$$\beta_{z_4} = (2\eta_\varphi - f_s)z_4 + \frac{(6 - \eta_\varphi)\lambda_4 z_4}{8\pi^2(1 + \lambda_2)^3} - \frac{5(6 - \eta_\varphi)z_{4,2}}{96\pi^2(1 + \lambda_2)^2}. \tag{7.10}$$

For $f_s = 0$ and $\lambda_4 > 0$ the terms proportional to z_4 are positive, the coupling z_4 hence is irrelevant.

This effect is amplified by gravitational fluctuations. The coupling z_4 remains irrelevant at the Gaussian fixed point. $\mathbb{Z}_4$-symmetric interactions are hence not generated along the flow towards the IR. This indicates that a $\mathbb{Z}_4$ symmetry is excluded both, at a UV fixed point and in the IR.

7.1.3 The Case $n = 3$

At the Gaussian fixed point the critical exponent for z_3 is $\theta = 1 + f_s$. The critical exponent does not change sign, as long as gravitational fluctuations remain weak, $|f_s| < 1$. As a consequence, the coupling z_3 remains relevant at the Gaussian fixed point. Hence, a perturbation in z_3 can grow towards the IR. Correspondingly a $\mathbb{Z}_3$ symmetry in the IR is compatible with an asymptotically safe UV completion.

Additionally, we search for an interacting fixed point. The beta function for the coupling z_3 reads

$$\beta_{z_3} = -(1 + f_s)z_3 + \frac{27z_3^3}{16\pi^2(1 + \lambda_2)^4} + \frac{3z_3\lambda_4}{8\pi^2(1 + \lambda_2)^3}, \tag{7.11}$$

where we already substituted the expression for the anomalous dimension η_φ. The beta function β_{z_3} features terms cubic in z_3. These give rise to non-trivial zeros. These zeros in β_{z_3} are associated with large values of the quartic coupling and relatively large deviations from canonical scaling.

For $-0.4 < f_s < 0$, $f_y = 0$ multiple zeros with $z_3 \neq 0$ exists. The most promising one, at $f_s \approx -0.4$, has critical exponents $\theta_1 = 1.58$, $\theta_{2/3} = -0.54 \pm 1.58i$. For $f_s \lesssim 0.4$ this zero collides with another one. Both move into the complex plane. Notice that this zero even exist for $f_s = f_y = 0$, and hence in the absence of gravity.

In addition, for $f_s \approx -1$ the beta function features an additional zero. For $f_s = -0.995$, $f_y = 0.0025$ there is a zero

$$y_* = 0.23 \quad \lambda_{2*} = 0.007 \quad \lambda_{4*} = -0.01 \quad z_{3*} = 0.16. \tag{7.12}$$

This zero has critical exponents

$$\theta_1 = 1.0 \quad \theta_2 = -0.001 \quad \theta_3 = -0.008 \quad \theta_4 = -0.9, \tag{7.13}$$

and hence features deviations from canonical scaling that are $\sim \mathcal{O}(1)$. While this zero of the beta function only exists for a tiny range of values in f_s, its cause is generic. Gravitational contributions balance the canonical scaling of z_3 and allow for a zero in the beta function with $z_3 \neq 0$. We checked that this zero of the beta function persists under an extension of the truncation to order 6. Notice that in this truncation $\lambda_{4*} < 0$, signaling a potential instability.

Even if this zero in the matter sector is genuine, realizing this zero required us to finely tune the value for f_s. It is rather unlikely that this value is realized in a matter-gravity system. We hence refrain from going into more detail on this fixed point and just mention that the large number of irrelevant directions would make this fixed point highly predictive.

In summary, an interacting $\mathbb{Z}_3$-symmetric fixed point might exist. In addition, the coupling z_3 is relevant at its Gaussian fixed point. This provides two independent possibilities that (i) are compatible with an asymptotically safe theory in the UV and (ii) realize a $\mathbb{Z}_3$ symmetry in the IR.

7.1.4 Two Fields

Our results have been obtained in a one-field model. In a two field model it might be possible to weaken some of our results even for $n > 3$.

Consider a field φ charged with charge 1 under a fundamental global $\mathbb{Z}_6$ symmetry. For φ all arguments of Sec. 7.1.1 apply and the $\mathbb{Z}_6$ symmetry cannot be realized in the

IR. In addition, consider a field χ charged with charge 2 under the $\mathbb{Z}_6$ symmetry. As χ carries charge 2, the $\mathbb{Z}_6$ symmetry allows for operators such as $z_{03}\chi^3$. Considered on its own, the field χ experiences an effective $\mathbb{Z}_3$ symmetry. The arguments from Sec. 7.1.3 apply and z_{03} either could feature an interacting fixed point or could be relevant at the Gaussian fixed point. In both cases the coupling z_3 does not vanish in the IR.

If φ and χ couple via interactions such as $z_{2,1}\left(\varphi^2\chi^* + (\varphi^*)^2\chi\right)$, then these interactions can act as a portal between the φ and the χ sector. If the χ sector features a non-vanishing coupling z_{03}, then these interactions might percolate into the φ sector.

Non-vanishing z_{03} will not directly induce the coupling $z_{2,1}$ as that coupling is protected by shift symmetry in φ. However, non-vanishing z_{03} will generate higher order terms in the beta function for $z_{2,1}$. These might allow for additional fixed points. The non-vanishing value of z_{03} could then be transferred from the χ to the φ sector. In such a case a $\mathbb{Z}_6$ symmetry for φ would be realizable in the IR.

In fact, the interacting fixed point candidate for $f_s \approx -1$ discussed in the last section extends to this multi-scalar system. One finds a fixed point at which the $U(1)$ symmetry might be broken to a $\mathbb{Z}_6$ symmetry. The resulting expressions are lengthy, see App. E. This example highlights an implicit assumption in our results. It illustrates that introducing multiple fields and assigning corresponding charges might allow to circumvent some of the arguments we presented. At this point we do not believe that such a case is particularly well motivated.

Apart from such engineered examples, our results indicate that asymptotically safe quantum gravity does not allow for global $\mathbb{Z}_n$ symmetries with $n > 3$ in a near-perturbative regime. In a fully non-perturbative regime we find no indications for the existence of such solutions. In contrast, a $\mathbb{Z}_3$ symmetry might be realizable, both at a fixed point and in the IR. This restricts the set of possible symmetries when constructing an asymptotically safe matter model, and might provide constraints for models that go beyond the SM.

7.2 Phenomenological Implications

As one observationally relevant example, a $\mathbb{Z}_3$-symmetric scalar field could account for dark matter [329, 374–376]. In this scenario we expect that the scalar mass and the coupling z_3 are relevant at the Gaussian matter fixed point. Their IR values can be adjusted. We conjecture that the portal coupling is irrelevant and becomes a function of the mass and the coupling z_3. As a result one would obtain a relation similar to the one in Sec. 6.4 featuring one more free parameter.

This phenomenological application focuses on the $\mathbb{Z}_3$ symmetry. Beyond the $\mathbb{Z}_3$ symmetry small violations of a $U(1)$ symmetry might be relevant in the context of baryogenesis, i.e. in explaining the abundance of matter over anti-matter. One possible explanation of this asymmetry requires small explicit violations of a global $U(1)_{\text{B-L}}$ symmetry by a $\mathbb{Z}_n$-symmetric interaction [377–381]. This setting might arise naturally in the models studied here.

In the following, we digress from our main line of argument and explore UV completions beyond asymptotic safety. Such UV completions might come to different conclusions and allow realizing general $\mathbb{Z}_n$ symmetries. We explore the consequences of such a $\mathbb{Z}_n$ symmetry.

A UV completion sets the initial conditions for the RG flow at a scale k_{UV}. We assume that the UV completion breaks the $U(1)$ symmetry explicitly, such that $z_n \neq 0$ at k_{UV}. To translate between k_{UV} and observationally relevant scales in the IR we apply the RG flow. The RG flow will lead to the occurrence of a large mass hierarchy in the scalar potential [365, 371–373]. We first explore the resulting potential on a classical level. We then focus on the case $k_{\mathrm{UV}} = M_{\mathrm{Pl}}$. In this case the flow is purely driven by matter fluctuations. Finally, we assume $M_{\mathrm{Pl}} < k_{\mathrm{UV}}$ and hence study an effective asymptotic safety scenario.

7.2.1 Classical Potential

We first consider the $U(1)$-symmetric part of the potential and focus on the symmetry broken regime with $\langle \varphi\varphi^* \rangle = \bar{\kappa}$. In this regime the potential reads

$$V_{\mathrm{U(1)}}(\varphi\varphi^*) = \frac{\lambda_4}{2}\left(\varphi\varphi^* - \bar{\kappa}\right)^2. \tag{7.14}$$

Excitations around the minimum have two distinct directions. The angular excitation is massless, $M_{\mathrm{trans}} = 0$. It is the Goldstone direction corresponding to the global $U(1)$ symmetry. The radial excitation has mass

$$M_{\mathrm{long}}^2 = 2\bar{\kappa}\lambda_4. \tag{7.15}$$

In addition, the fermion acquires a mass $M_{\mathrm{ferm}}^2 = y^2\bar{\kappa}$.

The $\mathbb{Z}_n$-symmetric interactions break the $U(1)$ symmetry. They turn the Goldstone boson into a pseudo-Goldstone boson that acquires a mass. To extract the resulting mass it is convenient to reparameterize the $\mathbb{Z}_n$-symmetric part of the scalar potential as

$$V_{\mathbb{Z}_n}(\varphi, \varphi^*) = \bar{z}_n\left(-(\varphi^n + (\varphi^*)^n) + 2(-1)^n(\varphi\varphi^*)^{n/2}\right). \tag{7.16}$$

This redefinition is only well-defined if n is even. For odd n, it introduces non-analyticities in $\phi\phi^*$. In the following we will hence focus on even n.

The resulting potential features n degenerate minima. The masses of excitations around these minima can be obtained by diagonalizing the corresponding field space Hessian. They are

$$M_{\mathrm{long}}^2 = 2\bar{\kappa}\lambda_4, \quad M_{\mathrm{trans}}^2 = n^2\bar{z}_n\bar{\kappa}^{n/2-1}. \tag{7.17}$$

Due to the redefinition (7.16), the longitudinal mass M_{long} agrees with the one in the pure $U(1)$ case. The transversal mass is proportional to $\bar{z}_n$. For $\bar{z}_n \to 0$ one recovers $M_{\mathrm{trans}} = 0$ as the $U(1)$ symmetry is restored. The potential for $n = 6$ is visualized in Fig. 7.3. For $z_6 = 0$ the potential features a flat angular direction. For $z_6 \neq 0$ the $n = 6$ minima become visible.

$z_6 = 0$ $z_6 \neq 0$
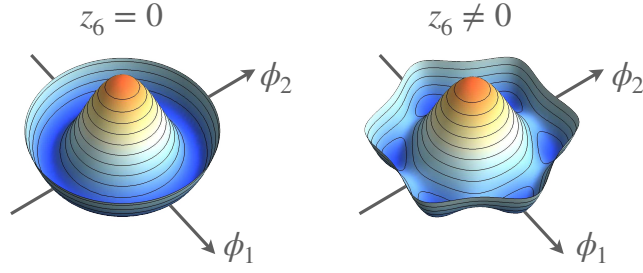
Fig. 7.3.: Potential for $z_n = 0$ (left) and $z_n \neq 0$ (right) with $n = 6$. If the $\mathbb{Z}_n$-symmetric terms contribute, then n degenerate minima emerge. Excitations around these minima are associated with two mass scales, a longitudinal/radial one and a transversal/angular one.

The ratio of the two scalar masses is given by

$$\gamma = \frac{M_{\text{trans}}^2}{M_{\text{long}}^2} = \frac{n^2 \bar{z}_n \bar{\kappa}^{\frac{n}{2}-2}}{2\lambda_4} = \frac{n^2 z_n \kappa^{\frac{n}{2}-2}}{2\lambda_4}, \tag{7.18}$$

where in the last equation we rewrote the mass ratio in terms of dimensionless quantities.

7.2.2 Flow Towards the Infrared

The description in terms of a symmetry-broken potential applies in the IR. Spontaneous symmetry breaking happens along the RG flow for particular UV initial conditions. In this section, the UV initial conditions are not provided by a fixed point. Instead, we assume generic values of $\mathcal{O}(0.1)$ for the z_n coupling. In the following, we illustrate how from such initial conditions one obtains a large mass hierarchy in the IR.

The longitudinal and the transversal masses are associated with the spontaneous and the explicit breaking of the $U(1)$ symmetry, respectively. We set the spontaneous symmetry breaking scale inspired by the SM. Within the SM, electroweak symmetry is broken spontaneously at a scale $k_{\text{SSB}} \sim \mathcal{O}(246\text{GeV})$. In particular, the symmetry breaking scale is much smaller than the UV scale, $k_{\text{SSB}}^2/k_{\text{UV}}^2 = k_{\text{SSB}}^2/M_{\text{Pl}}^2 \sim 10^{-34}$. This hierarchy of scales signals the near-criticality of the SM: at k_{UV} the Higgs mass parameter must be close to its critical value, where its flow vanishes. Sizable deviations from the critical point only occur after about 17 orders of magnitude along the RG flow. They trigger spontaneous symmetry breaking.

We do not explain the near-criticality of the SM. Instead, inspired by the SM, we adjust the scale k_{SSB} of spontaneous $U(1)$-breaking in our model. To obtain a hierarchy $k_{\text{SSB}}^2/k_{\text{UV}}^2 \sim 10^{-34}$ we tune κ close to its critical value κ_{crit}. Splitting $\kappa = \kappa_{\text{crit}} + \delta\kappa$, we observe that spontaneous symmetry breaking will occur once $\delta\kappa$ and κ_{crit} are of the same order. For scales $k > k_{\text{SSB}}$, this implies $\kappa \approx \kappa_{\text{crit}} \gg \delta\kappa$. For scales $k < k_{\text{SSB}}$, this implies $\kappa \approx \delta\kappa \gg \kappa_{\text{crit}}$. The deviation $\delta\kappa$ approximately scales with the canonical mass dimension

$$\delta\kappa \sim \left(\frac{k_{\text{UV}}}{k}\right)^2, \tag{7.19}$$
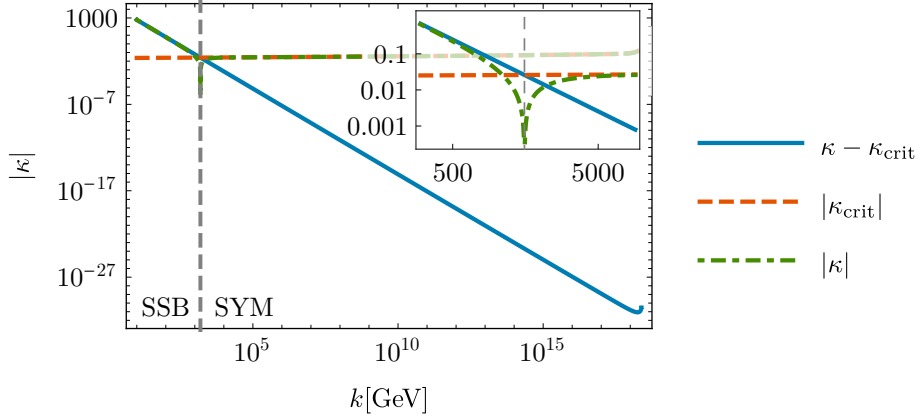
Fig. 7.4.: The running of the mass parameter $\kappa(k)$ for $n = 6$. κ is approximately constant above k_{SSB} and scales canonically for smaller k.

for all k. As a result κ scales as

$$
\kappa \approx \begin{cases} \text{const.} & \text{for } k > k_{\mathrm{SSB}} \\ \kappa(k_{\mathrm{SSB}}) \left(\frac{k_{\mathrm{SSB}}}{k} \right)^2 & \text{for } k < k_{\mathrm{SSB}} \end{cases}, \tag{7.20}
$$

see also Fig. 7.4. The scaling (7.19) also implies that $\delta\kappa$ needs to be fine-tuned at the level of $\sim 10^{-34}$ at k_{UV} to obtain the observed mass ratio between k_{SSB} and M_{Pl}.

Before we turn to the transversal mass, let us remark that our model features a global symmetry. The electroweak symmetry in the SM is gauged. It does not feature massless Goldstone bosons. The mechanism that we describe here is not directly applicable to the SM. However, the hierarchy in the SM indicates that such mass ratios could also be realized beyond the SM.

The transversal mass arises as a consequence of the explicit $U(1)$ breaking in our model due to the coupling z_n. The coupling z_n scales with its canonical mass dimension,

$$
z_n(k) \sim \left(\frac{k}{k_{\mathrm{UV}}} \right)^{n-4}. \tag{7.21}
$$

For generic values of z_n at k_{UV}, $z_n(k)$ rapidly decreases towards the infrared. In consequence, the transversal mass decreases.

As a result, the mass ratio γ rapidly decreases towards the IR. The mass ratio not only depends on κ and z_n, but also on λ_4, however this coupling only runs logarithmically, its running can be neglected. For $k > k_{\mathrm{SSB}}$ the running of γ is dominated by the running of z_n. In expression (7.18) only z_n changes, all other couplings remain approximately constant. The scaling of z_n implies that

$$
\gamma(k) \sim k^{n-4} \quad \text{for } k > k_{\mathrm{SSB}}. \tag{7.22}
$$

For $k < k_{\mathrm{SSB}}$ the various powers of k cancel and $\gamma \approx \text{const}$, see Fig. 7.5. As a result for generic starting values, the IR value for γ is tiny.
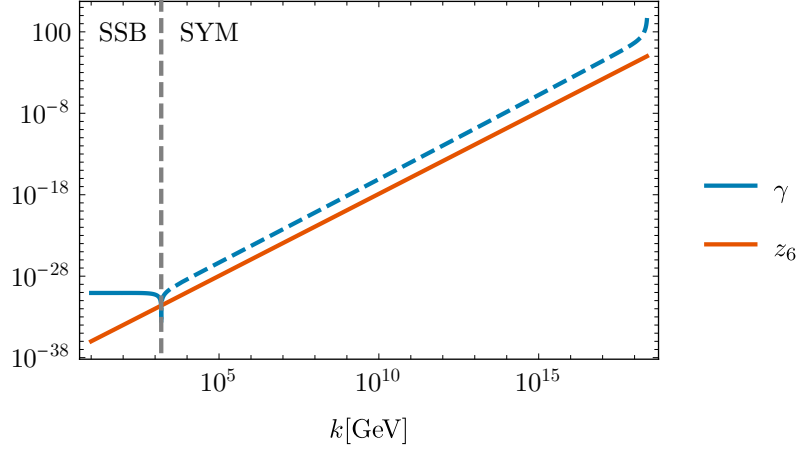
Fig. 7.5.: We show the $\gamma(k)$ and $z_n(k)$ for $n = 6$. In the symmetric regime γ is the combination of couplings given by (7.18). In the symmetry-broken regime γ corresponds to the ratio of the transversal and the longitudinal mass.
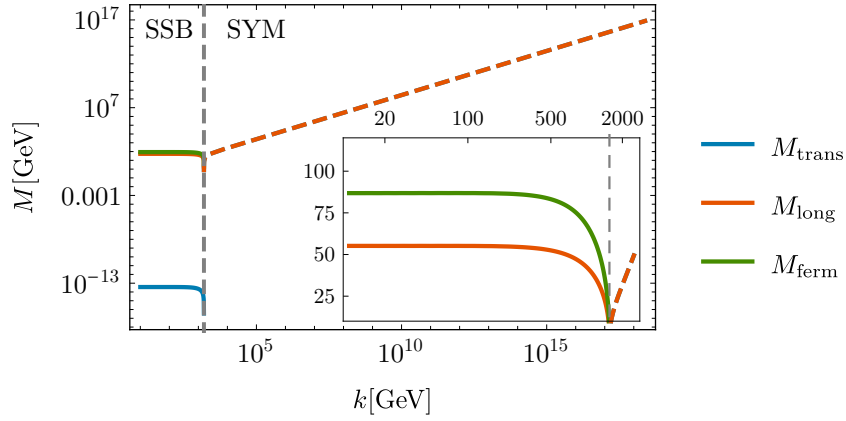
Fig. 7.6.: We show the transversal mass M_{trans}, the longitudinal mass M_{long} and the fermion mass M_{ferm} as a function of the RG scale k in the symmetry-broken regime (SSB) for the exemplary values given in the main text. In the symmetric regime (SYM) we show the scalar mass parameter (dashed).

The RG flow hence induces an *additional* mass hierarchy. The initial conditions for the RG flow in the UV are tuned in just one coupling: κ is close to its critical value. The coupling z_6 takes generic values. As a result of the RG flow the IR value for γ is automatically small. The small value of γ signals an *additional* hierarchy between the transversal and the longitudinal masses. This additional hierarchy occurs automatically, as long as the longitudinal mass and k_{UV} differ strongly.

As a concrete example, we again consider $n = 6$. We initialize the RG flow at $k_{\text{UV}} = M_{\text{Pl}}$ at values

$$y(M_{\text{Pl}}) = 0.4, \quad \lambda_4(M_{\text{Pl}}) = 0.001, \quad z_6(M_{\text{Pl}}) = 0.1, \tag{7.23}$$

and $\kappa(M_{\text{Pl}})$ tuned such that $\bar{\kappa} = (246\,\text{GeV})^2$ in the IR. The tuning in κ results in $M_{\text{long}}/M_{\text{Pl}} \sim 10^{-17}$, see Fig. 7.6. As a consequence $M_{\text{trans}}/M_{\text{Pl}} \sim 10^{-34}$ without any further tuning.
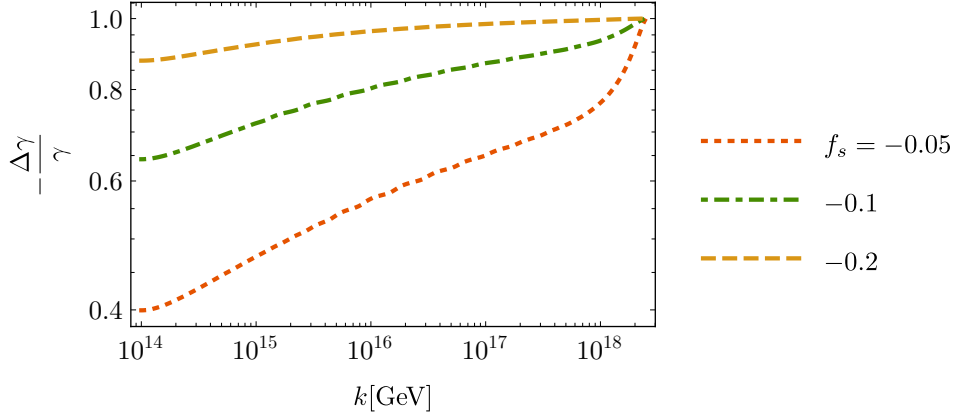
Fig. 7.7.: We show the difference $\frac{\Delta\gamma}{\gamma} = \frac{\gamma(f_s) - \gamma(f_s=0)}{\gamma(f_s=0)}$ in the mass ratio between the case with gravitational fluctuations $\gamma(f_s)$ and without gravitational fluctuations $\gamma(f_s = 0)$ for various values of f_s as a function of the RG scale k. In this figure we consider the case $n = 6$, and set $f_y = 0.004$ as a fiducial value.

7.2.3 Gravitational Corrections

So far we assumed that $k_{\mathrm{UV}} = M_{\mathrm{Pl}}$ and gravitational fluctuations do not contribute. We now study the effect of gravitational fluctuations or $k_{\mathrm{UV}} > M_{\mathrm{Pl}}$. Gravitational fluctuations alter the canonical scaling dimension of a coupling by a contribution f_s, such that

$$z_n \sim \left(\frac{k}{k_{\mathrm{UV}}}\right)^{n-4+f_s}. \tag{7.24}$$

The mass ratio γ is proportional to z_n and scales as $\gamma \sim k^{n-4-f_s}$ for $k > M_{\mathrm{Pl}}$. For gravity coupled to scalar fields one finds $f_s < 0$ [68, 145, 169–178]. Gravitational fluctuations hence further enhance the resulting mass hierarchy.

As an example, we again set $n = 6$. We artificially lower the Planck scale to $\tilde{M}_{\mathrm{Pl}} = 10^{14}\,\mathrm{GeV}$. Above $\tilde{M}_{\mathrm{Pl}}$ gravitational fluctuations contribute. We encode their effect by varying $f_s < 0$, see Fig. 7.7. All couplings apart from z_6 are kept constant at $k = \tilde{M}_{\mathrm{Pl}} = 10^{14}\,\mathrm{GeV}$. The coupling z_6 is kept constant at $k = M_{\mathrm{Pl}} \sim 10^{18}\,\mathrm{GeV}$. We enhance the effect of gravitational fluctuations by increasing $|f_s|$. For increasing $|f_s|$ the resulting IR mass ratio is reduced. As long as $|f_s| \ll n-4$, this effect is numerically subdominant.

7.3 Conclusions: the Challenge to Realize Discrete Symmetries

In the last section, we highlighted the observational consequences of a $\mathbb{Z}_n$ symmetry for a complex scalar φ. The complex scalar is naturally endowed with a global $U(1)$ symmetry. This symmetry can be spontaneously broken along the flow towards the IR at a scale k_{SSB}. If k_{SSB} is much smaller than k_{UV}, then in the presence of $\mathbb{Z}_n$-symmetric interactions ($n > 4$) an additional hierarchy will emerge. The scale associated with $\mathbb{Z}_n$-symmetric interactions is much smaller than k_{SSB} as a result of the RG running. The resulting mass hierarchy might be relevant in beyond-SM settings.

These conclusions hold within an effective-asymptotic-safety setting that features explicit $U(1)$-breaking in the UV. Within asymptotically safe gravity our results indicate that such a breaking is challenging to obtain.

We explored whether a discrete global $\mathbb{Z}_n$ symmetry for the scalar φ is compatible with asymptotically safe gravity. For $n = 3$ our results indicate that a global $\mathbb{Z}_3$ symmetry can be realized. There might be an interacting fixed point in this case. More importantly, the corresponding coupling z_3 is relevant at the Gaussian fixed point. As a consequence it can take non-vanishing values in the IR. On the converse, for $n > 3$ our results indicate that a discrete global $\mathbb{Z}_n$ theory cannot be realized, at least in a near-perturbative regime. We do not find an interacting fixed point realizing a $\mathbb{Z}_n$ symmetry. We also do not find a relevant direction that would allow to realize a $\mathbb{Z}_n$ symmetry along the RG flow. Within our approximations, this result might rule out an entire "ray" in the space of possible symmetries for beyond-SM physics. It highlights how the predictive power of asymptotically safe gravity could not only constrain parameters, but might even constrain which symmetries are available beyond the SM.

Conclusions and Outlook

<div align="right">8</div>

In this thesis, we studied the imprint of spacetime on matter. In this final chapter, we summarize our main findings and provide an outlook.

8.1 Conclusions

We first considered scales on which gravity is not dynamical. On these scales spacetime acts as a background for structures in the matter sector. To describe such structures, we studied real-world networks. We found that road networks carry a strong imprint of their spatial embedding. Their scale-dependent spectral dimension resembles that of networks constructed according to a Euclidean metric on two-dimensional space. We then studied complex real-world networks representing the internet and neural networks. These networks are heterogeneous and nodes differ in their local neighborhood. Walks starting from different nodes differ in their spectral dimension. We separated the walks into different classes. One class of walks is of particular interest. For this class, the scale-dependent spectral dimension exhibits a peak for small diffusion times σ. For intermediate σ, the spectral dimension plateaus at $d_{\mathrm{spec}} \approx 2 - 3$, i.e. close to the underlying spaces' topological dimensions. The same behavior for the spectral dimension appears in networks constructed according to a hybrid metric, that measures distances according to a Lorentzian metric at short (Euclidean) distances and according to a Euclidean metric at large (Euclidean) distances. We interpret this as indication that these complex real-world networks carry imprints of their embedding space. Surprisingly, synthetic networks constructed according to a hybrid metric, and not those constructed according to a Euclidean metric, provide a relevant template.

Such hybrid networks have been studied as a regularization of causal sets [44]. Their appearance in the context of real-world networks highlights that importing further concepts from quantum gravity research might provide new perspectives on real world networks.

As an aside, we studied the mean shortest path between two random nodes in a causal set embedded into d-dimensional Minkowski space. Varying the number of nodes of the causal set, the mean shortest path can grow, remain constant or shrink. We discovered that $d = 4$ is unique: for $d = 4$ the mean shortest path remains approximately constant.

We then turned to the central topic of this thesis: the imprint of quantum spacetime on matter. The interplay of spacetime and matter in the UV could be governed by a new symmetry principle: quantum scale symmetry. This additional symmetry might fix matter couplings at trans-Planckian scales. The trans-Planckian coupling values

can be mapped to the IR using the RG flow. Quantum scale symmetry could hence leave an imprint in the IR that might allow relating to observations.

Before we summarize potential observational implications let us remind the reader that all results are obtained within toy models in truncations of the Euclidean Renormalization group flow. In addition, large technical uncertainties affect the various gravitational beta functions and the corresponding contributions to the matter sector. Within these approximations, both, the U(1) gauge coupling and the Yukawa coupling could feature an interacting fixed point at which the coupling might be predicted. The resulting SM predictions fall in close vicinity of the measured values [147, 186]. We established that the fixed point underlying the prediction of the top mass [147] persists when including a non-minimal coupling ξ. For this to be the case, the non-minimal coupling ξ must fall into a narrow range of values. Non-trivially, the resulting fixed point realizes a value for ξ within this range.

We then took steps beyond the SM and studied the resulting implications for dark energy, inflation and dark matter. A recurring theme is the flattening of scalar potentials: we find indications that quantum scale symmetry prefers flat scalar potentials.

First, we focused on the accelerated expansion of the universe observed at present. Within quantum scale-symmetric models, this expansion could either be driven by the cosmological constant or a scalar field. In the former case, the potential is completely flat and an equation-of-state $w = -1$ is realized by construction. In the latter case, quantum scale symmetry might prefer potentials that are close to flat, leading to an equation of state of $w \approx -1$. In contrast to other approaches that put lower bounds on the flatness of the potential and hence require $w > -1$, asymptotically safe gravity hence might prefer an equation of state $w \approx -1$.

Second, we explored the accelerated expansion of the early universe, i.e. inflation. A phase of inflation generates primordial quantum fluctuations measurable in the cosmic microwave background. The spectrum of primordial scalar fluctuations is approximately scale invariant, encouraging the construction of quantum scale symmetric models of inflation. Within these models it remains challenging to accommodate the correct amplitude of scalar fluctuations. In single-field inflation, we find no indications that the couplings can be adjusted to provide the correct amplitude. In Higgs inflation, the required amplitude of scalar fluctuations might imply a tiny top Yukawa coupling, contradicting particle physics observations. In Starobinsky inflation, one could match the amplitude if the R^2 coupling is relevant. However, additional quantum corrections might spoil the flatness of the inflationary potential. These results highlight the need to further study a phase of inflation, taking into account the amplitude of scalar fluctuations. In conventional approaches to inflation this parameter is merely treated as a "normalization". The constraining power of asymptotically safe quantum gravity does not allow to dial this parameter independently. Instead, asymptotically safe gravity could strongly constrain the set of viable models.

Third, we investigated how the observational need for dark matter might be met by new degrees of freedom. We highlighted how asymptotically safe gravity disfavors a Higgs portal model with only a dark scalar: the resulting portal coupling could be too small to produce sufficient amounts of dark matter, both thermally and via visible-sector annihilations (at least without further assumptions on the cosmological history).

To produce realistic amounts of dark matter a larger portal coupling is needed. The larger portal coupling requires the presence of additional degrees of freedom. We discuss a model with an additional dark Dirac fermion. The resulting model is highly predictive: it only has one free parameter in the dark sector. The visible and the dark sector feature seven marginal couplings. All of them are predicted.

These results were obtained within a toy model. We conjectured that our toy-model can be extended to a model featuring the SM degrees of freedom, a dark scalar and a dark Dirac fermion. In this extension one region of parameter space might be phenomenologically preferred: if the dark scalar undergoes spontaneous symmetry breaking and acquires a mass that is of the same order of magnitude as the Higgs mass, then the model might (i) produce the correct relic density of dark matter and (ii) lower the predicted Higgs mass by a few GeV such that it agrees with the currently measured central value. Understanding if both these scenarios can be realized simultaneously in a quantum-scale-symmetric model requires to go beyond our toy model and include SM degrees of freedom.

Fourth and finally, we explored an extension of the SM by discrete global symmetries, and in particular $\mathbb{Z}_n$ symmetries. These symmetries could be of interest in the context of dark-matter models or models of baryogenesis. In addition, for $n > 4$ they might trigger the appearance of additional mass hierarchies. Theoretically, they are of interested as there are indications that such symmetries might be forbidden in a string-inspired context [364]. We found indications that in a near-perturbative regime quantum scale symmetry might allow a $\mathbb{Z}_3$ symmetry, but could forbid $\mathbb{Z}_n$ symmetries for $n \geq 4$.

All these results highlight how quantum scale symmetry could strongly constrain the SM and its extensions. By fixing the value of irrelevant couplings, a fixed point enhances predictivity within a given model. In some cases, this might go far enough to rule out a model, putting it into the asymptotically safe swampland. In other cases, it allows to tightly constrain models that otherwise exhibit a large amount of freedom.

8.2 Outlook

We have explored the constraining power of quantum scale symmetry in selected areas. Before we discuss how these results could be extended, we briefly comment on a curious result obtained in Chap. 2, that warrants further investigation. We found that the mean path between two nodes is independent of the size of the causal set for a causal set sprinkled into $d = 4$ Minkowski space, boldly summarized in the relation

$$(d = 4 \, \text{Minkowski causal set}) \Rightarrow (\text{mean shortest path length is N-independent}).$$
$$(8.1)$$

The obvious question is under which additional conditions this relation holds in reverse. For a fully connected graph the mean shortest path length is always one and hence N-independent. However, that graph does not resemble a four-dimensional manifold. To investigate which additional constraints are needed to grow $d_{\text{spec}} = 4$ causal sets one could follow ideas from models of transitive percolations [382]: one

could start with a small four-dimensional causal set, and then successively grow this causal set by adding nodes while keeping the mean shortest path length approximately constant. Studying the spectral dimension of the resulting causal set could provide new insights on how to grow causal sets that feature a fixed spectral dimension. Incorporating other quantities such as the curvature [383–387] into this growth process might shed light on how to grow manifold-like causal sets with a topological dimension $d = 4$.

The constraining power of quantum scale symmetry is at the heart of the results presented in Chap. 4 to Chap. 7. It could be applied in a variety of settings in and beyond the SM. Here, we focus on two promising future directions. First, studying the relation between canonically relevant and marginal couplings in beyond-SM settings could provide new constraints on these models. Second, refining the resulting constraints for scalar potentials might allow going beyond the qualitative constraints that we presented in this thesis.

Within the SM, the observationally most interesting property of quantum scale symmetry are potential predictions for marginal couplings. Extensions of the Standard Model in many cases will feature new relevant directions, for which coupling values are not yet known. As a result, the relation between relevant and irrelevant couplings becomes more important to understand. Obtaining relations such as the one in Fig. 6.4 between a relevant and an irrelevant coupling requires intricate fine-tuning. Developing better numerical techniques for this procedure and more importantly analytic estimates of the resulting relation, i.e. of the critical hypersurface, are important tools to develop. Such tools on one hand might allow incorporating constraints from asymptotically safe quantum gravity in conventional data analysis. On the other hand they allow to easily study new phenomenological scenarios. Two such scenarios are (i) $\mathbb{Z}_3$-symmetric dark matter, where asymptotic safety could fix the relation between the canonically relevant $\mathbb{Z}_3$ coupling and a portal coupling, see the discussion at the beginning of Sec. 7.2. (ii) Baryogenesis, leading to a small baryon-to-photon ratio η. The baryon-to-photon ratio can depend on the coupling of non-marginal $\mathbb{Z}_n$-symmetric operators [380, 381]. To obtain a small η our work in Chap. 7 could be relevant: in an effective asymptotic safety setting a small coupling z_n could arise naturally along the RG flow.

We highlighted the relation of dark energy and inflation to scalar potentials. Asymptotically safe gravity determines the shape of the scalar potentials. For n scalar fields, only $n + 1$ relevant directions (the cosmological constant and the masses), and correspondingly only $n + 1$ free parameters could be available. At the same time, observations constrain the potential: the potential needs to match the density of dark energy Ω_{DE}, the equation of state $w(a)$, the amplitude of primordial fluctuations A_s, the spectral tilt n_s, the tensor-to-scalar ratio r and additional constraints that arise throughout the cosmological evolution. Deriving the scalar fixed-point potential in the limit $k \to 0$ numerically could advance efforts to connect to observations. This task is numerically challenging, for work in this direction see Refs. [177, 295, 296]. It is also particularly worthwhile as it might allow refining our statements on dark energy and inflation, working towards a quantitative comparison to data.

These applications highlight how quantum scale symmetry could enhance the predictive power in beyond-SM scenarios. In doing so, quantum scale symmetry progresses towards a quantitative comparison with observational data.

Appendices

Derivation of the Flow Equation

A

In the following we perform a series of rather technical steps to obtain the flow equation. We follow Ref. [80]. Starting from the definition of $W_k[J]$, at the supremum value for J one obtains

$$\frac{\delta W_k[J]}{\delta J(x)} = \langle \phi(x) \rangle = \varphi(x). \tag{A.1}$$

Taking one functional derivative of (3.19) one obtains the quantum equation of motion

$$J(x) = \frac{\delta \Gamma_k[\varphi]}{\delta \varphi(x)} + \int_y R_k(x,y) \varphi(y), \tag{A.2}$$

where we the regulator on the right-hand side arises due to the modification of the Legendre transform. By taking a second functional derivative, one obtains

$$\frac{\delta J(x)}{\delta \varphi(y)} = \frac{\delta^2 \Gamma_k[\varphi]}{\delta \varphi(x) \delta \varphi(y)} + R_k(x,y). \tag{A.3}$$

Inverting this relation yields

$$\frac{\delta \varphi(y)}{\delta J(x)} = \frac{\delta^2 W_k[J]}{\delta J(x) \delta J(y)} = \left(\frac{\delta^2 \Gamma_k[\varphi]}{\delta \varphi(x) \delta \varphi(y)} + R_k(x,y) \right)^{-1}. \tag{A.4}$$

In addition, from the definition of $W_k[J]$ one computes

$$\begin{aligned}
\partial_t W_k[J] &= \frac{\partial_t Z_k[J]}{Z[k]} = -\frac{1}{2} \int \mathcal{D}\phi \, \phi(-q) \, \partial_t R_k \, \phi(q) \, e^{-S - \Delta S + \int J\phi} \\
&= -\frac{1}{2} \int \frac{\mathrm{d}^4 q}{(2\pi)^4} \partial_t R_k(q) \left(\langle \phi(-q)\phi(q) \rangle - \langle \phi(q) \rangle \langle \phi(-q) \rangle \right) + \partial_t \Delta S_k[\langle \phi \rangle] \\
&= -\frac{1}{2} \int \frac{\mathrm{d}^4 q}{(2\pi)^4} \partial_t R_k(q) \frac{\delta^2 W_k[J]}{\delta J \delta J} + \partial_t \Delta S_k[\langle \phi \rangle],
\end{aligned} \tag{A.5}$$

which holds at constant J. Taking a t derivative of Γ_k we obtain

$$\begin{aligned}
\partial_t \Gamma_k &= - \left. \partial_t W_k[J] \right|_{\varphi = \text{const}} + \int (\partial_t J)\varphi - \partial_t \Delta S_k[\varphi] \\
&= - \left. \partial_t W_k[J] \right|_{J = \text{const}} - \int \frac{\delta W_k[J]}{\delta J} \partial_t J + \int (\partial_t J)\varphi - \partial_t \Delta S_k[\varphi].
\end{aligned} \tag{A.6}$$

The second and third term cancel Substituting (A.5) and using (A.4) we obtain the flow equation [81–83]

$$\partial_t \Gamma_k[\varphi] = \frac{1}{2} \text{STr} \left(\frac{\partial_t R_k}{\Gamma_k^{(2)}[\varphi] + R_k} \right). \tag{A.7}$$

Networks

B.1 Data Sources

We implement the random walk as a diffusion process. To handle the network data we use the SNAP library [388]. For each time step $\sigma + 1$ and each node x in the network we update probabilities according to the following rule: We set the probability $p(\sigma + 1, x, x_0) = (1 - \delta)\, p(\sigma, x, x_0)$ and $p(\sigma + 1, y, x_0) = \delta\, w(x, y)\, p(\sigma, x, x_0)$ for each neighbor y of x. Here $w(x, y)$ is the weight for neighbor y at node x. In the case of an unweighted walk $w(x, y) = 1/\deg(x)$. We repeat this update for every x in the network and sum the resulting probabilities.

We extract $p(\sigma, x = x_0, x_0)$ for all σ. One can then compute the spectral dimension according to (2.6).

For the various networks that we study, we utilize the following datasets:

- The network of roads in Pennsylvania is part of the SNAP dataset collection [389].

- The European roadnet was originally published as part of the 10th DIMACS challenge [390]. It is based on OpenStreetMap data. The original graph contains many long strings of nodes that have degree two. To eliminate these strings we apply the following algorithm:

  1. We loop over all nodes.

  2. For every node x we check if it has degree two. If this is the case we check if the node and its two neighbors form a triangle. If this is not the case and one of its neighbors y has degree two, then we contract the nodes into one by making all neighbors of y neighbors of x and deleting node y.

  3. We repeat the second step until x does not have neighbors of degree two anymore.

  4. Finally, we only consider the largest connected component of the resulting network.

  We have confirmed that walking on the original graph yields similar results with a slightly reduced spectral dimension.

Graph	Nodes	Edges	Comment	Source
Internet	33304	69442	CAIDA dataset from Feb. 28th 2020	[59]
Drosophila	21739	2897925	Connectome of the Adult Drosophila Central Brain	[62]
Mouse	212894	143220733	Voxel correlations from Allen Mouse Brain Connectivity Atlas with cutoff $r = 5 \cdot 10^{-3}$	[391]
Roadnet Pennsylvania	1088092	1541898	Network of Streets in Pensylvania	[389]
Roadnet Europe	16664809	19807451	Network of Roads in Europe - reduced (see text)	[390]

Tab. B.1.: We list the real-world networks that we consider with the corresponding data sources. For more information see the main text.

- The drosophila connectome is taken from Ref. [62]. We use version 1.2 of the connectome and have constructed a weighted and an unweighted version for the drosophila graph. The two yield qualitatively similar results.

- The mouse network is constructed by considering the resulting correlation matrix from Ref. [391]. The correlation matrix measures co-activation between different voxels in a mouse brain. We introduce a cutoff $5 \cdot 10^{-3}$ and only consider correlations larger than this cutoff. We then build a network with edges weighted with the (absolute value) of the corresponding correlation.

- The internet network is extracted from the CAIDA database and maps a set of autonomous systems and their connections. We use the snapshot from Feb.28th 2020 [59].

Tab. B.1 lists the number of nodes and edges for each of the graphs.

B.2 Dimension-Dependent Scaling of the Shortest Distance

Numerically, for a causal set embedded into $d = 4$ dimensional Minkowski space we observe that the average shortest distance for two random nodes is approximately constant as a function of the number of nodes N. The same quantity is analytically hard to access. Instead, we perform a simple estimate.

We fix two nodes p and q at coordinates $(T/2, 0, \ldots, 0)$ and $(-T/2, 0, \ldots, 0)$. The volume V_{tot} enclosed by their respective backward- and foreward-lightcones contains N nodes, and hence features a density of nodes $\rho = N/V_{\mathrm{tot}}$.
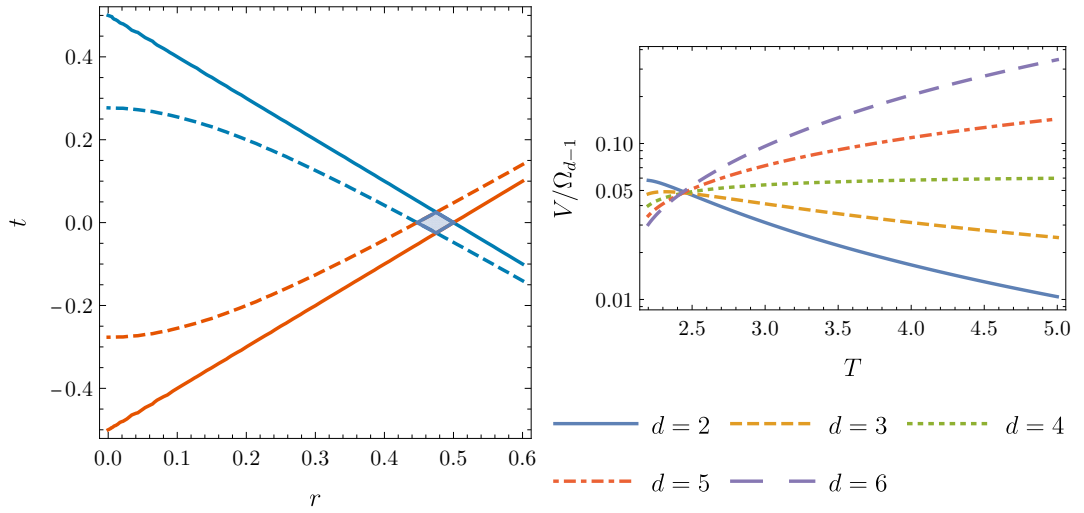
Fig. B.1.: (left) The red (blue) dashed line corresponds to (B.1) (the corresponding hyperbola for p), the red (blue) solid line is q's (p's) forward(backward) lightcone. The region V_q (V_p) between the two red(blue) lines contains points that are connected to $q(p)$ without intermediate nodes with high probability. The blue shaded region is the region V that contains points that directly connect points p and q with high probability. (right) The scaling of the corresponding region as a function of T.

The two nodes p and q are causally connected, $q \prec p$. As long as $N > 1$ they are not directly connected, instead their relation follows by transitivity. There are various transitive chains that imply $q \prec p$. We estimate the probability of the existence of a *single* node r such that $q \prec r \prec p$ is a minimal connection not implied by transitivity. r is then directly connected to both, p and q.

Most nodes that are directly connected to q lie in a volume V_q between q's forward-lightcone and the hyperbola described by [40]

$$-(t + T/2)^2 + r^2 = -1/\rho^{-2/d}. \tag{B.1}$$

Here the exponent on the right-hand side follows from dimensional arguments. For a sketch of the corresponding volume see the left panel of Fig. B.1.

A similar volume V_p exists for p. The intersection of the volumes V_q and V_p defines the volume V. Points directly connected to both p and q lie within this volume with a high probability.

To estimate the volume V we note that for large T the curvature of the hyperbola is negligible and one can expand the corresponding expression for $r(t)$ to first order in t. For the volume V one then obtains

$$V = \Omega_{d-1} \int_0^{\frac{\rho^{-2/d}}{2T}} \mathrm{d}t \int_{t_{\text{hyp}}}^{\frac{T}{2} - t} \mathrm{d}r \, r^{d-2} \tag{B.2}$$

with

$$t_{\text{hyp}} = \frac{T(T/2 + t) - 4\rho^{-2/d}}{\sqrt{T^2 - 4\rho^{-2/d}}}. \tag{B.3}$$

In this expression Ω_{d-1} is the integration over the $d-1$ dimensional unit sphere. The resulting d-dependent expression is lengthy, and we do not give it here for brevity. Instead, the right panel of Fig. B.1 shows the resulting relation. For $d < 4$ the volume V/Ω_{d-1} grows, for $d = 4$ it remains approximately constant and for $d > 4$ it shrinks. Indeed, for $d = 4$ one obtains the expansion $V(T) = \frac{\pi}{4\rho} + \mathcal{O}\left(\frac{1}{T^2}\right)$.

We assume that p and q are connected with only one intermediate node iff at least one node falls into the volume V. The probability for none of the nodes falling into V is given by

$$p_{\text{no-conn}} \equiv 1 - p_{\text{conn}} = (1 - V/V_{\text{tot}})^N. \tag{B.4}$$

In the limit $N \to \infty, \rho = \text{const}$ the probability p_{conn} tends to zero for $d < 4$. It tends to one for $d > 4$. For $d = 4$ it approaches a constant value $p_{\text{conn}} = 1 - e^{-\pi/4} \approx 0.54$.

These results are in qualitative agreement with our numerical findings.

Computational Setup

C.1 Scalar Sector

In this appendix we describe the computational procedure to obtain the beta functions for an effective action Γ_k of the form (5.15). We implement this procedure using the Mathematica package xAct [392, 393]. We split the metric according to (3.2) and the scalar as $\phi = \bar{\phi} + \varphi$. While it is not strictly necessary to introduce a non-trivial background $\bar{\phi}$ for the scalar field, this is done in common approximations, see e.g. [169].

As the background metric $\bar{g}_{\mu\nu}$ we choose to work on a maximally symmetric background. This drastically simplifies the resulting expressions as all curvature invariants are proportional to the Ricci scalar R. In addition, it allows to evaluate the trace on the right-hand side of the flow equation.

To fix the gauge symmetry in the gravitational sector one introduces a gauge fixing term

$$S_{\text{gf}} = \frac{1}{2\alpha} \int \mathrm{d}^4 x \, \sqrt{\bar{g}} \bar{g}^{\mu\nu} \mathcal{F}_\mu \mathcal{F}_\nu, \tag{C.1}$$

with

$$\mathcal{F}_\mu = \sqrt{\frac{1}{16\pi\bar{G}_N} + \alpha_{\text{GF}}\xi\bar{\phi}^2} \left(\bar{D}^\rho h_{\rho\mu} - \frac{1+\beta}{4} \bar{D}_\mu h^\rho_\rho \right). \tag{C.2}$$

This gauge fixing introduces a term that depends on the scalar background $\bar{\phi}$ for $\alpha_{\text{GF}} \neq 0$.

The choice $\alpha_{\text{GF}} = 1$ is particularly common, as the resulting gauge-fixed propagator simplifies significantly. The resulting Faddeev-Popov determinant is

$$\det\left(\frac{\delta\mathcal{F}_\mu}{\delta\zeta_\lambda}\right) = \det\left(\sqrt{\frac{1}{16\pi\bar{G}_N} + \alpha_{\text{GF}}\xi\bar{\phi}^2} \right.$$
$$\left. \left(\bar{D}^\rho \bar{g}^\rho_\mu g^\lambda_\sigma D_\rho + \bar{D}^\sigma \bar{g}^\rho_\mu g^\lambda_\sigma D_\rho - \frac{1+\beta}{2} \bar{D}_\mu \bar{g}^{\rho\sigma} g^\lambda_\sigma D_\rho \right) \right), \tag{C.3}$$

where ζ_λ is the parameter describing an infinitesimal diffeomorphism transformation.

The Faddeev-Popov determinant can then be evaluated by introducing corresponding ghost fields. Conventionally, one redefines the ghost field by a factor $\sqrt{16\pi\bar{G}_N}$. The resulting ghost term takes the form

$$S_{\text{gh}} = -\int \ \mathrm{d}^4x \ \sqrt{\bar{g}}\sqrt{1 + \alpha_{\text{GF}}(1 - \alpha_{\text{ghost}})16\pi\bar{G}_N\xi\bar{\phi}^2}$$
$$\bar{c}_\mu \left(\bar{D}^\rho \bar{g}^{\mu\kappa} g_{\kappa\nu} D_\rho + \bar{D}^\rho \bar{g}^{\mu\kappa} g_{\rho\nu} D_\kappa - \frac{1 + \beta}{2} \bar{D}^\mu \bar{g}^{\rho\sigma} g_{\rho\nu} D_\sigma \right) c^\nu. \quad \text{(C.4)}$$

In the above expression we introduced the part $(1 - \alpha_{\text{ghost}})$ by hand. The ghost term that arises from exponentiating (C.3) follows for $\alpha_{\text{ghost}} = 0$. However, in many applications the background scalar dependence of the ghost term is not taken into account, and instead one considers the case $\alpha_{\text{ghost}} = 1$. By comparing these two cases, in App. C.3 we study the viability of this approximation.

For the regulator we choose a regulator of the form

$$R_k(\bar{\mathcal{D}}) = \bar{\mathcal{D}} \, r\left(\frac{k^2}{\bar{\mathcal{D}}}\right) \quad \text{(C.5)}$$

with shape function $r(x) = (x - 1)\Theta(x - 1)$. Here $\bar{\mathcal{D}}$ is a generalized Laplacian constructed from background metric covariant derivatives.

To allow to easily evaluate the flow equation, the regulator should cancel all Laplacians that appear in $\Gamma_k^{(2)}$. In the presence of non-minimal couplings, such a choice of regulator entails a dependence of the regulator on the scalar background $\bar{\phi}$. In a non-gravitational context such background field dependencies can lead to spurious zeros of the beta function and modify the critical exponents [394].

We explore whether the dependence on the background scalar $\bar{\phi}$ affects our results, see also [68]. we introduced an additional parameter α_{reg} by the replacement $\bar{\phi} \to \sqrt{\alpha_{\text{reg}}}\bar{\phi}$ and consider the regulators

$$R_{k\,\text{TT}}^{\mu\nu\rho\sigma} = \frac{1}{4}\left(\frac{1}{16\pi G_N} + \xi\alpha_{\text{reg}}\bar{\phi}^2\right)\left(k^2 + (-\bar{D}^2)\right) \Theta\left(k^2 + (-\bar{D}^2)\right) \mathbb{1}_{\text{TT}}^{\mu\nu\rho\sigma} \quad \text{(C.6)}$$

$$R_{k\,vv}^{\mu\nu} = \frac{1}{2\alpha}\left(\frac{1}{16\pi G_N} + \xi\alpha_{\text{GF}}\bar{\phi}^2\right)\left(k^2 + (-\bar{D}^2)\right) \Theta\left(k^2 + (-\bar{D}^2)\right) \mathbb{1}_v^{\mu\nu} \quad \text{(C.7)}$$

$$R_{k\,hh} = -\frac{3}{32}\left(\frac{1}{16\pi G_N} + \xi\alpha_{\text{reg}}\bar{\phi}^2\right)\left(k^2 + (-\bar{D}^2)\right) \Theta\left(k^2 + (-\bar{D}^2)\right) \quad \text{(C.8)}$$

$$R_{k\,\sigma\sigma} = \frac{3}{32\alpha}\left(\frac{(3 - \alpha)}{16\pi G_N} - (\alpha\alpha_{\text{reg}} - 3\alpha_{\text{GF}})\xi\bar{\phi}^2\right) \cdot$$
$$\cdot \left(k^2 + (-\bar{D}^2)\right) \Theta\left(k^2 + (-\bar{D}^2)\right) \quad \text{(C.9)}$$

$$R_{k\,\phi\phi} = \frac{1}{2}\left(k^2 + (-\bar{D}^2)\right) Z_\phi \Theta\left(k^2 + (-\bar{D}^2)\right) \quad \text{(C.10)}$$

$$R_{k\,h\sigma} = -\frac{1}{16}\left(\frac{1}{16\pi G_N} + \xi\alpha_{\text{reg}}\bar{\phi}^2\right) \Theta\left(k^2 + (-\bar{D}^2)\right) \cdot$$
$$\cdot \left(\sqrt{3k^2(3k^2 - \bar{R})} - \sqrt{3(-\bar{D}^2)(3(-\bar{D}^2) + \bar{R})}\right) \quad \text{(C.11)}$$

$$\text{(C.12)}$$

$$R_{k\,h\phi} = -\frac{3}{2}\left(k^2 + (-\bar{D}^2)\right)\sqrt{\alpha_{\text{reg}}}\xi\bar{\phi}\,\Theta\left(k^2 + (-\bar{D}^2)\right) \tag{C.13}$$

$$R_{k\,\sigma\phi} = -\frac{1}{2}\left(\sqrt{3k^2(3k^2 - \bar{R})} - \sqrt{3(-\bar{D}^2)(3(-\bar{D}^2) + \bar{R})}\right)\cdot$$
$$\cdot\sqrt{\alpha_{\text{reg}}}\xi\bar{\phi}\,\Theta\left(k^2 + (-\bar{D}^2)\right), \tag{C.14}$$

where $\mathbb{1}_{\text{TT}}$ and $\mathbb{1}_v^{\mu\nu}$ are the identity in the space of transverse-traceless tensors and transverse vectors, respectively.

With this choice of regulator one can invert $\Gamma_k^{(2)} + R_k$. The regulator derivative $\dot{R}_k$ still contains Laplacians for each of the modes. Evaluating the trace then requires expressions of the form $\text{tr}(\triangle^n)$ on a sphere for transverse-traceless tensors, transverse vectors and scalars. This can either be done via heat kernel methods [395] or by an explicit sum over the eigenvalues of the Laplacian on a sphere. The summation runs from $i_{\min}$ to $i_{\max}$, where $i_{\min}$ differs for the various modes and $i_{\max}$ is set by the regulator. We use the corresponding expressions for the sum over eigenvalues from Ref. [144], see also Refs. [396–400], and apply the middle-of-the-staircase approximation introduced in Ref. [144].

Upon evaluating the sum one has evaluated the right hand side of the flow equation. One can then project on the individual couplings on both sides of the flow equation by taking appropriate derivatives with respect to $\bar{\phi}$ and R.

C.2 Fermionic Sector

Including fermionic fluctuations requires additional care due to their Grassmann nature. In the fermionic sector we choose the regulator

$$R_{k\bar{\psi}\psi} = iZ_\psi\bar{\slashed{\nabla}}\left(1 - \sqrt{k^2/(-\bar{\slashed{\nabla}})^2}\right)\Theta\left(k^2 - (-\bar{\slashed{\nabla}})^2\right), \tag{C.15}$$

see Ref. [397] for a discussion on how to choose regulators for fermions in the presence of non-vanishing gravitational backgrounds.

The resulting contributions to the flow are

$$\partial_t(V(\phi)/k^4)\Big|_{\text{ferm}} = \frac{-1}{8\pi^2(1 + y^2\phi^2/k^2)} \tag{C.16}$$

$$\partial_t\left(\frac{1}{16\pi G} + \xi\phi^2/k^2\right)\Big|_{\text{ferm}} = \frac{-1}{48\pi^2(1 + y^2\phi^2/k^2)} \tag{C.17}$$

To compute diagrams that involve gravitational interactions one needs to vary with respect to the metric. The variation with regard to the metric implies additional terms from a variation of the γ^μ-matrices. For a reference that gives more detail and provides explicit expressions for the corresponding variations see App. B of Ref. [401].

C.3 Background Scalar Dependence

In this appendix we explore the dependence on the background scalar $\bar{\phi}$ in more detail. The three parameters that we vary are $\alpha_{\mathrm{GF}}, \alpha_{\mathrm{ghost}}$ and α_{reg}.

The parameter α_{GF} determines the background-scalar dependence of the gauge fixing term. For $\alpha_{\mathrm{GF}} = 0$ the gauge fixing term is background-scalar independent.

The parameter α_{ghost} varies the field dependence of the corresponding ghost term. In principle, only the choice $\alpha_{\mathrm{ghost}} = 0$ is consistent. Here we also vary α_{ghost}, as $\alpha_{\mathrm{ghost}} = 1$ is used in many existing computations.

The parameter α_{reg} controls the background-scalar dependence of the regulator for gravitational fluctuations.

We consider the fixed point

$$\Lambda_* = 0.171, \quad G_* = 0.843, \quad m_*^2 = \lambda_{4*} = \xi_* = 0. \tag{C.18}$$

The fixed point coordinates do not depend on any of the α, as all dependencies are proportional to ξ and ξ vanishes at the fixed point. At the same time the critical exponents depend on the various α.

For $\alpha_{\mathrm{GF}} = \alpha_{\mathrm{reg}} = 0$ and arbitrary α_{ghost} the critical exponents are

$$\theta^{(1/2)} = 2.72 \pm 1.70i, \quad \theta^{(3/4)} = 0.63 \pm 2.55i, \quad \theta^{(5)} = -2.26, \tag{C.19}$$

whereas for $\alpha_{\mathrm{GF}} = \alpha_{\mathrm{reg}} = \alpha_{\mathrm{ghost}} = 1$, i.e. in the same approximation as Ref. [169] (but a different gauge) they are

$$\theta^{(1/2)} = 2.36 \pm 2.81i, \quad \theta^{(3/4)} = 0.36 \pm 2.81i, \quad \theta^{(5)} = -2.26. \tag{C.20}$$

The moderate variation in $\theta^{(3/4)}$ raises the question how strongly technical choices afflict our conclusions on the number of relevant directions. For moderate variations $|\alpha_{\mathrm{reg}}| \leq 1.5$ in the background-scalar dependence of the regulator the critical exponents remain stable, if $\alpha_{\mathrm{reg}} < -1.8$ or $\alpha_{\mathrm{reg}} > 4.1$ the critical exponents might potentially flip signs, see left panel of Fig. C.1. We do not consider such strong background-scalar dependence particularly well motivated and hence use $\alpha_{\mathrm{reg}} = 0$ throughout the main text.

While for α_{reg} no value is clearly preferred, the choice $\alpha_{\mathrm{ghost}} = 0$ is preferential. In this case the background field dependence from the ghost term and the gauge fixing term cancel, as they should and the results become independent of α_{GF}, see right panel of Fig. C.1. The approximation used in Ref. [169] leads to qualitatively similar results.

For an appropriate choice of α_{ghost} the only dependence on the scalar background remains in the regulator. This dependence is not too strong. In addition, it gets weaker for smaller values of Λ_*, as preferred in the presence of SM matter [140]. We hence
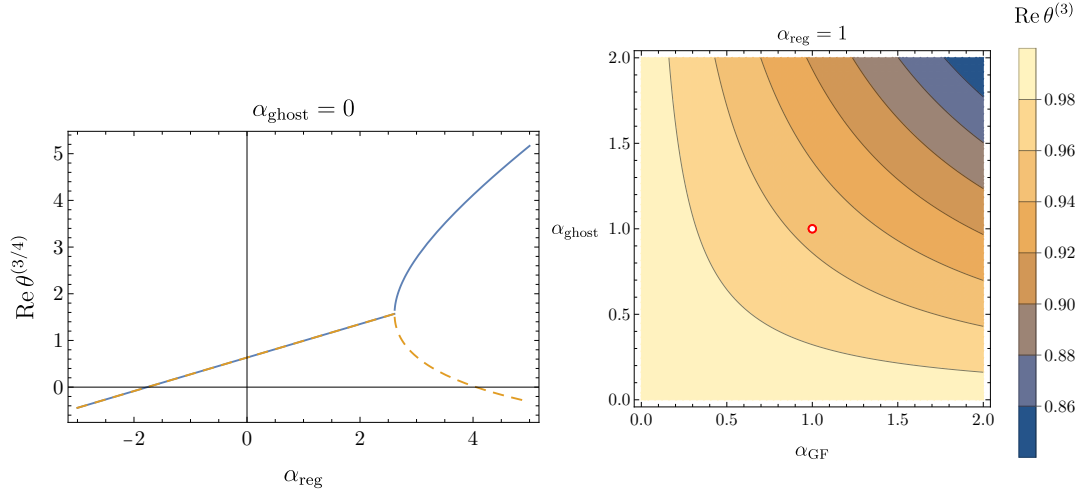
Fig. C.1.: (left) Real part of the critical exponents $\theta^{(3/4)}$ at $\alpha_{\text{ghost}} = 0$ evaluated at the fixed point (C.18). (right) Real part of the critical exponents $\theta^{(3)}$ at $\alpha_{\text{reg}} = 1$ evaluated at the fixed point (C.18). The red dot marks the choice of parameters from Ref. [169]. The approximation made in that reference does not significantly the results obtained.

conclude that our results are reasonably stable under this particular set of technical choices.

Dark Matter Relic Abundance D

In this appendix we specify how to compute a dark matter relic abundance for the model discussed in Sec. 6.3. We first compute the relevant cross-section, and then thermally average over the cross-section. Given a thermally averaged cross section we solve the Boltzmann equation.

We start by noting that for the scalar ϕ_d, the $\mathbb{Z}_2$ symmetry is spontaneously broken by the vacuum expectation value v_d. This allows ϕ_d to decay. In an extension of our model to the full SM this implies, that the scalar excitations will not be a stable dark matter candidate. On the contrary, the fermion ψ_d is stable. It might play the role of a dark matter candidate. In the following we will hence consider ψ_d as the dark matter candidate. As the mixing $\sin\alpha \ll 1$ is relatively small, we will neglect the mixing in the following. This hence will only yield an approximation of the dark matter properties. We leave a study of the full system to future work.

To describe how the density of ψ_d evolves throughout the history of the universe, one needs to compute when reactions involving ψ_d freeze out. The most relevant process in that regard is $\psi_d\bar{\psi}_d \to \phi_d\phi_d$. After ψ_d freeze-out, the ϕ_d subsequently decay to SM matter. The relevant Feynman diagrams are those in Fig. D.1.

We generate the necessary Feynman rules by means of the LanHEP software package [402]. One can then compute the squared matrix elements $|\mathcal{M}|^2$ using the software package CalcHEP [403]. The resulting expression is fairly lengthy. It depends on the Mandelstam variables s, t and the various couplings and masses. Next, one replaces t by a corresponding expression in terms of s and $\cos\theta$, where θ is the angle between one incoming and one outgoing momentum

$$t = m_{\psi_d}^2 + M_D^2 - \frac{s}{2}\left(1 - \cos\theta\sqrt{1 - \frac{4m_{\psi_d}}{s}}\sqrt{1 - \frac{4M_D}{s}}\right) \tag{D.1}$$

and computes the cross section

$$\sigma = \frac{2\pi}{64\pi^2 s}\int_{-1}^{1}\mathrm{d}\cos\theta\,|\mathcal{M}|^2 \tag{D.2}$$
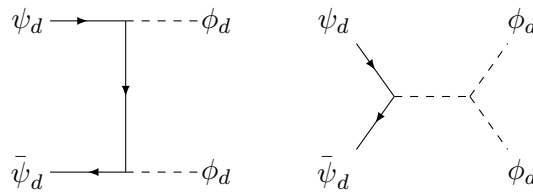
Fig. D.1.: Main diagrams contributing to $\psi_d\bar{\psi}_d \to \phi_d\phi_d$.

The total cross section is obtained by (i) summing over all relevant process, (ii) summing over all final external spin states and (iii) averaging over incoming spin states. At fixed s one can cross-check the result with cross-section estimates from Monte-Carlo event generation in CalcHEP.

Next one performs the thermal averaging at temperature T. Weighting the velocities with a Boltzmann factor $\exp(-E/T)$, one obtains [404]

$$\langle \sigma v \rangle = \frac{1}{8m_{\psi_d}^4 T K_2(m_{\psi_d}/T)^2} \int_{4m_{\psi_d}^2}^{\infty} \mathrm{d}s\,(s - 4m_{\psi_d}^2)\sigma\sqrt{s}K_1(\sqrt{s}/T) \qquad \text{(D.3)}$$

where K_i are the modified Bessel functions of the ith order. Here m_{ψ_d} is the mass of the input particles, i.e. the dark fermions. At a given temperature T this integral can be evaluated numerically.

Given a thermally averaged cross-section we need to solve the Boltzmann equation

$$\dot{n}(t) + 3H(t)n(t) = -\langle \sigma v \rangle \left(n(t)^2 - n_{\text{eq}}(t)^2 \right) \qquad \text{(D.4)}$$

that describes the evolution of the density of a particle species $n(t)$. Here the term proportional to the Hubble constant $H(t)$ arises due to the expansion of the universe. The term on the right-hand-side arises due to particle collisions. It acts as a restoring force that drives the density $n(t)$ towards its equilibrium value. Typically the time is measured in terms of the (dimensionless) inverse temperature $x = m/T$. The resulting differential equation cannot be solved exactly.

One possibility then is to rely on analytic approximations: as one example Ref. [405] proposes a solution applying a boundary layer technique. Here we pursue a different approach and solve the resulting equation numerically. To do so, it is convenient to introduce the yield $Y = n/s$, where $s = \frac{2\pi^2}{45}hT^3$ is the entropy density at temperature T. Here h is the number of degrees-of-freedom in the entropy. In the following we will estimate $h \approx g$, with g the number of degrees of freedom in the energy density. In addition one introduces the dimensionless time variable $x = m_{\psi_d}/T$. Using the Friedman equation in radiation domination, $H = \sqrt{\frac{8\pi^3}{90}}\sqrt{g}\frac{T^2}{M_{\text{Pl}}}$, one can then rewrite the Boltzmann equation as

$$\frac{\mathrm{d}Y}{\mathrm{d}x} = -\sqrt{\frac{\pi}{45}}\frac{mM_{\text{Pl}}}{x^2}\sqrt{g}\langle \sigma v \rangle \left(Y^2 - Y_{\text{eq}}^2 \right). \qquad \text{(D.5)}$$

To solve this equation numerically, it is useful to transform again to $W = \log(Y)$ and $\log(x)$ [406]. The Boltzmann equation then reads

$$\frac{\mathrm{d}W}{\mathrm{d}\log x} = -\sqrt{\frac{\pi}{45}}\frac{m_{\psi_d}M_{\text{Pl}}}{x}\sqrt{g}\langle \sigma v \rangle \left(\exp(W) - \exp(2W_{\text{eq}} - W) \right). \qquad \text{(D.6)}$$

While a precise estimate of the equilibrium quantity W_{eq} requires solving the corresponding phasespace integral for the density n numerically, one can get a rough estimate, by approximating n with Maxwell-Boltzmann statistics. In that case

$$Y_{\text{eq}} = \frac{1}{s}\left(\frac{m_{\psi_d}^2}{2\pi x} \right)^{3/2} g_f e^{-x} \left(1 + \frac{15}{8x} + \mathcal{O}\left(x^{-2} \right) \right). \qquad \text{(D.7)}$$
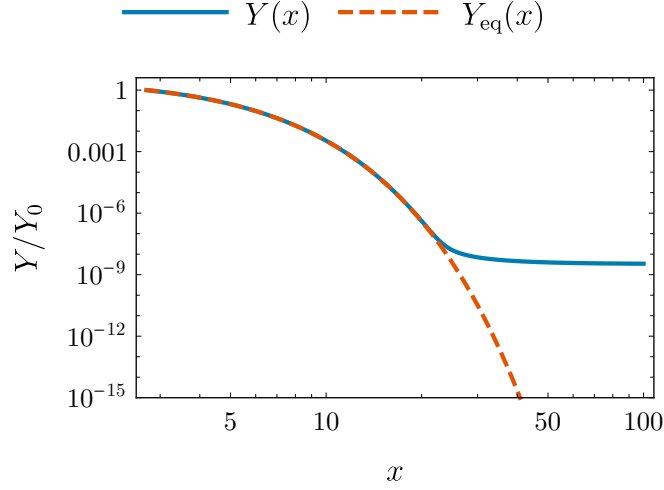
Fig. D.2.: Freeze-out curve for dark matter model discussed in the main text.

Here g_f is the degeneracy of the dark matter species. The last term encodes relativistic corrections, see the appendix of [405] for details.

Eq. D.6 can then be solved numerically. The result is shown for exemplary parameters in Fig. D.2. As evident from this curve, for late times the (entropy-scaled) dark matter density settles towards a constant value.

This value can easily be related to a fractional density by [317, 407]

$$\Omega_{\text{DM}} = m_{\psi_d} \frac{s\, Y(x \to \infty)}{\rho_{\text{crit}}}, \tag{D.8}$$

where the entropy density today is $s = 2891\text{cm}^{-3}$ and $\rho_{\text{crit}} = 1.05 h^2 \text{GeVcm}^{-3}$.

For a concrete benchmark scenario we assume that our toy model can be extended to the Standard Model plus a dark scalar and Dirac fermion. We take the following values

$$m_{\psi_d} = 45.8\text{GeV} \quad M_D = 41.3\text{GeV} \quad y_D = 0.32 \quad v_D = 143.7\text{GeV} \quad \lambda_{\text{HP}} = -0.0077 \tag{D.9}$$

in the dark sector and assume that the visible sector is given by the Standard Model. The quartic self-coupling in the dark sector is computed as $\lambda_d = (M_D/v_D)^2$, i.e. in a no-mixing approximation. We compute the relevant Feynman diagrams with LanHEP [402] and compute the relic density using microMegas [408]. The resulting dark matter relic density then is

$$\Omega_{\text{DM}} h^2 = 0.117, \tag{D.10}$$

in close vicinity to the measured value. Interestingly, the process that we consider only depends on the couplings λ_D and y_D of the dark sector.

Discrete Symmetries and Two Fields

In this appendix we detail a computation with two fields ϕ and χ that circumvents some of the arguments on discrete symmetries made in the main text. The two fields ϕ and χ carry charge 1 and -2 under a common $\mathbb{Z}_6$ symmetry. We consider the effective action

$$
\begin{aligned}
\Gamma_k &= \int \mathrm{d}^4 x \sqrt{g} \Big(g^{\mu\nu} \partial_\mu \phi \partial_\nu \phi^* + g^{\mu\nu} \partial_\mu \chi \partial_\nu \chi^* + \sum_{i=0}^{3} \sum_{j=0}^{3} \frac{1}{i!\,j!} \lambda_{2i\,2j} (\phi\phi^*)^i (\chi\chi^*)^j k^{4-2i-2j} \\
&\quad + z_{03} k \left(\chi^3 + (\chi^*)^3 \right) + z_{21} k \left((\phi^*)^2 \chi^* + \phi^2 \chi \right) \\
&\quad + z_{22} \left(\phi^2 (\chi^*)^2 + (\phi^*)^2 \chi^2 \right) \\
&\quad + z_{41} k^{-1} \left(\phi^4 \chi^* + (\phi^*)^4 \chi \right) + z_{41a} k^{-1} \phi\phi^* \left((\phi^*)^2 \chi^* + \phi^2 \chi \right) \\
&\quad + z_{23} k^{-1} \chi\chi^* \left(\phi^2 \chi + (\phi^*)^2 \chi^* \right) + z_{23a} k^{-1} \phi\phi^* \left(\chi^3 + (\chi^*)^3 \right) \\
&\quad + z_{60} k^{-2} \left(\phi^6 + (\phi^*)^6 \right) + z_{42} k^{-2} \left(\phi^2 \chi + (\phi^*)^2 \chi^* \right)^2 \\
&\quad + z_{24} k^{-2} \left(\phi^2 \chi^4 + (\phi^*)^2 (\chi^*)^4 \right) + \frac{1}{2} z_{06} k^{-2} \left(\chi^3 + (\chi^*)^3 \right)^2 \\
&\quad + z_{42a} k^{-2} \phi\phi^* \left(\phi^2 (\chi^*)^2 + (\phi^*)^2 \chi^2 \right) + z_{24a} k^{-2} \chi\chi^* \left(\phi^2 (\chi^*)^2 + (\phi^*)^2 \chi^2 \right) \Big).
\end{aligned} \tag{E.1}
$$

This action features all momentum-independent dimension six operators that can be build from ϕ and χ.

We also include an auxiliary Dirac fermion coupled to ϕ,

$$
\Gamma_k^{\text{ferm}} = \int \mathrm{d}^4 x \sqrt{g} \left(i \bar{\psi} \slashed{\nabla} \psi + y \left(\phi^* \bar{\psi}_R \psi_L - \phi \bar{\psi}_L \psi_R \right) \right). \tag{E.2}
$$

The gravitational contributions do not distinguish between the two scalars ϕ and χ. For gravitational contributions $f_s = -0.995$ and $f_y = 0.0025$ we find a fixed point

$$
\begin{array}{lll}
z_{03} = 0.15 & z_{21} = 0.30 & z_{06} = -5.0 \cdot 10^{-7} \\
z_{22} = -0.0026 & z_{23} = 0.00025 & z_{23a} = 0.00017 \\
z_{24} = -1.5 \cdot 10^{-6} & z_{24a} = -0.0017 & z_{41} = 2.1 \cdot 10^{-5} \\
z_{41a} = 9.4 \cdot 10^{-5} & z_{42} = -7.7 \cdot 10^{-7} & z_{42a} = -0.00097 \\
z_{60} = -2.6 \cdot 10^{-8} & \lambda_{02} = 0.0077 & \lambda_{04} = -0.012 \\
\lambda_{06} = -0.0097 & \lambda_{20} = 0.0052 & \lambda_{22} = -0.011 \\
\lambda_{24} = -0.012 & \lambda_{40} = -0.0032 & \lambda_{42} = -0.0064 \\
\lambda_{60} = -0.0012 & y = 0.24 &
\end{array} \tag{E.3}
$$

with critical exponents

$$\theta_1 = 1.02 \qquad \theta_2 = 1.00 \qquad \theta_3 = -0.000611$$
$$\theta_4 = -0.00466 \qquad \theta_5 = -0.00786 \qquad \theta_6 = -0.924$$
$$\theta_7 = -0.946 \qquad \theta_8 = -0.975 \qquad \theta_9 = -1.00$$
$$\theta_{10} = -1.93 \qquad \theta_{11} = -1.96 \qquad \theta_{12} = -1.99$$
$$\theta_{13} = -2.00 \qquad \theta_{14} = -2.85 \qquad \theta_{15} = -2.87$$
$$\theta_{16} = -2.91 \qquad \theta_{17} = -2.95 \qquad \theta_{18} = -2.96$$
$$\theta_{19} = -3.00 \qquad \theta_{20} = -3.00 \qquad \theta_{21} = -3.00$$
$$\theta_{22} = -3.01 \qquad \theta_{23} = -3.01. \tag{E.4}$$

The critical exponents are shifted by about $\sim \mathcal{O}(1)$ due to the gravitational contribution f_s.

This fixed point features non-vanishing z_{03} and z_{21}. The $U(1)$ violation percolates from the χ to the ϕ sector. As a consequence, the coupling z_{60} also does not vanish. The ϕ sector hence is interacting despite being $\mathbb{Z}_6$ symmetric.

Beta Functions

F.1 Yukawa System

The contribution to f_y from non-minimally coupled gravity is given by

$$f_y^{\min} = -g\frac{(96 - 235\lambda + 103\lambda^2 + 56\lambda^3)}{12\pi(3 - 4\lambda)^2(1 - 2\lambda)^2} \tag{F.1}$$

The non-minimal contribution $f_y^{\text{non-min}} = f_y^{\text{non-min-1}} + f_y^{\text{non-min-2}}$ consists of two parts associated with the two diagrams in Fig. 4.5, which for vanishing mass $m^2 = 0$ are given by

$$f_y^{\text{non-min-1}} = -g\frac{24(1 - \eta_h/8)\xi}{\pi(3 - 4\lambda)^2} - g\frac{8(1 - \eta_\phi/8)\xi}{\pi(3 - 4\lambda)} \tag{F.2}$$

$$f_y^{\text{non-min-2}} = g\frac{108(1 - \eta_h/9)\xi}{7\pi(3 - 4\lambda)^2} + g\frac{36(1 - \eta_\phi/9)\xi}{7\pi(3 - 4\lambda)} + g\frac{18(1 - \eta_\psi/8)\xi}{7\pi(3 - 4\lambda)} \tag{F.3}$$

The scalar anomalous dimension for $y = 0$ is given by

$$
\begin{aligned}
\eta_\phi &= g\frac{(8 - \eta_h)(1 + 48(\xi - \frac{1}{2}m^2)) + 8\eta_h m^2}{16\pi(3 - 4\lambda)^2(1 + m^2)} \\
&+ g\frac{(8 - \eta_\phi)(1 - 24\xi + 432\xi^2 - 144\xi m^2) + 48\eta_\phi\xi m^2}{48\pi(3 - 4\lambda)(1 + m^2)^2} \\
&- g\frac{108(\xi - \frac{1}{3}m^2)^2}{\pi(3 - 4\lambda)^2(1 + m^2)^2}.
\end{aligned}
\tag{F.4}
$$

F.2 Portal Beta Functions

In the following we report the full beta functions, mostly also including the masses.

F.2.1 Yukawa system

The beta functions for the three couplings m^2, ξ, λ_4 for gauge $\beta = 0$ and a background-scalar independent regulator are

$$
\begin{aligned}
\beta_{m^2} &= -(2 - \eta_\phi)m^2 - \frac{36g\xi^2\eta_\phi}{5\pi(3 - 4\lambda)(1 + m^2)^2} + \frac{4gm^2(12\xi - \eta_\phi(m^2 + 6\xi))}{3\pi(3 - 4\lambda)(1 + m^2)^2} \\
&\quad - \frac{3g\xi(6\xi - \eta_\phi(2m^2 + 3\xi))}{\pi(3 - 4\lambda)(1 + m^2)^2} - \frac{2gm^4(2 - \eta_\phi)}{\pi(3 - 4\lambda)(1 + m^2)^2} - \frac{108g\xi^2\eta_h}{5\pi(3 - 4\lambda)^2(1 + m^2)} \\
&\quad - \frac{9g\xi(6\xi - \eta_h(2m^2 + 3\xi))}{\pi(3 - 4\lambda)^2(1 + m^2)} - \frac{5g(\xi(8 - \eta_h) - m^2(6 - \eta_h))}{12\pi(1 - 2\lambda)^2} \\
&\quad - \frac{g(3\xi(8 - \eta_h) - 2m^2(6 - \eta_h))}{4\pi(3 - 4\lambda)^2} + \frac{4gm^2(12\xi - \eta_h(m^2 + 6\xi))}{\pi(3 - 4\lambda)^2(1 + m^2)} \\
&\quad - \frac{6gm^4(2 - \eta_h)}{\pi(3 - 4\lambda)^2(1 + m^2)} - \frac{\lambda_4(6 - \eta_\phi)}{64\pi^2(1 + m^2)^2} + \frac{y^2}{4\pi^2}, \quad\quad\quad\quad \text{(F.5)}
\end{aligned}
$$

$$
\begin{aligned}
\beta_{\lambda_4} &= 2\lambda_4\eta_\phi - \frac{64g^2(81m^2\xi^2(10 - \eta_\phi) - 45m^4\xi(8 - \eta_\phi) + 10m^6(6 - \eta_\phi) - 54\xi^3(12 - \eta_\phi))}{15(3 - 4\lambda)^2(1 + m^2)^2} \\
&\quad + \frac{512g^2(-756m^2\xi^3(12 - \eta_\phi) + 567m^4\xi^2(10 - \eta_\phi) - 210m^6\xi(8 - \eta_\phi))}{105(3 - 4\lambda)^2(1 + m^2)^3} \\
&\quad + \frac{512g^2(35m^8(6 - \eta_\phi) + 405\xi^4(14 - \eta_\phi))}{105(3 - 4\lambda)^2(1 + m^2)^3} \\
&\quad + \frac{8g^2(-10m^2\xi(8 - \eta_h) + 5m^4(6 - \eta_h) + 6\xi^2(10 - \eta_h))}{3(1 - 2\lambda)^3} \\
&\quad - \frac{16g^2(-30m^2\xi(\eta_h - 8) + 10m^4(\eta_h - 6) + 27\xi^2(\eta_h - 10))}{5(3 - 4\lambda)^3} \\
&\quad + \frac{128g^2(-81m^2\xi^2(10 - \eta_h) + 45m^4\xi(8 - \eta_h) - 10m^6(6 - \eta_h) + 54\xi^3(12 - \eta_h))}{5(3 - 4\lambda)^3(1 + m^2)} \\
&\quad + \frac{512g^2(-756m^2\xi^3(12 - \eta_h) + 567m^4\xi^2(10 - \eta_h) - 210m^6\xi(8 - \eta_h))}{35(3 - 4\lambda)^3(1 + m^2)^2} \\
&\quad + \frac{512g^2(35m^8(6 - \eta_h) + 405\xi^4(14 - \eta_h))}{35(3 - 4\lambda)^3(1 + m^2)^2} \\
&\quad + \frac{4g\lambda_4(-30m^2\xi(8 - \eta_\phi) + 10m^4(6 - \eta_\phi) + 27\xi^2(10 - \eta_\phi))}{5\pi(3 - 4\lambda)(1 + m^2)^3} \\
&\quad + \frac{4g\lambda_4(3\xi(8 - \eta_\phi) - 2m^2(6 - \eta_\phi))}{3\pi(3 - 4\lambda)(1 + m^2)^2} + \frac{g\lambda_4(6 - \eta_h)}{2\pi(3 - 4\lambda)^2} + \frac{3\lambda_4^2(6 - \eta_\phi)}{32\pi^2(1 + m^2)^3} \\
&\quad + \frac{6g\lambda_4(-30m^2\xi(8 - \eta_h) + 10m^4(6 - \eta_h) + 27\xi^2(10 - \eta_h))}{5\pi(3 - 4\lambda)^2(1 + m^2)^2} \\
&\quad - \frac{4g\lambda_4(2m^2(6 - \eta_h) - 3\xi(8 - \eta_h))}{\pi(3 - 4\lambda)^2(1 + m^2)} + \frac{5g\lambda_4(6 - \eta_h)}{12\pi(1 - 2\lambda)^2} - \frac{y^4}{\pi^2}, \quad\quad \text{(F.6)}
\end{aligned}
$$

$$\beta_\xi = \xi\eta_\phi + \frac{2g\left(18\xi^2\left(2-\eta_h\right) + m^6\eta_h - m^4(12\xi - \eta_h(1+6\xi)) - 6m^2\xi(2+3\xi(2-\eta_h)))\right)}{3\pi(3-4\lambda)^2\left(1+m^2\right)^2}$$

$$-\frac{5g\left(\xi(6+20\lambda - \eta_h(1+2\lambda)) - m^2\left(15 - 6\lambda + \eta_h(2\lambda - 3)\right)\right)}{36\pi(1-2\lambda)^3}$$

$$+\frac{g\left(12\xi - m^2\left(6-\eta_h\right)\right)}{12\pi(3-4\lambda)^2} + \frac{9g\xi^2\eta_\phi\left(5m^2+32\xi+5\right)}{20\pi(3-4\lambda)\left(1+m^2\right)^3}$$

$$-\frac{g\xi\left(-3\xi(4+18\xi + \eta_h(1-9\xi)) - m^2(12\xi - \eta_h(4+15\xi+4m^2))\right)}{\pi(3-4\lambda)^2\left(1+m^2\right)^2}$$

$$+\frac{27g\xi^2\eta_h\left(5+5m^2+16\xi\right)}{20\pi(3-4\lambda)^2\left(1+m^2\right)^2}$$

$$+\frac{gm^2\left(2-\eta_h\right)\left(m^2(1+m^2)-6\xi\right)}{\pi(3-4\lambda)^2\left(1+m^2\right)^2} - \frac{gm^2\left(2-\eta_\phi\right)\left(m^4+m^2(1+6\xi)-6\xi\right)}{3\pi(4\lambda-3)\left(1+m^2\right)^3}$$

$$+\frac{g\xi\left(3\xi(4+36\xi + \eta_\phi(1-18\xi)) + m^2(12\xi - \eta_\phi(4+4m^2+33\xi))\right)}{3\pi(3-4\lambda)\left(1+m^2\right)^3}$$

$$+\frac{2g\left(18\xi^2\left(2-\eta_\phi\right) + m^6\eta_\phi - m^4\left(12\xi - \eta_\phi(1+12\xi)\right) - 6m^2\xi\left(2+9\xi\left(2-\eta_\phi\right)\right)\right)}{9\pi(3-4\lambda)\left(1+m^2\right)^3}$$

$$+\frac{\lambda_4\left(6-\eta_\phi\right)\left(1+m^2+12\xi\right)}{384\pi^2\left(1+m^2\right)^3} + \frac{y^2}{48\pi^2}. \tag{F.7}$$

The beta function for the Yukawa coupling is

$$\beta_y = y\,\eta_\psi + y\frac{\eta_\phi}{2} + y^3\left(\frac{5-\eta_\psi}{80\pi^2\left(1+m^2\right)} + \frac{6-\eta_\phi}{96\pi^2\left(1+m^2\right)^2}\right)$$

$$-\frac{3y\,g}{16}\left(\frac{16\left(6-\eta_\psi\right)}{15\pi(3-4\lambda)} + \frac{192(7-\eta_h)}{35\pi(3-4\lambda)^2}\right) + \frac{9y\,g}{256}\left(\frac{32\left(7-\eta_\psi\right)}{21\pi(3-4\lambda)} + \frac{4(8-\eta_h)}{\pi(3-4\lambda)^2}\right)$$

$$+\frac{5y\,g(6-\eta_h)}{12\pi(1-2\lambda)^2} + \frac{y\,g(6-\eta_h)}{2\pi(3-4\lambda)^2}$$

$$-\frac{y\,g\left(45\xi\left(8-\eta_\psi\right) - 28m^2\left(6-\eta_\psi\right)\right)}{140\pi(3-4\lambda)\left(1+m^2\right)} + \frac{y\,g\left(36m^2\left(7-\eta_\phi\right) - 60\xi\left(9-\eta_\phi\right)\right)}{105\pi(3-4\lambda)\left(1+m^2\right)^2}$$

$$+\frac{y\,g\left(3\xi\left(8-\eta_\phi\right) - 2m^2\left(6-\eta_\phi\right)\right)}{3\pi(3-4\lambda)\left(1+m^2\right)^2}$$

$$-\frac{y\,g\left(2(6-\eta_h)m^2 - 3(8-\eta_h)\xi\right)}{\pi(3-4\lambda)^2\left(1+m^2\right)} + \frac{y\,g\left(36(7-\eta_h)m^2 - 60(9-\eta_h)\xi\right)}{35\pi(3-4\lambda)^2\left(1+m^2\right)}. \tag{F.8}$$

F.2.2 Portal System

The portal system features two copies of these beta functions, one for the visible and one for the dark sector. Due to the presence of the portal couplings additional contributions

$$\Delta\beta_{m_v^2} = -\frac{(6-\eta_{\phi_d})\lambda_{\mathrm{HP}}}{192\pi^2(1+m_d^2)^2}, \tag{F.9}$$

$$\Delta\beta_{\lambda_{4,v}} = \frac{(6-\eta_{\phi_d})\lambda_{\mathrm{HP}}^2}{96\pi^2(1+m_d^2)^3}, \tag{F.10}$$

$$\Delta\beta_{\xi_v} = \frac{(6-\eta_{\phi_d})\lambda_{\mathrm{HP}}(1+m_d^2+12\xi_d)}{1152\pi^2(1+m_d^2)^3}, \tag{F.11}$$

arise in the beta functions for the three visible couplings and vice versa for the dark sector. The portal beta function is

$$
\begin{aligned}
\beta_{\lambda_{\mathrm{HP}}} =\ & \left(\eta_{\phi_d}+\eta_{\phi_v}\right)\lambda_{\mathrm{HP}} \\
& + \frac{41472g^2\xi_d^2\left(14-\eta_h\right)\xi_v^2}{7(3-4\lambda)^3} + \frac{16g^2\xi_d\left(10-\eta_h\right)\xi_v}{(1-2\lambda)^3} + \frac{432g^2\xi_d\left(10-\eta_h\right)\xi_v}{5(3-4\lambda)^3} \\
& + \frac{6912g^2\xi_d^2\xi_v^2\left(28-\eta_{\phi_d}-\eta_{\phi_v}\right)}{7(3-4\lambda)^2} + \frac{36g\xi_d\lambda_{\mathrm{HP}}\xi_v\left(20-\eta_{\phi_d}-\eta_{\phi_v}\right)}{5\pi(3-4\lambda)} \\
& + \frac{108g\xi_d\left(10-\eta_h\right)\lambda_{\mathrm{HP}}\xi_v}{5\pi(3-4\lambda)^2} + \frac{5g\left(6-\eta_h\right)\lambda_{\mathrm{HP}}}{12\pi(1-2\lambda)^2} + \frac{g\left(6-\eta_h\right)\lambda_{\mathrm{HP}}}{2\pi(3-4\lambda)^2} \\
& + \frac{3456g^2\xi_v^2\xi_d\left(12-\eta_h\right)}{5(3-4\lambda)^3} + \frac{3456g^2\xi_v\xi_d^2\left(12-\eta_h\right)}{5(3-4\lambda)^3} + \frac{576g^2\xi_d\xi_v^2\left(12-\eta_{\phi_v}\right)}{5(3-4\lambda)^2} \\
& + \frac{576g^2\xi_d^2\xi_v\left(12-\eta_{\phi_d}\right)}{5(3-4\lambda)^2} + \frac{6g\xi_d\left(8-\eta_h\right)\lambda_{\mathrm{HP}}}{\pi(3-4\lambda)^2} + \frac{6g\xi_v\left(8-\eta_h\right)\lambda_{\mathrm{HP}}}{\pi(3-4\lambda)^2} \\
& + \frac{27g\xi_d^2\left(10-\eta_h\right)\lambda_{\mathrm{HP}}}{5\pi(3-4\lambda)^2} + \frac{27g\xi_v^2\left(10-\eta_h\right)\lambda_{\mathrm{HP}}}{5\pi(3-4\lambda)^2} \\
& + \frac{18g\xi_d^2\lambda_{\mathrm{HP}}\left(10-\eta_{\phi_d}\right)}{5\pi(3-4\lambda)} + \frac{18g\lambda_{\mathrm{HP}}\xi_v^2\left(10-\eta_{\phi_v}\right)}{5\pi(3-4\lambda)} + \frac{2g\xi_d\lambda_{\mathrm{HP}}\left(8-\eta_{\phi_d}\right)}{\pi(3-4\lambda)} \\
& + \frac{2g\xi_v\lambda_{\mathrm{HP}}\left(8-\eta_{\phi_v}\right)}{\pi(3-4\lambda)} + \frac{\lambda_{\mathrm{HP}}^2\left(6-\eta_{\phi_v}\right)}{48\pi^2} + \frac{\lambda_{\mathrm{HP}}^2\left(6-\eta_{\phi_d}\right)}{48\pi^2} \\
& + \frac{\lambda_{\mathrm{HP}}\lambda_{4v}\left(6-\eta_{\phi_v}\right)}{32\pi^2} + \frac{\lambda_{4d}\lambda_{\mathrm{HP}}\left(6-\eta_{\phi_d}\right)}{32\pi^2}. \tag{F.12}
\end{aligned}
$$

In this expression we already set the masses to zero for readability. For the full beta functions see the supplemental material of Ref. [2].

F.3 Slow-Roll Inspired Parameters

The flow for the dimensionless potential $v = V/k^4$ is

$$
\begin{aligned}
\partial_t v \;=\; & \frac{1}{96\pi^2 g(1 - 16\pi g v)\left(3(1+\epsilon_2) - 32\pi g(v - 2\epsilon_1^2 + v\epsilon_2)\right)} \Bigg(\\
& 3g\left(19 + 16\epsilon_2 - 384\pi^2 v(1+\epsilon_2)\right) \\
+ \; & 16\pi g^2\left(48\epsilon_1^2 + 1920\pi^2 v^2(1+\epsilon_2) - 3v(9 + 512\pi^2\epsilon_1^2 + 4\epsilon_2)\right) \\
+ \; & 512\pi^2 g^3 v\left(16\epsilon_1^2 - 384\pi^2 v^2(1+\epsilon_2) - v(5 - 768\pi^2\epsilon_1^2 + 8\epsilon_2)\right)\Bigg). \quad \text{(F.13)}
\end{aligned}
$$

By taking appropriate derivatives with respect to ϕ one can obtain beta functions for the ϵ_i.

F.4 Discrete Symmetries

Below are the beta functions obtained with the functional renormalization group for the $\mathbb{Z}_n$-symmetric model with $n \geq 6$, and n even. We report the beta functions both in the symmetric and in the symmetry-broken regime. In both regimes we project by taking derivatives with respect to $\rho = \phi\phi^*$ and $\tau = -\left(\phi^{n/2} - (\phi^*)^{n/2}\right)^2$.

F.4.1 Symmetric Regime

In the symmetric regime the beta functions for the couplings κ, λ_4 and z_n are

$$
\beta_\kappa \;=\; -(2 + \eta_\phi)\kappa + \frac{(6 - \eta_\phi)(1 - 6\kappa\lambda_4)}{48\pi^2(1 - \kappa\lambda_4)^3} + \frac{3z_n(6 - \eta_\phi)\kappa\delta_{6,n}}{8\pi^2\lambda_4(1 - \kappa\lambda_4)^2} \quad \text{(F.14)}
$$

$$
\beta_{\lambda_4} \;=\; 2\eta_\phi\lambda_4 + \frac{5(6 - \eta_\phi)\lambda_4^2}{48\pi^2(1 - \kappa\lambda_4)^3} - \frac{3z_n(6 - \eta_\phi)\delta_{6,n}}{8\pi^2(1 - \kappa\lambda_4)^2} \quad \text{(F.15)}
$$

$$
\beta_{z_n} \;=\; \left(n - 4 + \frac{n}{2}\eta_\phi\right)z_n + \frac{z_n n(n-1)(6 - \eta_\phi)\lambda_4}{96\pi^2(1 - \kappa\lambda_4)^3}. \quad \text{(F.16)}
$$

In this expression $\delta_{6,n}$ is the Kronecker Delta. The beta function for the Yukawa coupling does not feature any direct contributions

$$
\beta_y = \left(\eta_\psi + \frac{1}{2}\eta_\phi\right)y. \quad \text{(F.17)}
$$

F.4.2 Symmetry-Broken Regime

In the symmetry-broken regime the beta functions for the couplings κ, λ_4 and z_n are

$$
\begin{aligned}
\beta_\kappa =\ & -(2+\eta_\phi)\kappa + \frac{(6-\eta_\phi)z_n^2 n^4 \kappa^n}{64\pi^2(1+2\kappa\lambda_4)^2(\kappa+z_n n^2 \kappa^{n/2})^2} \\
& + \frac{(6-\eta_\phi)\kappa^2(1+\kappa\lambda_4+\kappa^2\lambda_4^2)}{48\pi^2(1+2\kappa\lambda_4)^2(\kappa+z_n n^2 \kappa^{n/2})^2} \\
& - \frac{(6-\eta_\phi)z_n n^2 \kappa^{n/2}(2-4\kappa\lambda_4+8\kappa^2\lambda_4^2-n(1+2\kappa\lambda_4)^2)}{384\pi^2\lambda_4(1+2\kappa\lambda_4)^2(\kappa+z_n n^2 \kappa^{n/2})^2}
\end{aligned}
\tag{F.18}
$$

$$
\begin{aligned}
\beta_{\lambda_4} =\ & 2\eta_\phi\lambda_4 + \frac{\kappa^6\lambda_4^5\,(6-\eta_\phi)}{12\pi^2\left(1+2\kappa\lambda_4\right)^3\left(\kappa+n^2 z_n \kappa^{n/2}\right)^3} + \frac{\kappa^5\lambda_4^4\,(6-\eta_\phi)}{8\pi^2\left(1+2\kappa\lambda_4\right)^3\left(\kappa+n^2 z_n \kappa^{n/2}\right)^3} \\
& + \frac{\kappa^4\lambda_4^3\,(6-\eta_\phi)}{16\pi^2\left(1+2\kappa\lambda_4\right)^3\left(\kappa+n^2 z_n \kappa^{n/2}\right)^3} + \frac{5\kappa^3\lambda_4^2\,(6-\eta_\phi)}{48\pi^2\left(1+2\kappa\lambda_4\right)^3\left(\kappa+n^2 z_n \kappa^{n/2}\right)^3} \\
& - \frac{n^2 z_n\,(6-\eta_\phi)\left(16\kappa^4\lambda_4^4+32\kappa^3\lambda_4^3-3\kappa^2\lambda_4^2+8\kappa\lambda_4+1\right)\kappa^{n/2}}{96\pi^2\left(1+2\kappa\lambda_4\right)^3\left(\kappa+n^2 z_n \kappa^{n/2}\right)^3} \\
& + \frac{n^6 z_n^2\,(6-\eta_\phi)\,\kappa^{n-1}}{768\pi^2\left(\kappa+n^2 z_n \kappa^{n/2}\right)^3} + \frac{3\lambda_4^2 n^6 z_n^3\,(6-\eta_\phi)\,\kappa^{\frac{3n}{2}}}{32\pi^2\left(1+2\kappa\lambda_4\right)^3\left(\kappa+n^2 z_n \kappa^{n/2}\right)^3} \\
& - \frac{n^5 z_n^2\,(6-\eta_\phi)\,\kappa^{n-1}}{384\pi^2\left(\kappa+n^2 z_n \kappa^{n/2}\right)^3} - \frac{n^4 z_n\,(6-\eta_\phi)\,\kappa^{n/2}}{768\pi^2\left(\kappa+n^2 z_n \kappa^{n/2}\right)^3} \\
& + \frac{9\lambda_4^2 n^4 z_n^2\,(6-\eta_\phi)\,\kappa^{n+1}}{32\pi^2\left(1+2\kappa\lambda_4\right)^3\left(\kappa+n^2 z_n \kappa^{n/2}\right)^3} + \frac{n^3 z_n\,(6-\eta_\phi)\left(4\kappa\lambda_4+3\right)\kappa^{n/2}}{384\pi^2\left(\kappa+n^2 z_n \kappa^{n/2}\right)^3}
\end{aligned}
\tag{F.19}
$$

$$
\begin{aligned}
\beta_{z_n} =\ & \left(n-4+\frac{n}{2}\eta_\phi\right)z_n + \frac{z_n^2(6-\eta_\phi)n^2(n-1)\kappa^{n/2}(n-2+2(n-1)\kappa\lambda_4)}{192\pi^2(1+2\kappa\lambda_4)^2(\kappa+z_n n^2 \kappa^{n/2})^2} \\
& + \frac{z_n(6-\eta_\phi)n(n-1)\kappa^2\lambda_4(1+\kappa\lambda_4)}{96\pi^2(1+2\kappa\lambda_4)^2(\kappa+z_n n^2 \kappa^{n/2})^2} \\
& + \frac{z_n^3(6-\eta_\phi)n^4(n^2-3n+2)\kappa^{n-1}}{384\pi^2(1+2\kappa\lambda_4)^2(\kappa+z_n n^2 \kappa^{n/2})^2}
\end{aligned}
\tag{F.20}
$$

The Yukawa beta function is

$$
\begin{aligned}
\beta_y &= \left(\eta_\psi + \frac{\eta_\phi}{2}\right) y - \frac{y^3}{32\pi^2 \left(1 + \kappa y^2\right)^2 \left(1 + 2\kappa\lambda_4\right)} + \frac{y^3}{16\pi^2 \left(1 + \kappa y^2\right)^3 \left(1 + 2\kappa\lambda_4\right)} \\
&\quad + \frac{3n^2 y^3 z_n \lambda_4 \kappa^{\frac{n}{2}+2}}{8\pi^2 \left(1 + \kappa y^2\right) \left(\kappa + n^2 z_n \kappa^{n/2}\right)^2 \left(1 + 2\kappa\lambda_4\right)^2} - \frac{y^3 \kappa}{16\pi^2 \left(1 + \kappa y^2\right)^3 \left(\kappa + n^2 z_n \kappa^{n/2}\right)} \\
&\quad + \frac{3 y^3 \lambda_4 \kappa^3}{8\pi^2 \left(1 + \kappa y^2\right) \left(\kappa + n^2 z_n \kappa^{n/2}\right)^2 \left(1 + 2\kappa\lambda_4\right)^2} + \frac{y^3 \left((n-2)n^2 z_n \kappa^{n/2} + 2\lambda_4 \kappa^2\right) \kappa^2}{16\pi^2 \left(1 + \kappa y^2\right) \left(\kappa + n^2 z_n \kappa^{n/2}\right)^3} \\
&\quad + \frac{y^5 \left(n^2 z_n \kappa^{n/2} + 2\left(1 + \kappa\lambda_4\right)\kappa\right)\kappa^2}{32\pi^2 \left(1 + \kappa y^2\right)^2 \left(\kappa + n^2 z_n \kappa^{n/2}\right)^2 \left(1 + 2\kappa\lambda_4\right)} - \frac{y^5 \kappa}{16\pi^2 \left(1 + \kappa y^2\right)^3 \left(1 + 2\kappa\lambda_4\right)} \\
&\quad + \frac{y^5 \kappa^2}{16\pi^2 \left(1 + \kappa y^2\right)^3 \left(\kappa + n^2 z_n \kappa^{n/2}\right)} - \frac{y^3 \lambda_4 \left((n-2)n^2 z_n \kappa^{n/2} + 2\lambda_4 \kappa^2\right) \kappa^2}{8\pi^2 \left(1 + \kappa y^2\right) \left(\kappa + n^2 z_n \kappa^{n/2}\right)^2 \left(1 + 2\kappa\lambda_4\right)^2} \\
&\quad - \frac{3 y^3 \lambda_4 \kappa^2}{8\pi^2 \left(1 + \kappa y^2\right) \left(\kappa + n^2 z_n \kappa^{n/2}\right) \left(1 + 2\kappa\lambda_4\right)^2} + \frac{y^3 \left((n-2)n^2 z_n \kappa^{n/2} + 2\lambda_4 \kappa^2\right) \kappa}{32\pi^2 \left(1 + \kappa y^2\right)^2 \left(\kappa + n^2 z_n \kappa^{n/2}\right)^2} \\
&\quad + \frac{y^3 \left((n-2)n^2 z_n \kappa^{n/2} + 2\lambda_4 \kappa^2\right) \kappa}{16\pi^2 \left(1 + \kappa y^2\right) \left(\kappa + n^2 z_n \kappa^{n/2}\right)^2 \left(1 + 2\kappa\lambda_4\right)} + \frac{y^3 \kappa}{32\pi^2 \left(1 + \kappa y^2\right)^2 \left(\kappa + n^2 z_n \kappa^{n/2}\right)} \\
&\quad - \frac{y^3 \left(n^2 z_n \kappa^{n/2} + 2\left(\kappa\lambda_4 + 1\right)\kappa\right) \kappa}{32\pi^2 \left(1 + \kappa y^2\right)^2 \left(\kappa + n^2 z_n \kappa^{n/2}\right)^2 \left(1 + 2\kappa\lambda_4\right)} - \frac{3 y^3 \lambda_4 \kappa}{16\pi^2 \left(1 + \kappa y^2\right)^2 \left(1 + 2\kappa\lambda_4\right)^2} \\
&\quad - \frac{y^5 \left(n^2 z_n \kappa^{n/2} + 2\left(\kappa\lambda_4 + 1\right)\kappa\right) \kappa}{32\pi^2 \left(1 + \kappa y^2\right)^2 \left(\kappa + n^2 z_n \kappa^{n/2}\right) \left(1 + 2\kappa\lambda_4\right)^2} - \frac{3 y^3 \lambda_4 \kappa}{8\pi^2 \left(1 + \kappa y^2\right) \left(1 + 2\kappa\lambda_4\right)^3} \\
&\quad - \frac{y^3 \left((n-2)n^2 z_n \kappa^{n/2} + 2\lambda_4 \kappa^2\right) \kappa}{16\pi^2 \left(1 + \kappa y^2\right) \left(\kappa + n^2 z_n \kappa^{n/2}\right)^2 \left(1 + 2\kappa\lambda_4\right)^2} \\
&\quad + \frac{y^3 \left(n^2 z_n \kappa^{n/2} + 2\left(\kappa\lambda_4 + 1\right)\kappa\right)}{32\pi^2 \left(1 + \kappa y^2\right)^2 \left(\kappa + n^2 z_n \kappa^{n/2}\right) \left(1 + 2\kappa\lambda_4\right)^2}.
\end{aligned}
\tag{F.21}
$$

In the last expression we neglected the anomalous dimensions in the numerators for brevity.

Bibliography

[1] Astrid Eichhorn and Martin Pauly. "Safety in darkness: Higgs portal to simple Yukawa systems". In: *Phys. Lett. B* 819 (2021), p. 136455. DOI: 10.1016/j.physletb.2021.136455. arXiv: 2005.03661 [hep-ph].

[2] Astrid Eichhorn and Martin Pauly. "Constraining power of asymptotic safety for scalar fields". In: *Phys. Rev. D* 103.2 (2021), p. 026006. DOI: 10.1103/PhysRevD.103.026006. arXiv: 2009.13543 [hep-th].

[3] Passant Ali et al. "Constraints on discrete global symmetries in quantum gravity". In: *JHEP* 05 (2021), p. 036. DOI: 10.1007/JHEP05(2021)036. arXiv: 2012.07868 [gr-qc].

[4] Astrid Eichhorn and Martin Pauly. "A sprinkling of hybrid-signature discrete spacetimes in real-world networks". In: (July 2021). arXiv: 2107.07325 [cond-mat.dis-nn].

[5] Astrid Eichhorn, Martin Pauly, and Shouryya Ray. "Towards a Higgs mass determination in asymptotically safe gravity with a dark portal". In: (July 2021). arXiv: 2107.07949 [hep-ph].

[6] B. P. Abbott et al. "Observation of Gravitational Waves from a Binary Black Hole Merger". In: *Phys. Rev. Lett.* 116.6 (2016), p. 061102. DOI: 10.1103/PhysRevLett.116.061102. arXiv: 1602.03837 [gr-qc].

[7] Kazunori Akiyama et al. "First M87 Event Horizon Telescope Results. I. The Shadow of the Supermassive Black Hole". In: *Astrophys. J. Lett.* 875 (2019), p. L1. DOI: 10.3847/2041-8213/ab0ec7. arXiv: 1906.11238 [astro-ph.GA].

[8] Georges Aad et al. "Observation of a new particle in the search for the Standard Model Higgs boson with the ATLAS detector at the LHC". In: *Phys. Lett. B* 716 (2012), pp. 1–29. DOI: 10.1016/j.physletb.2012.08.020. arXiv: 1207.7214 [hep-ex].

[9] Serguei Chatrchyan et al. "Observation of a New Boson at a Mass of 125 GeV with the CMS Experiment at the LHC". In: *Phys. Lett. B* 716 (2012), pp. 30–61. DOI: 10.1016/j.physletb.2012.08.021. arXiv: 1207.7235 [hep-ex].

[10] N. Aghanim et al. "Planck 2018 results. VI. Cosmological parameters". In: *Astron. Astrophys.* 641 (2020), A6. DOI: 10.1051/0004-6361/201833910. arXiv: 1807.06209 [astro-ph.CO].

[11] M. Gockeler et al. "Is there a Landau pole problem in QED?" In: *Phys. Rev. Lett.* 80 (1998), pp. 4119–4122. DOI: 10.1103/PhysRevLett.80.4119. arXiv: hep-th/9712244.

[12] M. Gockeler et al. "Resolution of the Landau pole problem in QED". In: *Nucl. Phys. B Proc. Suppl.* 63 (1998). Ed. by C. T. H. Davies et al., pp. 694–696. DOI: 10.1016/S0920-5632(97)00875-X. arXiv: hep-lat/9801004.

[13] Holger Gies and Joerg Jaeckel. "Renormalization flow of QED". In: *Phys. Rev. Lett.* 93 (2004), p. 110405. DOI: 10.1103/PhysRevLett.93.110405. arXiv: hep-ph/0405183.

[14] P. A. Zyla et al. "Review of Particle Physics". In: *PTEP* 2020.8 (2020), p. 083C01. DOI: 10.1093/ptep/ptaa104.

[15] Luca Bombelli et al. "Space-Time as a Causal Set". In: *Phys. Rev. Lett.* 59 (1987), pp. 521–524. DOI: 10.1103/PhysRevLett.59.521.

[16] Ed Bullmore and Olaf Sporns. "Complex brain networks: graph theoretical analysis of structural and functional systems". In: *Nature reviews neuroscience* 10.3 (2009), pp. 186–198.

[17] Olaf Sporns. "The human connectome: a complex network". In: *Annals of the new York Academy of Sciences* 1224.1 (2011), pp. 109–125.

[18] Luiz Pessoa. "Understanding brain networks and brain organization". In: *Physics of life reviews* 11.3 (2014), pp. 400–435.

[19] Marc Barthélemy. "Spatial networks". In: *Physics Reports* 499.1-3 (2011), pp. 1–101.

[20] Marian Boguna, Dmitri Krioukov, and Kimberly C Claffy. "Navigability of complex networks". In: *Nature Physics* 5.1 (2009), pp. 74–80.

[21] Dmitri Krioukov et al. "Hyperbolic geometry of complex networks". In: *Physical Review E* 82.3 (2010), p. 036106.

[22] Marián Boguná, Fragkiskos Papadopoulos, and Dmitri Krioukov. "Sustaining the internet with hyperbolic mapping". In: *Nature communications* 1.1 (2010), pp. 1–8.

[23] M Ángeles Serrano, Marián Boguná, and Francesc Sagués. "Uncovering the hidden geometry behind metabolic networks". In: *Molecular biosystems* 8.3 (2012), pp. 843–850.

[24] Guillermo García-Pérez et al. "The hidden hyperbolic geometry of international trade: World Trade Atlas 1870–2013". In: *Scientific reports* 6.1 (2016), pp. 1–10.

[25] Fan RK Chung and Fan Chung Graham. *Spectral graph theory*. 92. American Mathematical Soc., 1997.

[26] O. Lauscher and M. Reuter. "Fractal spacetime structure in asymptotically safe gravity". In: *JHEP* 10 (2005), p. 050. DOI: 10.1088/1126-6708/2005/10/050. arXiv: hep-th/0508202.

[27] Stefan Rechenberger and Frank Saueressig. "The R^2 phase-diagram of QEG and its spectral dimension". In: *Phys. Rev. D* 86 (2012), p. 024018. DOI: 10.1103/PhysRevD.86.024018. arXiv: 1206.0657 [hep-th].

[28] Martin Reuter and Frank Saueressig. "Fractal space-times under the microscope: A Renormalization Group view on Monte Carlo data". In: *JHEP* 12 (2011), p. 012. DOI: 10.1007/JHEP12(2011)012. arXiv: 1110.5224 [hep-th].

[29] J. Ambjorn, J. Jurkiewicz, and R. Loll. "Spectral dimension of the universe". In: *Phys. Rev. Lett.* 95 (2005), p. 171301. DOI: 10.1103/PhysRevLett.95.171301. arXiv: hep-th/0505113.

[30] Dario Benedetti and Joe Henson. "Spectral geometry as a probe of quantum spacetime". In: *Phys. Rev. D* 80 (2009), p. 124036. DOI: 10.1103/PhysRevD.80.124036. arXiv: 0911.0401 [hep-th].

[31] J. Laiho et al. "Lattice Quantum Gravity and Asymptotic Safety". In: *Phys. Rev. D* 96.6 (2017), p. 064015. DOI: 10.1103/PhysRevD.96.064015. arXiv: 1604.02745 [hep-th].

[32] Gianluca Calcagni, Daniele Oriti, and Johannes Thürigen. "Dimensional flow in discrete quantum geometries". In: *Phys. Rev. D* 91.8 (2015), p. 084047. DOI: 10.1103/PhysRevD.91.084047. arXiv: 1412.8390 [hep-th].

[33] Astrid Eichhorn, Sebastian Mizera, and Sumati Surya. "Echoes of Asymptotic Silence in Causal Set Quantum Gravity". In: *Class. Quant. Grav.* 34.16 (2017), 16LT01. DOI: 10.1088/1361-6382/aa7d1b. arXiv: 1703.08454 [gr-qc].

[34] Astrid Eichhorn, Sumati Surya, and Fleur Versteegen. "Spectral dimension on spatial hypersurfaces in causal set quantum gravity". In: *Class. Quant. Grav.* 36.23 (2019), p. 235013. DOI: 10.1088/1361-6382/ab47cd. arXiv: 1905.13498 [gr-qc].

[35] Petr Horava. "Spectral Dimension of the Universe in Quantum Gravity at a Lifshitz Point". In: *Phys. Rev. Lett.* 102 (2009), p. 161301. DOI: 10.1103/PhysRevLett.102.161301. arXiv: 0902.3657 [hep-th].

[36] Dario Benedetti. "Fractal properties of quantum spacetime". In: *Phys. Rev. Lett.* 102 (2009), p. 111303. DOI: 10.1103/PhysRevLett.102.111303. arXiv: 0811.1396 [hep-th].

[37] Gianluca Calcagni, Astrid Eichhorn, and Frank Saueressig. "Probing the quantum nature of spacetime by diffusion". In: *Phys. Rev. D* 87.12 (2013), p. 124028. DOI: 10.1103/PhysRevD.87.124028. arXiv: 1304.7247 [hep-th].

[38] M. E. J. Newman and D. J. Watts. "Renormalization group analysis of the small-world network model". In: *Physics Letters A* 263.4-6 (Dec. 1999), pp. 341–346. DOI: 10.1016/S0375-9601(99)00757-4. arXiv: cond-mat/9903357 [cond-mat.stat-mech].

[39] Mark EJ Newman and Duncan J Watts. "Scaling and percolation in the small-world network model". In: *Physical review E* 60.6 (1999), p. 7332.

[40] Sumati Surya. "The causal set approach to quantum gravity". In: *Living Rev. Rel.* 22.1 (2019), p. 5. DOI: 10.1007/s41114-019-0023-1. arXiv: 1903.11544 [gr-qc].

[41] David Mattingly. "Modern tests of Lorentz invariance". In: *Living Rev. Rel.* 8 (2005), p. 5. DOI: 10.12942/lrr-2005-5. arXiv: gr-qc/0502097.

[42] NH Christ, R Friedberg, and T_D Lee. "Random lattice field theory: General formulation". In: *Nuclear Physics B* 202.1 (1982), pp. 89–125.

[43] William Cunningham, Konstantin Zuev, and Dmitri Krioukov. "Navigability of Random Geometric Graphs in the Universe and Other Spacetimes". In: *Sci. Rep.* 7.1 (2017), p. 8699. DOI: 10.1038/s41598-017-08872-4. arXiv: 1703.09057 [gr-qc].

[44] Astrid Eichhorn and Sebastian Mizera. "Spectral dimension in causal set quantum gravity". In: *Class. Quant. Grav.* 31 (2014), p. 125007. DOI: 10.1088/0264-9381/31/12/125007. arXiv: 1311.2530 [gr-qc].

[45] S. Carlip. "Dimensional reduction in causal set gravity". In: *Class. Quant. Grav.* 32.23 (2015), p. 232001. DOI: 10.1088/0264-9381/32/23/232001. arXiv: 1506.08775 [gr-qc].

[46] S. Carlip. "Spontaneous Dimensional Reduction in Quantum Gravity". In: *Int. J. Mod. Phys. D* 25.12 (2016), p. 1643003. DOI: 10.1142/S0218271816430033. arXiv: 1605.05694 [gr-qc].

[47] Jan Myrheim. *Statistical geometry*. Tech. rep. Geneva: CERN, Aug. 1978. URL: https://cds.cern.ch/record/293594.

[48] Luca Bombelli. "Space-time as a causal set". PhD thesis. Massachusetts Institute of Technology, 1988. URL: https://surface.syr.edu/phy_etd/88.

[49] David D. Reid. "The Manifold dimension of a causal set: Tests in conformally flat spacetimes". In: *Phys. Rev. D* 67 (2003), p. 024034. DOI: 10.1103/PhysRevD.67.024034. arXiv: gr-qc/0207103.

[50] Lisa Glaser and Sumati Surya. "Towards a Definition of Locality in a Manifoldlike Causal Set". In: *Phys. Rev. D* 88.12 (2013), p. 124026. DOI: 10.1103/PhysRevD.88.124026. arXiv: 1309.3403 [gr-qc].

[51] M. Aghili, L. Bombelli, and BB Pilgrim. "Discrete Spacetime: a Web of Chains". In: *Class. Quant. Grav.* 36.18 (2019), p. 185015. DOI: 10.1088/1361-6382/ab30e3. arXiv: 1807.08701 [gr-qc].

[52] James R Clough and Tim S Evans. "What is the dimension of citation space?" In: *Physica A: Statistical Mechanics and its Applications* 448 (2016), pp. 235–247.

[53] Duncan J Watts and Steven H Strogatz. "Collective dynamics of 'small-world'networks". In: *nature* 393.6684 (1998), pp. 440–442.

[54] Parongama Sen, Kinjal Banerjee, and Turbasu Biswas. "Phase transitions in a network with a range-dependent connection probability". In: *Physical Review E* 66.3 (2002), p. 037102.

[55] Sven Bilke and Carsten Peterson. "Topological properties of citation and metabolic networks". In: *Physical Review E* 64.3 (2001), p. 036106.

[56] Raffaella Burioni et al. "Topological thermal instability and length of proteins". In: *Proteins: Structure, Function, and Bioinformatics* 55.3 (2004), pp. 529–535.

[57] Zhihao Wu et al. "Emergent complex network geometry". In: *Scientific reports* 5.1 (2015), pp. 1–12.

[58] Lawrence Page et al. *The PageRank citation ranking: Bringing order to the web.* Tech. rep. Stanford InfoLab, 1999.

[59] *The CAIDA UCSD IPv4 Routed /24 Topology Dataset - Feb. 28th, 2020*. http://www.caida.org/data/active/ipv4_routed_24_topology_dataset.xml. Accessed: 2021-04-19.

[60] Danielle S Bassett and Olaf Sporns. "Network neuroscience". In: *Nature neuroscience* 20.3 (2017), pp. 353–364.

[61] Andrea Avena-Koenigsberger, Bratislav Misic, and Olaf Sporns. "Communication dynamics in complex brain networks". In: *Nature Reviews Neuroscience* 19.1 (2018), p. 17.

[62] C Shan Xu et al. "A connectome of the adult drosophila central brain". In: *BioRxiv* (2020).

[63] A. Anderson and Bryce S. DeWitt. "Does the Topology of Space Fluctuate?" In: *Found. Phys.* 16 (1986), pp. 91–105. DOI: 10.1007/BF01889374.

[64] Corinne A Manogue, ED Copeland, and Tevian Dray. "The trousers problem revisited". In: *Pramana* 30.4 (1988), pp. 279–292.

[65] Andreas Nink. "Field Parametrization Dependence in Asymptotically Safe Quantum Gravity". In: *Phys. Rev. D* 91.4 (2015), p. 044030. DOI: 10.1103/PhysRevD.91.044030. arXiv: 1410.7816 [hep-th].

[66] Holger Gies, Benjamin Knorr, and Stefan Lippoldt. "Generalized Parametrization Dependence in Quantum Gravity". In: *Phys. Rev. D* 92.8 (2015), p. 084020. DOI: 10.1103/PhysRevD.92.084020. arXiv: 1507.08859 [hep-th].

[67] Kevin Falls. "Renormalization of Newton's constant". In: *Phys. Rev. D* 92.12 (2015), p. 124057. DOI: 10.1103/PhysRevD.92.124057. arXiv: 1501.05331 [hep-th].

[68] Peter Labus, Roberto Percacci, and Gian Paolo Vacca. "Asymptotic safety in $O(N)$ scalar models coupled to gravity". In: *Phys. Lett. B* 753 (2016), pp. 274–281. DOI: 10.1016/j.physletb.2015.12.022. arXiv: 1505.05393 [hep-th].

[69] Gustavo P. De Brito et al. "Asymptotic safety and field parametrization dependence in the $f(R)$ truncation". In: *Phys. Rev. D* 98.2 (2018), p. 026027. DOI: 10.1103/PhysRevD.98.026027. arXiv: 1805.09656 [hep-th].

[70] Alessio Baldazzi, Roberto Percacci, and Vedran Skrinjar. "Wicked metrics". In: *Class. Quant. Grav.* 36.10 (2019), p. 105008. DOI: 10.1088/1361-6382/ab187d. arXiv: 1811.03369 [gr-qc].

[71] Gerard 't Hooft and M. J. G. Veltman. "One loop divergencies in the theory of gravitation". In: *Ann. Inst. H. Poincare Phys. Theor. A* 20 (1974), pp. 69–94.

[72] Marc H. Goroff and Augusto Sagnotti. "QUANTUM GRAVITY AT TWO LOOPS". In: *Phys. Lett. B* 160 (1985), pp. 81–86. DOI: 10.1016/0370-2693(85)91470-4.

[73] Marc H. Goroff and Augusto Sagnotti. "The Ultraviolet Behavior of Einstein Gravity". In: *Nucl. Phys. B* 266 (1986), pp. 709–736. DOI: 10.1016/0550-3213(86)90193-8.

[74] A. E. M. van de Ven. "Two loop quantum gravity". In: *Nucl. Phys. B* 378 (1992), pp. 309–366. DOI: 10.1016/0550-3213(92)90011-Y.

[75] S. Deser and P. van Nieuwenhuizen. "Nonrenormalizability of the Quantized Einstein-Maxwell System". In: *Phys. Rev. Lett.* 32 (1974), pp. 245–247. DOI: 10.1103/PhysRevLett.32.245.

[76] John F. Donoghue. "Leading quantum correction to the Newtonian potential". In: *Phys. Rev. Lett.* 72 (1994), pp. 2996–2999. DOI: 10.1103/PhysRevLett.72.2996. arXiv: gr-qc/9310024.

[77] John F. Donoghue. "General relativity as an effective field theory: The leading quantum corrections". In: *Phys. Rev. D* 50 (1994), pp. 3874–3888. DOI: 10.1103/PhysRevD.50.3874. arXiv: gr-qc/9405057.

[78] Daniel F. Litim and Francesco Sannino. "Asymptotic safety guaranteed". In: *JHEP* 12 (2014), p. 178. DOI: 10.1007/JHEP12(2014)178. arXiv: 1406.2337 [hep-th].

[79] Kenneth G. Wilson and Michael E. Fisher. "Critical exponents in 3.99 dimensions". In: *Phys. Rev. Lett.* 28 (1972), pp. 240–243. DOI: 10.1103/PhysRevLett.28.240.

[80] Holger Gies. "Introduction to the functional RG and applications to gauge theories". In: *Lect. Notes Phys.* 852 (2012), pp. 287–348. DOI: 10.1007/978-3-642-27320-9_6. arXiv: hep-ph/0611146.

[81] Christof Wetterich. "Exact evolution equation for the effective potential". In: *Phys. Lett. B* 301 (1993), pp. 90–94. DOI: 10.1016/0370-2693(93)90726-X. arXiv: 1710.05815 [hep-th].

[82] Ulrich Ellwanger. "FLow equations for N point functions and bound states". In: *Z. Phys. C* 62 (1994). Ed. by B. Geyer and E. M. Ilgenfritz, pp. 503–510. DOI: 10.1007/BF01555911. arXiv: hep-ph/9308260.

[83] Tim R. Morris. "The Exact renormalization group and approximate solutions". In: *Int. J. Mod. Phys. A* 9 (1994), pp. 2411–2450. DOI: 10.1142/S0217751X94000972. arXiv: hep-ph/9308265.

[84] Daniel F. Litim. "Optimized renormalization group flows". In: *Phys. Rev. D* 64 (2001), p. 105007. DOI: 10.1103/PhysRevD.64.105007. arXiv: hep-th/0103195.

[85] Benjamin Knorr. "Exact solutions and residual regulator dependence in functional renormalisation group flows". In: *J. Phys. A* 54.27 (2021), p. 275401. DOI: 10.1088/1751-8121/ac00d4. arXiv: 2012.06499 [hep-th].

[86] Jobst Ziebell. "Existence and construction of exact functional-renormalization-group flows of a UV-interacting scalar field theory". In: *Phys. Rev. D* 103.2 (2021), p. 025002. DOI: 10.1103/PhysRevD.103.025002. arXiv: 2009.13100 [hep-th].

[87] Alfio Bonanno et al. "Critical reflections on asymptotically safe gravity". In: *Front. in Phys.* 8 (2020), p. 269. DOI: 10.3389/fphy.2020.00269. arXiv: 2004.06810 [gr-qc].

[88] Alessandro Codello. "Polyakov Effective Action from Functional Renormalization Group Equation". In: *Annals Phys.* 325 (2010), pp. 1727–1738. DOI: 10.1016/j.aop.2010.04.013. arXiv: 1004.2171 [hep-th].

[89] Astrid Eichhorn and Holger Gies. "Ghost anomalous dimension in asymptotically safe quantum gravity". In: *Phys. Rev. D* 81 (2010), p. 104010. DOI: 10.1103/PhysRevD.81.104010. arXiv: 1001.5033 [hep-th].

[90] Matthew D. Schwartz. *Quantum Field Theory and the Standard Model*. Cambridge University Press, Mar. 2014. ISBN: 978-1-107-03473-0, 978-1-107-03473-0.

[91] N. Dupuis et al. "The nonperturbative functional renormalization group and its applications". In: *Phys. Rept.* 910 (2021), pp. 1–114. DOI: 10.1016/j.physrep.2021.01.001. arXiv: 2006.04853 [cond-mat.stat-mech].

[92] Juergen Berges, Nikolaos Tetradis, and Christof Wetterich. "Nonperturbative renormalization flow in quantum field theory and statistical physics". In: *Phys. Rept.* 363 (2002), pp. 223–386. DOI: 10.1016/S0370-1573(01)00098-9. arXiv: hep-ph/0005122.

[93] Jan M. Pawlowski. "Aspects of the functional renormalisation group". In: *Annals Phys.* 322 (2007), pp. 2831–2915. DOI: 10.1016/j.aop.2007.01.007. arXiv: hep-th/0512261.

[94] Oliver J. Rosten. "Fundamentals of the Exact Renormalization Group". In: *Phys. Rept.* 511 (2012), pp. 177–272. DOI: 10.1016/j.physrep.2011.12.003. arXiv: 1003.1366 [hep-th].

[95] Steven Weinberg. "ULTRAVIOLET DIVERGENCES IN QUANTUM THEORIES OF GRAVITATION". In: *General Relativity: An Einstein Centenary Survey*. 1980.

[96] M. Reuter. "Nonperturbative evolution equation for quantum gravity". In: *Phys. Rev. D* 57 (1998), pp. 971–985. DOI: 10.1103/PhysRevD.57.971. arXiv: hep-th/9605030.

[97] Max Niedermaier and Martin Reuter. "The Asymptotic Safety Scenario in Quantum Gravity". In: *Living Rev. Rel.* 9 (2006), pp. 5–173. DOI: 10.12942/lrr-2006-5.

[98] M. Reuter and C. Wetterich. "Effective average action for gauge theories and exact evolution equations". In: *Nucl. Phys. B* 417 (1994), pp. 181–214. DOI: 10.1016/0550-3213(94)90543-6.

[99] Benjamin Knorr and Stefan Lippoldt. "Correlation functions on a curved background". In: *Phys. Rev. D* 96.6 (2017), p. 065020. DOI: 10.1103/PhysRevD.96.065020. arXiv: 1707.01397 [hep-th].

[100] Benjamin Knorr. "The derivative expansion in asymptotically safe quantum gravity: general setup and quartic order". In: (Apr. 2021). arXiv: 2104.11336 [hep-th].

[101] Robert Percacci. *An Introduction to Covariant Quantum Gravity and Asymptotic Safety*. Vol. 3. 100 Years of General Relativity. World Scientific, 2017. ISBN: 978-981-320-717-2, 978-981-320-719-6. DOI: 10.1142/10369.

[102] Astrid Eichhorn. "An asymptotically safe guide to quantum gravity and matter". In: *Front. Astron. Space Sci.* 5 (2019), p. 47. DOI: 10.3389/fspas.2018.00047. arXiv: 1810.07615 [hep-th].

[103] Martin Reuter and Frank Saueressig. *Quantum Gravity and the Functional Renormalization Group: The Road towards Asymptotic Safety*. Cambridge University Press, Jan. 2019. ISBN: 978-1-107-10732-8, 978-1-108-67074-6.

[104] Antonio D. Pereira. "Quantum spacetime and the renormalization group: Progress and visions". In: *Progress and Visions in Quantum Theory in View of Gravity: Bridging foundations of physics and mathematics*. Apr. 2019. arXiv: 1904.07042 [gr-qc].

[105] Astrid Eichhorn. "Asymptotically safe gravity". In: *57th International School of Subnuclear Physics: In Search for the Unexpected*. Feb. 2020. arXiv: 2003.00044 [gr-qc].

[106] Manuel Reichert. "Lecture notes: Functional Renormalisation Group and Asymptotically Safe Quantum Gravity". In: *PoS* 384 (2020), p. 005. DOI: 10.22323/1.384.0005.

[107] Jan M. Pawlowski and Manuel Reichert. "Quantum gravity: a fluctuating point of view". In: (July 2020). arXiv: 2007.10353 [hep-th].

[108] M. Reuter and H. Weyer. "Quantum gravity at astrophysical distances?" In: *JCAP* 12 (2004), p. 001. DOI: 10.1088/1475-7516/2004/12/001. arXiv: hep-th/0410119.

[109] Giulia Gubitosi et al. "Consistent early and late time cosmology from the RG flow of gravity". In: *JCAP* 12 (2018), p. 004. DOI: 10.1088/1475-7516/2018/12/004. arXiv: 1806.10147 [hep-th].

[110] K. Falls et al. "A bootstrap towards asymptotic safety". In: (Jan. 2013). arXiv: 1301.4191 [hep-th].

[111] Kevin Falls et al. "Further evidence for asymptotic safety of quantum gravity". In: *Phys. Rev. D* 93.10 (2016), p. 104022. DOI: 10.1103/PhysRevD.93.104022. arXiv: 1410.4815 [hep-th].

[112] Kevin Falls et al. "Asymptotic safety of quantum gravity beyond Ricci scalars". In: *Phys. Rev. D* 97.8 (2018), p. 086006. DOI: 10.1103/PhysRevD.97.086006. arXiv: 1801.00162 [hep-th].

[113] Kevin G. Falls, Daniel F. Litim, and Jan Schröder. "Aspects of asymptotic safety for quantum gravity". In: *Phys. Rev. D* 99.12 (2019), p. 126015. DOI: 10.1103/PhysRevD.99.126015. arXiv: 1810.08550 [gr-qc].

[114] Yannick Kluth and Daniel F. Litim. "Fixed Points of Quantum Gravity and the Dimensionality of the UV Critical Surface". In: (Aug. 2020). arXiv: 2008.09181 [hep-th].

[115] Dario Benedetti, Pedro F. Machado, and Frank Saueressig. "Asymptotic safety in higher-derivative gravity". In: *Mod. Phys. Lett. A* 24 (2009), pp. 2233–2241. DOI: 10.1142/S0217732309031521. arXiv: 0901.2984 [hep-th].

[116] Holger Gies et al. "Gravitational Two-Loop Counterterm Is Asymptotically Safe". In: *Phys. Rev. Lett.* 116.21 (2016), p. 211302. DOI: 10.1103/PhysRevLett.116.211302. arXiv: 1601.01800 [hep-th].

[117] Kevin Falls, Nobuyoshi Ohta, and Roberto Percacci. "Towards the determination of the dimension of the critical surface in asymptotically safe gravity". In: *Phys. Lett. B* 810 (2020), p. 135773. DOI: 10.1016/j.physletb.2020.135773. arXiv: 2004.04126 [hep-th].

[118] Nicolai Christiansen et al. "Global Flows in Quantum Gravity". In: *Phys. Rev. D* 93.4 (2016), p. 044036. DOI: 10.1103/PhysRevD.93.044036. arXiv: 1403.1232 [hep-th].

[119] Nicolai Christiansen et al. "Local Quantum Gravity". In: *Phys. Rev. D* 92.12 (2015), p. 121501. DOI: 10.1103/PhysRevD.92.121501. arXiv: 1506.07016 [hep-th].

[120] Tobias Denz, Jan M. Pawlowski, and Manuel Reichert. "Towards apparent convergence in asymptotically safe quantum gravity". In: *Eur. Phys. J. C* 78.4 (2018), p. 336. DOI: 10.1140/epjc/s10052-018-5806-0. arXiv: 1612.07315 [hep-th].

[121] Benjamin Knorr, Chris Ripken, and Frank Saueressig. "Form Factors in Asymptotic Safety: conceptual ideas and computational toolbox". In: *Class. Quant. Grav.* 36.23 (2019), p. 234001. DOI: 10.1088/1361-6382/ab4a53. arXiv: 1907.02903 [hep-th].

[122] Lando Bosma, Benjamin Knorr, and Frank Saueressig. "Resolving Spacetime Singularities within Asymptotic Safety". In: *Phys. Rev. Lett.* 123.10 (2019), p. 101301. DOI: 10.1103/PhysRevLett.123.101301. arXiv: 1904.04845 [hep-th].

[123] Alfio Bonanno et al. "Reconstructing the graviton". In: (Feb. 2021). arXiv: 2102.02217 [hep-th].

[124] Ivan Donkin and Jan M. Pawlowski. "The phase diagram of quantum gravity from diffeomorphism-invariant RG-flows". In: (Mar. 2012). arXiv: 1203.4207 [hep-th].

[125] Astrid Eichhorn et al. "Effective universality in quantum gravity". In: *SciPost Phys.* 5.4 (2018), p. 031. DOI: 10.21468/SciPostPhys.5.4.031. arXiv: 1804.00012 [hep-th].

[126] Nicolai Christiansen et al. "Curvature dependence of quantum gravity". In: *Phys. Rev. D* 97.4 (2018), p. 046007. DOI: 10.1103/PhysRevD.97.046007. arXiv: 1711.09259 [hep-th].

[127] Nicolai Christiansen et al. "Fixed points and infrared completion of quantum gravity". In: *Phys. Lett. B* 728 (2014), pp. 114–117. DOI: 10.1016/j.physletb.2013.11.025. arXiv: 1209.4038 [hep-th].

[128] Nicolai Christiansen. "Four-Derivative Quantum Gravity Beyond Perturbation Theory". In: (Dec. 2016). arXiv: 1612.06223 [hep-th].

[129] Astrid Eichhorn et al. "How perturbative is quantum gravity?" In: *Phys. Lett. B* 792 (2019), pp. 310–314. DOI: 10.1016/j.physletb.2019.01.071. arXiv: 1810.02828 [hep-th].

[130] Astrid Eichhorn, Stefan Lippoldt, and Marc Schiffer. "Zooming in on fermions and quantum gravity". In: *Phys. Rev. D* 99.8 (2019), p. 086002. DOI: 10.1103/PhysRevD.99.086002. arXiv: 1812.08782 [hep-th].

[131] Max R. Niedermaier. "Gravitational Fixed Points from Perturbation Theory". In: *Phys. Rev. Lett.* 103 (2009), p. 101303. DOI: 10.1103/PhysRevLett.103.101303.

[132] M. Niedermaier. "Gravitational fixed points and asymptotic safety from perturbation theory". In: *Nucl. Phys. B* 833 (2010), pp. 226–270. DOI: 10.1016/j.nuclphysb.2010.01.016.

[133] R. Gastmans, R. Kallosh, and C. Truffin. "Quantum Gravity Near Two-Dimensions". In: *Nucl. Phys. B* 133 (1978), pp. 417–434. DOI: 10.1016/0550-3213(78)90234-1.

[134] S. M. Christensen and M. J. Duff. "Quantum Gravity in Two + ϵ Dimensions". In: *Phys. Lett. B* 79 (1978), pp. 213–216. DOI: 10.1016/0370-2693(78)90225-3.

[135] Hikaru Kawai and Masao Ninomiya. "Renormalization Group and Quantum Gravity". In: *Nucl. Phys. B* 336 (1990), pp. 115–145. DOI: 10.1016/0550-3213(90)90345-E.

[136] I. Jack and D. R. T. Jones. "The Epsilon expansion of two-dimensional quantum gravity". In: *Nucl. Phys. B* 358 (1991), pp. 695–712. DOI: 10.1016/0550-3213(91)90430-6.

[137] Toshiaki Aida and Yoshihisa Kitazawa. "Two loop prediction for scaling exponents in (2+epsilon)-dimensional quantum gravity". In: *Nucl. Phys. B* 491 (1997), pp. 427–460. DOI: 10.1016/S0550-3213(97)00091-6. arXiv: hep-th/9609077.

[138] R. Loll. "Quantum Gravity from Causal Dynamical Triangulations: A Review". In: *Class. Quant. Grav.* 37.1 (2020), p. 013002. DOI: 10.1088/1361-6382/ab57c7. arXiv: 1905.08669 [hep-th].

[139] Astrid Eichhorn, Tim Koslowski, and Antonio D. Pereira. "Status of background-independent coarse-graining in tensor models for quantum gravity". In: *Universe* 5.2 (2019), p. 53. DOI: 10.3390/universe5020053. arXiv: 1811.12909 [gr-qc].

[140] Pietro Donà, Astrid Eichhorn, and Roberto Percacci. "Matter matters in asymptotically safe quantum gravity". In: *Phys. Rev. D* 89.8 (2014), p. 084035. DOI: 10.1103/PhysRevD.89.084035. arXiv: 1311.2898 [hep-th].

[141] Jan Meibohm, Jan M. Pawlowski, and Manuel Reichert. "Asymptotic safety of gravity-matter systems". In: *Phys. Rev. D* 93.8 (2016), p. 084035. DOI: 10.1103/PhysRevD.93.084035. arXiv: 1510.07018 [hep-th].

[142] Pietro Donà et al. "Asymptotic safety in an interacting system of gravity and scalar matter". In: *Phys. Rev. D* 93.4 (2016). [Erratum: Phys.Rev.D 93, 129904 (2016)], p. 044049. DOI: 10.1103/PhysRevD.93.129904. arXiv: 1512.01589 [gr-qc].

[143] Jorn Biemans, Alessia Platania, and Frank Saueressig. "Renormalization group fixed points of foliated gravity-matter systems". In: *JHEP* 05 (2017), p. 093. DOI: 10.1007/JHEP05(2017)093. arXiv: 1702.06539 [hep-th].

[144] Natália Alkofer and Frank Saueressig. "Asymptotically safe $f(R)$-gravity coupled to matter I: the polynomial case". In: *Annals Phys.* 396 (2018), pp. 173–201. DOI: 10.1016/j.aop.2018.07.017. arXiv: 1802.00498 [hep-th].

[145] Christof Wetterich and Masatoshi Yamada. "Variable Planck mass from the gauge invariant flow equation". In: *Phys. Rev. D* 100.6 (2019), p. 066017. DOI: 10.1103/PhysRevD.100.066017. arXiv: 1906.01721 [hep-th].

[146] Astrid Eichhorn and Stefan Lippoldt. "Quantum gravity and Standard-Model-like fermions". In: *Phys. Lett. B* 767 (2017), pp. 142–146. DOI: 10.1016/j.physletb.2017.01.064. arXiv: 1611.05878 [gr-qc].

[147] Astrid Eichhorn and Aaron Held. "Top mass from asymptotic safety". In: *Phys. Lett. B* 777 (2018), pp. 217–221. DOI: 10.1016/j.physletb.2017.12.040. arXiv: 1707.01107 [hep-th].

[148] Senarath de Alwis et al. "Asymptotic safety, string theory and the weak gravity conjecture". In: *Phys. Lett. B* 798 (2019), p. 134991. DOI: 10.1016/j.physletb.2019.134991. arXiv: 1907.07894 [hep-th].

[149] Roberto Percacci and Gian Paolo Vacca. "Asymptotic Safety, Emergence and Minimal Length". In: *Class. Quant. Grav.* 27 (2010), p. 245026. DOI: 10.1088/0264-9381/27/24/245026. arXiv: 1008.3621 [hep-th].

[150] Aaron Held. "Effective asymptotic safety and its predictive power: Gauge-Yukawa theories". In: *Front. in Phys.* 8 (2020), p. 341. DOI: 10.3389/fphy.2020.00341. arXiv: 2003.13642 [hep-th].

[151] B. Pendleton and Graham G. Ross. "Mass and Mixing Angle Predictions from Infrared Fixed Points". In: *Phys. Lett. B* 98 (1981), pp. 291–294. DOI: 10.1016/0370-2693(81)90017-4.

[152] Christopher T. Hill. "Quark and Lepton Masses from Renormalization Group Fixed Points". In: *Phys. Rev. D* 24 (1981), p. 691. DOI: 10.1103/PhysRevD.24.691.

[153] Eran Palti. "The Swampland: Introduction and Review". In: *Fortsch. Phys.* 67.6 (2019), p. 1900037. DOI: 10.1002/prop.201900037. arXiv: 1903.06239 [hep-th].

[154] Astrid Eichhorn. "Status of the asymptotic safety paradigm for quantum gravity and matter". In: *Found. Phys.* 48.10 (2018), pp. 1407–1429. DOI: 10.1007/s10701-018-0196-6. arXiv: 1709.03696 [gr-qc].

[155] Yu Hamada, Jan M. Pawlowski, and Masatoshi Yamada. "Gravitational instantons and anomalous chiral symmetry breaking". In: *Phys. Rev. D* 103.10 (2021), p. 106016. DOI: 10.1103/PhysRevD.103.106016. arXiv: 2009.08728 [hep-th].

[156] Tom Banks and Lance J. Dixon. "Constraints on String Vacua with Space-Time Supersymmetry". In: *Nucl. Phys. B* 307 (1988), pp. 93–108. DOI: 10.1016/0550-3213(88)90523-8.

[157] Marc Kamionkowski and John March-Russell. "Planck scale physics and the Peccei-Quinn mechanism". In: *Phys. Lett. B* 282 (1992), pp. 137–141. DOI: 10.1016/0370-2693(92)90492-M. arXiv: hep-th/9202003.

[158] Renata Kallosh et al. "Gravity and global symmetries". In: *Phys. Rev. D* 52 (1995), pp. 912–935. DOI: 10.1103/PhysRevD.52.912. arXiv: hep-th/9502069.

[159] Tom Banks and Nathan Seiberg. "Symmetries and Strings in Field Theory and Gravity". In: *Phys. Rev. D* 83 (2011), p. 084019. DOI: 10.1103/PhysRevD.83.084019. arXiv: 1011.5120 [hep-th].

[160] Daniel Harlow and Hirosi Ooguri. "Constraints on Symmetries from Holography". In: *Phys. Rev. Lett.* 122.19 (2019), p. 191601. DOI: 10.1103/PhysRevLett.122.191601. arXiv: 1810.05337 [hep-th].

[161] Daniel Harlow and Hirosi Ooguri. "Symmetries in quantum field theory and quantum gravity". In: *Commun. Math. Phys.* 383.3 (2021), pp. 1669–1804. DOI: 10.1007/s00220-021-04040-y. arXiv: 1810.05338 [hep-th].

[162] Daniel Harlow and Edgar Shaghoulian. "Global symmetry, Euclidean gravity, and the black hole information problem". In: *JHEP* 04 (2021), p. 175. DOI: 10.1007/JHEP04(2021)175. arXiv: 2010.10539 [hep-th].

[163] Astrid Eichhorn. "Quantum-gravity-induced matter self-interactions in the asymptotic-safety scenario". In: *Phys. Rev. D* 86 (2012), p. 105021. DOI: 10.1103/PhysRevD.86.105021. arXiv: 1204.0965 [gr-qc].

[164] Gustavo P. de Brito, Astrid Eichhorn, and Rafael Robson Lino dos Santos. "The weak-gravity bound and the need for spin in asymptotically safe matter-gravity models". In: (July 2021). arXiv: 2107.03839 [gr-qc].

[165] Nicolai Christiansen and Astrid Eichhorn. "An asymptotically safe solution to the U(1) triviality problem". In: *Phys. Lett. B* 770 (2017), pp. 154–160. DOI: 10.1016/j.physletb.2017.04.047. arXiv: 1702.07724 [hep-th].

[166] Astrid Eichhorn, Aaron Held, and Jan M. Pawlowski. "Quantum-gravity effects on a Higgs-Yukawa model". In: *Phys. Rev. D* 94.10 (2016), p. 104027. DOI: 10.1103/PhysRevD.94.104027. arXiv: 1604.02041 [hep-th].

[167] Astrid Eichhorn, Stefan Lippoldt, and Vedran Skrinjar. "Nonminimal hints for asymptotic safety". In: *Phys. Rev. D* 97.2 (2018), p. 026002. DOI: 10.1103/PhysRevD.97.026002. arXiv: 1710.03005 [hep-th].

[168] Astrid Eichhorn and Aaron Held. "Viability of quantum-gravity induced ultraviolet completions for matter". In: *Phys. Rev. D* 96.8 (2017), p. 086025. DOI: 10.1103/PhysRevD.96.086025. arXiv: 1705.02342 [gr-qc].

[169] Gaurav Narain and Roberto Percacci. "Renormalization Group Flow in Scalar-Tensor Theories. I". In: *Class. Quant. Grav.* 27 (2010), p. 075001. DOI: 10.1088/0264-9381/27/7/075001. arXiv: 0911.0386 [hep-th].

[170] Gaurav Narain and Christoph Rahmede. "Renormalization Group Flow in Scalar-Tensor Theories. II". In: *Class. Quant. Grav.* 27 (2010), p. 075002. DOI: 10.1088/0264-9381/27/7/075002. arXiv: 0911.0394 [hep-th].

[171] Roberto Percacci and Gian Paolo Vacca. "Search of scaling solutions in scalar-tensor gravity". In: *Eur. Phys. J. C* 75.5 (2015), p. 188. DOI: 10.1140/epjc/s10052-015-3410-0. arXiv: 1501.00888 [hep-th].

[172] Kin-ya Oda and Masatoshi Yamada. "Non-minimal coupling in Higgs–Yukawa model with asymptotically safe gravity". In: *Class. Quant. Grav.* 33.12 (2016), p. 125011. DOI: 10.1088/0264-9381/33/12/125011. arXiv: 1510.03734 [hep-th].

[173] Christof Wetterich and Masatoshi Yamada. "Gauge hierarchy problem in asymptotically safe gravity–the resurgence mechanism". In: *Phys. Lett. B* 770 (2017), pp. 268–271. DOI: 10.1016/j.physletb.2017.04.049. arXiv: 1612.03069 [hep-th].

[174] Yuta Hamada and Masatoshi Yamada. "Asymptotic safety of higher derivative quantum gravity non-minimally coupled with a matter system". In: *JHEP* 08 (2017), p. 070. DOI: 10.1007/JHEP08(2017)070. arXiv: 1703.09033 [hep-th].

[175] Astrid Eichhorn et al. "Quantum gravity fluctuations flatten the Planck-scale Higgs potential". In: *Phys. Rev. D* 97.8 (2018), p. 086004. DOI: 10.1103/PhysRevD.97.086004. arXiv: 1712.00319 [hep-th].

[176] Jan M. Pawlowski et al. "Higgs scalar potential in asymptotically safe quantum gravity". In: *Phys. Rev. D* 99.8 (2019), p. 086010. DOI: 10.1103/PhysRevD.99.086010. arXiv: 1811.11706 [hep-th].

[177] C. Wetterich. "Effective scalar potential in asymptotically safe quantum gravity". In: *Universe* 7.2 (2021), p. 45. DOI: 10.3390/universe7020045. arXiv: 1911.06100 [hep-th].

[178] Gustavo P. De Brito, Astrid Eichhorn, and Antonio D. Pereira. "A link that matters: Towards phenomenological tests of unimodular asymptotic safety". In: *JHEP* 09 (2019), p. 100. DOI: 10.1007/JHEP09(2019)100. arXiv: 1907.11173 [hep-th].

[179] O. Zanusso et al. "Gravitational corrections to Yukawa systems". In: *Phys. Lett. B* 689 (2010), pp. 90–94. DOI: 10.1016/j.physletb.2010.04.043. arXiv: 0904.0938 [hep-th].

[180] G. P. Vacca and O. Zanusso. "Asymptotic Safety in Einstein Gravity and Scalar-Fermion Matter". In: *Phys. Rev. Lett.* 105 (2010), p. 231601. DOI: 10.1103/PhysRevLett.105.231601. arXiv: 1009.1735 [hep-th].

[181] Aaron Held. "From particle physics to black holes: The predictive power of asymptotic safety." PhD thesis. U. Heidelberg (main), 2019. DOI: 10.11588/heidok.00027607.

[182] Jan-Eric Daum, Ulrich Harst, and Martin Reuter. "Running Gauge Coupling in Asymptotically Safe Quantum Gravity". In: *JHEP* 01 (2010), p. 084. DOI: 10.1007/JHEP01(2010)084. arXiv: 0910.4938 [hep-th].

[183] Sarah Folkerts, Daniel F. Litim, and Jan M. Pawlowski. "Asymptotic freedom of Yang-Mills theory with gravity". In: *Phys. Lett. B* 709 (2012), pp. 234–241. DOI: 10.1016/j.physletb.2012.02.002. arXiv: 1101.5552 [hep-th].

[184] Nicolai Christiansen et al. "Asymptotic safety of gravity with matter". In: *Phys. Rev. D* 97.10 (2018), p. 106012. DOI: 10.1103/PhysRevD.97.106012. arXiv: 1710.04669 [hep-th].

[185] U. Harst and M. Reuter. "QED coupled to QEG". In: *JHEP* 05 (2011), p. 119. DOI: 10.1007/JHEP05(2011)119. arXiv: 1101.6007 [hep-th].

[186] Astrid Eichhorn and Fleur Versteegen. "Upper bound on the Abelian gauge coupling from asymptotic safety". In: *JHEP* 01 (2018), p. 030. DOI: 10.1007/JHEP01(2018)030. arXiv: 1709.07252 [hep-th].

[187] Astrid Eichhorn and Marc Schiffer. "$d = 4$ as the critical dimensionality of asymptotically safe interactions". In: *Phys. Lett. B* 793 (2019), pp. 383–389. DOI: 10.1016/j.physletb.2019.05.005. arXiv: 1902.06479 [hep-th].

[188] N. Cabibbo et al. "Bounds on the Fermions and Higgs Boson Masses in Grand Unified Theories". In: *Nucl. Phys. B* 158 (1979), pp. 295–305. DOI: 10.1016/0550-3213(79)90167-6.

[189] M. Lindner. "Implications of Triviality for the Standard Model". In: *Z. Phys. C* 31 (1986), p. 295. DOI: 10.1007/BF01479540.

[190] Joan Elias-Miro et al. "Higgs mass implications on the stability of the electroweak vacuum". In: *Phys. Lett. B* 709 (2012), pp. 222–228. DOI: 10.1016/j.physletb.2012.02.013. arXiv: 1112.3022 [hep-ph].

[191] Fedor Bezrukov et al. "Higgs Boson Mass and New Physics". In: *JHEP* 10 (2012). Ed. by Gudrid Moortgat-Pick, p. 140. DOI: 10.1007/JHEP10(2012)140. arXiv: 1205.2893 [hep-ph].

[192] Giuseppe Degrassi et al. "Higgs mass and vacuum stability in the Standard Model at NNLO". In: *JHEP* 08 (2012), p. 098. DOI: 10.1007/JHEP08(2012)098. arXiv: 1205.6497 [hep-ph].

[193] Dario Buttazzo et al. "Investigating the near-criticality of the Higgs boson". In: *JHEP* 12 (2013), p. 089. DOI: 10.1007/JHEP12(2013)089. arXiv: 1307.3536 [hep-ph].

[194] Jose R. Espinosa et al. "The cosmological Higgstory of the vacuum instability". In: *JHEP* 09 (2015), p. 174. DOI: 10.1007/JHEP09(2015)174. arXiv: 1505.04825 [hep-ph].

[195] A. V. Bednyakov et al. "Stability of the Electroweak Vacuum: Gauge Independence and Advanced Precision". In: *Phys. Rev. Lett.* 115.20 (2015), p. 201802. DOI: 10.1103/PhysRevLett.115.201802. arXiv: 1507.08833 [hep-ph].

[196] Jose R. Espinosa et al. "Gauge-Independent Scales Related to the Standard Model Vacuum Instability". In: *Phys. Rev. D* 95.5 (2017), p. 056004. DOI: 10.1103/PhysRevD.95.056004. arXiv: 1608.06765 [hep-ph].

[197] Vincenzo Branchina and Emanuele Messina. "Stability, Higgs Boson Mass and New Physics". In: *Phys. Rev. Lett.* 111 (2013), p. 241801. DOI: 10.1103/PhysRevLett.111.241801. arXiv: 1307.5193 [hep-ph].

[198] Holger Gies, Clemens Gneiting, and René Sondenheimer. "Higgs Mass Bounds from Renormalization Flow for a simple Yukawa model". In: *Phys. Rev. D* 89.4 (2014), p. 045012. DOI: 10.1103/PhysRevD.89.045012. arXiv: 1308.5075 [hep-ph].

[199] Vincenzo Branchina, Emanuele Messina, and Marc Sher. "Lifetime of the electroweak vacuum and sensitivity to Planck scale physics". In: *Phys. Rev. D* 91 (2015), p. 013003. DOI: 10.1103/PhysRevD.91.013003. arXiv: 1408.5302 [hep-ph].

[200] Vincenzo Branchina, Emanuele Messina, and Alessia Platania. "Top mass determination, Higgs inflation, and vacuum stability". In: *JHEP* 09 (2014), p. 182. DOI: 10.1007/JHEP09(2014)182. arXiv: 1407.4112 [hep-ph].

[201] Holger Gies and René Sondenheimer. "Higgs Mass Bounds from Renormalization Flow for a Higgs-top-bottom model". In: *Eur. Phys. J. C* 75.2 (2015), p. 68. DOI: 10.1140/epjc/s10052-015-3284-1. arXiv: 1407.8124 [hep-ph].

[202] Astrid Eichhorn et al. "The Higgs Mass and the Scale of New Physics". In: *JHEP* 04 (2015), p. 022. DOI: 10.1007/JHEP04(2015)022. arXiv: 1501.02812 [hep-ph].

[203] Julia Borchardt, Holger Gies, and René Sondenheimer. "Global flow of the Higgs potential in a Yukawa model". In: *Eur. Phys. J. C* 76.8 (2016), p. 472. DOI: 10.1140/epjc/s10052-016-4300-9. arXiv: 1603.05861 [hep-ph].

[204] André H. Hoang. "What is the Top Quark Mass?" In: *Ann. Rev. Nucl. Part. Sci.* 70 (2020), pp. 225–255. DOI: 10.1146/annurev-nucl-101918-023530. arXiv: 2004.12915 [hep-ph].

[205] Albert M Sirunyan et al. "Measurement of double-differential cross sections for top quark pair production in pp collisions at $\sqrt{s} = 8$ TeV and impact on parton distribution functions". In: *Eur. Phys. J. C* 77.7 (2017), p. 459. DOI: `10.1140/epjc/s10052-017-4984-5`. arXiv: `1703.01630` `[hep-ex]`.

[206] Albert M Sirunyan et al. "Measurement of $t\bar{t}$ normalised multi-differential cross sections in pp collisions at $\sqrt{s} = 13$ TeV, and simultaneous determination of the strong coupling strength, top quark pole mass, and parton distribution functions". In: *Eur. Phys. J. C* 80.7 (2020), p. 658. DOI: `10.1140/epjc/s10052-020-7917-7`. arXiv: `1904.05237` `[hep-ex]`.

[207] Georges Aad et al. "Measurement of the top-quark mass in $t\bar{t} + 1$-jet events collected with the ATLAS detector in pp collisions at $\sqrt{s} = 8$ TeV". In: *JHEP* 11 (2019), p. 150. DOI: `10.1007/JHEP11(2019)150`. arXiv: `1905.02302` `[hep-ex]`.

[208] Mikhail Shaposhnikov and Christof Wetterich. "Asymptotic safety of gravity and the Higgs boson mass". In: *Phys. Lett. B* 683 (2010), pp. 196–200. DOI: `10.1016/j.physletb.2009.12.022`. arXiv: `0912.0208` `[hep-th]`.

[209] Fedor Bezrukov and Mikhail Shaposhnikov. "Why should we care about the top quark Yukawa coupling?" In: *J. Exp. Theor. Phys.* 120 (2015), pp. 335–343. DOI: `10.1134/S1063776115030152`. arXiv: `1411.1923` `[hep-ph]`.

[210] Astrid Eichhorn and Aaron Held. "Mass difference for charged quarks from asymptotically safe quantum gravity". In: *Phys. Rev. Lett.* 121.15 (2018), p. 151302. DOI: `10.1103/PhysRevLett.121.151302`. arXiv: `1803.04027` `[hep-th]`.

[211] Reinhard Alkofer et al. "Quark masses and mixings in minimally parameterized UV completions of the Standard Model". In: *Annals Phys.* 421 (2020), p. 168282. DOI: `10.1016/j.aop.2020.168282`. arXiv: `2003.08401` `[hep-ph]`.

[212] Astrid Eichhorn and Holger Gies. "Light fermions in quantum gravity". In: *New J. Phys.* 13 (2011), p. 125012. DOI: `10.1088/1367-2630/13/12/125012`. arXiv: `1104.5366` `[hep-th]`.

[213] Jan Meibohm and Jan M. Pawlowski. "Chiral fermions in asymptotically safe quantum gravity". In: *Eur. Phys. J. C* 76.5 (2016), p. 285. DOI: `10.1140/epjc/s10052-016-4132-7`. arXiv: `1601.04597` `[hep-th]`.

[214] Gustavo P. de Brito, Astrid Eichhorn, and Marc Schiffer. "Light charged fermions in quantum gravity". In: *Phys. Lett. B* 815 (2021), p. 136128. DOI: `10.1016/j.physletb.2021.136128`. arXiv: `2010.00605` `[hep-th]`.

[215] I. L. Buchbinder and E. N. Kirillova. "Phase transitions induced by curvature in the Gross-Neveu model". In: *Sov. Phys. J.* 32 (1989), pp. 446–450. DOI: `10.1007/BF00898628`.

[216] I. L. Buchbinder and E. N. Kirillova. "Gross-Neveu Model in Curved Space-time: The Effective Potential and Curvature Induced Phase Transition". In: *Int. J. Mod. Phys. A* 4 (1989), pp. 143–149. DOI: `10.1142/S0217751X89000054`.

[217] T. Inagaki, T. Muta, and S. D. Odintsov. "Nambu-Jona-Lasinio model in curved space-time". In: *Mod. Phys. Lett. A* 8 (1993), pp. 2117–2124. DOI: `10.1142/S0217732393001835`. arXiv: `hep-th/9306023`.

[218] I. Sachs and A. Wipf. "Temperature and curvature dependence of the chiral symmetry breaking in 2-D gauge theories". In: *Phys. Lett. B* 326 (1994), pp. 105–110. DOI: `10.1016/0370-2693(94)91200-9`. arXiv: `hep-th/9310085`.

[219] Holger Gies and Stefan Lippoldt. "Renormalization flow towards gravitational catalysis in the 3d Gross-Neveu model". In: *Phys. Rev. D* 87 (2013), p. 104026. DOI: 10.1103/PhysRevD.87.104026. arXiv: 1303.4253 [hep-th].

[220] Holger Gies and Riccardo Martini. "Curvature bound from gravitational catalysis". In: *Phys. Rev. D* 97.8 (2018), p. 085017. DOI: 10.1103/PhysRevD.97.085017. arXiv: 1802.02865 [hep-th].

[221] Holger Gies and Abdol Sabor Salek. "Curvature bound from gravitational catalysis in thermal backgrounds". In: *Phys. Rev. D* 103.12 (2021), p. 125027. DOI: 10.1103/PhysRevD.103.125027. arXiv: 2103.05542 [hep-th].

[222] Kamila Kowalska, Enrico Maria Sessolo, and Yasuhiro Yamamoto. "Flavor anomalies from asymptotically safe gravity". In: *Eur. Phys. J. C* 81.4 (2021), p. 272. DOI: 10.1140/epjc/s10052-021-09072-1. arXiv: 2007.03567 [hep-ph].

[223] Kamila Kowalska and Enrico Maria Sessolo. "Minimal models for g-2 and dark matter confront asymptotic safety". In: *Phys. Rev. D* 103.11 (2021), p. 115032. DOI: 10.1103/PhysRevD.103.115032. arXiv: 2012.15200 [hep-ph].

[224] Y. Fukuda et al. "Evidence for oscillation of atmospheric neutrinos". In: *Phys. Rev. Lett.* 81 (1998), pp. 1562–1567. DOI: 10.1103/PhysRevLett.81.1562. arXiv: hep-ex/9807003.

[225] Q. R. Ahmad et al. "Direct evidence for neutrino flavor transformation from neutral current interactions in the Sudbury Neutrino Observatory". In: *Phys. Rev. Lett.* 89 (2002), p. 011301. DOI: 10.1103/PhysRevLett.89.011301. arXiv: nucl-ex/0204008.

[226] Ivan Esteban et al. "Global analysis of three-flavour neutrino oscillations: synergies and tensions in the determination of θ_{23}, δ_{CP}, and the mass ordering". In: *JHEP* 01 (2019), p. 106. DOI: 10.1007/JHEP01(2019)106. arXiv: 1811.05487 [hep-ph].

[227] Arthur Loureiro et al. "On The Upper Bound of Neutrino Masses from Combined Cosmological Observations and Particle Physics Experiments". In: *Phys. Rev. Lett.* 123.8 (2019), p. 081301. DOI: 10.1103/PhysRevLett.123.081301. arXiv: 1811.02578 [astro-ph.CO].

[228] M. Aker et al. "Improved Upper Limit on the Neutrino Mass from a Direct Kinematic Method by KATRIN". In: *Phys. Rev. Lett.* 123.22 (2019), p. 221802. DOI: 10.1103/PhysRevLett.123.221802. arXiv: 1909.06048 [hep-ex].

[229] Gustavo P. De Brito et al. "On the impact of Majorana masses in gravity-matter systems". In: *JHEP* 08 (2019), p. 142. DOI: 10.1007/JHEP08(2019)142. arXiv: 1905.11114 [hep-th].

[230] Guillem Domènech, Mark Goodsell, and Christof Wetterich. "Neutrino masses, vacuum stability and quantum gravity prediction for the mass of the top quark". In: *JHEP* 01 (2021), p. 180. DOI: 10.1007/JHEP01(2021)180. arXiv: 2008.04310 [hep-ph].

[231] Astrid Eichhorn, Aaron Held, and Christof Wetterich. "Predictive power of grand unification from quantum gravity". In: *JHEP* 08 (2020), p. 111. DOI: 10.1007/JHEP08(2020)111. arXiv: 1909.07318 [hep-th].

[232] Astrid Eichhorn, Aaron Held, and Christof Wetterich. "Quantum-gravity predictions for the fine-structure constant". In: *Phys. Lett. B* 782 (2018), pp. 198–201. DOI: 10.1016/j.physletb.2018.05.016. arXiv: 1711.02949 [hep-th].

[233] I. L. Buchbinder, S. D. Odintsov, and I. L. Shapiro. *Effective action in quantum gravity*. 1992.

[234] Adam G. Riess et al. "Observational evidence from supernovae for an accelerating universe and a cosmological constant". In: *Astron. J.* 116 (1998), pp. 1009–1038. DOI: 10.1086/300499. arXiv: astro-ph/9805201.

[235] S. Perlmutter et al. "Measurements of Ω and Λ from 42 high redshift supernovae". In: *Astrophys. J.* 517 (1999), pp. 565–586. DOI: 10.1086/307221. arXiv: astro-ph/9812133.

[236] D. M. Scolnic et al. "The Complete Light-curve Sample of Spectroscopically Confirmed SNe Ia from Pan-STARRS1 and Cosmological Constraints from the Combined Pantheon Sample". In: *Astrophys. J.* 859.2 (2018), p. 101. DOI: 10.3847/1538-4357/aab9bb. arXiv: 1710.00845 [astro-ph.CO].

[237] Luca Amendola et al. "Cosmology and fundamental physics with the Euclid satellite". In: *Living Rev. Rel.* 21.1 (2018), p. 2. DOI: 10.1007/s41114-017-0010-3. arXiv: 1606.00180 [astro-ph.CO].

[238] Jean-Luc Lehners and K. S. Stelle. "A Safe Beginning for the Universe?" In: *Phys. Rev. D* 100.8 (2019), p. 083540. DOI: 10.1103/PhysRevD.100.083540. arXiv: 1909.01169 [hep-th].

[239] Alexei A. Starobinsky. "Spectrum of relict gravitational radiation and the early state of the universe". In: *JETP Lett.* 30 (1979). Ed. by I. M. Khalatnikov and V. P. Mineev, pp. 682–685.

[240] Alexei A. Starobinsky. "A New Type of Isotropic Cosmological Models Without Singularity". In: *Phys. Lett. B* 91 (1980). Ed. by I. M. Khalatnikov and V. P. Mineev, pp. 99–102. DOI: 10.1016/0370-2693(80)90670-X.

[241] Alan H. Guth. "The Inflationary Universe: A Possible Solution to the Horizon and Flatness Problems". In: *Phys. Rev. D* 23 (1981). Ed. by Li-Zhi Fang and R. Ruffini, pp. 347–356. DOI: 10.1103/PhysRevD.23.347.

[242] Andrei D. Linde. "A New Inflationary Universe Scenario: A Possible Solution of the Horizon, Flatness, Homogeneity, Isotropy and Primordial Monopole Problems". In: *Phys. Lett. B* 108 (1982). Ed. by Li-Zhi Fang and R. Ruffini, pp. 389–393. DOI: 10.1016/0370-2693(82)91219-9.

[243] Andreas Albrecht and Paul J. Steinhardt. "Cosmology for Grand Unified Theories with Radiatively Induced Symmetry Breaking". In: *Phys. Rev. Lett.* 48 (1982). Ed. by Li-Zhi Fang and R. Ruffini, pp. 1220–1223. DOI: 10.1103/PhysRevLett.48.1220.

[244] Daniel Baumann. "Inflation". In: *Theoretical Advanced Study Institute in Elementary Particle Physics: Physics of the Large and the Small*. July 2009. DOI: 10.1142/9789814327183_0010. arXiv: 0907.5424 [hep-th].

[245] T. S. Bunch and P. C. W. Davies. "Quantum Field Theory in de Sitter Space: Renormalization by Point Splitting". In: *Proc. Roy. Soc. Lond. A* 360 (1978), pp. 117–134. DOI: 10.1098/rspa.1978.0060.

[246] Steven Weinberg. "Adiabatic modes in cosmology". In: *Phys. Rev. D* 67 (2003), p. 123504. DOI: 10.1103/PhysRevD.67.123504. arXiv: astro-ph/0302326.

[247] David H. Lyth, Karim A. Malik, and Misao Sasaki. "A General proof of the conservation of the curvature perturbation". In: *JCAP* 05 (2005), p. 004. DOI: 10.1088/1475-7516/2005/05/004. arXiv: astro-ph/0411220.

[248] Y. Akrami et al. "Planck 2018 results. X. Constraints on inflation". In: *Astron. Astrophys.* 641 (2020), A10. DOI: 10.1051/0004-6361/201833887. arXiv: 1807.06211 [astro-ph.CO].

[249] Jerome Martin, Christophe Ringeval, and Vincent Vennin. "Encyclopædia Inflationaris". In: *Phys. Dark Univ.* 5-6 (2014), pp. 75–235. DOI: 10.1016/j.dark.2014.01.003. arXiv: 1303.3787 [astro-ph.CO].

[250] C. Wetterich. "Quantum scale symmetry". In: (Jan. 2019). arXiv: 1901.04741 [hep-th].

[251] Mikhail Shaposhnikov and Daniel Zenhausern. "Scale invariance, unimodular gravity and dark energy". In: *Phys. Lett. B* 671 (2009), pp. 187–192. DOI: 10.1016/j.physletb.2008.11.054. arXiv: 0809.3395 [hep-th].

[252] Juan Garcia-Bellido et al. "Higgs-Dilaton Cosmology: From the Early to the Late Universe". In: *Phys. Rev. D* 84 (2011), p. 123504. DOI: 10.1103/PhysRevD.84.123504. arXiv: 1107.2163 [hep-ph].

[253] Fedor Bezrukov et al. "Higgs-Dilaton Cosmology: an effective field theory approach". In: *Phys. Rev. D* 87.9 (2013), p. 096001. DOI: 10.1103/PhysRevD.87.096001. arXiv: 1212.4148 [hep-ph].

[254] Valentin V. Khoze. "Inflation and Dark Matter in the Higgs Portal of Classically Scale Invariant Standard Model". In: *JHEP* 11 (2013), p. 215. DOI: 10.1007/JHEP11(2013)215. arXiv: 1308.6338 [hep-ph].

[255] Kristjan Kannike et al. "Dynamically Induced Planck Scale and Inflation". In: *JHEP* 05 (2015), p. 065. DOI: 10.1007/JHEP05(2015)065. arXiv: 1502.01334 [astro-ph.CO].

[256] Pedro G. Ferreira, Christopher T. Hill, and Graham G. Ross. "Scale-Independent Inflation and Hierarchy Generation". In: *Phys. Lett. B* 763 (2016), pp. 174–178. DOI: 10.1016/j.physletb.2016.10.036. arXiv: 1603.05983 [hep-th].

[257] Pedro G. Ferreira, Christopher T. Hill, and Graham G. Ross. "Weyl Current, Scale-Invariant Inflation and Planck Scale Generation". In: *Phys. Rev. D* 95.4 (2017), p. 043507. DOI: 10.1103/PhysRevD.95.043507. arXiv: 1610.09243 [hep-th].

[258] Fedor L. Bezrukov and Mikhail Shaposhnikov. "The Standard Model Higgs boson as the inflaton". In: *Phys. Lett. B* 659 (2008), pp. 703–706. DOI: 10.1016/j.physletb.2007.11.072. arXiv: 0710.3755 [hep-th].

[259] Javier Rubio. "Higgs inflation". In: *Front. Astron. Space Sci.* 5 (2019), p. 50. DOI: 10.3389/fspas.2018.00050. arXiv: 1807.02376 [hep-ph].

[260] Mario Galante et al. "Unity of Cosmological Inflation Attractors". In: *Phys. Rev. Lett.* 114.14 (2015), p. 141302. DOI: 10.1103/PhysRevLett.114.141302. arXiv: 1412.3797 [hep-th].

[261] Fedor Bezrukov and Mikhail Shaposhnikov. "Higgs inflation at the critical point". In: *Phys. Lett. B* 734 (2014), pp. 249–254. DOI: 10.1016/j.physletb.2014.05.074. arXiv: 1403.6078 [hep-ph].

[262] Georgios K. Karananas and Javier Rubio. "On the geometrical interpretation of scale-invariant models of inflation". In: *Phys. Lett. B* 761 (2016), pp. 223–228. DOI: 10.1016/j.physletb.2016.08.037. arXiv: 1606.08848 [hep-ph].

[263] C. Wetterich. "Cosmology and the Fate of Dilatation Symmetry". In: *Nucl. Phys. B* 302 (1988), pp. 668–696. DOI: 10.1016/0550-3213(88)90193-9. arXiv: 1711.03844 [hep-th].

[264] C. Wetterich. "Cosmologies With Variable Newton's 'Constant'". In: *Nucl. Phys. B* 302 (1988), pp. 645–667. DOI: 10.1016/0550-3213(88)90192-7.

[265] Bharat Ratra and P. J. E. Peebles. "Cosmological Consequences of a Rolling Homogeneous Scalar Field". In: *Phys. Rev. D* 37 (1988), p. 3406. DOI: 10.1103/PhysRevD.37.3406.

[266] Edmund J. Copeland, Andrew R Liddle, and David Wands. "Exponential potentials and cosmological scaling solutions". In: *Phys. Rev. D* 57 (1998), pp. 4686–4690. DOI: 10.1103/PhysRevD.57.4686. arXiv: gr-qc/9711068.

[267] Javier Rubio and Christof Wetterich. "Emergent scale symmetry: Connecting inflation and dark energy". In: *Phys. Rev. D* 96.6 (2017), p. 063509. DOI: 10.1103/PhysRevD.96.063509. arXiv: 1705.00552 [gr-qc].

[268] Georges Obied et al. "De Sitter Space and the Swampland". In: (June 2018). arXiv: 1806.08362 [hep-th].

[269] Prateek Agrawal et al. "On the Cosmological Implications of the String Swampland". In: *Phys. Lett. B* 784 (2018), pp. 271–276. DOI: 10.1016/j.physletb.2018.07.040. arXiv: 1806.09718 [hep-th].

[270] Tommi Tenkanen. "Resurrecting Quadratic Inflation with a non-minimal coupling to gravity". In: *JCAP* 12 (2017), p. 001. DOI: 10.1088/1475-7516/2017/12/001. arXiv: 1710.02758 [astro-ph.CO].

[271] Ippocratis D. Saltas. "Higgs inflation and quantum gravity: An exact renormalisation group approach". In: *JCAP* 02 (2016), p. 048. DOI: 10.1088/1475-7516/2016/02/048. arXiv: 1512.06134 [hep-th].

[272] Alessia Platania. "From renormalization group flows to cosmology". In: *Front. in Phys.* 8 (2020), p. 188. DOI: 10.3389/fphy.2020.00188. arXiv: 2003.13656 [gr-qc].

[273] Alfio Bonanno and Alessia Platania. "Asymptotically safe inflation from quadratic gravity". In: *Phys. Lett. B* 750 (2015), pp. 638–642. DOI: 10.1016/j.physletb.2015.10.005. arXiv: 1507.03375 [gr-qc].

[274] Alfio Bonanno and Alessia Platania. "Asymptotically Safe R+R^2 gravity". In: *PoS* CORFU2015 (2016), p. 159. DOI: 10.22323/1.263.0159.

[275] Alfio Bonanno, Alessia Platania, and Frank Saueressig. "Cosmological bounds on the field content of asymptotically safe gravity–matter models". In: *Phys. Lett. B* 784 (2018), pp. 229–236. DOI: 10.1016/j.physletb.2018.06.047. arXiv: 1803.02355 [gr-qc].

[276] Alessia Platania. "The inflationary mechanism in Asymptotically Safe Gravity". In: *Universe* 5.8 (2019). Ed. by Astrid Eichhorn, Roberto Percacci, and Frank Saueressig, p. 189. DOI: 10.3390/universe5080189. arXiv: 1908.03897 [gr-qc].

[277] Aaron Held. "Invariant Renormalization-Group improvement". In: (May 2021). arXiv: 2105.11458 [gr-qc].

[278] Mark Hindmarsh and Ippocratis D. Saltas. "f(R) Gravity from the renormalisation group". In: *Phys. Rev. D* 86 (2012), p. 064029. DOI: 10.1103/PhysRevD.86.064029. arXiv: 1203.3957 [gr-qc].

[279] Daniel Baumann and Daniel Green. "Desensitizing Inflation from the Planck Scale". In: *JHEP* 09 (2010), p. 057. DOI: 10.1007/JHEP09(2010)057. arXiv: 1004.3801 [hep-th].

[280] Qing-Guo Huang. "A polynomial f(R) inflation model". In: *JCAP* 02 (2014), p. 035. DOI: 10.1088/1475-7516/2014/02/035. arXiv: 1309.3514 [hep-th].

[281] Dhong Yeon Cheong, Hyun Min Lee, and Seong Chan Park. "Beyond the Starobinsky model for inflation". In: *Phys. Lett. B* 805 (2020), p. 135453. DOI: 10.1016/j.physletb.2020.135453. arXiv: 2002.07981 [hep-ph].

[282] Steven Weinberg. "Asymptotically Safe Inflation". In: *Phys. Rev. D* 81 (2010), p. 083535. DOI: 10.1103/PhysRevD.81.083535. arXiv: 0911.3165 [hep-th].

[283] Alfio Bonanno, Adriano Contillo, and Roberto Percacci. "Inflationary solutions in asymptotically safe f(R) theories". In: *Class. Quant. Grav.* 28 (2011), p. 145026. DOI: 10.1088/0264-9381/28/14/145026. arXiv: 1006.0192 [gr-qc].

[284] Alfio Bonanno. "An effective action for asymptotically safe gravity". In: *Phys. Rev. D* 85 (2012), p. 081503. DOI: 10.1103/PhysRevD.85.081503. arXiv: 1203.1962 [hep-th].

[285] Kevin Falls et al. "On de Sitter solutions in asymptotically safe $f(R)$ theories". In: *Class. Quant. Grav.* 35.13 (2018), p. 135006. DOI: 10.1088/1361-6382/aac440. arXiv: 1607.04962 [gr-qc].

[286] H. Sugai et al. "Updated Design of the CMB Polarization Experiment Satellite LiteBIRD". In: *J. Low. Temp. Phys.* 199.3-4 (2020), pp. 1107–1117. DOI: 10.1007/s10909-019-02329-w. arXiv: 2001.01724 [astro-ph.IM].

[287] Rafael D Sorkin. "Spacetime and causal sets." In: *Relativity and Gravitation* (1991), p. 150.

[288] Rafael D. Sorkin. "Forks in the road, on the way to quantum gravity". In: *Int. J. Theor. Phys.* 36 (1997), pp. 2759–2781. DOI: 10.1007/BF02435709. arXiv: gr-qc/9706002.

[289] Maqbool Ahmed et al. "Everpresent Λ". In: *Phys. Rev. D* 69 (2004), p. 103523. DOI: 10.1103/PhysRevD.69.103523. arXiv: astro-ph/0209274.

[290] Lavinia Heisenberg et al. "Dark Energy in the Swampland". In: *Phys. Rev. D* 98.12 (2018), p. 123502. DOI: 10.1103/PhysRevD.98.123502. arXiv: 1808.02877 [astro-ph.CO].

[291] Michael E. Levi et al. "The Dark Energy Spectroscopic Instrument (DESI)". In: (July 2019). arXiv: 1907.10688 [astro-ph.IM].

[292] S. Ilić et al. "*Euclid* preparation: XV. Forecasting cosmological constraints for the *Euclid* and CMB joint analysis". In: (June 2021). arXiv: 2106.08346 [astro-ph.CO].

[293] David J. Bacon et al. "Cosmology with Phase 1 of the Square Kilometre Array Red Book 2018: Technical specifications and performance forecasts". In: *Publications of the Astronomical Society of Australia* 37 (2020), e007. DOI: 10.1017/pasa.2019.51.

[294] G. Zhao et al. "Model-independent constraints on dark energy and modified gravity with the SKA". In: *Advancing Astrophysics with the Square Kilometre Array (AASKA14)*. Apr. 2015, p. 165. arXiv: 1501.03840 [astro-ph.CO].

[295] Tobias Henz et al. "Dilaton Quantum Gravity". In: *Phys. Lett. B* 727 (2013), pp. 298–302. DOI: 10.1016/j.physletb.2013.10.015. arXiv: 1304.7743 [hep-th].

[296] Tobias Henz, Jan Martin Pawlowski, and Christof Wetterich. "Scaling solutions for Dilaton Quantum Gravity". In: *Phys. Lett. B* 769 (2017), pp. 105–110. DOI: 10.1016/j.physletb.2017.01.057. arXiv: 1605.01858 [hep-th].

[297] Lisa Alexander-Nunneley and Apostolos Pilaftsis. "The Minimal Scale Invariant Extension of the Standard Model". In: *JHEP* 09 (2010), p. 021. DOI: 10.1007/JHEP09(2010)021. arXiv: 1006.5916 [hep-ph].

[298] Christopher D. Carone and Raymundo Ramos. "Classical scale-invariance, the electroweak scale and vector dark matter". In: *Phys. Rev. D* 88 (2013), p. 055020. DOI: 10.1103/PhysRevD.88.055020. arXiv: 1307.8428 [hep-ph].

[299] Arsham Farzinnia, Hong-Jian He, and Jing Ren. "Natural Electroweak Symmetry Breaking from Scale Invariant Higgs Mechanism". In: *Phys. Lett. B* 727 (2013), pp. 141–150. DOI: 10.1016/j.physletb.2013.09.060. arXiv: 1308.0295 [hep-ph].

[300] Martin Holthausen et al. "Electroweak and Conformal Symmetry Breaking by a Strongly Coupled Hidden Sector". In: *JHEP* 12 (2013), p. 076. DOI: 10.1007/JHEP12(2013)076. arXiv: 1310.4423 [hep-ph].

[301] Dong-Won Jung, Jungil Lee, and Soo-Hyeon Nam. "Scalar dark matter in the conformally invariant extension of the standard model". In: *Phys. Lett. B* 797 (2019), p. 134823. DOI: 10.1016/j.physletb.2019.134823. arXiv: 1904.10209 [hep-ph].

[302] Massimo Persic, Paolo Salucci, and Fulvio Stel. "The Universal rotation curve of spiral galaxies: 1. The Dark matter connection". In: *Mon. Not. Roy. Astron. Soc.* 281 (1996), p. 27. DOI: 10.1093/mnras/278.1.27. arXiv: astro-ph/9506004.

[303] Mariangela Lisanti. "Lectures on Dark Matter Physics". In: *Theoretical Advanced Study Institute in Elementary Particle Physics: New Frontiers in Fields and Strings*. Mar. 2016. DOI: 10.1142/9789813149441_0007. arXiv: 1603.03797 [hep-ph].

[304] Matthias Bartelmann. "Gravitational Lensing". In: *Class. Quant. Grav.* 27 (2010), p. 233001. DOI: 10.1088/0264-9381/27/23/233001. arXiv: 1010.3829 [astro-ph.CO].

[305] Keiichi Umetsu et al. "CLASH: Joint Analysis of Strong-Lensing, Weak-Lensing Shear and Magnification Data for 20 Galaxy Clusters". In: *Astrophys. J.* 821.2 (2016), p. 116. DOI: 10.3847/0004-637X/821/2/116. arXiv: 1507.04385 [astro-ph.CO].

[306] G. B. Caminha et al. "A refined mass distribution of the cluster MACS J0416.1−2403 from a new large set of spectroscopic multiply lensed sources". In: *Astron. Astrophys.* 600 (2017), A90. DOI: 10.1051/0004-6361/201629297. arXiv: 1607.03462 [astro-ph.GA].

[307] Benoit Famaey and Stacy McGaugh. "Modified Newtonian Dynamics (MOND): Observational Phenomenology and Relativistic Extensions". In: *Living Rev. Rel.* 15 (2012), p. 10. DOI: 10.12942/lrr-2012-10. arXiv: 1112.3960 [astro-ph.CO].

[308] Bernard Carr and Florian Kuhnel. "Primordial Black Holes as Dark Matter: Recent Developments". In: *Ann. Rev. Nucl. Part. Sci.* 70 (2020), pp. 355–394. DOI: 10.1146/annurev-nucl-050520-125911. arXiv: 2006.02838 [astro-ph.CO].

[309] Jose Maria Ezquiaga, Juan Garcia-Bellido, and Ester Ruiz Morales. "Primordial Black Hole production in Critical Higgs Inflation". In: *Phys. Lett. B* 776 (2018), pp. 345–349. DOI: 10.1016/j.physletb.2017.11.039. arXiv: 1705.04861 [astro-ph.CO].

[310] Fedor Bezrukov, Martin Pauly, and Javier Rubio. "On the robustness of the primordial power spectrum in renormalized Higgs inflation". In: *JCAP* 02 (2018), p. 040. DOI: 10.1088/1475-7516/2018/02/040. arXiv: 1706.05007 [hep-ph].

[311] Konstantinos Dimopoulos. "Ultra slow-roll inflation demystified". In: *Phys. Lett. B* 775 (2017), pp. 262–265. DOI: 10.1016/j.physletb.2017.10.066. arXiv: 1707.05644 [hep-ph].

[312] Cristiano Germani and Tomislav Prokopec. "On primordial black holes from an inflection point". In: *Phys. Dark Univ.* 18 (2017), pp. 6–10. DOI: 10.1016/j.dark.2017.09.001. arXiv: 1706.04226 [astro-ph.CO].

[313] Juan Garcia-Bellido and Ester Ruiz Morales. "Primordial black holes from single field models of inflation". In: *Phys. Dark Univ.* 18 (2017), pp. 47–54. DOI: 10.1016/j.dark.2017.09.007. arXiv: 1702.03901 [astro-ph.CO].

[314] Guillermo Ballesteros and Marco Taoso. "Primordial black hole dark matter from single field inflation". In: *Phys. Rev. D* 97.2 (2018), p. 023501. DOI: 10.1103/PhysRevD.97.023501. arXiv: 1709.05565 [hep-ph].

[315] J. R. Espinosa, D. Racco, and A. Riotto. "Cosmological Signature of the Standard Model Higgs Vacuum Instability: Primordial Black Holes as Dark Matter". In: *Phys. Rev. Lett.* 120.12 (2018), p. 121301. DOI: 10.1103/PhysRevLett.120.121301. arXiv: 1710.11196 [hep-ph].

[316] Bernard Carr et al. "Constraints on Primordial Black Holes". In: (Feb. 2020). arXiv: 2002.12778 [astro-ph.CO].

[317] Martin Bauer and Tilman Plehn. *Yet Another Introduction to Dark Matter: The Particle Physics Approach*. Vol. 959. Lecture Notes in Physics. Springer, 2019. DOI: 10.1007/978-3-030-16234-4. arXiv: 1705.01987 [hep-ph].

[318] Vanda Silveira and A. Zee. "SCALAR PHANTOMS". In: *Phys. Lett. B* 161 (1985), pp. 136–140. DOI: 10.1016/0370-2693(85)90624-0.

[319] John McDonald. "Gauge singlet scalars as cold dark matter". In: *Phys. Rev. D* 50 (1994), pp. 3637–3649. DOI: 10.1103/PhysRevD.50.3637. arXiv: hep-ph/0702143.

[320] C. P. Burgess, Maxim Pospelov, and Tonnis ter Veldhuis. "The Minimal model of non-baryonic dark matter: A Singlet scalar". In: *Nucl. Phys. B* 619 (2001), pp. 709–728. DOI: 10.1016/S0550-3213(01)00513-2. arXiv: hep-ph/0011335.

[321] James M. Cline et al. "Update on scalar singlet dark matter". In: *Phys. Rev. D* 88 (2013). [Erratum: Phys.Rev.D 92, 039906 (2015)], p. 055025. DOI: 10.1103/PhysRevD.88.055025. arXiv: 1306.4710 [hep-ph].

[322] Ankit Beniwal et al. "Combined analysis of effective Higgs portal dark matter models". In: *Phys. Rev. D* 93.11 (2016), p. 115016. DOI: 10.1103/PhysRevD.93.115016. arXiv: 1512.06458 [hep-ph].

[323] Jennifer M. Gaskins. "A review of indirect searches for particle dark matter". In: *Contemp. Phys.* 57.4 (2016), pp. 496–525. DOI: 10.1080/00107514.2016.1175160. arXiv: 1604.00014 [astro-ph.HE].

[324] Giorgio Arcadi et al. "The waning of the WIMP? A review of models, searches, and constraints". In: *Eur. Phys. J. C* 78.3 (2018), p. 203. DOI: 10.1140/epjc/s10052-018-5662-y. arXiv: 1703.07364 [hep-ph].

[325] Leszek Roszkowski, Enrico Maria Sessolo, and Sebastian Trojanowski. "WIMP dark matter candidates and searches—current status and future prospects". In: *Rept. Prog. Phys.* 81.6 (2018), p. 066201. DOI: 10.1088/1361-6633/aab913. arXiv: 1707.06277 [hep-ph].

[326] Giorgio Arcadi, Abdelhak Djouadi, and Martti Raidal. "Dark Matter through the Higgs portal". In: *Phys. Rept.* 842 (2020), pp. 1–180. DOI: 10.1016/j.physrep.2019.11.003. arXiv: 1903.03616 [hep-ph].

[327] Peter Athron et al. "Status of the scalar singlet dark matter model". In: *Eur. Phys. J. C* 77.8 (2017), p. 568. DOI: 10.1140/epjc/s10052-017-5113-1. arXiv: 1705.07931 [hep-ph].

[328] Peter Athron et al. "Global analyses of Higgs portal singlet dark matter models using GAMBIT". In: *Eur. Phys. J. C* 79.1 (2019), p. 38. DOI: 10.1140/epjc/s10052-018-6513-6. arXiv: 1808.10465 [hep-ph].

[329] Peter Athron et al. "Impact of vacuum stability, perturbativity and XENON1T on global fits of $\mathbb{Z}_2$ and $\mathbb{Z}_3$ scalar singlet dark matter". In: *Eur. Phys. J. C* 78.10 (2018), p. 830. DOI: 10.1140/epjc/s10052-018-6314-y. arXiv: 1806.11281 [hep-ph].

[330] Yohei Ema, Kazunori Nakayama, and Yong Tang. "Production of Purely Gravitational Dark Matter". In: *JHEP* 09 (2018), p. 135. DOI: 10.1007/JHEP09(2018)135. arXiv: 1804.07471 [hep-ph].

[331] Mathias Garny, McCullen Sandora, and Martin S. Sloth. "Planckian Interacting Massive Particles as Dark Matter". In: *Phys. Rev. Lett.* 116.10 (2016), p. 101302. DOI: 10.1103/PhysRevLett.116.101302. arXiv: 1511.03278 [hep-ph].

[332] Mathias Garny et al. "Theory and Phenomenology of Planckian Interacting Massive Particles as Dark Matter". In: *JCAP* 02 (2018), p. 027. DOI: 10.1088/1475-7516/2018/02/027. arXiv: 1709.09688 [hep-ph].

[333] Manuel Reichert and Juri Smirnov. "Dark Matter meets Quantum Gravity". In: *Phys. Rev. D* 101.6 (2020), p. 063015. DOI: 10.1103/PhysRevD.101.063015. arXiv: 1911.00012 [hep-ph].

[334] Yu Hamada, Koji Tsumura, and Masatoshi Yamada. "Scalegenesis and fermionic dark matters in the flatland scenario". In: *Eur. Phys. J. C* 80.5 (2020), p. 368. DOI: 10.1140/epjc/s10052-020-7929-3. arXiv: 2002.03666 [hep-ph].

[335] Richard H. Cyburt et al. "Big Bang Nucleosynthesis: 2015". In: *Rev. Mod. Phys.* 88 (2016), p. 015004. DOI: 10.1103/RevModPhys.88.015004. arXiv: 1505.01076 [astro-ph.CO].

[336] Cyril Pitrou et al. "Precision big bang nucleosynthesis with improved Helium-4 predictions". In: *Phys. Rept.* 754 (2018), pp. 1–66. DOI: 10.1016/j.physrep.2018.04.005. arXiv: 1801.08023 [astro-ph.CO].

[337] Grace Dupuis. "Collider Constraints and Prospects of a Scalar Singlet Extension to Higgs Portal Dark Matter". In: *JHEP* 07 (2016), p. 008. DOI: 10.1007/JHEP07(2016)008. arXiv: 1604.04552 [hep-ph].

[338] D. S. Akerib et al. "Results from a search for dark matter in the complete LUX exposure". In: *Phys. Rev. Lett.* 118.2 (2017), p. 021303. DOI: 10.1103/PhysRevLett.118.021303. arXiv: 1608.07648 [astro-ph.CO].

[339] R. Agnese et al. "Low-mass dark matter search with CDMSlite". In: *Phys. Rev. D* 97.2 (2018), p. 022002. DOI: 10.1103/PhysRevD.97.022002. arXiv: 1707.01632 [astro-ph.CO].

[340] Xiangyi Cui et al. "Dark Matter Results From 54-Ton-Day Exposure of PandaX-II Experiment". In: *Phys. Rev. Lett.* 119.18 (2017), p. 181302. DOI: 10.1103/PhysRevLett.119.181302. arXiv: 1708.06917 [astro-ph.CO].

[341] E. Aprile et al. "Dark Matter Search Results from a One Ton-Year Exposure of XENON1T". In: *Phys. Rev. Lett.* 121.11 (2018), p. 111302. DOI: 10.1103/PhysRevLett.121.111302. arXiv: 1805.12562 [astro-ph.CO].

[342] Donal O'Connell, Michael J. Ramsey-Musolf, and Mark B. Wise. "Minimal Extension of the Standard Model Scalar Sector". In: *Phys. Rev. D* 75 (2007), p. 037701. DOI: 10.1103/PhysRevD.75.037701. arXiv: hep-ph/0611014.

[343] Georges Aad et al. "Search for invisible decays of a Higgs boson using vector-boson fusion in pp collisions at $\sqrt{s} = 8$ TeV with the ATLAS detector". In: *JHEP* 01 (2016), p. 172. DOI: 10.1007/JHEP01(2016)172. arXiv: 1508.07869 [hep-ex].

[344] Georges Aad et al. "Constraints on new phenomena via Higgs boson couplings and invisible decays with the ATLAS detector". In: *JHEP* 11 (2015), p. 206. DOI: 10.1007/JHEP11(2015)206. arXiv: 1509.00672 [hep-ex].

[345] Vardan Khachatryan et al. "Searches for invisible decays of the Higgs boson in pp collisions at $\sqrt{s} = 7$, 8, and 13 TeV". In: *JHEP* 02 (2017), p. 135. DOI: 10.1007/JHEP02(2017)135. arXiv: 1610.09218 [hep-ex].

[346] Albert M Sirunyan et al. "Search for invisible decays of a Higgs boson produced through vector boson fusion in proton-proton collisions at $\sqrt{s} = 13$ TeV". In: *Phys. Lett. B* 793 (2019), pp. 520–551. DOI: 10.1016/j.physletb.2019.04.025. arXiv: 1809.05937 [hep-ex].

[347] Astrid Eichhorn and Michael M. Scherer. "Planck scale, Higgs mass, and scalar dark matter". In: *Phys. Rev. D* 90.2 (2014), p. 025023. DOI: 10.1103/PhysRevD.90.025023. arXiv: 1404.5962 [hep-ph].

[348] Aaron Held and René Sondenheimer. "Higgs stability-bound and fermionic dark matter". In: *JHEP* 02 (2019), p. 166. DOI: 10.1007/JHEP02(2019)166. arXiv: 1811.07898 [hep-ph].

[349] Jan H. Kwapisz. "Asymptotic safety, the Higgs boson mass, and beyond the standard model physics". In: *Phys. Rev. D* 100.11 (2019), p. 115001. DOI: 10.1103/PhysRevD.100.115001. arXiv: 1907.12521 [hep-ph].

[350] Matthew Gonderinger et al. "Vacuum Stability, Perturbativity, and Scalar Singlet Dark Matter". In: *JHEP* 01 (2010), p. 053. DOI: 10.1007/JHEP01(2010)053. arXiv: 0910.3167 [hep-ph].

[351] Valentin V. Khoze, Christopher McCabe, and Gunnar Ro. "Higgs vacuum stability from the dark matter portal". In: *JHEP* 08 (2014), p. 026. DOI: 10.1007/JHEP08(2014)026. arXiv: 1403.4953 [hep-ph].

[352] Oleg Lebedev. "On Stability of the Electroweak Vacuum and the Higgs Portal". In: *Eur. Phys. J. C* 72 (2012), p. 2058. DOI: 10.1140/epjc/s10052-012-2058-2. arXiv: 1203.0156 [hep-ph].

[353] Joan Elias-Miro et al. "Stabilization of the Electroweak Vacuum by a Scalar Threshold Effect". In: *JHEP* 06 (2012), p. 031. DOI: 10.1007/JHEP06(2012)031. arXiv: 1203.0237 [hep-ph].

[354] Adam Falkowski, Christian Gross, and Oleg Lebedev. "A second Higgs from the Higgs portal". In: *JHEP* 05 (2015), p. 057. DOI: 10.1007/JHEP05(2015)057. arXiv: 1502.01361 [hep-ph].

[355] Lawrence J. Hall et al. "Freeze-In Production of FIMP Dark Matter". In: *JHEP* 03 (2010), p. 080. DOI: 10.1007/JHEP03(2010)080. arXiv: 0911.1120 [hep-ph].

[356] Nicolás Bernal et al. "The Dawn of FIMP Dark Matter: A Review of Models and Constraints". In: *Int. J. Mod. Phys. A* 32.27 (2017), p. 1730023. DOI: 10.1142/S0217751X1730023X. arXiv: 1706.07442 [hep-ph].

[357] Carlos E. Yaguna. "The Singlet Scalar as FIMP Dark Matter". In: *JHEP* 08 (2011), p. 060. DOI: 10.1007/JHEP08(2011)060. arXiv: 1105.1654 [hep-ph].

[358] Xiaoyong Chu, Thomas Hambye, and Michel H. G. Tytgat. "The Four Basic Ways of Creating Dark Matter Through a Portal". In: *JCAP* 05 (2012), p. 034. DOI: 10.1088/1475-7516/2012/05/034. arXiv: 1112.0493 [hep-ph].

[359] Jerome Martin, Christophe Ringeval, and Vincent Vennin. "Observing Inflationary Reheating". In: *Phys. Rev. Lett.* 114.8 (2015), p. 081303. DOI: 10.1103/PhysRevLett.114.081303. arXiv: 1410.7958 [astro-ph.CO].

[360] Mustafa A. Amin et al. "Nonperturbative Dynamics Of Reheating After Inflation: A Review". In: *Int. J. Mod. Phys. D* 24 (2014), p. 1530003. DOI: 10.1142/S0218271815300037. arXiv: 1410.3808 [hep-ph].

[361] Matti Heikinheimo et al. "Observational Constraints on Decoupled Hidden Sectors". In: *Phys. Rev. D* 94.6 (2016). [Erratum: Phys.Rev.D 96, 109902 (2017)], p. 063506. DOI: 10.1103/PhysRevD.94.063506. arXiv: 1604.02401 [astro-ph.CO].

[362] Fatemeh Elahi, Christopher Kolda, and James Unwin. "UltraViolet Freeze-in". In: *JHEP* 03 (2015), p. 048. DOI: 10.1007/JHEP03(2015)048. arXiv: 1410.6157 [hep-ph].

[363] Marco Chianese, Bowen Fu, and Stephen F. King. "Impact of Higgs portal on gravity-mediated production of superheavy dark matter". In: *JCAP* 06 (2020), p. 019. DOI: 10.1088/1475-7516/2020/06/019. arXiv: 2003.07366 [hep-ph].

[364] Gia Dvali, Cesar Gomez, and Sebastian Zell. "Discrete Symmetries Excluded by Quantum Breaking". In: (Nov. 2018). arXiv: 1811.03077 [hep-th].

[365] F. Léonard, B. Delamotte, and N. Wschebor. "Naturally light scalar particles: a generic and simple mechanism". In: (Feb. 2018). arXiv: 1802.09418 [hep-ph].

[366] Holger Gies and Christof Wetterich. "Renormalization flow of bound states". In: *Phys. Rev. D* 65 (2002), p. 065001. DOI: 10.1103/PhysRevD.65.065001. arXiv: hep-th/0107221.

[367] Holger Gies, Stefan Rechenberger, and Michael M. Scherer. "Towards an Asymptotic-Safety Scenario for Chiral Yukawa Systems". In: *Eur. Phys. J. C* 66 (2010), pp. 403–418. DOI: 10.1140/epjc/s10052-010-1257-y. arXiv: 0907.0327 [hep-th].

[368] F. Léonard and B. Delamotte. "Critical Exponents Can Be Different on the Two Sides of a Transition: A Generic Mechanism". In: *Phys. Rev. Lett.* 115.20 (2015), p. 200601. DOI: 10.1103/PhysRevLett.115.200601. arXiv: 1508.07852 [cond-mat.stat-mech].

[369] Laura Classen, Igor F. Herbut, and Michael M. Scherer. "Fluctuation-induced continuous transition and quantum criticality in Dirac semimetals". In: *Phys. Rev. B* 96.11 (2017), p. 115132. DOI: 10.1103/PhysRevB.96.115132. arXiv: 1705.08973 [cond-mat.str-el].

[370] Riccardo Ben Alì Zinati and Alessandro Codello. "Functional RG approach to the Potts model". In: *J. Stat. Mech.* 1801.1 (2018), p. 013206. DOI: 10.1088/1742-5468/aa9dcc. arXiv: 1707.03410 [cond-mat.stat-mech].

[371] Emilio Torres et al. "Fermion-induced quantum criticality with two length scales in Dirac systems". In: *Phys. Rev. B* 97.12 (2018), p. 125137. DOI: 10.1103/PhysRevB.97.125137. arXiv: 1802.00364 [cond-mat.str-el].

[372] Shao-Kai Jian, Michael M. Scherer, and Hong Yao. "Mass hierarchy in collective modes of pair-density-wave superconductors". In: *Phys. Rev. Res.* 2.1 (2020), p. 013034. DOI: 10.1103/PhysRevResearch.2.013034. arXiv: 1810.01415 [cond-mat.str-el].

[373] A. Codello et al. "Multicritical Landau-Potts field theory". In: *Phys. Rev. D* 102.12 (2020), p. 125024. DOI: 10.1103/PhysRevD.102.125024.

[374] Genevieve Belanger et al. "Z_3 Scalar Singlet Dark Matter". In: *JCAP* 01 (2013), p. 022. DOI: 10.1088/1475-7516/2013/01/022. arXiv: 1211.1014 [hep-ph].

[375] Andi Hektor, Andrzej Hryczuk, and Kristjan Kannike. "Improved bounds on $\mathbb{Z}_3$ singlet dark matter". In: *JHEP* 03 (2019), p. 204. DOI: 10.1007/JHEP03(2019)204. arXiv: 1901.08074 [hep-ph].

[376] Aigeng Yang and Hao Sun. "Scalar dark matter with Z_3 symmetry in Type-II Seesaw". In: (Apr. 2021). arXiv: 2104.01045 [hep-ph].

[377] Ian Affleck and Michael Dine. "A New Mechanism for Baryogenesis". In: *Nucl. Phys. B* 249 (1985), pp. 361–380. DOI: 10.1016/0550-3213(85)90021-5.

[378] Michael Dine, Lisa Randall, and Scott D. Thomas. "Baryogenesis from flat directions of the supersymmetric standard model". In: *Nucl. Phys. B* 458 (1996), pp. 291–326. DOI: 10.1016/0550-3213(95)00538-2. arXiv: hep-ph/9507453.

[379] Michael Dine and Alexander Kusenko. "The Origin of the matter - antimatter asymmetry". In: *Rev. Mod. Phys.* 76 (2003), p. 1. DOI: 10.1103/RevModPhys.76.1. arXiv: hep-ph/0303065.

[380] Rouzbeh Allahverdi and Anupam Mazumdar. "A mini review on Affleck-Dine baryogenesis". In: *New J. Phys.* 14 (2012), p. 125013. DOI: 10.1088/1367-2630/14/12/125013.

[381] Mark P. Hertzberg and Johanna Karouby. "Baryogenesis from the Inflaton Field". In: *Phys. Lett. B* 737 (2014), pp. 34–38. DOI: 10.1016/j.physletb.2014.08.021. arXiv: 1309.0007 [hep-ph].

[382] D. P. Rideout and R. D. Sorkin. "A Classical sequential growth dynamics for causal sets". In: *Phys. Rev. D* 61 (2000), p. 024002. DOI: 10.1103/PhysRevD.61.024002. arXiv: gr-qc/9904062.

[383] Dionigi M. T. Benincasa and Fay Dowker. "The Scalar Curvature of a Causal Set". In: *Phys. Rev. Lett.* 104 (2010), p. 181301. DOI: 10.1103/PhysRevLett.104.181301. arXiv: 1001.2725 [gr-qc].

[384] N. Klitgaard and R. Loll. "Introducing Quantum Ricci Curvature". In: *Phys. Rev. D* 97.4 (2018), p. 046008. DOI: 10.1103/PhysRevD.97.046008. arXiv: 1712.08847 [hep-th].

[385] N. Klitgaard and R. Loll. "Implementing quantum Ricci curvature". In: *Phys. Rev. D* 97.10 (2018), p. 106017. DOI: 10.1103/PhysRevD.97.106017. arXiv: 1802.10524 [hep-th].

[386] Pim van der Hoorn et al. "Ollivier-Ricci curvature convergence in random geometric graphs". In: *Phys. Rev. Res.* 3.1 (2021), p. 013211. DOI: 10.1103/PhysRevResearch.3.013211. arXiv: 2008.01209 [math.PR].

[387] Pim van der Hoorn et al. "Ollivier curvature of random geometric graphs converges to Ricci curvature of their Riemannian manifolds". In: (Sept. 2020). arXiv: 2009.04306 [math.PR].

[388] Jure Leskovec and Rok Sosič. "SNAP: A General-Purpose Network Analysis and Graph-Mining Library". In: *ACM Transactions on Intelligent Systems and Technology (TIST)* 8.1 (2016), p. 1.

[389] Jure Leskovec et al. "Community structure in large networks: Natural cluster sizes and the absence of large well-defined clusters". In: *Internet Mathematics* 6.1 (2009), pp. 29–123.

[390] *10th DIMACS Challenge.* https://www.cc.gatech.edu/dimacs10/archive/streets.shtml. Accessed: 2021-04-19.

[391] Joseph E Knox et al. "High-resolution data-driven model of the mouse connectome". In: *Network Neuroscience* 3.1 (2018), pp. 217–236.

[392] David Brizuela, Jose M. Martin-Garcia, and Guillermo A. Mena Marugan. "xPert: Computer algebra for metric perturbation theory". In: *Gen. Rel. Grav.* 41 (2009), pp. 2415–2431. DOI: 10.1007/s10714-009-0773-2. arXiv: 0807.0824 [gr-qc].

[393] José M. Martín-García. "xPerm: fast index canonicalization for tensor computer algebra". In: *Computer Physics Communications* 179.8 (2008), 597–603. ISSN: 0010-4655. DOI: 10.1016/j.cpc.2008.05.009. URL: http://dx.doi.org/10.1016/j.cpc.2008.05.009.

[394] I. Hamzaan Bridle, Juergen A. Dietz, and Tim R. Morris. "The local potential approximation in the background field formalism". In: *JHEP* 03 (2014), p. 093. DOI: 10.1007/JHEP03(2014)093. arXiv: 1312.2846 [hep-th].

[395] Yannick Kluth and Daniel F. Litim. "Heat kernel coefficients on the sphere in any dimension". In: *Eur. Phys. J. C* 80.3 (2020), p. 269. DOI: 10.1140/epjc/s10052-020-7784-2. arXiv: 1910.00543 [hep-th].

[396] Astrid Eichhorn, Holger Gies, and Michael M. Scherer. "Asymptotically free scalar curvature-ghost coupling in Quantum Einstein Gravity". In: *Phys. Rev. D* 80 (2009), p. 104003. DOI: 10.1103/PhysRevD.80.104003. arXiv: 0907.1828 [hep-th].

[397] Pietro Dona and Roberto Percacci. "Functional renormalization with fermions and tetrads". In: *Phys. Rev. D* 87.4 (2013), p. 045002. DOI: 10.1103/PhysRevD.87.045002. arXiv: 1209.3649 [hep-th].

[398] Dario Benedetti and Francesco Caravelli. "The Local potential approximation in quantum gravity". In: *JHEP* 06 (2012). [Erratum: JHEP 10, 157 (2012)], p. 017. DOI: 10.1007/JHEP06(2012)017. arXiv: 1204.3541 [hep-th].

[399] Nobuyoshi Ohta, Roberto Percacci, and Gian Paolo Vacca. "Flow equation for $f(R)$ gravity and some of its exact solutions". In: *Phys. Rev. D* 92.6 (2015), p. 061501. DOI: 10.1103/PhysRevD.92.061501. arXiv: 1507.00968 [hep-th].

[400] Nobuyoshi Ohta, Roberto Percacci, and Gian Paolo Vacca. "Renormalization Group Equation and scaling solutions for f(R) gravity in exponential parametrization". In: *Eur. Phys. J. C* 76.2 (2016), p. 46. DOI: 10.1140/epjc/s10052-016-3895-1. arXiv: 1511.09393 [hep-th].

[401] Holger Gies and Stefan Lippoldt. "Fermions in gravity with local spin-base invariance". In: *Phys. Rev. D* 89.6 (2014), p. 064040. DOI: 10.1103/PhysRevD.89.064040. arXiv: 1310.2509 [hep-th].

[402] A. Semenov. "LanHEP: A Package for the automatic generation of Feynman rules in field theory. Version 3.0". In: *Comput. Phys. Commun.* 180 (2009), pp. 431–454. DOI: 10.1016/j.cpc.2008.10.012. arXiv: 0805.0555 [hep-ph].

[403] Alexander Belyaev, Neil D. Christensen, and Alexander Pukhov. "CalcHEP 3.4 for collider physics within and beyond the Standard Model". In: *Comput. Phys. Commun.* 184 (2013), pp. 1729–1769. DOI: 10.1016/j.cpc.2013.01.014. arXiv: 1207.6082 [hep-ph].

[404] Paolo Gondolo and Graciela Gelmini. "Cosmic abundances of stable particles: Improved analysis". In: *Nucl. Phys. B* 360 (1991), pp. 145–179. DOI: 10.1016/0550-3213(91)90438-4.

[405] Carl M. Bender and Sarben Sarkar. "Asymptotic Analysis of the Boltzmann Equation for Dark Matter Relics". In: *J. Math. Phys.* 53 (2012), p. 103509. DOI: 10.1063/1.4753990. arXiv: 1203.1822 [hep-th].

[406] Logan Morrison. *Solving the Boltzmann Equation*. https://loganamorrison.github.io/2019/08/24/solving-the-boltzmann-equation.html. Accessed: 2021-07-19.

[407] Daniel Baumann. "Primordial Cosmology". In: *PoS* TASI2017 (2018), p. 009. DOI: 10.22323/1.305.0009. arXiv: 1807.03098 [hep-th].

[408] Geneviève Bélanger et al. "micrOMEGAs5.0 : Freeze-in". In: *Comput. Phys. Commun.* 231 (2018), pp. 173–186. DOI: 10.1016/j.cpc.2018.04.027. arXiv: 1801.03509 [hep-ph].